A Thesis Submitted to Indian Institute of Technology Guwahati for the Degree of

Doctor of Philosophy

Atomistic Modelling of Structurally Engineered 2D Materials for Enhanced Gas Sensing and CO_2 Conversion

Submitted by

Upasana Nath

Roll No. 186122113

Under the Supervision of

Prof. Manabendra Sarma

Department of Chemistry

Indian Institute of Technology Guwahati

Guwahati, Assam, India

Academic Year 2019-2025

INDIAN INSTITUTE OF TECHNOLOGY GUWAHATI

Department of Chemistry

CERTIFICATE

It is certified that the work entitled *"Atomistic Modelling of Structurally Engineered 2D Materials for Enhanced Gas Sensing and CO_2 Conversion"* by *Upasana Nath*, a Ph.D student in the Department of Chemistry, Indian Institute of Technology Guwahati, Guwahati, Assam, India, was carried out under my supervision and has not been submitted elsewhere for the award of any degree.

Prof. Manbendra Sarma

Professor, Department of Chemistry

Indian Institute of Technology Guwahati

Guwahati, Assam

India, 781039

DATE:

INDIAN INSTITUTE OF TECHNOLOGY GUWAHATI

Department of Chemistry

DECLARATION

I hereby declare that the thesis entitled *"Atomistic Modelling of Structurally Engineered 2D Materials for Enhanced Gas Sensing and CO_2 Conversion"* has been carried out by me under the supervision of *Prof. Manabendra Sarma*, Department of Chemistry, Indian Institute of Technology Guwahati, submitted for the award of the degree of Doctor of Philosophy, is my original work. It has not been submitted to any other university or institution for any degree or qualification.

Upasana Nath

Roll No. 186122113

Department of Chemistry

Indian Institute of Technology Guwahati

Guwahati, Assam

India, 781039

DATE:

DEDICATED TO

My dearest family – my greatest cheerleaders & All my teachers – pillars of scholarly guidance – for nurturing my curiosity, shaping my values, and believing in me.

– **With Deepest Gratitude**

ACKNOWLEDGMENTS

I take this opportunity to convey my sincere gratitude and respect to all who supported me during my research journey.

First and foremost, I owe my deepest sense of gratitude to my research supervisor, ***Prof. Manabendra Sarma***, Professor, Department of Chemistry, Indian Institute of Technology Guwahati, for his constant encouragement, insightful mentorship, and thought-provoking discussions. He provided me with exposure to diverse fields of science and enabled me to undergo rigorous training. His continuous support and belief in my abilities greatly enhanced my confidence and enabled me to complete this work. His profound knowledge of the subject, strong analytical thinking, and systematic approach to experimentation have consistently guided me throughout these years. I remain deeply grateful to him and consider it a privilege to have conducted my research under his mentorship.

I express my sincere gratitude to my Doctoral Committee members ***Prof. Kalyan Raidongia***, Professor, Department of Chemistry, Indian Institute of Technology Guwahati, ***Prof. Aditya Narayan Panda***, Professor, Department of Chemistry, Indian Institute of Technology Guwahati, ***Prof. P.K. Giri*** Professor, Department of Physics, Indian Institute of Technology Guwahati for evaluating my research throughout my Ph.D. journey and generously sharing their knowledge through valuable feedback, which significantly contributed to enhancing the quality of my work.

I am thankful to the Department of Chemistry, Indian Institute of Technology Guwahati, for providing me with the opportunity and the necessary infrastructure to carry out my research. I would also like to acknowledge the ***Param-Ishan*** and ***Param-Kamrupa*** supercomputing facilities, without which this work would not have been possible. My sincere thanks to the HPC Support and Param-Kamrupa Support teams for their continuous assistance throughout the course of my

research.

I take this opportunity to thank ***Prof. P.K. Giri***, Professor, Department of Physics, Indian Institute of Technology Guwahati, and ***Prof. Mohammad Qureshi***, Professor, Department of Chemistry, Indian Institute of Technology Guwahati, for giving us the opportunity to collaborate with them. The experience, along with their thoughtful guidance and enriching discussions, greatly enhanced my understanding of the subject and contributed meaningfully to my research journey.

My sincere thanks to ***Dr. Prasanta Jyoti Gautam***, Associate Professor, Assam Kaziranga University and ***Dr. Nabajyoti Saikia***, Professor & Dean, Assam Kaziranga University, for their insightful suggestions and constant encouragement that played a pivotal role in shaping my interest in research.

I gratefully acknowledge the ***INSPIRE Fellowship*** from the Department of Science and Technology (DST), India, for providing financial support throughout the duration of my research. This fellowship played a vital role in enabling me to pursue my work without interruption.

I whole-heartedly thank all my seniors, colleagues, juniors, and friends – Dr. Kisan, Dr. Himanshu, Bittu, Dr. Juhi, Niharika, Monalisha, Rabu, Biman, Subham, Manash, Samsung, Rimi, Ananad, Yugant, Madhab, and Tadasha for their cooperation at various stages of this work, lively company, experienced advice, valuable collaborations, and helpful discussions. Their presence made this experience both enriching and memorable.

Words cannot truly capture the depth of my gratitude to my family, whose unconditional love, constant encouragement, and countless sacrifices have been the backbone of my Ph.D. journey. Their unwavering belief in me gave me strength during the most challenging times and joy during the milestones. Without their support, both emotional and practical, this journey would not have been possible. I feel truly blessed to have them by my side every step of the way.

My sincere regards to all my teachers over the years, my well-wishers, and everyone, both directly and indirectly, who have contributed to this journey.

Sincerely

Upasana Nath

ABSTRACT

The emission of various air pollutants originating from natural sources and rapid urbanization led to the depletion of the environment, public health, and economies worldwide. Therefore, developing a highly efficient gas sensor and catalyst for the conversion of pollutants into valuable resources is integral to monitoring and protecting global sustainability. The atomically thin two-dimensional (2D) materials with remarkable properties unlock new possibilities or enhance solutions to many energy and environmental challenges. However, 2D materials with fixed properties are not flexible enough to meet the diverse demands of emerging applications. Atomic-scale structural (ASS) modifications provide a precise and effective strategies for tuning the material properties, enabling the design of highly functional and versatile materials. ASS modification alters charge density, lattice symmetry, and electronic properties of the materials and thereby broadens the scope of potential applications. Thus, this thesis explores the ASS modification of various 2D materials, including graphene, oxygen-functionalized boron sulfide monolayer (Oh-B_2S_2), and bilayer borophene, to enhance their functionality for gas sensing and electrocatalytic applications.

SYNOPSIS REPORT

Chapter 1: Introduction

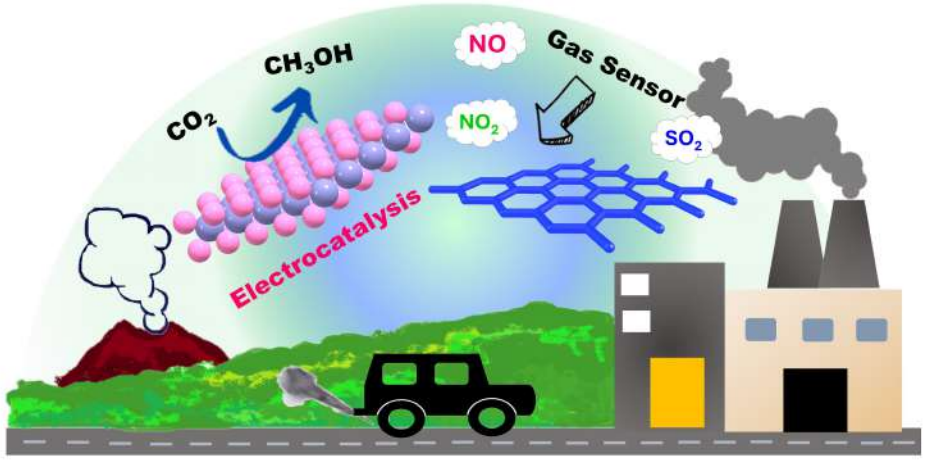

The success of graphene has paved the way for the exploration and development of next-generation 2D materials. The unique properties of 2D materials, including high surface area, flexibility, tunable band gap, atomic thickness, and high conductivity, make them ideal for various applications. Global air pollution has become a constant threat to the environment and human health over the past few decades. Hence, a potential solution to address global air pollution is (1) the detection of toxic gases (sensing) and (2) the catalytic reduction of toxic pollutants into value-added chemicals and feedstocks. However, pristine 2D materials with fixed properties may not meet the needs of diverse developing applications. Therefore, property tweaking with atomic-scale structure (ASS) modification is critical in functional devices. Thus, this chapter describes various 2D materials used throughout our thesis, along with different ASS and their applications in energy and environmental sustainability.

Chapter 2: Theoretical Background

This chapter introduces the fundamental concepts and mathematical principles of materials to understand their behavior, properties, and applications at various structural scales. This begins with the Schrödinger equation (SE), which gives a fully quantum-mechanical description of materials with many nuclei and many-electron wave functions. The underlying principles of density function theory (DFT) and Kohn-Sham formalism have been discussed. Considering the intrinsic periodic nature of solid-state materials, this chapter also includes concepts such as periodic boundary conditions (PBCs), Bloch's theorem, and pseudopotentials. This chapter also covers different types of basis sets and functions that are utilized in the calculations. Additionally, this chapter explores various Ab initio molecular dynamics (AIMD) methods for computing finite-temperature dynamical trajectories of the structures. Finally, it includes an introduction to the Non-Equilibrium Green's Function (NEGF) approach, combined with the Landauer formalism, to describe quantum transport in materials.

Chapter 3: Pyridinic-N Graphene as an efficient SO_2 Sensor

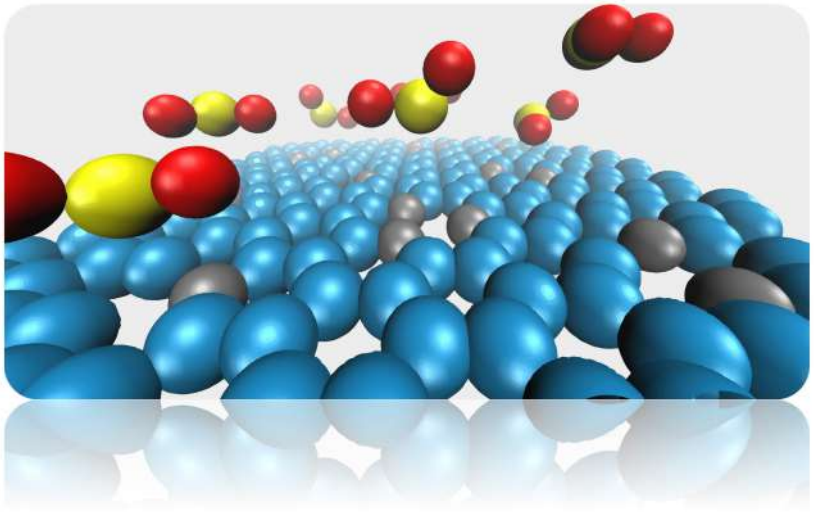

In this chapter, we explore the SO_2 sensing potential of pyridinic N-doped graphene (PNG) under the framework of spin-polarized DFT incorporating van der Waals correction and AIMD simulation. PNG is of great importance since doping and defects create an active region on the surface through overlapping charge and spin densities. Our findings imply that SO_2 binds with energies between -0.30 and -0.80 eV, which shows that the PNG monolayer towards SO_2 detection is reversible. The environmental selectivity of PNG towards SO_2 was also revealed by studying the effect of major environmental composites such as CO_2, N_2, O_2, and H_2O. Furthermore, the adsorption potential of SO_2 on PNG can be strengthened or weakened by applying external strains or electric fields, which is highly desirable to control the sensing performance of the monolayers. Our work is a step toward the vision of developing efficient gas sensors for the detection of toxic gas molecules in the environment.

Chapter 4: Surface Oxygen Functionalized B_2S_2 Monolayer for NO and NO_2 Detection

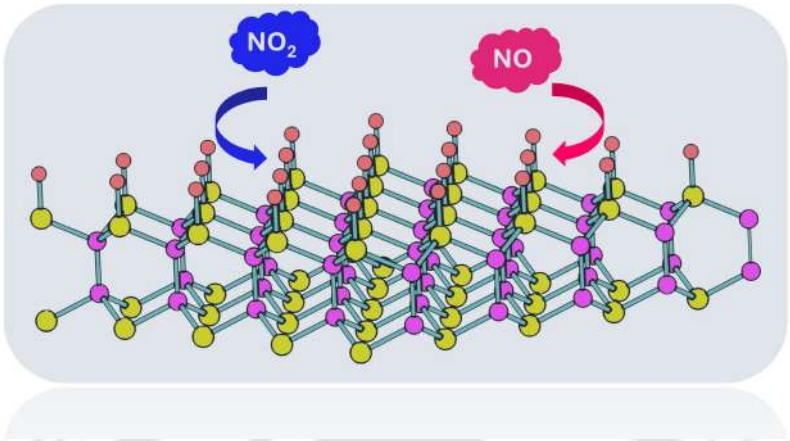

In this chapter, we functionalized the h-phase boron sulfide monolayer with an oxygen atom for the first time, denoted as Oh-B_2S_2, and studied its structure, stability, and electronic properties. The charge carrier mobility was 789 $\times$ 10^2 cm^2 V^{-1} s^{-1}, significantly higher than the mobility of MoS_2 monolayer (200 cm^2 V^{-1} s^{-1}). The gas sensing potential of the 2D Oh-B_2S_2 nanosheet was assessed using DFT, AIMD, and NEGF simulations. The higher adsorption energy and charge transfer values of the Oh-B_2S_2 nanosheet make it a superior NO and NO_2 selective sensing material compared to graphene and MoS_2. The current-voltage (I-V) plots demonstrate the existence of gas molecules after a 1.0 V bias voltage. Further, the observed negative difference resistance (NDR) of the Oh-B_2S_2 nanosensor after the adsorption of gases can be elucidated through the analysis of transmission spectra plots obtained under different biases. Overall, the findings of our study demonstrate the potential viability of novel and MoS_2-like 2D materials with lighter elements such as boron in the realm of forthcoming nanosensors.

Chapter 5: Defect-Induced Bilayer Borophene for Charge Controlled CO_2 Activation

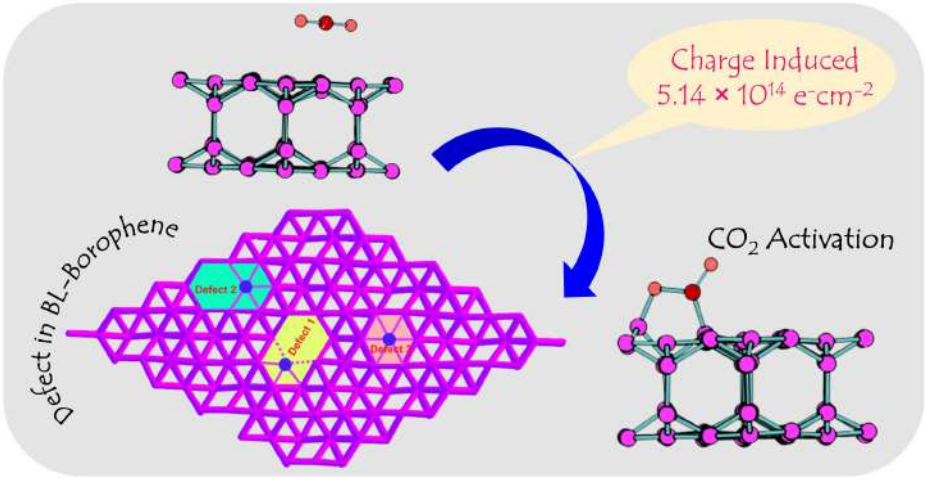

This chapter investigates different point defects in bilayer borophene (BL-B) to understand their impact on CO_2 activation by modulating its charge states. Our findings reveal that at charge density 5.12×10^{14} $e^{-}cm^{-2}$, the defect-induced bilayer borophene (BL-B-Def-1) leads to the activation of CO_2 with the adsorption energy -1.89 eV. The underlying mechanism of CO_2 activation over a BL-B-Def-1 was elucidated via frontier molecular orbitals (FMOs) and p-band center, where localization of charge at the defect site is crucial. With a charge density of 2.21×10^{15} $e^{-}cm^{-2}$, BL-B-Def-1 had a maximum adsorption capacity of 2.66×10^{14} cm^{-2}. Dissociation (CO^{*} + O^{*}) is observed at 300 K from AIMD simulations. Further, negatively charged BL-B-Def-1 selectively captures CO_2 from gas mixtures. Thus, the study highlights BL-B-Def-1 as a charge-modulated CO_2 capture material with excellent stability, capacity, and selectivity that can be achieved experimentally.

Chapter 6: CO_2 Reduction on Defective Bilayer Borophene: Charge Neutral Method vs. Constant Potential Method

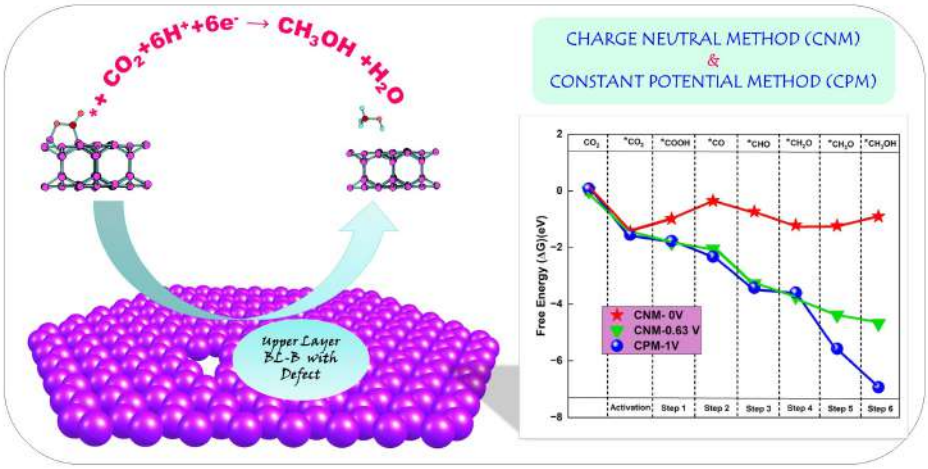

In this chapter, we have studied the electrocatalytic performance of point defects bilayer borophene (BL-B-Def-1) by modulating its charge states using density functional theory (DFT). A computational hydrogen electrode with the charge neutral method (CNM) and constant potential method (CPM) was used to study the catalytic activity of BL-B-Def-1. The CNM assumed the catalyst was a constant or zero-charged system and ignored the applied potential, but the CPM charged the catalyst to align its Fermi level (E_F) in response to the applied electrode potential. We found that CNM and CPM have an overpotential of 0.63 V and 1.0 V, respectively, with product selectivity for CH_3OH. Our findings may help to develop catalysts for CO_2 reduction using charge-induced CO_2 activation and understanding the effect of applied potential on electrochemical processes.

Chapter 7: Conclusions

In this thesis, we explored various ASS modifications such as defects, doping, functionalization, and strain engineering across different 2D surfaces, enhancing material diversity for high-performance gas sensors and electrocatalysts. This chapter summarizes the key findings, conclusions, and overview of our work so far and outlines future research opportunities in the field.

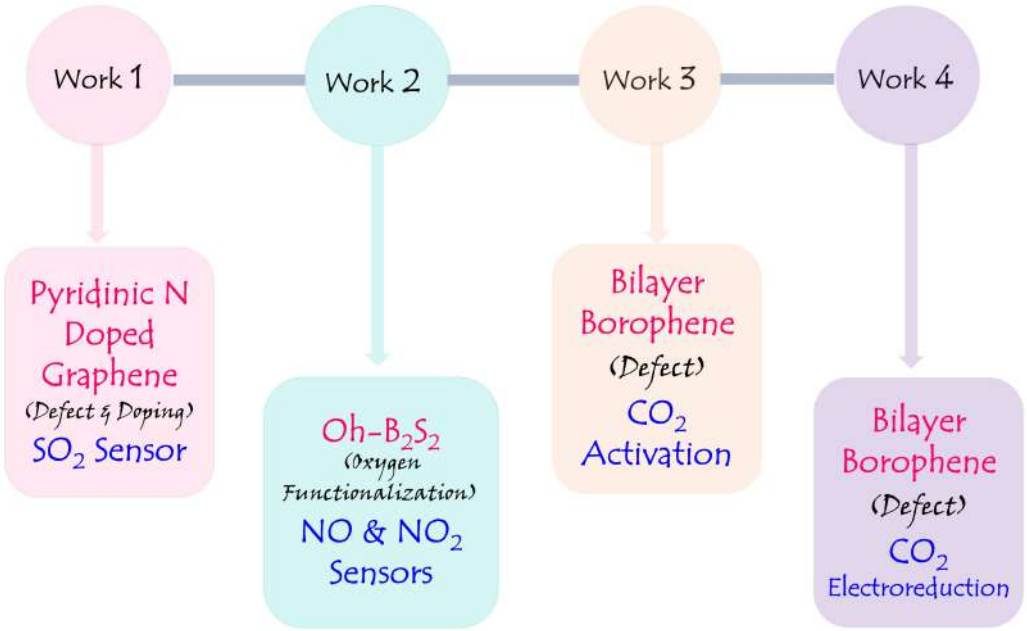

LIST OF PUBLICATIONS

Thesis

1. **Upasana Nath** and Manabendra Sarma. CO_2 Activation and Electrochemical Reduction to CH_3OH via Charge Modulation on Defect-Induced Free-Standing Bilayer Borophene, *J. Phys. Chem. C* 129, 13939−13953, 2025.

2. **Upasana Nath** and Manabendra Sarma. Realization of efficient and selective NO and NO_2 detection via surface functionalized h-B_2S_2 monolayer. *Phys. Chem. Chem. Phys.*, 26, 12386−12396, 2024. (Selected and featured in 2024 PCCP HOT Article).

3. **Upasana Nath** and Manabendra Sarma. Pyridinic dominance N-doped graphene: A potential material for SO_2 gas detection. *J. Phys. Chem. A*, 127, 1112−1123, 2023.

Out of Thesis

1. Nitul Kalita, **Upasana Nath**, Anjana Singha, Manabendra Sarma and Mohammad Qureshi. Electronic structure tuning to facilitate charge transfer in Z-scheme mediated CuO/Se@WO_3 aided by synchronized $Cu(OH)_2$ for efficient overall water splitting *J. Mater. Chem. A*, 13, 10723-10735, 2025.

2. Biman Medhi, **Upasana Nath**, and Manabendra Sarma. Revisiting fulgide photochromism: Mechanistic decoding and electron transport from computational exploration. *J. Chem. Phys.*, 160, 154308, 2024.

3. Tadasha Jena, Garima Choudhary, Md Tarik Hossain, **Upasana Nath**, Manabendra Sarma, and PK Giri. Salt-catalyzed directed growth of bilayer palladium diselenide ($PdSe_2$) dendrites and Pd nanoparticle-decorated $PdSe_2$-Pd_2Se_3 junction exhibiting very high surface enhanced raman scattering sensitivity. *Chem. Mater.*, 36, 5922−5934, 2024.

4. Md Tarik Hossain, Larionette PL Mawlong, Tadasha Jena, Abhilasha Bora, **Upasana Nath**, Manabendra Sarma, and PK Giri. Interlayer charge-transfer-induced photoluminescence quenching and enhanced photoconduction in two-dimensional Bi_2O_2Se/MoS_2 type-II heterojunction. *ACS Appl. Nano Mater.*, 6, 11023−11036, 2023.

5. Haobam Kisan Singh, **Upasana Nath**, Niharika Keot, and Manabendra Sarma. Exploring π-π interactions and electron transport in complexes involving a hexacationic host and PAH guest: a promising avenue for molecular devices. *Phys. Chem. Chem. Phys.*, 25, 26767−26778, 2023.

6. Md Tarik Hossain, Tadasha Jena, **Upasana Nath**, Manabendra Sarma, and PK Giri. Room temperature exciton formation and robust optical properties of CVD-grown ultrathin Bi_2O_2Se crystals on arbitrary substrates. *Nanoscale*, 15,11222−11236, 2023.

7. Tadasha Jena, Md Tarik Hossain, **Upasana Nath**, Manabendra Sarma, Hiroshi Sugimoto, Minoru Fujii, and PK Giri. Evidence for intrinsic defects and nanopores as hotspots in 2D $PdSe_2$ dendrites for plasmon-free SERS substrate with a high enhancement factor. *npj 2D Mater. Appl.*, 7,8, 2023.

List of Conferences Attended

Conference Proceedings

1. Rimi Chyrmang, Upasana Nath, and Manabendra Sarma. Insight into the structural, electronic, and magnetic properties of Mn, Fe, and Co-doped bilayer borophene. Quantum Systems in Chemistry and Physics. Springer Nature, 2024.

Conferences Attended (Poster)

1. Upasana Nath and Manabendra Sarma. Charge-controlled CO_2 activation and electrochemical reduction on free-standing defect-induced bilayer borophene. Physics and Chemistry of Atomic, Molecular and Condensed Matter Systems (PCAMC), Kolkata, Assam, India, 2024.

2. Upasana Nath and Manabendra Sarma. Two-dimensional oxygen functionalized boron sulfide (Oh-B_2S_2) monolayer: An effective nanosensor for NO and NO_2 detection detection. Spectroscopy and Dynamics of Molecules and Clusters (SDMC), Kaziranga, Assam, India, 2024.

3. Upasana Nath and Manabendra Sarma. Insight into the surface oxygen functionalized B_2S_2 monolayer for NO and NO_2 detection. Theoretical Chemistry Symposium, Indian Institute of technology Madras, Chennai, India, 2023.

4. Upasana Nath and Manabendra Sarma. First principle investigation of pyridinic N-doped graphene as a potential SO_2 gas sensor. Graphene 2023, Manchester, UK, 2023.

5. Upasana Nath and Manabendra Sarma. Temperature-dependent NO adsorption and desorption in N-doped graphene monolayer. Recent Advances in Chemistry: Theoretical and Computational Aspects, National Institute of Technology Meghalaya, 2022.

6. Upasana Nath and Manabendra Sarma. Pyridinic dominance graphene as an efficient and selective gas-sensor toward SO_2 detection. North-East Research Conclave, Indian Institute of Technology, Guwahati, 2022.

7. Upasana Nath and Manabendra Sarma. Computational investigation of pyridinic dominance graphene as sensor for oxide-containing triatomic gas molecules. Current Trends in theoretical Chemistry, DAE Convention Center, Mumbai, India, 2022.

8. Upasana Nath and Manabendra Sarma. Role of vacancy on electronic and magnetic properties of pyridinic N-doped graphene. Theoretical Chemistry Symposium, Kolkata, 2021.

9. Upasana Nath and Manabendra Sarma. Adsorption of individual CO gas molecule on graphene using different computational accuracy. Recent Trends In Chemical Science, Indian Chemical Society, Kolkata, 2020.

LIST OF SYMBOLS AND ABBREVIATIONS

2D	Two Dimensional
AIMD	Ab Initio Molecular Dynamics
AD	Adsorption Distance
AE	All Electron
AO	Antibonding Orbital
ASS	Atomic Scale Structural
BOMD	Born Oppenheimer Molecular Dynamics
BL-B	Bilayer Borophene
CO	Carbon Monoxide
CNT	Carbon Nanotube
CDD	Charge Density Difference
C_{2D}	Elastic Modulus
CNM	Charge Neutral Method
CT	Charge Transfer
CB	Conduction Band
CBM	Conduction Band Minimum
CPM	Constant Potential Method
CGF	Contracted Gaussian Function
DFPT	Density Functional Perturbation Theory
DOS	Density of States
DPT	Deformation Potential Theory
DMFC	Direct Methanol Fuel Cell

E-field	Electric Field
ECRR	Electrochemical CO_2 Reduction Reaction
E_X	Exchange Term
E_C	Correlation Term
E_F	Fermi Energy
E_{coh}	Cohesive Energy
E_{form}	Formation Energy
E_{ads}	Adsorption Energy
E_g	Band Gap
E_{vac}	Vacuum Level
E_l^i	Deformation Potential
FET	Field Effect Transistors
GTH	Goedecker-Teter-Hutter
GGA	Generalized Gradient Approximation
GTO	Gaussian Type Orbital
G^n	Correlation Function
h-B_2S_2	Hexagonal-Boron Dichalcogenides
HF	Hartree-Fock
HER	Hydrogen Evolution Reaction
HSE	Heyd, Scuseria, and Ernzerhof
H_2S	Hydrogen Sulfide
I-V	Current-Voltage
KS Method	Kohn-Sham Method
K_B	Boltzmann Constant
LDA	Local Density Approximations
LOD	Limit of Detection
LUMO	Lowest Unoccupied Molecular Orbital
MoS_2	Molybdenum Disulfide
m^*	Effective Mass

NO_x	Nitrogen Oxide
NEGF	Non-Equilibrium Green's Function
NVT	Number-Volume-Temperature
NDR	Negative Differential Resistance
NC-PP	Norm- Conserving Pseudopotentials
OER	Oxygen Evolution Reaction
OER	Oxygen Reduction Reaction
Oh-B_2S_2	Oxygen Functionalized Hexagonal Boron Dichalcogenides
OPW	Orthogonalized Plane-Wave
PNG	Pyridinic Dominance N-doped Graphene
PPA	Pseudopotential Approximation
PBC	Periodic Boundary Condition
PAW	Projector Augmented Wave
PBE	Perdew-Burke-Ernzerhof
PG	Pristine Graphene
PEC	Potential Energy Curve
PDOS	Projected Density of States
PDS	Potential Determining Steps
PECT	Proton Coupled Electron Transfer
QE	Quantum ESPRESSO
RHE	Relative Hydrogen Electrode
SO_x	Sulfur Oxide
SAW	Surface Acoustic Wave
SE	Schrodinger Equation
SPDOS	Spin-Polarized Density of States
SW	Stone-Wales
TMDC	Transition Metal Dichalcogenide
TDSE	Time Dependent Schrodinger Equation
TDOS	Total Density of States

T(E)	Transmission Spectra
U(r)	Coulomb Potential
US-PP	Ultrasoft Pseudopotentials
U_L	Limiting Potential
UV	Ultra Violet
VOC	Volatile Organic Compounds
vdW	van der Waals
VB	Valence Band
VBM	Valence Band Maximum
ϕ	Work Function
ρ	Charge Density
η	Overpotential
ϕ_{SHE}	Standard Hydrogen Electrode
τ	Recovery time
$\Delta\rho(z)$	Plane-Averaged Charge Density Difference
μ	Charge Carrier Mobility

LIST OF FIGURES

LIST OF TABLES

CONTENTS

Chapter 1

INTRODUCTION

This chapter explores the remarkable characteristics of graphene and two recently synthesized two-dimensional (2D) materials: boron dichalcogenides (B_2S_2) and bilayer borophene (BL-B). Various strategies for enhancing their performance, paving the way for promising applications in energy and environmental technologies, have also been addressed in this chapter.

1.1 2D Materials: Graphene and Beyond

The horizon of materials science experienced a groundbreaking advancement in 2004 as Andre Geim and Kostya Novoselov successfully isolated the first 2D monolayer, graphene, using the Scotch tape method to exfoliate graphite mechanically. The impact of this discovery was established through the Nobel Prize in physics (2010) to both scientists [1, 2]. Graphene is an atomically thin material composed of sp^2 hybridized carbon (C) atoms arranged in a hexagonal lattice, where the C−C bond distance is 0.142 nm with three $\sigma-$bonds [2–4]. The pronounced effects of the quantum size of 2D materials from their nanoscale thickness led to notable modifications in their physical and chemical properties [5]. The distinct electronic properties of graphene are characterized by the absence of a band gap, with zero density of states (DOS) near the Fermi level (E_F). Within the honeycomb lattice, electron propagation leads to a complete loss of effective mass, giving rise to quasi-particles governed by a Dirac-like equation rather than the Schrödinger equation, which has been a focus point of scientific interest [2, 3, 6]. In addition to these, graphene has a large surface area (2630 m^2/g), exceptionally high charge carrier mobility ($\sim$ 10000 $cm^2V^{-1}s^{-1}$) [7], outstanding heat conductivity (5×10^3 W/mK) with a thickness of

approximately 0.35 nm [8], and mechanical strength (tensile strength of 125 GPa and elastic modulus of 1.1 TPa) [3]. Thus, these features open up exciting possibilities for graphene over conventional bulk materials [6].

The breakthrough of graphene has increased significant interest in the diverging spectrum of 2D materials, ranging from zero band gap semiconductors to metals to p/n−type semiconductors to insulators to superconductors, with most elements in the periodic table [5, 9–11]. Besides graphene, this thesis focuses on two other recently synthesized boron-based 2D materials: boron dichalcogenide (B_2S_2, 2022) [12] and bilayer borophene (BL-B, 2021) [13]. Boron (B) is the neighboring non-metallic element to carbon (C) with analogous valence orbitals, showing various bonding possibilities with the tendency to form an electron-deficient 3e−2c bond [12, 14]. In addition, it has the ability to adopt sp^2 hybridization, enabling the formation of low-dimensional structures [15].

Boron Dichalcogenide (B_2S_2): A new 2D material, B_2S_2, has been recently synthesized using hydrothermal reactions, and the results are further verified using first-principles calculation [12]. The structure of B_2S_2 resembles that of the transition metal dichalcogenides (TMDCs) such as molybdenum disulfide (MoS_2), where Mo is replaced by a B_2 pair. The B_2 pair, consisting of two boron atoms, has six valence electrons, equivalent to molybdenum (Mo), with a $4d^5 5s^1$ valence electron configuration. Consequently, the B_2 pair can contribute to four valence electrons and is involved in the ionic bond formation with sulfur atoms, analogous to the bonding behavior of Mo in MoS_2. Prior to the experimental fabrication, inspired by the valence electron similarity between Mo and B_2 pairs, Tang *et al.* [16] theoretically predicted the monolayer of B_2S_2. Combining global minimization search with density functional theory (DFT) calculations, they identify two energetically favorable phases of B_2S_2 similar to MoS_2: T-B_2S_2 and H-B_2S_2. The T-B_2S_2 has two B-atoms and two S-atoms in a hexagonal primitive cell with a lattice constant (a) 3.056 Å and space group P3m1, while H-B_2S_2 has space group p6m2 and a = 3.041 Å. Both phases were energetically stable based on cohesive energy calculations (5.78 eV/atom for T-B_2S_2 and 5.77 eV/atom for H-B_2S_2). T-phase and H-phase B_2S_2 show an indirect band gap of 4.09 eV and 3.92 eV, respectively. Additionally, H-B_2S_2 exhibits higher carrier mobility than T-B_2S_2, with an electron carrier mobility of 1.30×10^5 $cm^2V^{-1}s^{-1}$ in the K-M direction, similar to other

graphene-related materials [7, 16–18].

Bilayer Borophene (BL-B): In 2021, Liu *et al.* first synthesized BL-B on Ag(111) using molecular beam epitaxy under ultra-high vacuum conditions [13]. The structure of BL-B is resolved through atomic-scale spatial imaging and DFT calculations. This analysis reveals that the material has two covalently bonded $\alpha-$phase borophene layers, termed BL$-\alpha-$B, which exhibit metallic properties and a distinct moiré pattern [13]. Later, a team led by Xiaojun Wu, Kehui Wu, and Lan Chen synthesized a large-size uniform BL-B over a Cu(111) substrate. Using DFT and scanning tunneling microscopy (STM), they observed that the borophene structure grown on Cu(111) adopts a $\beta_{12}-$type configuration [19]. Furthermore, a wide spectrum of BL-B polymorphs has been theoretically investigated to date [20–22]. Theoretically, the stability of BL-B has been characterized by two key parameters (a) pillar density (ζ-bond between the upper and lower B-sheets) and (b) hexagonal hole density (η) [20].

$$\zeta = \frac{Number\ of\ atoms\ forming\ the\ pillars}{Total\ atoms\ in\ the\ unit\ cell} \tag{1.1}$$

$$\eta = \frac{Number\ of\ hexagonal\ hole}{Total\ atoms\ in\ the\ original\ sheet} \tag{1.2}$$

BL-B exhibits enhanced stability and oxidation resistance compared to its monolayer counterpart, as reported from experimental observations and theoretical predictions. Further, theoretical data predicted that interlayer covalent bond formation is crucial for the stability of the bilayer structure [23]. Recently, Xu *et al.* [24], based on structural search, found that BL-B with vacancy concentration $\eta = \frac{1}{12}$ reaches a global minimum on the Ag (111) substrate. The $\eta_{\frac{1}{12}}$ bilayer consists of two covalently linked borophene layers arranged in an AB configuration, demonstrating structural stability up to 800 K. Furthermore, even in vacuum conditions, the $\eta_{\frac{1}{12}}$ BL-B remains the most thermodynamically stable phase. After the substrate is removed, structural relaxation leads to a slight reduction in energy (0.02 eV/atom) in the bilayer, indicating the freestanding nature of the BL-B. The freestanding $\eta_{\frac{1}{12}}$ BL-B exhibits semiconducting behavior with an indirect bandgap of 1.13 eV; however, interfacial electronic hybridization induces metallization when supported on Ag (111). This theoretically designed $\eta_{\frac{1}{12}}$ bilayer closely aligns with recently reported experimental findings on BL-B, exhibiting features such

as a rhombic motif, interlayer B−B bonding, and a lattice periodicity of 5.71 Å× 5.71 Å [13]. Figure 1.1 shows the structure and fundamental characteristics of graphene, H-B_2S_2, and BL-B [3, 16, 24].

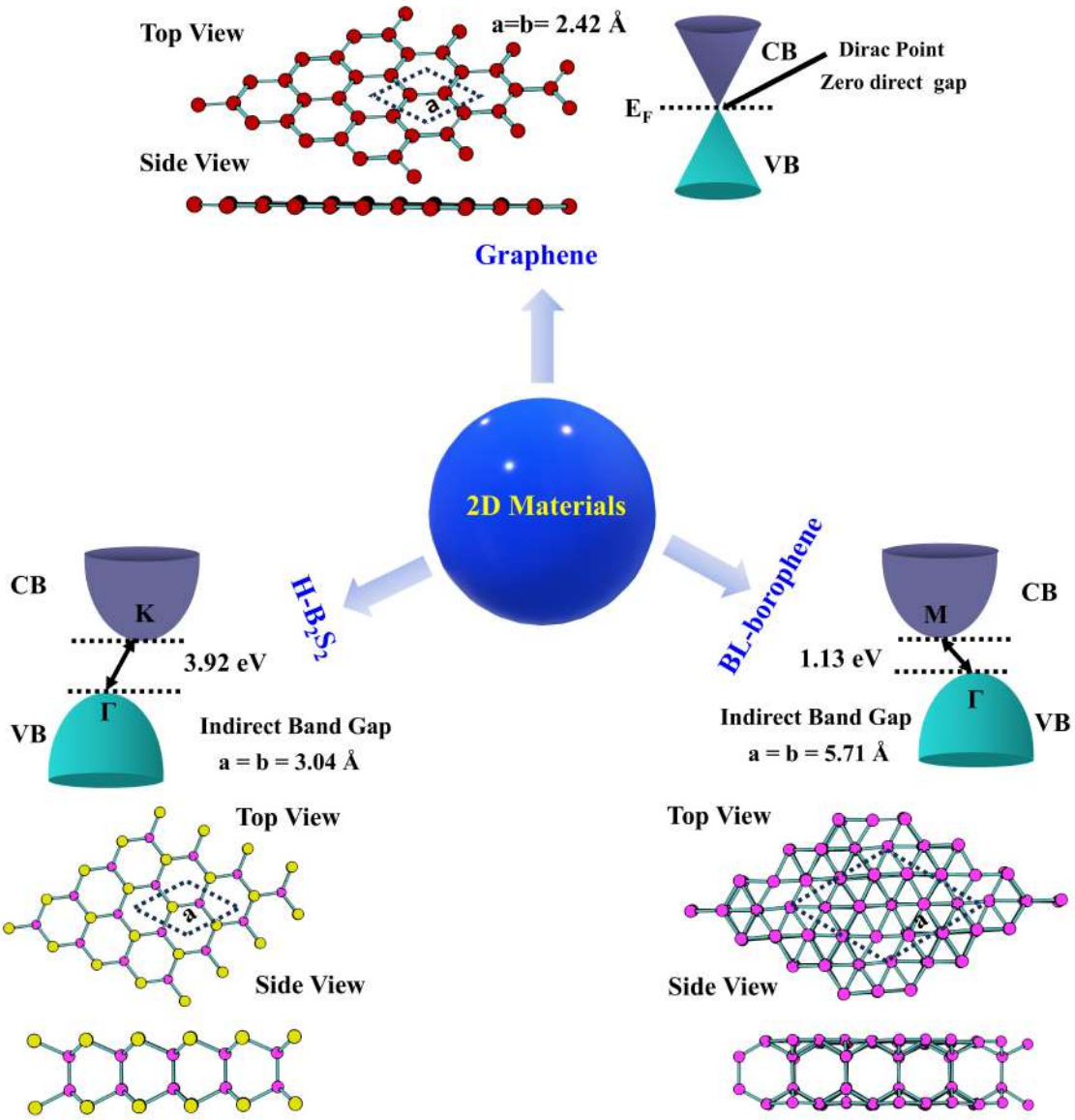

Figure 1.1: Structure and fundamental characteristics of graphene, H-B_2S_2, and BL-B. Red, pink, and yellow balls represent C-atom, B-atom, and S-atom, respectively. The black dotted rhombus represents the unit cell of the respective structures.

1.2 2D Materials as a Scavenger of Toxic Gases: Sensing and Catalytic Reduction

Energy and the environment are two major concerns in recent times. Rapid industrialization, natural disasters, and population growth have led to severe atmospheric pollution, causing widespread environmental degradation and serious threats to human health and global climate stability [25]. Some common hazardous air pollutants are nitrogen oxides (NO_x), sulfur oxides (SO_x), carbon monoxide (CO), hydrogen sulfide (H_2S), ammonia (NH_3), and various nitrogen and sulfur-based, volatile organic compounds (VOCs), etc. [26]. According to the World Health Organization (WHO), SO_x and NO_x are among the major air pollutants, having detrimental impacts on air quality, groundwater, and soil [27]. The SO_2 and NO_2 emissions are primarily due to the combustion of fossil fuels to meet current energy needs. They also contribute to photochemical smog and acid rain formation, causing serious threats to the environment and human health [26]. High NO_2 levels are harm to crops and vegetation, and prolonged exposure can contribute to chronic lung disease. Additionally, SO_2 emissions in industrialized areas are linked to major health issues, including increased mucus production, respiratory irritation, and bronchitis [28]. Therefore, to minimize environmental damage from air pollution, advanced gas-sensing technologies are essential for rapid and selective gas detection with a low detection limit.

Carbon dioxide (CO_2) is a rapidly increasing greenhouse gas due to the excessive combustion of fossil fuels, contributing to severe environmental, ecological, and climate challenges [29]. In this context, with the growing focus on global carbon neutrality, CO_2 removal and conversion have become key areas of focus [30]. Thus, efficient adsorption, activation, and conversion of these gaseous pollutants are of utmost importance to pave the way for a sustainable environment [26]. Figure 1.2 shows the various toxic gases and their common sources. To facilitate a sustainable environment and energy, the potential solutions to address global air pollution are

1. Monitoring toxic gases for environmental safety and emission control (sensor) [31, 32].

2. The catalytic reduction of the toxic pollutants into value-added feedstocks [33, 34].

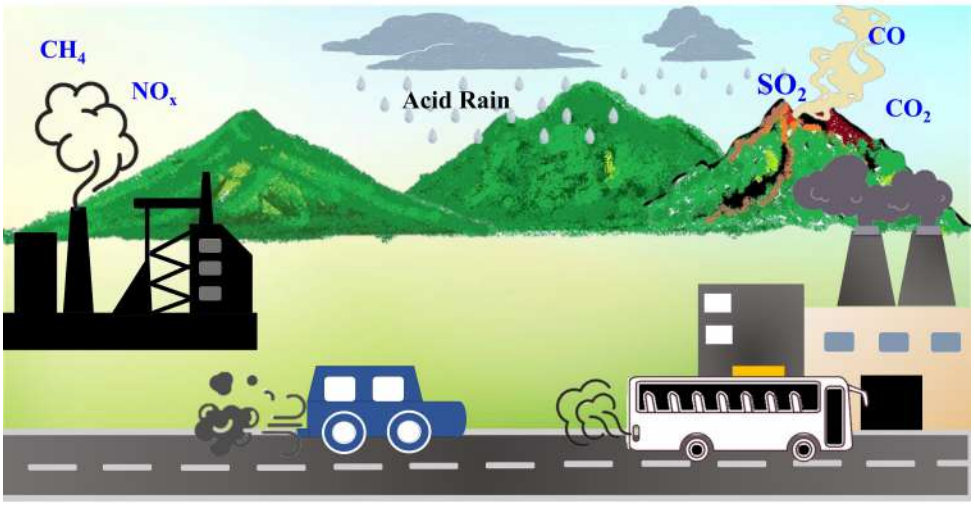

Figure 1.2: Various toxic gases and their common sources.

1.2.1 Gas Sensing

2D materials are emerging candidates for the advancement of gas sensing technology, driven by two fundamental factors: (a) as atomically thin systems, 2D materials are entirely surface exposed, offering exceptional sensitivity for gas detection, and (b) their minimal thickness enables the fabrication of highly miniaturized sensing devices while preserving mechanical integrity and flexibility [35]. Based on the working principle of the sensing devices, they can be classified as chemiresistors, field effect transistors (FETs), optical gas sensors, impedance sensors, surface acoustic wave (SAW) sensors, etc. [36, 37]. The gas sensing performance of the sensor is characterized by several key parameters, which are defined as follows [16].

1. **Sensitivity:** The sensor response or sensitivity (S) is the relative change in resistance. It is expressed as the ratio of the resistance variation induced by gas exposure to that of the pristine material.

$$S(\%) = \frac{R_a - R_g}{R_a} \times 100 \tag{1.3}$$

   Here, R_a and R_g are the resistance of the sensor before and after interaction with the target gas, respectively [38].

2. **Selectivity:** Selectivity refers to the capability of the sensor to detect a targeted molecule from a mixture of gases or interfering molecules and shows a sensor response selective to the target analyte.

3. **Limit of Detection (LOD):** A gas sensor can effectively detect the minimum detectable amount of analytes.

4. **Stability:** The stability of a gas sensor refers to its ability to consistently deliver reliable results over a set period. Long-term stability of a sensor is a critical parameter that depends on several factors, including material sensitivity, strategic elemental doping, variation in humidity, etc [39].

5. **Recovery time:** It is the duration a sensor takes to return to its original state. Recovery time (τ) of a sensor plays a vital role in continuous monitoring and can be expressed as

$$\tau = v_0^{-1} e^{-E_{des}/k_B T} \tag{1.4}$$

Here, v_0 is the attempt frequency (10^{13} s^{-1}) [40], E_{des} is the desorption energy, and k_B is the Boltzmann's constant [40].

Gas Sensing Mechanism of 2D Materials

The gas sensing mechanism of 2D materials relies mainly on adsorption energy (E_{ads}) and charge transfer (CT) between the surface and the gas molecules. The CT effect induces modulation in the surface channel conductance. The process is shaped by the nature of the charge carriers (electrons or holes) in the channel and the redox potential of the gas, determining its role as an oxidizing or reducing agent [41]. The reactivity-dependent interaction between adsorbates and adsorbents alters the electronic landscape of the sensing material, opening new pathways and leading to resistance changes and gas detection [42]. Figure 1.3 presents a conceptual overview of the gas sensing mechanism, illustrating the interaction between MoS_2 and gas molecules (NH_3 and NO_2). NO_2 acts as an electron acceptor and shifts the E_F closer to the valence band (VB), resulting in p-type doping. The unpaired electrons in the nitrogen atom of NO_2 facilitate strong charge transfer and interaction between NO_2 and MoS_2, giving rise to a new electronic state and significantly lowering the band gap. In contrast, NH_3 generates an n-type doping by shifting the E_F towards VB due to its electron donor nature. However, due to low interaction and minimal CT value, the alteration of the electronic band structure is negligible [42–44].

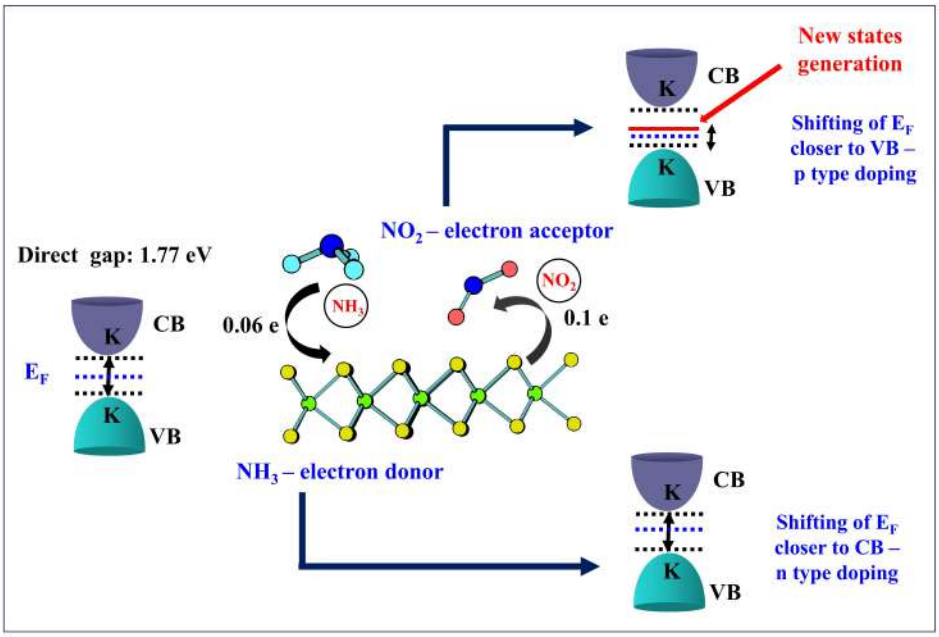

Figure 1.3: Schematic illustration of the gas sensing mechanism of MoS_2 on adsorbing NO_2 (acceptor) and NH_3 (donor) gas molecules.

1.2.2 2D Material as Electrocatalyst

Electrochemical energy conversion through the water and carbon cycles plays a key role in transforming small molecules into organic fuels and precursors, contributing to energy and environmental sustainability. However, developing high-performance electrocatalysts for efficient electrochemical energy conversion technologies remains a key focus of extensive research [45–47]. The discovery of graphene has opened up the possibilities for 2D materials to become promising electrocatalyst candidates due to the following aspects [45].

1. The electrocatalytic advantages of 2D nanomaterials originate from their distinctive morphology and atomic features. The high surface-area-to-volume ratio, combined with unsaturated coordination and dangling bonds at nanosheet edges, creates catalytic sites that reduce activation energy [48–50].

2. 2D electrocatalyst outperforms the powder catalysts by preventing agglomeration [50].

3. High conductivity facilitates efficient charge transfer during the electrocatalysis process. Additionally, the DOS is substantially higher at the surface of a 2D material compared to its bulk counterpart [49, 51].

4. 2D materials show good stability even under extreme reaction conditions, such as highly acidic or alkaline environments, making them well-suited for catalysis reactions [51].

5. Enhanced mass transport: Atomically thin 2D materials promote efficient reactant adsorption and desorption at active sites, thereby accelerating reaction kinetics and improving catalytic performance [51].

However, most pristine 2D materials inherently exhibit weak interaction, lack intrinsic selectivity in their interactions with targeted molecules, and have low catalytic activity. Thus, strategies such as atomic-scale structural (ASS) modification have been introduced to design next-generation high-performance 2D materials [52] for gas sensing and electrocatalytic reduction.

1.3 Rational Designing of 2D Material for Gas Sensing and Electrocatalytic Reduction with Atomic-Scale Structural (ASS) Modification

Conventional 2D materials with inherent properties may not always meet the demands of evolving applications. Therefore, property tweaking is essential for optimizing performance in functional devices. 2D structures provide an open canvas for tailoring properties through ASS modifications and offer great flexibility in terms of electronic properties, charge density, surface characteristics, and lattice symmetry [52–54]. This thesis explores various techniques of ASS of 2D materials that enhance functionality, as outlined below:

Point Defect: Defects or structural disorders in 2D materials can be attained through controlled precursor selection during synthesis or post-synthetic treatments involving external influences like high-energy plasma or ion/electron beams [55]. However, achieving controllable and effective results with minimal structural damage to the material is necessary, as the deep and undesirable defects act as scattering centers that lower carrier mobility and recombination centers that shorten carrier lifetime, eventually degrading device performance [56].

- **Atomic vacancies:** Structural defects, such as vacancies, arise inevitably despite high-precision fabrication methods of the 2D materials [57]. This common defect in 2D materials arises when one or more atoms are absent from a lattice site, forming single,

double, or multiple vacancies. These vacancies play a crucial role in modifying the intrinsic properties of the material [55, 58]. For example, oxygen and sulfur vacancies have been widely investigated in 2D-TMDC and other materials electrocatalysts, as they play a crucial role in catalytic phenomena and serve as reaction centers for the hydrogen evolution reaction (HER) and oxygen evolution reaction (OER) [59–61]. It was also reported that the introduction of vacancies or pores in graphene, i.e., nanoporous graphene, enhances CO_2 adsorption capabilities as the vacancies or pores with appropriate radii can accumulate the CO_2 molecule [62]. Graphene-based sensor performance significantly improved with controlled defect density, achieving a higher response to NO_2 (13 times higher than pristine graphene sensors) [63].

- **Substitutional Doping:** Substitutional doping replaces host atoms with foreign atoms of different valence electrons, introducing acceptor or donor states. These impurities create highly stable defects due to strong covalent bonding with the host lattice [55]. For example, substitutional doping of nitrogen atoms in carbon-based material (i.e., graphene, carbon nanotubes) gives different doping configurations, including graphitic N, pyridinic N, and pyrrolic N, with various doping effects such as n-type and p-type semiconductors, etc. [64]. Experimental results align with DFT simulations, showing that the pyridinic N configuration with a single electron pair is capable of CO_2 binding. In contrast, graphitic N localizes electrons within the π^* orbital, reducing their accessibility for CO_2 adsorption in the N-doped CNT [65]. Furthermore, extensive studies have shown that substitutional doping with heteroatoms considerably improves the sensing performance of materials [66–69].

The influence of point defects on the sensing and electrocatalytic performance of 2D materials is discussed below: [70]

1. **Function as an active site**

   The imperfection on the 2D surfaces improves their performance, which originates from the increased electron density at the active center, i.e., the defect site.

2. **Tuning of the electronic structure**

Defects modulate the electronic properties of active sites, thereby optimizing the local electronic environment.

3. **Additional roles**

   Defect incorporation enhances electrical conductivity and hydrophobicity while increasing the reactive surface area of electrocatalysts. This exposes additional active sites and improves electrolyte interaction, facilitating higher reaction efficiency.

Functionalization: Chemical functionalization of 2D materials with elements such as hydrogen, oxygen, halogens, or organic moieties has emerged as a rapidly evolving research area. This approach plays an important role in effectively inhibiting the aggregation of 2D materials in solvents, thereby maintaining their high surratio and surface area. Additionally, functionalization enhances dispersibility, wettability, and processability while enabling precise tuning of physicochemical properties. It also improves environmental stability and functionalities, expanding the application potential of these materials across diverse fields. Chemical functionalization can be classified into two categories based on the nature of the interaction: (a) covalent functionalization and (b) non-covalent functionalization [71, 72]. Covalent functionalization induces structural modifications, with the newly formed bonds enhancing the material's stability. In contrast, non-covalent functionalization relies on weak, reversible interactions, preserving the intrinsic structure of the material while allowing dynamic tunability [73]. For example, the functionalization of thiolated ligands with MoS_2 improved the sensitivity of VOCs, where they preferably interact with the oxygen functional group in VOCs through H-bonding [41]. The sensing potential of Ti_3C_2 functionalized with different functional groups, such as $-O$, $-OH$, $-F$, and $-Cl$, was studied by Weng *et al.* [74]. They found that $Ti_3C_2O_2$ is highly efficient, lowers energy consumed, and is a selective NH_3 sensor [74]. Thus, surface functionalization represents a promising strategy for achieving high sensitivity, selectivity, and reproducibility in gas sensing applications. By modulating the surface charge density, functionalization directly influences the electronic properties of the material, enabling ultra-low detection limits [75].

Strain Engineering: Strain engineering is an effective strategy to tailor the electrical, magnetic, optical, and mechanical properties of 2D materials, allowing the design of multifunctional materials and composites for advanced electromechanical and sensing applications [76]. The

exceptional mechanical flexibility and strain tolerance (tensile strain up to 30 %) of 2D materials allow controlled tuning of their physical properties under different modes of strain, in-plane (compressive) or out-of-plane (tensile) [77]. The applied external strain alters the interatomic spacing in ultrathin 2D materials, modulating their intrinsic properties by increasing (decreasing) bond length under tensile (compressive) strain, which weakens (strengthens) bond interactions. The shifting of the atomic position and the breaking of the symmetry lead to the lattice mismatch of the nanomaterial, which affects the surface properties [36, 77, 78]. Strain-dependent gas sensing in atomically thin 2D materials has been extensively studied, highlighting strain engineering as a crucial factor in optimizing sensitivity, selectivity, and stability [79–83]. Figure 1.4 shows various possible ASS modifications on 2D materials.

1.4 Problem Statement and Overview of the Thesis

Environmental pollution and the energy crisis have escalated globally to significant problematic levels. To address this issue, it is imperative to prioritize monitoring of harmful gases and catalytic conversion into valuable industrial resources. Advancements in nanotechnology have facilitated the development of 2D materials with unique atomic-scale thicknesses and structure-property relationships. Despite this, the rational design of 2D materials is essential for opening up their immense potential in the realms of enhancing energy efficiency and promoting sustainability, as the pristine systems are chemically inert and have weak surface-analyte interaction. ASS modification effectively alters the properties of 2D materials and broadens their structural and functional diversity. Computational chemistry helps in designing materials through precise atomistic design, offering enhanced performance for targeted applications. It often predicts molecular adsorption, electronic properties alteration, device performance, active site, and catalytic conversion reaction pathways, thus providing a valuable guide for experimental explorations toward the synthesis of 2D materials with specific structures and properties. Therefore, this thesis aims to introduce structural modifications such as doping, defects, functionalization, and strain application in graphene, h-B_2S_2, and BL-B in a controlled manner and allow them to serve as an efficient gas sensor and electrocatalyst through computational simulation, as summarized in Figure 1.5.

The research presented in this thesis is structured into seven chapters, which include the research

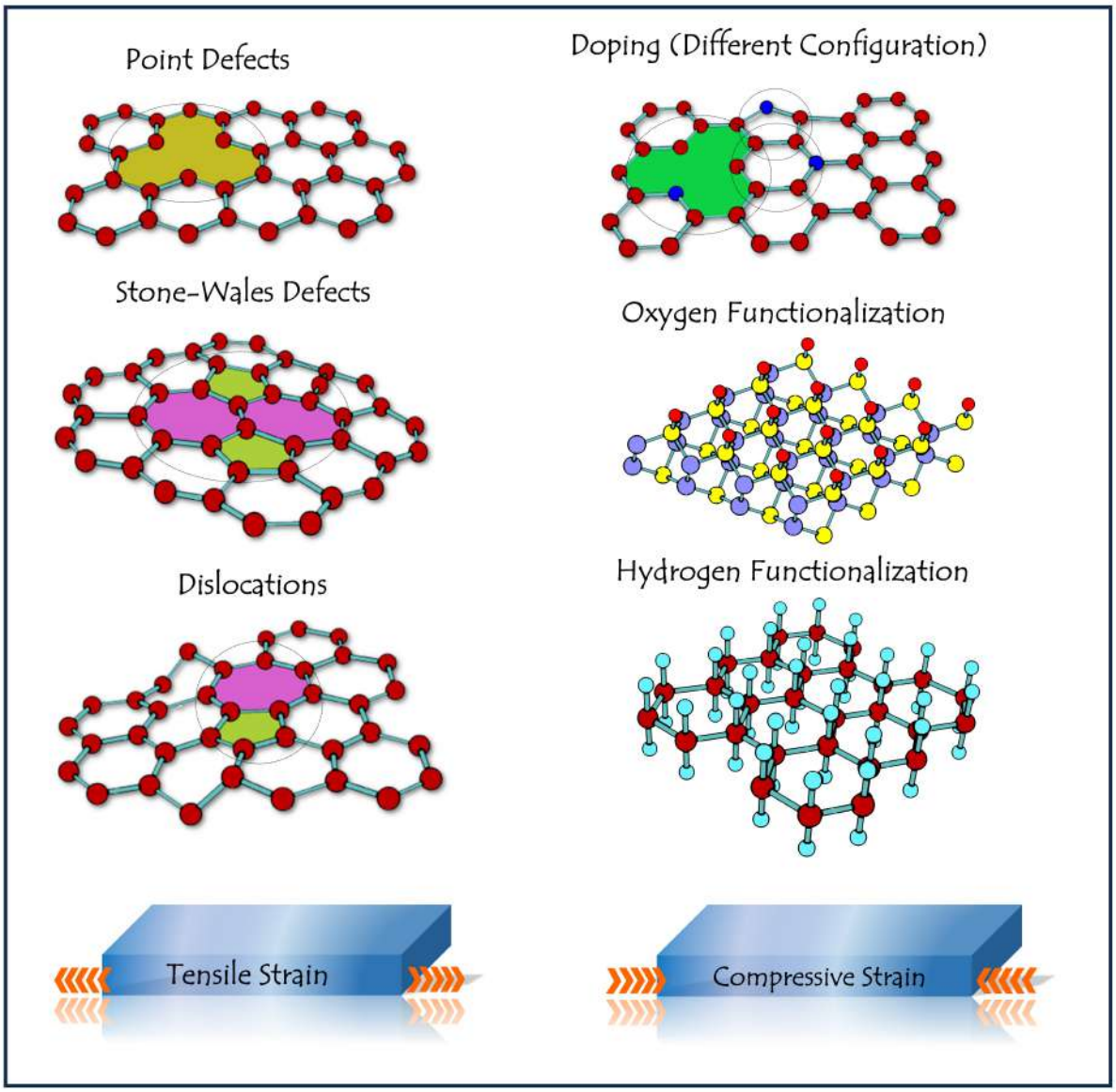

Figure 1.4: Different possible ASS modifications on 2D materials.

background, computational methodologies, research findings, and the overall conclusion. A summary of each chapter is provided below:

1. **Chapter 1 :** This is the introductory Chapter with the background and motivation of the thesis work.

2. **Chapter 2 :** This Chapter provides a concise overview of various computational techniques employed in the simulations, including density functional theory (DFT), ab initio molecular

dynamics (AIMD), and the non-equilibrium Green's function (NEGF) formalism.

3. **Chapter 3 :** In Chapter 3, we explore the gas-sensing potential of pyridinic dominance N-doped (PNG) graphene. The graphene structure is modified by introducing a single vacancy defect with N-doping. Our findings indicate that PNG is an efficient SO_2 sensor, exhibiting significant adsorption energy, charge transfer, and orbital hybridization. Additionally, we investigate the impact of applied external strain and electric fields on the performance of the sensor.

4. **Chapter 4 :** In Chapter 4, the gas-sensing potential of oxygen functionalized h-B_2S_2 has been studied. This work provides an in-depth analysis of the structure, stability, and sensing potential of the Oh-B_2S_2 nanosheet in the context of future sensing devices.

5. **Chapter 5 :** In Chapter 5, we have introduced three (3) point defects in the upper layer of the BL-B depending on the bonding environment of each B-atom. The charge states of the systems over these surfaces are modulated to study their CO_2 activation potential termed "charge-induced CO_2 activation".

6. **Chapter 6 :** In Chapter 6, we studied the electrochemical reduction of CO_2 to CH_3OH performance over defect-induced BL-B. This work includes the potential effect of charge during an electrocatalytic cycle.

7. **Chapter 7 :** In Chapter 7, we have summarized the overall research work with the key findings.

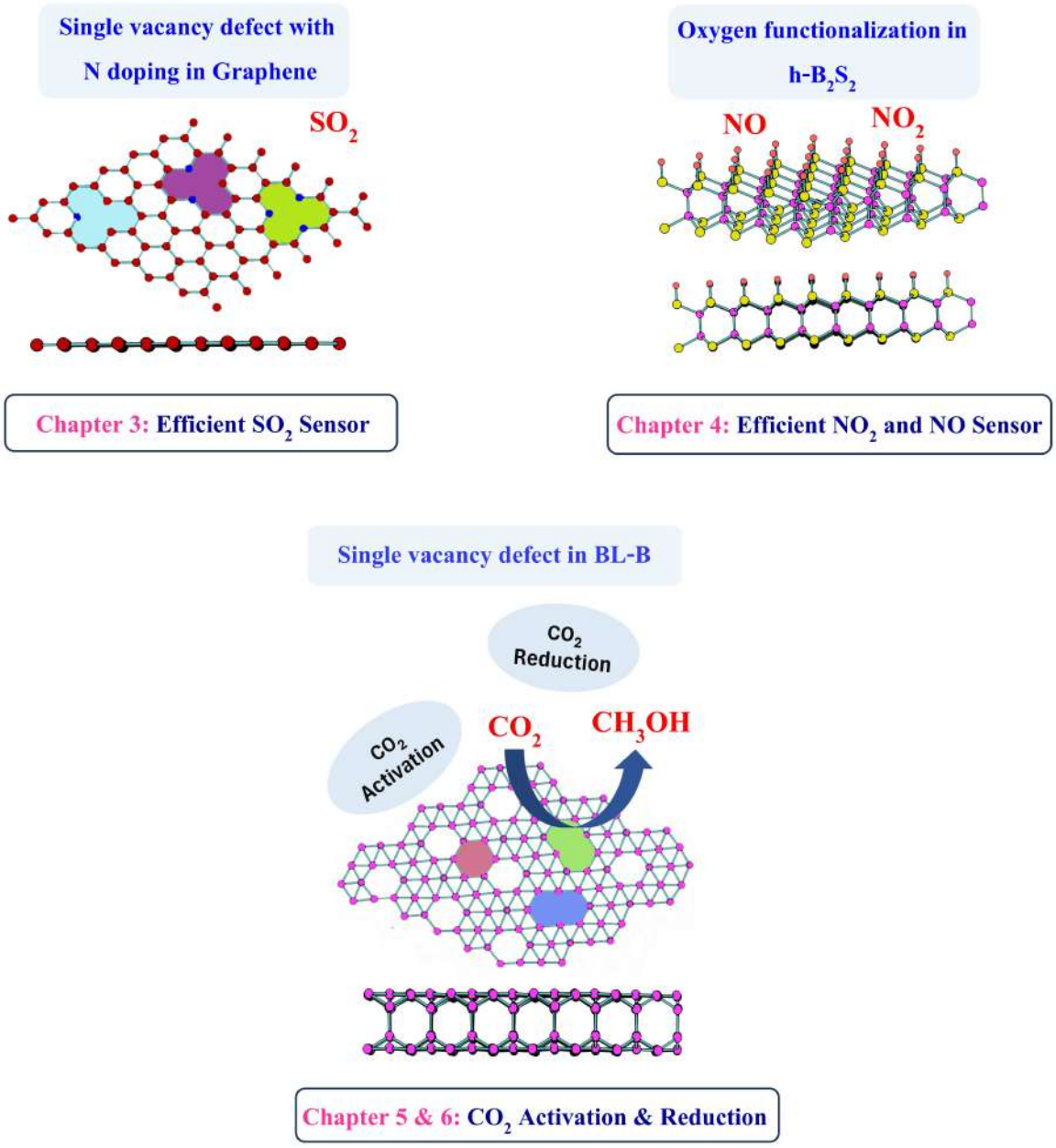

Figure 1.5: Summary of the research work presented in the thesis.

Chapter 2

THEORETICAL BACKGROUND

This chapter briefly introduces quantum-mechanical methods for studying materials, including the Schrödinger equation, Density functional theory (DFT), periodic systems, ab initio molecular dynamics (AIMD) simulations, and quantum transport using Non-Equilibrium Green's Function (NEGF) and Landauer formalism.

2.1 The Schrödinger Equation

The time-independent Schrödinger equation (SE) of a multi-particle system with nuclei "M" and electrons "N" can be expressed as

$$\hat{H}\Psi(r_1, r_2, ..., r_n, R_1, R_2, ..., R_M) = E\Psi(r_1, r_2, ..., r_n, R_1, R_2, ..., R_M) \tag{2.1}$$

$\hat{H}$ is the Hamiltonian operator with the expression

$$\hat{H} = \underbrace{-\frac{1}{2}\sum_{i=1}^{N}\nabla_i^2 - \sum_{A=1}^{M}\frac{1}{2M_A}\nabla_A^2}_{\text{Kinetic energy terms}} \underbrace{-\sum_{i=1}^{N}\sum_{A=1}^{M}\frac{Z_A}{r_{iA}} + \sum_{i=1}^{N}\sum_{j>i}^{N}\frac{1}{r_{ij}} + \sum_{A=1}^{M}\sum_{B>A}^{M}\frac{Z_A Z_B}{R_{AB}}}_{\text{Potential energy terms}} \tag{2.2}$$

M_A and Z_A are the mass and the charge of the nucleus A, r_{ij} is the distance between i^{th} and j^{th} electron, r_{iA} is the distance between the i^{th} and the A^{th} nucleus, and R_{AB} is the distance between the A^{th} and B^{th} nucleus.

2.2 Born-Oppenheimer Approximation

SE is further simplified by considering the greater mass of nuclei compared to electrons. Due to the large mass of nuclei relative to electrons, the nuclear kinetic energy (KE) is neglected, and nuclear-electron interactions are assumed to be constant [84]. This is the Born-Oppenheimer (BO) approximation, which separates nuclear and electronic motion, and the total Hamiltonian simplifies to the electronic Hamiltonian [85].

$$\hat{H} = \underbrace{-\frac{1}{2}\sum_{i=1}^{N}\nabla_i^2}_{\hat{T}} \underbrace{-\sum_{i=1}^{N}\sum_{A=1}^{M}\frac{Z_A}{r_{iA}}}_{\hat{V}_{Ne}} + \underbrace{\sum_{i=1}^{N}\sum_{j>i}^{N}\frac{1}{r_{ij}}}_{\hat{V}_{ee}} = \hat{T} + \hat{V}_{Ne} + \hat{V}_{ee} \tag{2.3}$$

2.3 Density Functional Theory

DFT is considered among the most promising and efficient ways to numerically solve the structure-property relationship of many-electron species, such as atomic and molecular systems, clusters, periodic solids, etc. In DFT, the "N" electron interacting system is described in terms of electron density $\rho(r)$ rather than the electron wave function [86]. The earliest formulation of DFT was developed by Thomas and Fermi. The Thomas-Fermi model established a relationship between the KE and the $\rho(r)$. However, this approach lacks essential physics and chemistry, such as atomic shell structures and molecular binding, making it inadequate for accurately describing electrons in matter [84]. Later, in 1964−1965, Hohenberg and Kohn, followed by Kohn and Sham, developed DFT, providing a strong basis and a practical framework for studying many-electron systems [87].

2.3.1 The Hohenberg-Kohn Theorems

Theorem I: *The ground state (GS) density $\rho(r)$ determines the external potential energy $v(r)$ to within a trivial additive constant.*

This implies that for a given density, there is a unique V_{ext}(r), i.e., it is impossible for two different V_{ext}(r) to correspond to the same $\rho(r)$. Thus, the theorem shows that the electron density uniquely determines the Hamiltonian operator. ρ_0 contains information on N, Z_A, and

R_A and is summarized as [85, 88, 89]

$$\rho_0 \Rightarrow N_A, Z_A, R_A \Rightarrow \hat{H} \Rightarrow \Psi_0 \Rightarrow E_0(all\ other\ properties) \tag{2.4}$$

Theorem-II: *The Hohenberg-Kohn functional $F_{HK}[\rho]$ that delivers the ground state energy if and only if the input density is the true ground state density.*

$F_{HK}[\rho]$ is a universal function and it is independent of the external potential [85, 89, 90].

$$F_{HK}[\rho] = T[\rho] + E_{ee}[\rho] = \langle \Psi | \hat{T} + \hat{V}_{\text{ee}} | \Psi \rangle \tag{2.5}$$

For a trial density $\rho(r')$, which satisfy the boundary condition $\rho(r') \geq 0$ and $\tilde{\rho}(r) \geq 0$, $\int \tilde{\rho}(r)dr = N$. $E[\rho] \leq E[\rho']$. $E[\rho']$ is the energy functional corresponding to $\rho(r')$.

$$E[\rho'] = \int \rho(r')V_{ext}(r)dr + F_{HK}[\rho'] \tag{2.6}$$

The main challenge is that the exact functional forms $T[\rho]$ and E_{ee} remain unknown.

2.3.2 Kohn-Sham Method

To approximate the KE and electron-electron terms in $F_{HK}[\rho]$, Kohn-Sham (KS) introduced a non-interacting system, where $V_{ee} = 0$. This system is represented by a single determinant wavefunction in N "orbitals" ϕ_i from which the KE and $\rho(r)$ can be exactly obtained. For a non-interacting system, the GS energy $E[\rho]$ includes both kinetic and external potential contributions.

$$E[\rho] = T_0[\rho] + V_{ext}[\rho] = T_0[\rho] + \int \rho(r)V_{ext}(r)d^3r \tag{2.7}$$

Its GS wavefunction can be described by a Slater determinant with the orbitals represented by the single-particle SE below,

$$\left[-\frac{1}{2}\nabla^2 + V_{ext}(r)\right]\phi_m^0(r) = \mathscr{E}_m^0\phi_m^0 \tag{2.8}$$

Thus, the $\rho(r)$ is defined by summing over the occupied states, where ϕ_m^0 is normalized.

$$\rho(r) = \sum_{m}^{occup} \left|\phi_m^0(r)\right|^2 \tag{2.9}$$

In a many-electron system, the total energy functional $E[\rho]$ can be formulated as

$$E[\rho] = T_0[\rho] + \int \rho(r) V_{ext}(r) d^3r + \underbrace{\frac{1}{2}\int\int \frac{\rho(r_1)\rho(r_2)}{|r_1 - r_2|} d^3r_1 d^3r_2}_{\text{Hartree Energy}} + E_{XC}[\rho(r)] \tag{2.10}$$

$E_{XC}[\rho(r)]$ represents the exchange-correlation energy. It incorporates all remaining contributions beyond the non-interacting KE, external potential energy, and Hartree energy. The equation 2.11 for the non-interacting case can be adapted to the interacting electron system as follows:

$$\left[-\frac{1}{2}\nabla^2 + V_{eff}(r)\right]\phi_m(r) = \mathscr{E}_m \phi_m \tag{2.11}$$

Here, $\phi_m(r)$ is the KS orbital that reproduces $\rho(r)$ of the original many-body problem, $\mathscr{E}_m$ is the KS eigenvalue, and the above equation is known as the KS equation.

$$V_{eff} = V_{ext}(r) + V_H(r) + V_{XC}(r) \tag{2.12}$$

Where, $V_H(r) = \int \frac{\rho(r')}{(|r-r'|)} d^3r'$ and $V_{XC}(r) = \int \frac{\delta E_{XC}[\rho]}{\delta\rho(r)}$ are the Hartree potential and exchange-correlation potential, respectively [89, 90]. In practical DFT calculations within the KS approach, self-consistent equations are iteratively solved with an approximate form of the exchange-correlation functional [90].

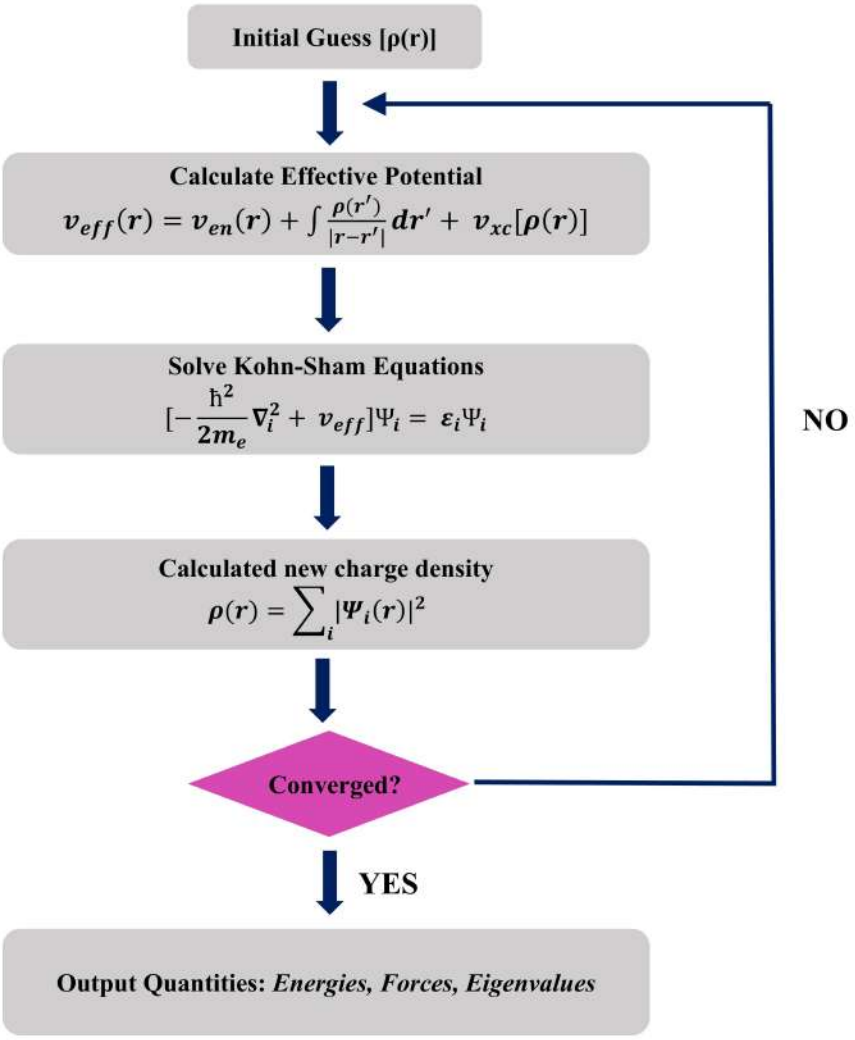

Figure 2.1: Flowchart of the self-consistent KS-DFT method.

2.3.3 Exchange-Correlation Functionals

The accuracy of the KS approach depends on the accuracy of the approximation of E_{XC}, which is a combination of both exchange (E_X) and correlation term (E_C)

$$E_{XC} = E_X + E_C \tag{2.13}$$

The E_{XC} can be viewed as the coupling between an electron at r and its Fermi-Coulomb hole charge density [91]. The following section covers some commonly used approximations for the exchange-correlation functional.

Local Density Approximations (LDA)

Kohn and Sham introduced the earliest and simplest explicit form of E_{XC} in 1965 [92]. In local density approximations (LDA), a hypothetical uniform electron gas was considered where the electron density ρ is constant everywhere. The E_{XC} in LDA is approximated as

$$E_{XC}^{LDA}[\rho] = \int \rho(r)\varepsilon_{XC}[\rho(r)]dr \tag{2.14}$$

Here, ε_{XC} is the exchange-correlation energy per particle of uniform electron gas density $\rho(r)$. The ε_{XC} is further split into ε_X and ε_C terms. ε_X is given by $-\frac{3}{4}\sqrt[3]{\frac{3\rho(r)}{\pi}}$. Although there isn't an explicit expression for the correlation term, ε_C, quantum Monte Carlo simulations of the homogeneous electron gas produced analytical expressions for ε_C using various interpolation techniques. In a spin-unrestricted case, LDA can be written as

$$E_{XC}^{LSD}[\rho_\alpha, \rho_\beta] = \int \rho(r)\varepsilon_{XC}(\rho_\alpha(r), \rho_\beta(r))dr \tag{2.15}$$

This is known as local spin-density approximation (LSD), and $\rho_\alpha(r) = \rho_\beta(r) = \frac{1}{2}\rho(r)$. For basic metals like sodium, the uniform electron gas makes a somewhat accurate physical model. However, it is far from a realistic scenario in atoms or molecules, which are typically distinguished by rapidly changing densities [85].

Generalized Gradient Approximation (GGA)

An improvement in LDA is achieved by incorporating a gradient of the charge density ($\nabla\rho$). Hence, in generalized gradient approximation (GGA), the exchange-correlation density is not determined exclusively by $\rho(r)$ but also by its gradient $\nabla_\rho(r)$.

$$E_{XC}^{GGA}[\rho_\alpha, \rho_\beta] = \int f(\rho_\alpha, \rho_\beta, \nabla\rho_\alpha, \nabla\rho_\beta)dr \tag{2.16}$$

The exchange part can be written as,

$$E_X^{GGA} = E_X^{LDA} - \sum \int F(S_\sigma)\rho_\sigma^{\frac{4}{3}}(r)dr \tag{2.17}$$

where F is the reduced density gradient for spin σ and S_σ is the local inhomogeneity parameter. In the exchange term, F can be classified into two types:

1. The first one was developed by Becke in 1988 and termed B or B88.

$$F^B = \frac{\beta s_\sigma^2}{1+6\beta s_\sigma^2 sinh^{-1} s_\sigma}; \beta \, is the \, empirical \, parameter \tag{2.18}$$

2. Second E_X^{GGA} used a rational function of the reduced density gradient for F. It is termed as P86 or PBE [85].

$$F^{\mathrm{PB86}} = \left(1+1.296\left(\frac{s_\sigma}{(24\pi^2)^{1/3}}\right)^2+14\left(\frac{s_\sigma}{(24\pi^2)^{1/3}}\right)^4+0.2\left(\frac{s_\sigma}{(24\pi^2)^{1/3}}\right)^6\right)^{1/15} \tag{2.19}$$

Heyd-Scuseria-Ernzerhof (HSE) Functional

Hybrid density functionals include a portion of Hartree-Fock (HF) exchange and have enhanced the results obtained from GGA functionals. Heyd, Scuseria, and Ernzerhof (HSE) suggested a more precise and efficient screened hybrid functional based on a screened Coulomb potential for the exchange interaction [93]. The expression for the exchange-correlation energy (HSE03) is formulated as follows.

$$E_{xc}^{\mathrm{HSE\ 03}} = \frac{1}{4}E_x^{\mathrm{SR},\mu} + \frac{3}{4}E_x^{\mathrm{PBE,\ SR},\mu} + E_x^{\mathrm{PBE,\ LR},\mu} + E_c^{\mathrm{PBE}}. \tag{2.20}$$

In range-separated hybrid functionals, the exchange component of the electron-electron interaction is partitioned into short-range (SR) and long-range (LR) contributions, while correlation is treated using the PBE functional. The range-separation parameter μ becomes negligible at short-range interactions and in the case of HSE03, is approximately 0.3 Å^{-1} while in HSE06 it is reduced to 0.2 Å^{-1} [94].

2.4 Periodic Boundary Condition (PBC)

Periodic boundary conditions (PBCs) allow the representation of an infinitely large system by replicating a small domain in all three spatial directions. The periodic arrangement of atoms in a crystal is defined by its unit cell. In 3D, PBCs are defined using a cuboid unit cell, as illustrated in

Figure 2.2. This unit cell is replicated in all three dimensions to simulate a continuous structure [95, 96].

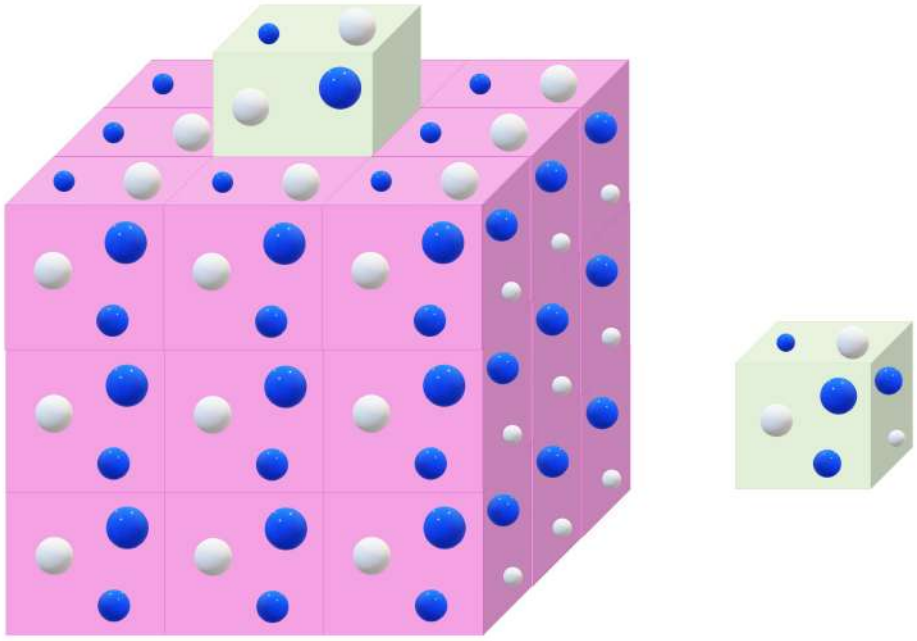

Figure 2.2: Schematic representation of a PBC using a cuboid unit cell, repeated in all directions to form a continuous structure.

Bloch Theorem

In periodic solids, electrons move with a periodic potential rather than with a constant one. Hence $V(x) = V(x+a)$, where a is the lattice constant. The SE for the electron moving in a 1D periodic potential can be written as

$$\frac{d^2\psi}{dx^2} + \frac{2m}{\hbar}[E - V(x)]\psi = 0 \tag{2.21}$$

The solution of the equation above is given by $\psi(x) = e^{\pm ikx}u_k(x)$. Here, $e^{\pm ikx}$ is the plane wave, and $u_k(x) = u_k(x+a)$ is the periodic function.

2.5 Basis Sets

1. **Plane Wave:** Plane waves (PWs) are delocalized basis functions distributed uniformly across the space rather than being localized near the nuclei. They are widely used in solid-state physics due to their inherent incorporation of periodic boundary conditions [85]. They formed a complete, orthonormal basis consistent with the periodicity imposed by the

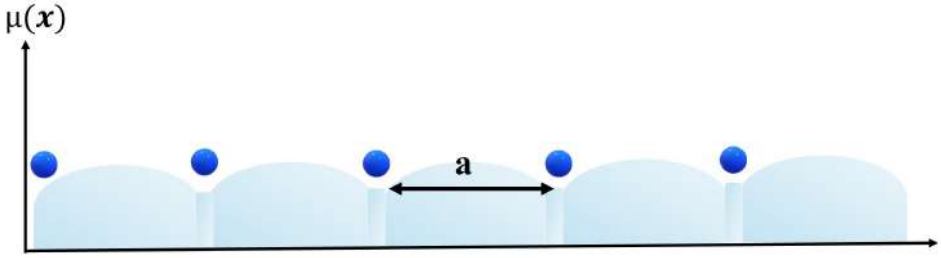

Figure 2.3: This shows the movement of the electron with periodic potential, having lattice constant "a".

crystal lattice

$$\eta^{PW} = \frac{1}{\sqrt{\Omega}} exp[iGr] \tag{2.22}$$

G is the reciprocal space vector, and Ω is the volume of the periodic cell. In solid-state physics, the periodic lattice generates a periodic potential and thus implements periodicity in density. The periodic part of $[\nu(x)]$ can be expanded in the Fourier series using a plane-wave basis.

$$\nu(r) = \nu(r+a) = \frac{1}{\sqrt{\Omega}} \sum_G \nu(G) exp[iGr] \tag{2.23}$$

In KS, the potential of the periodic lattice has the same periodicity as the direct lattice, $V^{KS} = V^{KS}(r+a)$. The charge density $[\rho(r)]$ can also be expanded into a plane wave basis and written as

$$\rho(r) = \sum_G n(G) exp(iGr) \tag{2.24}$$

In practice, the infinite sums over the G vector and cells need to be truncated. The truncation of the plane wave basis relies on the rapid convergence of the Kohn–Sham potential $V^{KS}(G)$ as the modulus of G increases. Consequently, at each k-point, only G vectors with kinetic energy below a specified maximum cutoff are considered, which is given

$$\frac{1}{2}\left|k+G\right| \leq E_{cut} \tag{2.25}$$

With this basis choice, calculation precision in DFT is governed by plane wave energy cutoff, i.e., E_{cut} [97].

2. **Gaussian Type Orbital (GTO):** GTO basis function is a very efficient algorithm for

calculating a large number of $4c-2e^{-}$ integrals occurring in Coulomb and HF exchange terms. The general form of GTO can be written as

$$\eta^{GTO} = Nx^{l}y^{m}z^{n}exp[-\alpha r^{2}] \tag{2.26}$$

N is the normalization constant, where $< \eta_u | \eta_u >= 1$, α is the orbital exponent, where a larger α yields a more compact form and a smaller α produces a more diffuse one. $L = l+m+n$, where $L = 1, 2$, and 3 s, p, and d functions. Further, the Gaussian functions are combined in a linear combination, known as the contracted Gaussian function (CGF) [85].

$$\eta_{\tau}^{CGF} = \sum_{a}^{A} d_{a\tau}\eta_{a}^{GTO} \tag{2.27}$$

The DZVP-MOLOPT-SR-GTH is a GTO basis set used primarily in CP2K. Here, DZVP is a double zeta valence with polarization (it uses two functions to describe each valence orbital and includes polarization functions to better capture angular distortions in the electron cloud), MOLOPT refers to molecular optimized [98], SR is short range (indicates that the basis functions are contracted for short-range behavior, making them more efficient for condensed-phase or periodic systems), and GTH is Goedecker-Teter-Hutter pseudopotentials (which replace the core electrons with a smooth effective potential to reduce computational cost).

2.5.1 Dispersion Correction

A common limitation of all functionals is the replacement of the local exchange with a nonlocal HF exchange, thereby enabling the inclusion of long-range electron correlation underlying dispersive interactions such as van der Waals (vdW) interactions. In dispersion interaction corrected DFT, the total energy can be expressed as

$$E_{DFT-D} = E_{KS-DFT} - E_{dis} \tag{2.28}$$

E_{dis} is an empirical dispersion term given by

$$E_{disp} = -S_6 \sum_{i=1}^{N_{at}-1} \sum_{j=i+1}^{N_{at}} \frac{C_6^{ij}}{R_{ij}^6} f_{dmp}(R_{ij}) \tag{2.29}$$

$$f_{dmp}(R_{ij}) = \frac{1}{1+e^{-d(R_{ij}/R_r-1)}} \tag{2.30}$$

N_{at}, C_6^{ij}, S_6, R_{ij}, and R_r represent the atoms present in the system, the dispersion coefficient for atom pair ij, the global scaling factor that is a function of the DF used, the interatomic distance, and the sum of atomic vdW radii, respectively [99].

2.5.2 Pseudopotential

The pseudopotential approximation (PPA) simplifies particle interactions by substituting the exact Hamiltonian (H_{exact}) with a pseudopotential operator. This operator aims to produce a pseudo-Hamiltonian with an eigenvalue spectrum similar to H_{exact} (or a desired subset) and pseudo-eigenfunctions that approximate the exact ones, in the required region. In the case of

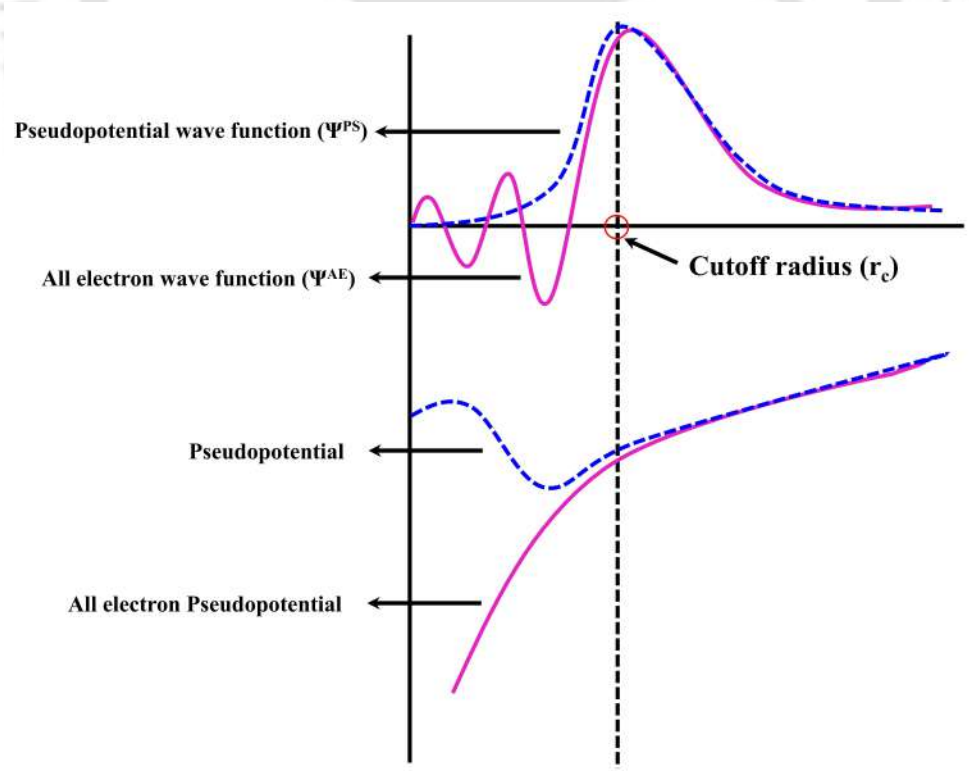

Figure 2.4: A comparison between the wavefunction in the Coulomb potential of the nucleus (purple) and that in the pseudopotential (blue) shows that both the wavefunctions and their corresponding potentials coincide beyond a certain cutoff radius, r_c.

plane waves, expansions converge slowly when describing large oscillations in the core region. Hence, the KS-DFT methods, using a plane-wave basis and pseudopotentials, are widely used in solid-state calculations. Different kinds of pseudopotentials in DFT include norm-conserving pseudopotentials (NC-PP), ultrasoft pseudopotentials (US-PP), projector augmented wave (PAW) pseudopotentials, and Goedecker-Teter-Hutter (GTH) pseudopotentials.

- **Norm-conserving pseudopotentials (NC-PP):** NC-PP, developed by Hamann, Schlüter, and others, originated from the orthogonalized plane-wave (OPW) approximation and KS equation. In this approach, a smooth, nodeless pseudo-wave function is used in place of the all-electron (AE) wave function, where the pseudo-wave function has to match the norm of the AE wave function within the core radius. Beyond this radius, the two wave functions are the same. Nevertheless, a large plane-wave basis set is necessary for elements with highly localized orbitals and the resulting pseudopotentials, and expanding the core radius to solve this problem has a negative effect on transferability [100].

- **Ultrasoft pseudopotentials (US-PP):** A solution to this was proposed by Vanderbilt in 1990, known as US-PP. This approach relaxes the norm-conservation constraint, facilitating a broader choice of cutoff radius, r_C, thereby improving smoothness and transferability. Further, the resulting charge deficiency is corrected by adding localized atom-centered augmentation charges. The core radius of the PP is half the distance to the nearest atom and does not depend on the maximum of the corresponding AE wave function [100, 101].

- **Projector augmented-wave (PAW):** Blöchl formulated a linear transformation that maps the pseudo-wave function to the all-electron (AE) wave function from which the PAW total energy functional was derived by applying it to the KS formalism. In this method, full AE wave functions and potentials are employed using atom-centered radial grids instead of a regular uniform grid [100]. This technique reduces computational costs while achieving results close to all-electron.

- **GTH Pseudopotential:** GTH pseudopotential has separable energy contributions into a long-range local part and a short-range non-local part. It also conserves the charge density norm, which is crucial for accurately describing long-range interactions. GTH

pseudopotentials, combined with a mixed Gaussian-plane wave (GPW) scheme, enable efficient and effective AIMD simulations with linear scaling [102, 103].

GTH-PBE integrates norm-conserving GTH pseudopotentials with the PBE exchange-correlation functional to perform efficient and accurate DFT calculations, especially in plane-wave and mixed Gaussian-plane wave methods prevalent in materials and molecular modelling.

2.6 Electrostatic Potential Analysis

The electrostatic potential $V(r)$ is widely used to study intermolecular interactions and identify regions of chemical reactivity. It is defined mathematically at any point r as follows

$$V(\mathbf{r}) = \sum_A \frac{Z_A}{|\mathbf{R}_A - \mathbf{r}|} - \int \frac{\rho(\mathbf{r}')\, d\mathbf{r}'}{|\mathbf{r}' - \mathbf{r}|} \tag{2.31}$$

Here, Z_A and R_A represent the charge and position of nucleus A, respectively, while $\rho(r')$ denotes the electron density at point r', obtained from Kohn–Sham DFT [104].

2.7 Phonon Analysis

Phonons represent quantized modes of vibrational energy in a crystal lattice and are essential for understanding many fundamental properties of solids. Within the harmonic approximation, phonon frequencies (ω) are obtained from the eigenvalues of the dynamical matrix that governs the vibrational modes of the lattice.

$$Det|D - \omega^2 I| = 0 \tag{2.32}$$

Where D and I are the dynamical matrix (DM) and identity matrix, respectively. For computing phonons and their associated properties, two principal approaches within density functional theory are commonly employed: (i) the finite displacement (FD) and (ii) density functional perturbation theory (DFPT). In our study, we used DFPT to perform phonon calculations. [105].

2.8 Strain Analysis

The strain of 2D materials can be defined as

$$\varepsilon = (I_b - I_a)/I_a \tag{2.33}$$

Where ε, I_a and I_b denote the strain magnitude, lattice constant before and after the application of strain, respectively. In practical conditions, however, the strain within a material is often non-uniform due to structural imperfections and local atomic rearrangements. [106].

2.9 Electron Localization Function (ELF)

The electron localization function (ELF) offers a novel way to describe chemical bonding across nearly all classes of compounds. ELF is based on Lennard-Jones concept of the pair probability function, which describes the likelihood of finding one electron at (x,y,z) and another with the same spin at (x',y',z'). This concept shows that electrons with identical spins tend to avoid each other, leading to distinct spatial regions. Because this applies to both spin types, it results in areas where electrons are paired. Becke and Edgecombe clarified that regions with a high probability of finding another electron of the same spin correspond to low electron localization, while regions with low pair probability indicate strong localization. The ELF for a system with σ-spin electron density $\rho_\sigma(x,y,z)$ (where σ denotes α or β spin) and a set of occupied molecular orbitals is mathematically defined as follows.

$$ELF = \frac{1}{1+\left(\frac{D_\sigma(x,y,z)}{D_{\sigma,\mathrm{gas}}(x,y,z)}\right)^2} \tag{2.34}$$

In equation 2.34, D_σ represents the first-order term in the Taylor expansion of the spherically averaged σ-spin pair probability, with the subscript "gas" indicating its value for a homogeneous electron gas, the fully delocalized reference state.

The ELF ranges from 0 to 1 and equals 0.5 for a homogeneous electron gas. An ELF value of 1.0 indicates complete localization, while 0.5 signifies perfect delocalization [107].

2.10 Ab Initio Molecular Dynamics (AIMD) Simulation

AIMD reshapes molecular simulations by integrating molecular dynamics with electronic structure theory, making it a widely used computational tool for studying diverse physical, chemical, and biological phenomena [97]. AIMD calculates forces "on the fly" as the simulation continues from electronic structure calculations, enabling bond forming, breaking, and electronic polarization effects [108].

2.10.1 Born Oppenheimer Molecular Dynamics (BOMD)

BOMD incorporates electronic structure into molecular dynamics (MD) by treating nuclei classically and solving the static electronic SE at each time step using the fixed nuclear configuration. This reduces the electronic structure calculation to a time-independent quantum problem, such as solving the time-independent SE, while the nuclear motion is treated using classical molecular dynamics [97]. Consider a system with N nuclei and N_e electrons where the BO approximation holds. In this framework, the nuclei evolve classically on the electronic GS potential energy surface. The corresponding total Hamiltonian is given by equation 2.35

$$H = T_e + V_{ee} + V_{Ne} + T_N + T_{NN} = H_{elec} + T_N + T_{NN} \tag{2.35}$$

If R_1, R_2,...., $R_N \equiv R$ represent the nuclear positions, and their classical dynamics follow an equation of motion.

$$M_I \ddot{R} = - \bigtriangledown_I [\varepsilon_0(R) - V_{NN}(R)] \tag{2.36}$$

Here, $\varepsilon_0(R)$ is the GS energy eigenvalue in R. To solve the GS electronic energy $H_{elec}(R)\Psi_0(R)$ = $\varepsilon_0(R)\Psi_0(R)$ electronic structure methods, such as Kohn–Sham (KS) formulation of DFT, were used. The total energy is expressed as a functional of n mutually orthonormal single-particle electron orbitals $\Psi_0(R)$ i= 1, 2, …., n. The electron density of this orbital n(r) is given by $\Sigma f_i |\Psi_i(r)|^2$. f_i is the occupation in the i^{th} orbital. Hence, the total energy can be written as

$$E[\{\Psi\}, R] = \frac{1}{2} \sum_{i=1} f_i \int \Psi_i^*(r) \bigtriangledown^2 \Psi_i(r) + \frac{1}{2} \int dr dr' \frac{\rho(r)\rho(r')}{|r - r'|} + E_{xc}[\rho] + \int dr \rho(r) V_{ext}(r, R) \tag{2.37}$$

Minimizing this functional over orbitals, subject to an orthonormality condition $< \phi_i | \phi_j >= \delta_{ij}$, yields the ground state energy ε_0 in equation 2.36. Equation 2.36 is numerically integrated using a symplectic integrator such as velocity Verlet, while forces at each time step are obtained by minimizing the KS energy functional in equation 2.37 for the current nuclear configuration. This approach is known as Born-Oppenheimer dynamics [108].

2.10.2 Verlet and Velocity Verlet Algorithm

Verlet and velocity Verlet algorithm is a numerical integration scheme allowing to solve Newton's equations of motion to generate trajectories of particles in MD simulations. The Verlet algorithm updates particle positions at time $t+\Delta t$ using the current positions (r) and accelerations at time (t), along with the positions from the previous time step $t-\Delta t$.

$$r(t+\Delta t) = 2r(t) - r(t-\Delta t) + a(t)\Delta t^2 \tag{2.38}$$

The Verlet algorithm does not calculate the velocities explicitly. Velocities can be calculated from the position r by using equation 2.39

$$v(t) = \frac{r(t+\Delta t) - r(t-\Delta t)}{2\Delta t} \tag{2.39}$$

The Velocity Verlet algorithm is the reformulation of the Verlet algorithm where velocity is incorporated explicitly, which gives position (r), velocities (v), and acceleration (a) at time t+Δt [109].

$$\begin{aligned} r(t+\Delta t) &= r(t) - v(t)\Delta t + \frac{1}{2}a(t)\Delta t^2 \\ v(t+\Delta t) &= v(t) + \frac{1}{2}[a(t) + a(t+\Delta t)]\Delta t \end{aligned} \tag{2.40}$$

2.11 TranSIESTA: Electron Transport in Device

Transport of electrons, spin, and other excitations is a widespread fundamental problem, which is now increasingly significant due to technological advancements that rely on devices where atomistic structure plays a critical role [110]. Transport via a molecule under applied potential is a nonequilibrium quantum kinetic phenomenon where coupling with two leads creates a continuous DOS. When the bias is applied, the split in the electrochemical potentials of the leads

drives the molecule out of equilibrium as it strives to balance with both contacts. The NEGF formalism offers an atomistic framework to describe quantum transport in these systems [111]. TranSIESTA is a quantum electronic transport code that integrates both the DFT and NEGF [112]. It has an interface with SIESTA and calculates the density matrix of the system self-consistently at different external biases [113]. A simplified molecular electronics model where

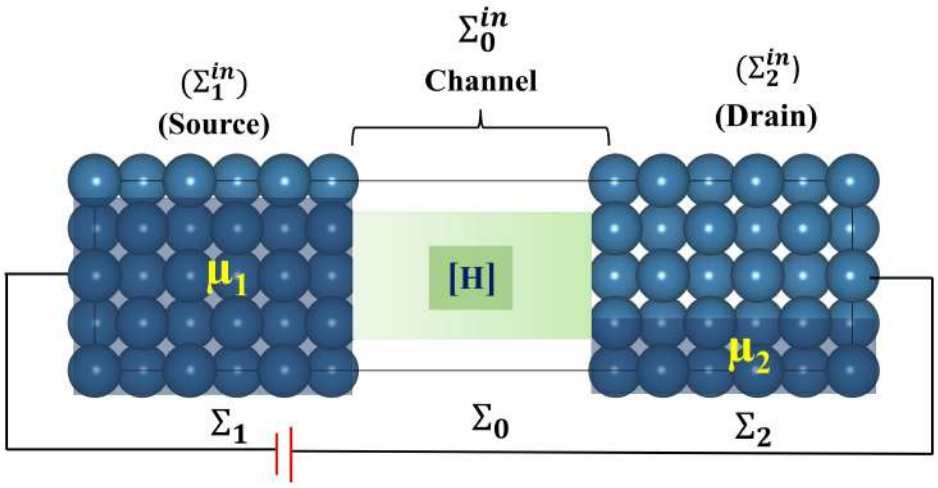

Figure 2.5: Electron transport device model consists of a channel with two contacts, i.e., source and drain. [H] is the Hamiltonian matrix representing the channel, while Σ and Σ^{in} are the self-energy functions.

the scattering region (channel) is sandwiched between two electrodes (source and drain) is illustrated in Figure 2.5 [114]. Quantum mechanical models often begin with a Hamiltonian matrix H, whose eigenvalues represent energy levels. An applied bias to the source and drain, maintaining an electrochemical potential difference μ_1-μ_1=qV. This open system is characterized by two contacts labeled 1 and 2 through self-energy functions $\Sigma_{1,2}$, $\Sigma_{1,2}^{in}$. Here, the Hermitian part of $\Sigma_{1,2}$ regulates the Hamiltonian, and the electron escape rate from the channel is determined by the anti-Hermitian part. In addition, $\Sigma_{1,2}^{in}$ represents the electron inflow from the contact into the channel. In addition, other self-energy functions, Σ_0, and Σ_0^{in} denote lattice-electron interactions and the interaction with other electrons, respectively [114]. Thus, using H and Σ, the NEGF approach calculates the current flow throughout a device [114].

2.11.1 Non-Equilibrium Green's Function (NEGF)

The NEGF approach begins with the standard time-independent Schrödinger equation (SE)

$$H\Psi = E\Psi \tag{2.41}$$

For an open system, two terms, inflow (s) and outflow ($\Sigma\Psi$) of electrons from contact, are incorporated in equation 2.41 and can be written as

$$H\Psi = E\Psi + \Sigma\Psi + s \Rightarrow \Psi = (EI - H - \Sigma)^{-1}s = G^R s \tag{2.42}$$

Where Σ is non-Hermitian in nature. Further, bilinear quantities are introduced to combine multiple incoherent sources (s) because the resulting Ψ from these sources cannot be directly superposed.

$$\Psi\Psi^\dagger = G^R ss^\dagger G^A \tag{2.43}$$

$G^{R\dagger} = G^A$; G^A is the Hermitian conjugate of G^R. Here, G^A is the advanced Green function, and G^R is the retarded Green function [114].

Correlation Function (G^n)

Defining $\Psi\Psi^\dagger = \frac{G^n}{2\Pi}$ and $ss^\dagger = \frac{\Sigma^{in}}{2\Pi}$; equation 2.44 can be written as

$$G^n = G^R \Sigma^{in} G^A \tag{2.44}$$

Here, G^n is a matrix where diagonal elements represent probabilities, and non-diagonal elements represent correlations. Σ^{in} is the inelastic term that can be written as $\Sigma^{in} = \Gamma_1 f_1 + \Gamma_1 f_1$ [115]. f_1 and f_2 are the Fermi functions for the source and the drain terminal, respectively. The term Γ refers to the broadening of the DOS caused by its interaction with the two contacts and represents the antiHermitian parts Σ, which is defined by [115]

$$\Gamma = i[\Sigma - \Sigma^\dagger] \tag{2.45}$$

The density matrix (ρ) of the channel is given by equation 2.46

$$\rho = \int \frac{G^n}{2\pi} dE \tag{2.46}$$

G^n can also be written as

$$G^n = G^R(\Gamma_1 f_1 + \Gamma_1 f_1)G^A = G^R\Gamma_1 G^A f_1 + G^R\Gamma_2 G^A f2 = A_1 f_1 + A_2 f_2 \tag{2.47}$$

A is the spectral function.

Spectral Function (A)

A is the matrix version of the DOS that interacts with the source and drain contacts within the device channel. Hence, the DOS of the device channel can be calculated from the trace of A.

$$DOS = \frac{1}{2\Pi} TraceA \tag{2.48}$$

For an open system, in the eigenstate representation, A can be written as,

$$A = 2\Pi\delta(EI - H) \tag{2.49}$$

The delta term in the above equation can be represented as a Lorentzian function, resulting in the A expressed in terms of the G^R and G^A [115].

$$A = i[G^R - G^A] \tag{2.50}$$

Current Equation

For an isolated system, the current equation can be obtained by applying time-dependent SE (TDSE).

$$\frac{d}{dt}\Psi\Psi^\dagger + \frac{i}{\hbar}[H, \Psi\Psi^\dagger] = 0 \tag{2.51}$$

However, for the entire two-terminal device, since the electron is flowing through the system, the density is not conserved. The current operator (I_{op}) for such a system can be defined $I_{op} \equiv$

$\frac{ie}{h}[H, G^n]$. Since its diagonal element gives the current (I). Hence, I can be written as

$$I = Trace[I_{op}] = \frac{q}{h} Trace[\Sigma^{in} A - \Gamma G^n] \tag{2.52}$$

The terms of an inflow are Σ^{in}A, and an outflow is ΓG^n [116].

Landauer formula

Landauer used scattering theory to connect electrical conductance and transmission function, stating, “Conductance is transmission." The flow of current arises from the difference in electrochemical potentials between the source and the drain, each maintaining local equilibrium with distinct Fermi functions: $f_1 = f_0(E - \mu_1)$ and $f_2 = f_0(E - \mu_2)$. By integrating over energy, the Landauer formula can be obtained, which represents the total current flowing through the i^{th} terminal [116].

$$I_i = (q/h) \int_{-\infty}^{+\infty} T(E)[f_0(E - \mu_1) - f_0(E - \mu_2)]dE \tag{2.53}$$

Here, T(E) = Trace($\Gamma_1 A_1$) = Trace($\Gamma_1 G^A \Gamma_2 G^R$); This T(E) in the current equation is the **Transmission Function**. This describes the rate at which electrons flow from the source to the drain as they propagate through the system or device. It is based on the H and the $\Sigma_{1,2}$ of electrodes [115, 116].

Poisson Equation

The Coulomb potential U(r) is a key component of Σ_0, resulting from the electron density $\frac{G^n}{2\pi}$, and can be determined by solving the Poisson equation [117, 118].

Figure 2.6 illustrates the NEGF flowchart for calculating device currents at the source (1) and drain (2) terminals [115]. The Poisson equation is iteratively solved with Green’s function G^R using an initial guessed channel potential U(r) until convergence. The Hamiltonian (H) carries information about the nanoscale device, geometry, defects, etc. Once U(r) converged, the spectral function (A), broadening terms ($\Gamma_{1,2}$), and subsequently the terminal currents ($I_{1,2}$) can be determined [115].

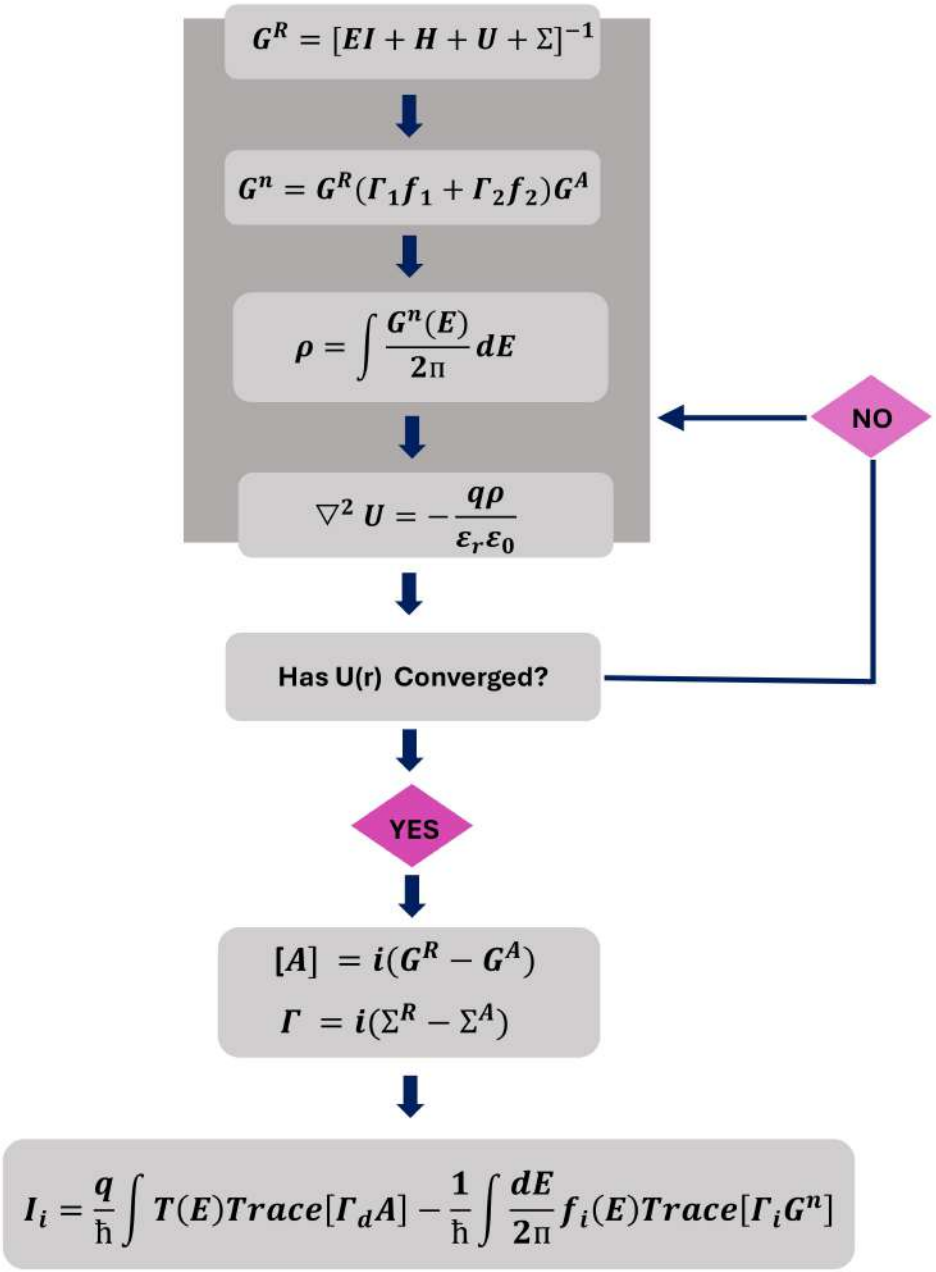

Figure 2.6: The NEGF flowchart outlines for a nanodevice.

Chapter 3

PYRIDINIC-N GRAPHENE AS AN EFFICIENT SO_2 SENSOR

(This work in this Chapter is published in *J. Phys. Chem. A* 2023, 127, 5, 1112–1123.)

3.1 Introduction

With ever-increasing industrialization and urbanization, air pollution has become the most crucial global challenge, which significantly impacts climate change and human health [27, 119, 120]. Sulfur dioxide (SO_2) is considered a toxic and hazardous pollutant that reacts with nitrogen oxides in the atmosphere, causing acid rain, reducing crop yields, and threatening ecological stability [121]. Moreover, prolonged exposure to SO_2 causes infections of the skin and eyes, damage and failure of the lungs, and a higher death rate [122]. In the past, a wide variety of nanomaterials and nanoparticles have been found to be effective SO_2 sensors, including Sc_2CO_2 monolayers [79], g-C_3N_4 nanosheets [123], Ag/Ag_2S nanoparticles [124], and others. Nevertheless, inherent shortcomings of these materials, such as limited stability [125], high adsorption strength [123], lengthy recovery time, etc., have limited their practical applicability as a gas sensor. Therefore, developing a highly efficient SO_2 gas sensor is integral to monitoring and protecting the global environment.

Over the past few decades, graphene received remarkable research attention owing to its high surface area, mechanical stability, exceptional electron mobility, and high surface reactivity [6], hence becoming a promising alternative to metal-oxide-based sensors [126–128]. Novoselov and co-workers studied the very first application of graphene monolayer as a gas-sensor [129].

Since then, graphene has been extensively studied in gas sensing applications due to its distinct features mentioned earlier. But from the device perspective, the major disadvantage of graphene is its zero-band gap, which makes it challenging to regulate the carrier density [130]. Doping with a foreign atom is a major approach to fabricating a highly efficient graphene-based device via band gap engineering and enhancing surface reactivity [126, 131]. Nitrogen is an excellent element for doping in graphene, having comparable atomic radii and electronegativity [132] with carbon. Furthermore, an active region on the surface is generated by overlapping the charge and spin densities [133]. Many experimental and theoretical studies signify the high binding affinity of N-doped graphene toward the detection of gaseous pollutants compared to pristine graphene [66, 134]. Moreover, the inclusion of defects such as Stone-Wales (SW) and point defects [135, 136] can also enhance the gas sensing ability of the system [137, 138] due to the accumulation of charge in the defect region. In addition, other essential aspects that effectively alter the sensing performance of 2D material are doping concentration [127], applying biaxial strain [139], and external electric field [79].

Pyridinic dominance N-doped graphene (PNG) includes both potential factor doping and defect, which efficiently tune the electronic as well as structural properties of graphene [140]. This system already has an extensive research interest due to its possible applications in catalysis [141], sensors [142, 143], batteries, [144], and so on. Guo *et al.* [145] recently demonstrated the better activity of PNG monolayers toward oxygen reduction reaction (ORR) compared to the graphitic N. Furthermore, the presence of a defect site leads to the repulsion of the most common environmental composites (i.e., N_2 and O_2) and makes PNG a selective gas sensor in the atmosphere [142, 143]. To the best of our knowledge, the PNG monolayers have not yet been comprehensively investigated to detect sulfur dioxide (SO_2) gas.

Considering the parameters mentioned above, we have studied pyridinic dominance N-doped graphene (PNG) nanosheets to explore their sensing potential for SO_2 within the framework of spin-polarized density functional theory and ab initio molecular dynamics (AIMD) simulation. Since larger vacancies would cause structural instability, we have considered only single vacancy monolayers having different doping concentrations [146]. Further, to verify the selectivity of PNG monolayers toward SO_2 molecule, we look into the adsorption of several major air

constituents such as O_2, N_2, humidity (H_2O), and CO_2. The impact of applied biaxial strain and the external electric field was also examined to tailor further the strength of the interaction between the SO_2 molecule and the sensor.

3.2 Computational Details

All calculations in this work, including structural relaxation and electronic properties analysis, were performed with the Quantum ESPRESSO software package [147] using spin-polarized density functional theory (DFT) [148]. The core electron of the atoms was replaced by an ultra-soft pseudopotential [149], and the exchange−correlation potential has been approximated using the generalized gradient approximation of Perdew−Burke−Ernzerhof (GGA−PBE) [150]. For structural relaxation, a plane wave kinetic energy cutoff of 540 eV was used to describe the wave function with a Monkhorst−Pack grid [151] of $5 \times 5 \times 1$. Grimme's D3 method was incorporated to include the van der Waals (vdW) corrections [152]. For the density of states, a $30 \times 30 \times 1$ k-grid was sampled to integrate the Brillouin zone. Self-consistency was attained using a force of 10^{-2} eV/Å and a convergence tolerance of 10^{-5} eV. The k-point and cutoff energy sampling is taken through a convergence test with respect to energy.

A 4×4 supercell of graphene with 32 carbon atoms was considered with 15 Å of vacuum along the $z-$axis to avoid the periodic image interaction. Initially, one carbon atom was removed from the pristine graphene (PG) sheet, resulting in a monovacancy structure. The native C-atoms were then replaced with one, two, and three nitrogen atoms and designated as pysvn1, pysvn2, and pysvn3, respectively [153]. The stability of these monolayers was analyzed through defect formation energy (E_{form}) and cohesive energies (E_{coh}) calculations defined in equation A.1 and A.2, respectively (Appendix A. Supporting Data). The adsorption energy (E_{ads}) of the targeted gas molecule on the PNG systems was computed by equation 3.1 [79].

$$E_{ads} = E_{suface+gas} - (E_{suface} + E_{gas}) \tag{3.1}$$

Here, $E_{suface+gas}$, E_{suface}, and E_{gas} are fully relaxed energies of gas molecule adsorbed surface, surface, and gas molecules, respectively. The more negative E_{ads} corresponds to a stronger interaction. Accordingly, Bader charge analyses [154] were carried out using Henkelman code

[155] to understand the charge transfer phenomenon. To visualize the charge allocation upon adsorption, charge density difference (CDD) is analyzed using equation 3.2 [79], and the profile was plotted using the VESTA code [156].

$$\rho_{CDD} = \rho_{surface+gas} - \rho_{surface} - \rho_{gas} \tag{3.2}$$

Here, $\rho_{surface+gas}$, $\rho_{surface}$, and ρ_{gas} stand for charge densities of gas adsorbed surface, surface, and gas molecule, respectively. All AIMD simulations were performed using the QUICKSTEP module employed in the CP2K code [157]. GTH-PBE pseudopotential [158] and corresponding DZVP-MOLOPT-SR-GTH [98] basis sets have been used to describe all the atoms with Grimme's (DFT-D3) dispersion correction [152]. The simulation was carried out by applying an NVT ensemble with a Nose−Hoover thermostat [159] at a constant temperature of 300 K.

3.3 Results and Discussion

3.3.1 Structural Properties Analysis

The structure of pristine graphene (PG) and three monolayers of pyridinic dominance N-doped graphene (PNG) are shown in Figure 3.1. Considering the PG unit cell as a reference, the estimated lattice constants and C−C bond distance were observed to be a=b=2.46 Å and 1.42 Å, respectively, which are quite close to the experimental values [160]. Figure 3.1(b) shows that the stabilization of the pysvn1 by the formation of a pentagon supports earlier findings [153]. In order to assess the stability, we first estimated the formation energy and cohesive energy for each system, and the resulting plots are displayed in Figure 3.2. The formation energy (E_{form}) plot in Figure 3.2 depicts that all the formation energy values are positive except pristine graphene. There are previously reported studies that addressed the possibility of endothermic formation energies [161, 162]. However, formation energy can be regulated by different factors like pressure, temperature, and type of feedstock [146]. The cohesive energy (E_{coh}) plot in Figure 3.2 shows the vacancy introduces instability into the structure, PNG monolayers' calculated cohesive energy values are lower than those for pristine graphene. However, these values are comparable with PG [163], indicating the feasibility of the PNG monolayers to be produced experimentally.

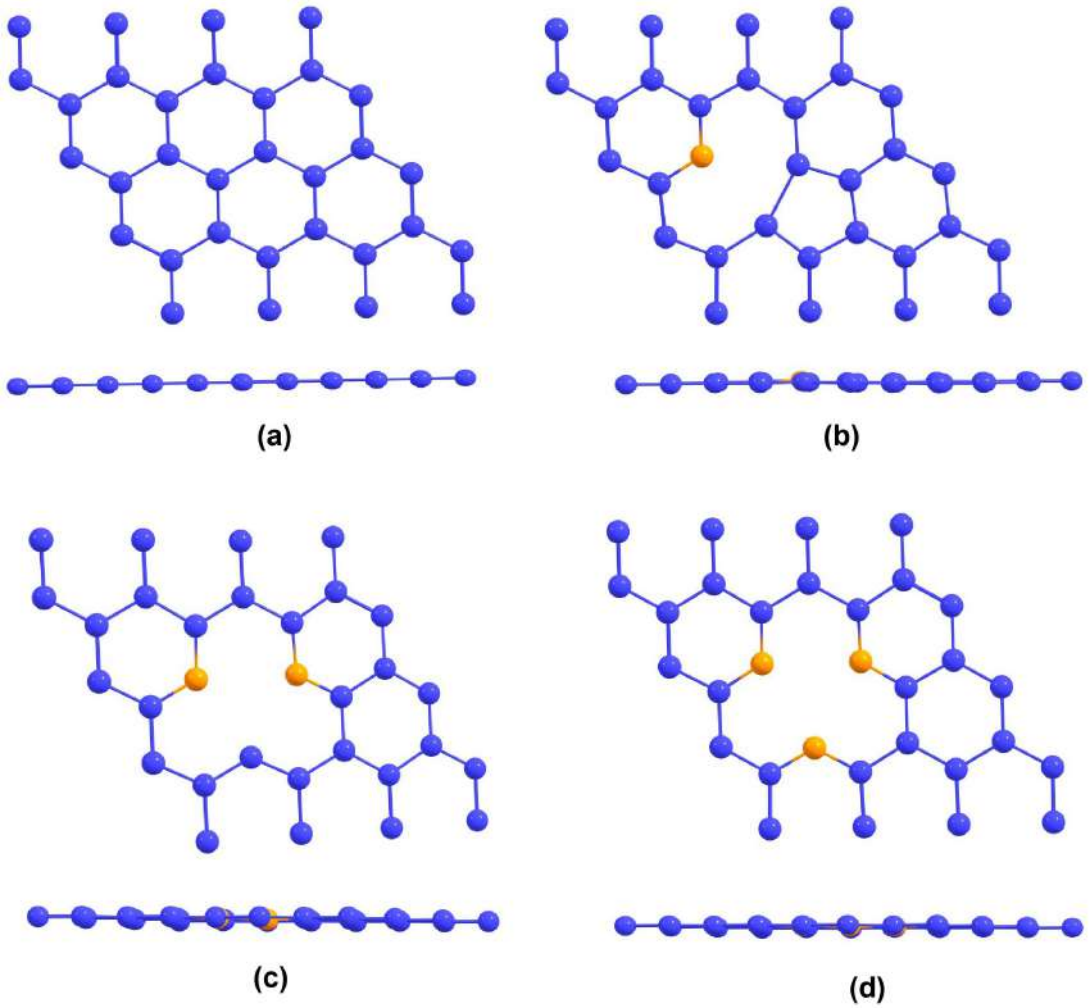

Figure 3.1: Top and side perspective of the relaxed structure of (a) pristine graphene (PG), (b) pysvn1, (c) pysvn2, and (d) pysvn3. Blue and orange balls depict the carbon and nitrogen atoms, respectively.

The electronic properties of PNG are further examined from the electronic band structure calculation using the PBE functional, as shown in Figure A.1 (Appendix A. Supporting Data). The plots in Figure A.1 (Appendix A. Supporting Data) demonstrated that the Fermi level (E_F) overlaps the valence band (VB), and hence, these materials behave as metals [153]. The presence of a single vacancy in the pyridinic configuration results in an electron-deficient system, which generates an acceptor state in the VB and subsequent lowering of the E_F. Despite this fact, earlier research has demonstrated that the pyridinic form of graphene exhibits p-type conductivity [132, 140, 164]. In a recent study, Yutomo *et al.* stated that the presence of extra states in the VB causes p-type conductivity in the pyridinic configuration [153]. Accordingly, we classified our systems as p-type semiconductors. Furthermore, the work function (ϕ) for each system was

calculated, and it has been observed that all monolayers exhibit higher work functions than pristine graphene. According to Schiros *et al.* [140], the removal of charge from graphene by pyridinic nitrogen causes an increase in the work function [140]. All computed bandgap (E_g) values, ϕ, and doping effect of PG and PNG monolayers were listed in Table A.1 (Appendix A. Supporting Data) [140, 153, 165]. The thermal stability of the monolayers was confirmed by AIMD simulations for 5 ps at an interval of 1 fs at 300 K, presented in Figure A.2 (Appendix A. Supporting Data). Furthermore, the bond length (S−O) and bond angle (O−S−O) for the SO_2 molecule are calculated to be 1.45 Å and 119.40°, respectively, which are close to the reported values [166].

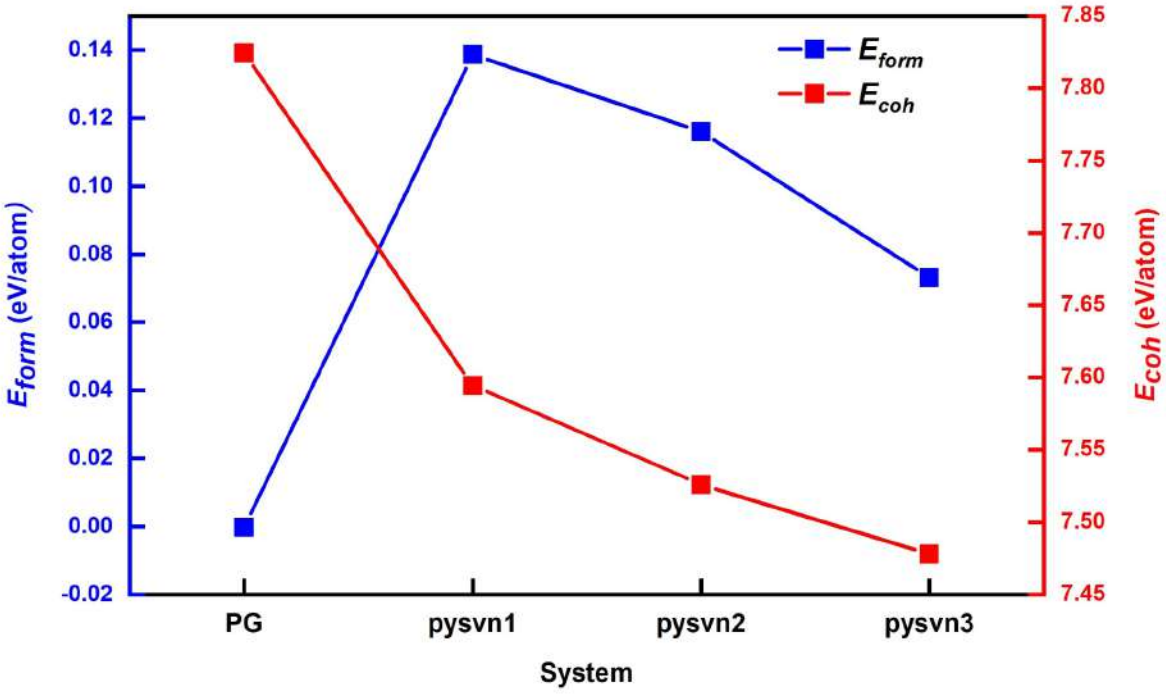

Figure 3.2: Formation energies (E_{form}) and cohesive energies (E_{coh}) of PG and PNG monolayers.

3.3.2 Sensing Properties of PNG Monolayers

Energetics and Charge Analysis

To assess the adsorption potential of PNG monolayers toward SO_2, we have determined the lowest adsorption energy configuration by positioning the gas molecules at various possible orientations and sites, as shown in A.3 (Appendix A. Supporting Data). The exothermic character of the adsorption is confirmed by the negative adsorption energies in Figure 3.3, suggesting a favorable sensing application. To ensure that the SO_2 molecule is adsorbed at the optimal

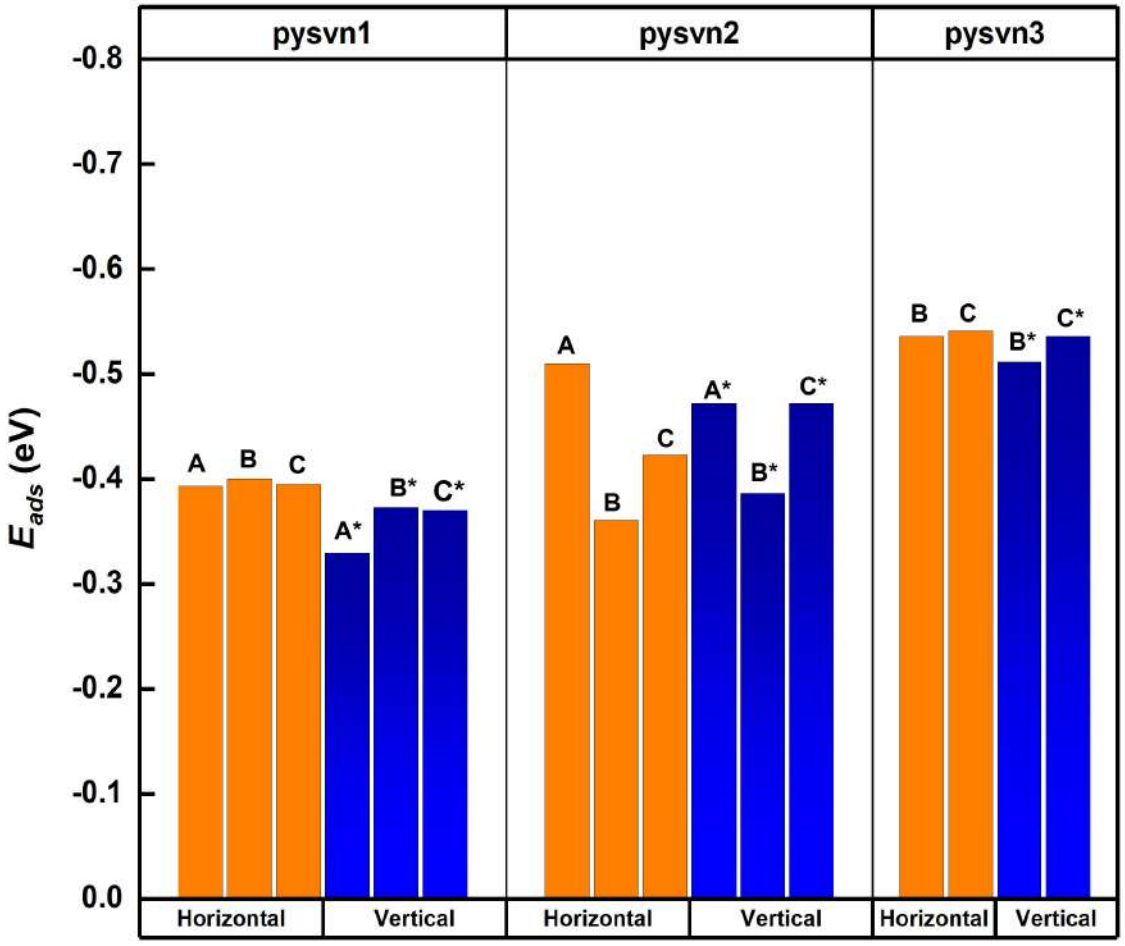

Figure 3.3: Calculated adsorption energies (E_{ads}) of SO_2 at different binding sites and orientations of pysvn1, pysvn2, and pysvn3 monolayers. (For pysvn3, two binding sites are considered).

separation at a preferable site, we employed two approaches (a) keeping the gas molecules more than 3 Å away from the PNG surfaces, and (b) in the preferred adsorption configuration, shifting the gas molecule along the z-axis and creating potential energy curves (PECs) [167], [Figure A.4 (Appendix A. Supporting Data)]. Figure 3.4 depicts the most suitable adsorption configurations of PNG monolayers. The adsorption distance (AD) of the minimum energy structures in PECs was found to be similar to the AD obtained from the preferable structures (Figure 3.4). It has been noted that the SO_2 preferred to bind through the C*-site (vacancy sites) for pysvn1 and pysvn3. On the other hand, since pysvn2 has a dangling carbon bond, the SO_2 chose the A*-site (carbon site) to bind. The SO_2 molecules are nearly parallel to the PNG surfaces in these configurations, and there is a decrease in bond angle ranging from 1.17° to 2.35° compared to the free-standing SO_2. The optimal adsorption energies of SO_2 over pysvn1, pysvn2, and pysvn3

are −0.39, −0.51, and −0.54 eV, respectively. Table 3.1 summarizes the adsorption energies, charge transfer values, optimized binding distance, bond angle, and bond length of adsorbed SO_2. The negative charge transfer value (Q_e) indicates that charge transfer occurs from PNG surfaces to gas molecules, which further delineates the acceptor nature of the SO_2 molecule. From Table 3.1, it can be observed that there is a decrement of adsorption potential in the order of pysvn3 > pysvn2 > pysvn1. We have not observed any correlation between the E_{ads} and charge transfer value, but a linear relation between adsorption distance and interaction strength. In addition, to verify the accuracy of computations in a 4×4 supercell, we performed similar calculations in a 5×5 supercell, as shown in Figure A.5 and Table A.2 (Appendix A. Supporting Data). We observed marginal differences in E_{ads} and Q_e values between the 4×4 and 5×5 supercells. Furthermore, Figure 3.5 visualizes the charge density difference (CDD) plots and planar average charge density difference to unveil the charge distribution nature between PNG monolayers and SO_2 molecules. The CDD plot illustrates the charge accumulation zones in purple color, whereas the charge depletion regions are in golden color. In all three cases [Figures 3.5(a-c)], there is clear evidence of charge accumulation in the gas molecules, indicating the acceptor nature of the SO_2 molecule. Additionally, the CDD calculation results agree well with the Bader charge analyzed data (Table 3.1). The real space diagram represents the planar-averaged charge density difference along the z-direction shown in Figure 3.5(d). The following observations are drawn from this comparative profile: (1) it is consistent with prior CDD studies that indicate electrons are transported from the PNG surface to the SO_2 molecule, and (2) as pysvn2 experiences a greater charge transfer, its corresponding curve amplitude is higher, followed by pysvn3 and pysvn1.

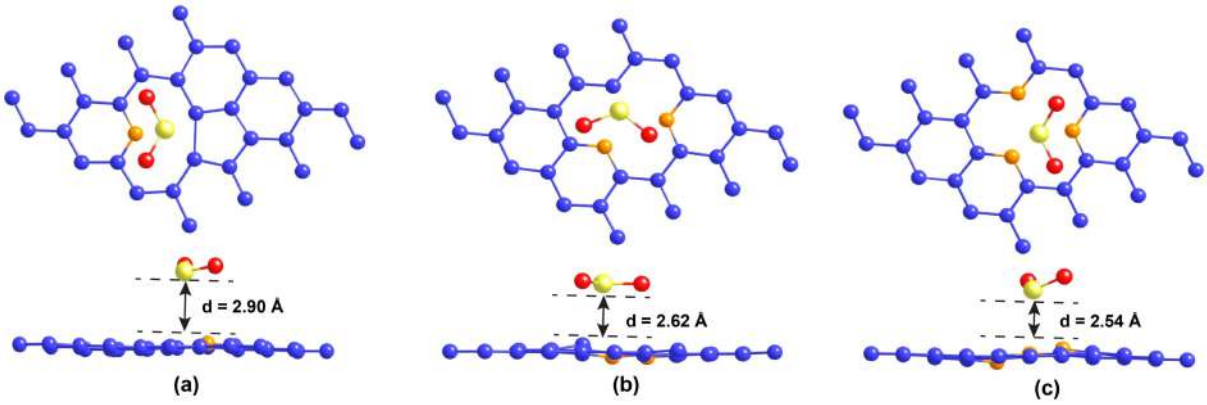

Figure 3.4: Optimized structures of the preferred adsorption configuration of SO_2 molecules on (a) pysvn1, (b) pysvn2, and (c) pysvn3.

Table 3.1: Adsorption energy (E_{ads}), charge transfer value (Q_e), adsorption distance (d), O−S bond length (l), and O−S−O bond angle (Θ) of SO_2 molecule on PNG monolayers.

System	E_{ads} (eV)	Q_e	d (Å)	l (Å)	$\Theta(^\circ)$
pysvn1	−0.39	−0.11	2.90	1.46	118.23
pysvn2	−0.51	−0.22	2.62	1.47	117.05
pysvn3	−0.54	−0.12	2.54	1.46	117.46

Electronic Properties of SO_2 Adsorbed on PNG Monolayers

We further analyzed the spin-polarized density of states (SPDOS) for all three SO_2 adsorbed PNG monolayers to have a better understanding of the adsorption behavior. Orbital mixing is crucial in determining the interaction between a molecule and an adsorbent [168]. The interactions are chemisorption if the overlapping orbitals are near the E_F; in this case, a large amount of charge is transferred from the substrate to the molecule (or vice versa), making the system a sensitive sensor. In contrast, a weaker interaction between the gas molecules and the sensor is revealed by the absence of hybridizing states around the E_F and demonstrates small charge density redistributions [79]. Figure 3.6 presents the SPDOS of the PNG monolayers before and after the adsorption of the gas molecule and isolated SO_2 molecules for all three scenarios. The positive and negative DOS describe the spin-up and spin-down states. Figure 3.6 shows that after adsorption, pysvn2 and pysvn3 experience significant changes around the E_F than pysvn1. On the contrary, no hybridized states appear at the E_F for either isolated or adsorbed SO_2. Further, as demonstrated in Figure 3.6(a)(v), a significant orbital hybridization exists between pysvn1 and the SO_2 molecule localized around 1.5 eV in the conduction band (CB) and around $2.0-3.0$

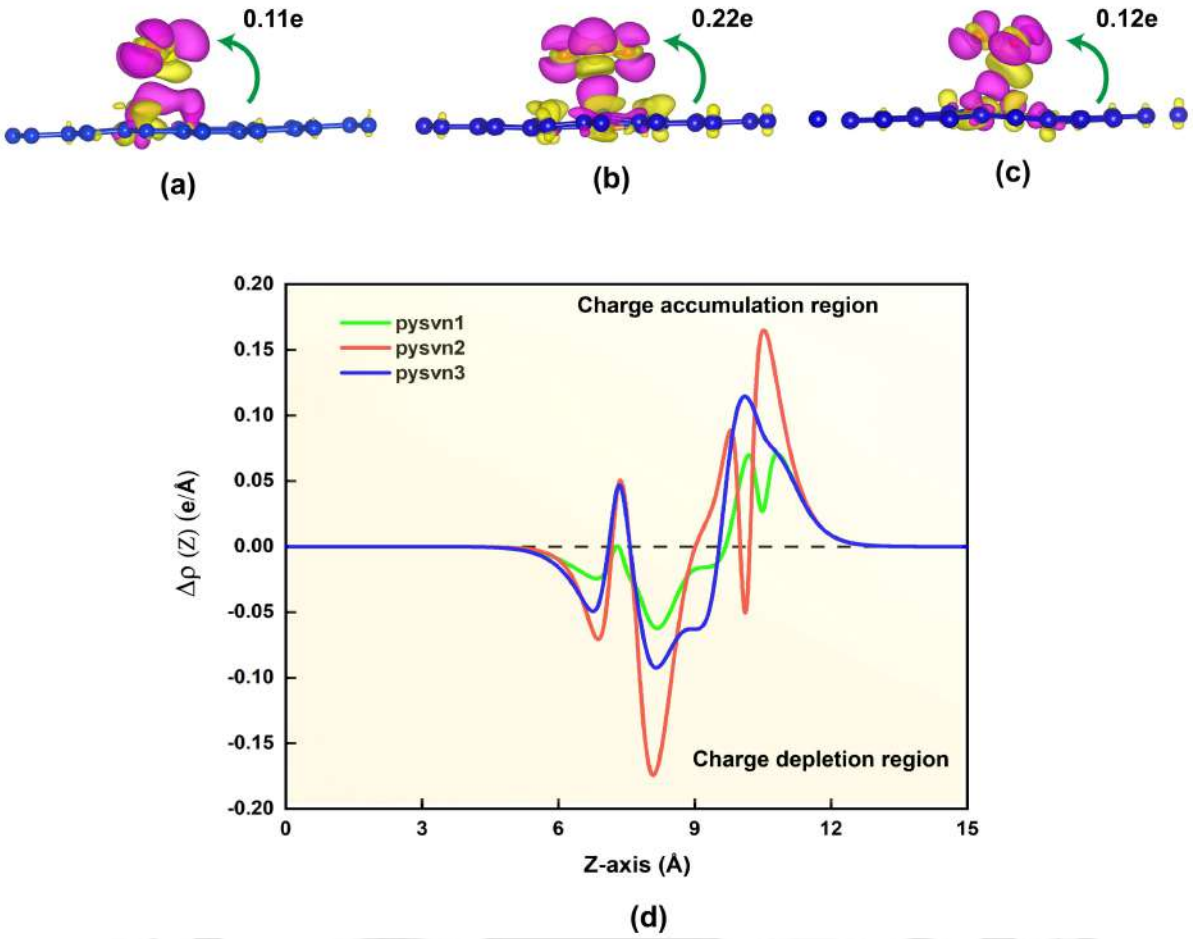

Figure 3.5: Charge density difference (CDD) plots of SO_2 molecule adsorbed on (a) pysvn1, (b) pysvn2, and (c) pysvn3. Purple and golden colors represent the charge accumulation and depletion, respectively (iso-surface value: 0.0009 e/bohr^3). (d) Planar-averaged charge density difference plots.

eV in the valence band (VB) region. The DOS of pysvn2 and SO_2 have considerable orbital overlap near $1.5-3.0$ eV in VB and around 2.0 eV in CB, as seen in Figure 3.6(b)(v). Again, the orbital interactions in the VB and CB regions of SO_2-adsorbed pysvn3 [Figure 3.6(c)(v)] share the same energy window as pysvn2. Previous studies have suggested that the electronic states of gas molecules contribute to adsorption systems near the E_F, ranging from -2.5 to 2.5 eV. This shows that the presence of these gas molecules may significantly impact the system's electronic features. [169, 170] Since the overlapping orbital range in our PNG monolayers and the SO_2 molecules are comparable to the previous literature, these PNG monolayers can serve as an effective SO_2 gas sensor. The asymmetric behavior of spin-up and down channels reveals the magnetic properties of SO_2 adsorbed pysvn2 and pysvn3 with magnetic moments of 0.07 and 0.44 μ_B, respectively. Since the magnetic moment value (μ_B) of SO_2 adsorbed pysvn2 seems to

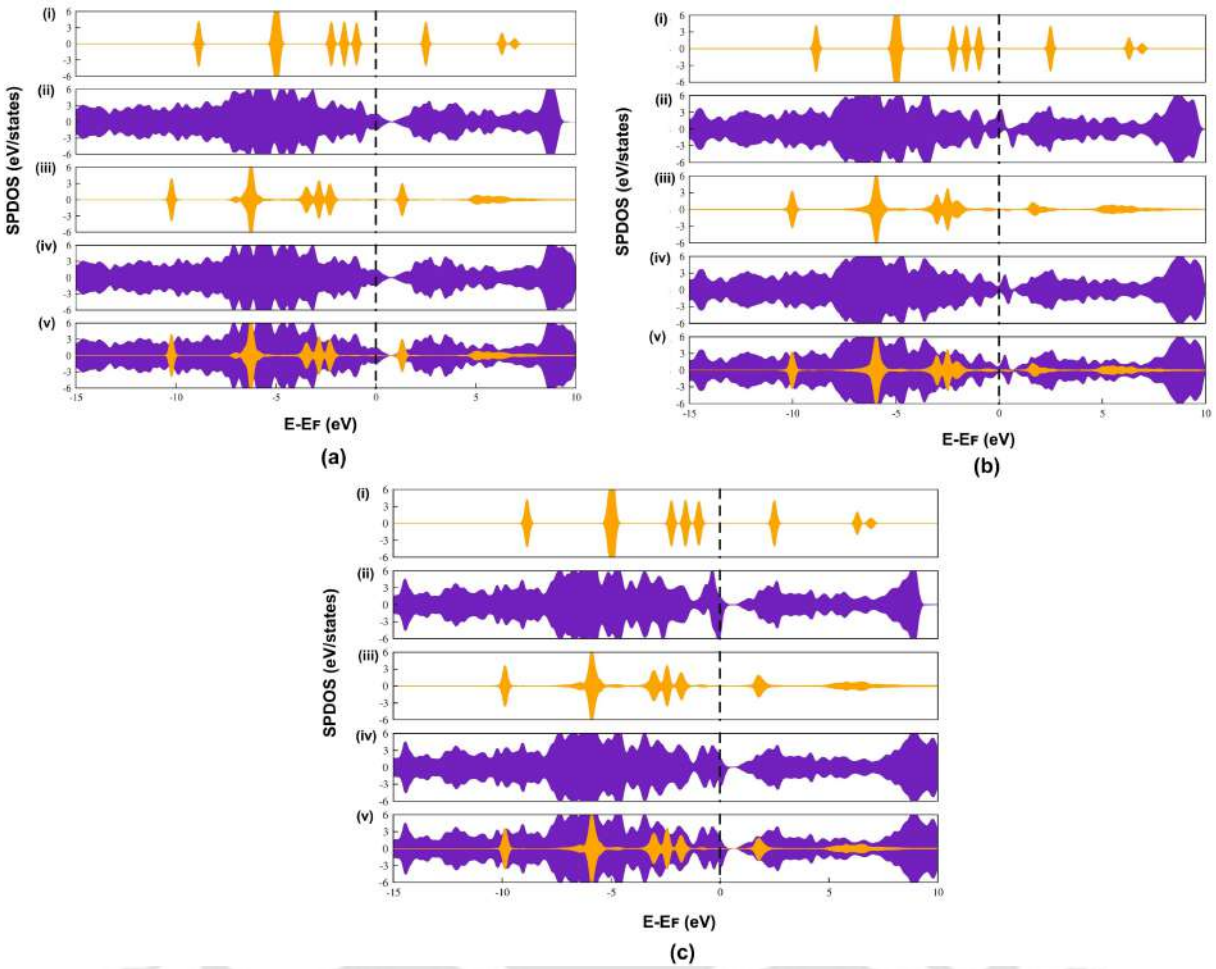

Figure 3.6: Spin-polarized density of states (SPDOS) of (a) pysvn1, (b) pysvn2, and (c) pysvn3 monolayers before and after adsorption of SO_2. (i) isolated-SO_2, (ii) PNG, (iii) SO_2 (after adsorption), (iv) PNG (after adsorption), (v) overlapping between SO_2-orbital and PNG-orbitals. The black dashed line represents the Fermi level.

be very small, we conducted a convergence test for non-magnetic and magnetic solutions with respect to energy and shown in Table A.3 (Appendix A. Supporting Data). Table A.3 shows that the energies are well converged, allowing us to predict that SO_2 adsorbed pysvn2 has a reliable magnetic moment of 0.07 μ_B. In addition, because SO_2 is an oxidizing agent in this circumstance, the number of holes in the VB increases, resulting in increased semiconductor conductivity.

Work Function and Recovery Time

Field effect gas sensing, which is based on a change in work function, is another intriguing approach for detecting gaseous pollutants [171]. Work function (ϕ) can be determined by the minimal energy needed to eject one electron from the E_F to vacuum level (E_{vac}) using equation

3.3. The Fermi energy and the vacuum level energy are denoted by E_F and E_{vac}, respectively [167]. E_{vac} is determined by the electrostatic potential calculation in a vacuum zone away from the system.

$$\phi = E_{vac} - E_F \tag{3.3}$$

The change in work functions before and after SO_2 adsorption in the systems under study are presented in Figure 3.7(a). Due to the fact that the SO_2 molecule acts as an acceptor, the plot reveals that there is an increase in the work function upon adsorption. Notably, we observed no link between change in work function ($\Delta\phi$) and charge transfer value (Q_e) but a linear correlation with adsorption energy (E_{ads}), as shown in Figure A.6 (Appendix A. Supporting Data). Changes in the work function of PNG monolayers upon gas adsorption show a significant interaction. This suggests that the work function can be tuned by selective gas molecule adsorption. In addition, a strong interaction leads to severe pruning of the gas molecules, which eventually results in a long recovery time. Thus, recovery time (τ) analysis is an essential parameter for predicting the multi-time reusability of a sensor. It can be evaluated by equation 3.4 (using transition state theory) [172].

$$\tau = A^{-1} exp \frac{-E_{ads}}{k_B T} \tag{3.4}$$

In equation 3.4, A, E_{ads}, k_B, and T stand for attempt frequency (10^{13} s^{-1}), adsorption energy, Boltzmann constant, and temperature (300 K), respectively [173]. It is evident from the equation 3.4 that with higher adsorption energy (E_{ads}), the recovery rate reduces, and the sensor responds differently toward the gas at various operational frequencies. Interestingly, all three adsorption energies fall within the range of -0.30 to -0.80 eV, which eventually describes the reversibility of the sensors [172, 174]. Figure 3.7(b) displays the calculated recovery times for SO_2 adsorbed PNG monolayers. Following this, it has been determined that the recovery time for the SO_2 molecule is 0.59 μs for pysvn1, 72 μs for pysvn2, and 24 ms (millisecond) for pysvn3. With such minimal recovery times, PNG monolayers are expected to be reusable gas sensors.

Selectivity

PNG monolayers have so far been shown to be efficient SO_2 sensors. Furthermore, as air contains few predominating elements, including N_2, O_2, CO_2, and humidity, it is worth investigating

the selectivity of the pyridinic dominance N-doped graphene (PNG) for SO_2. The interaction strength for O_2, N_2, CO_2, and humidity in the three PNG monolayers has been examined to evaluate the selectivity of SO_2 for environmental monitoring. We employed the effect of H_2O in order to take humidity into account [175]. All computed E_{ads} and Q_e values for the stable adsorption configuration are displayed in Table A.4 (Appendix A. Supporting Data). The E_{ads} and Q_e values between SO_2 and PNG monolayers are considerably stronger than that of other gas molecules, implying that monolayers of PNG have a high selectivity to hazardous SO_2 gas.

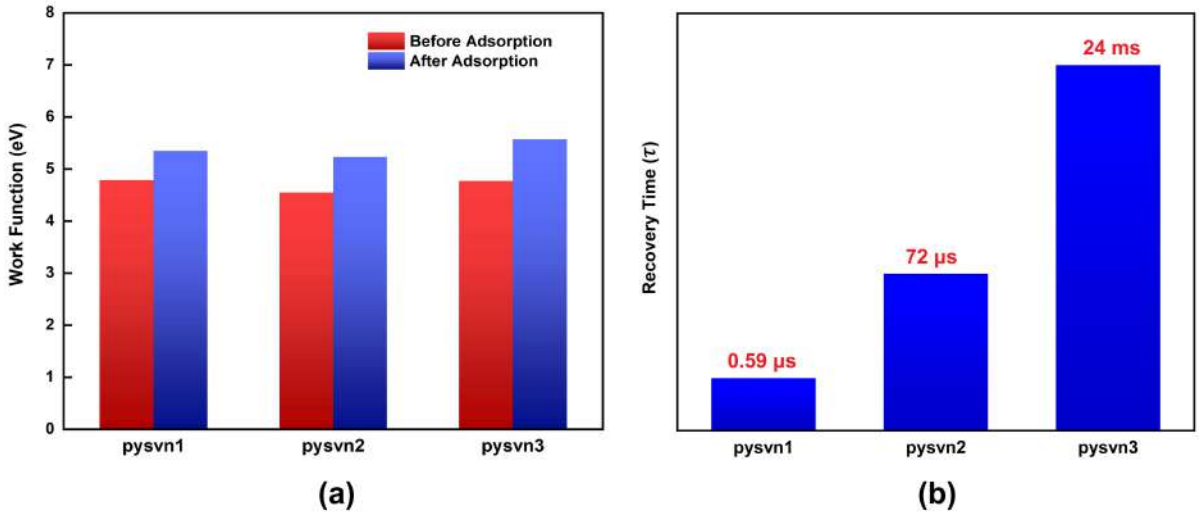

Figure 3.7: (a) Calculated work function (ϕ) of PNG monolayers before and after adsorption of SO_2 gas molecule. (b) Calculated recovery time (τ) for PNG monolayers.

Thermal Stability

The thermal stability of SO_2-adsorbed monolayers was further analyzed by AIMD simulations at 300 K for 5 ps with a time step of 1 fs using NVT ensemble, and the results are depicted in Figure 3.8. Clearly, the oscillations of energy over time remain relatively constant for pysvn2 and pysvn3 adsorption monolayers and do not experience significant structural deformation or modification. Conversely, with pysvn1, we observed that the gas molecule is moving away from the surface over time, which may result from relatively weak adsorption energy. Hence, we predict that SO_2-adsorbed pysvn2 and pysvn3 will sustain their stability at room temperature.

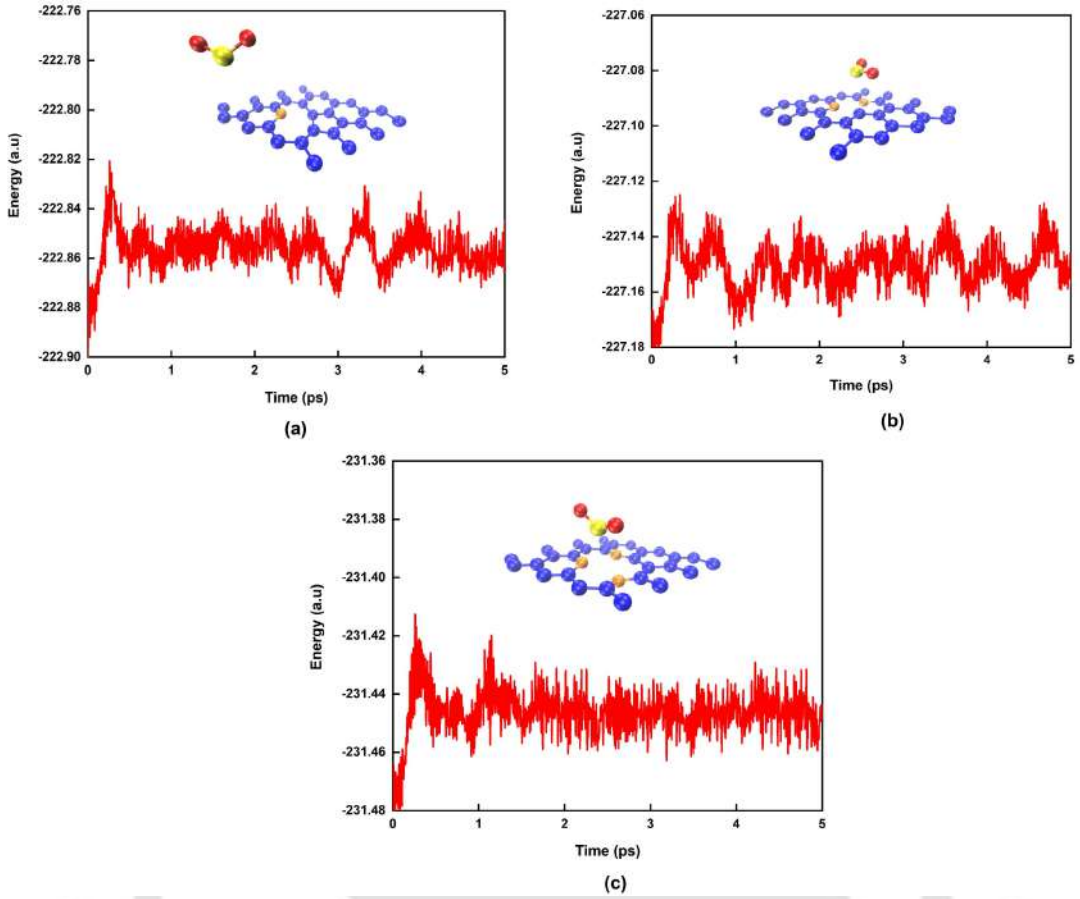

Figure 3.8: AIMD simulation results for SO_2-adsorbed PNG monolayers at $T = 300$ K with snapshots of structural configurations after 5 ps for (a) pysvn1, (b) pysvn2, and (c) pysvn3.

3.3.3 Modulation of the Sensing Performance of PNG Towards SO_2 Gas

Applied External Mechanical Strain

Many prior works demonstrated the strain-dependent sensitivity of gas molecule adsorption on 2D monolayers [79–81]. In the present work, we introduced biaxial strain (from -3% to $+3\%$) to the simulation model to examine the gas sensing capabilities of the PNG monolayers under strain. The relation between biaxial strain and lattice parameter is defined as strain $(\varepsilon) = \frac{a-a_0}{a_0}$, where a_0 and a represent the lattice constant of the monolayers without and with applied strain, respectively [79]. A negative strain indicates applied compressive strain. In contrast, a positive strain means tensile strain was used [139]. The geometries of the systems after applying strain are depicted in Figures A.7 (Appendix A. Supporting Data). After applying compressive strain, it has been seen that the pysvn1 and pysvn3 monolayers are buckled; however pysvn2 monolayer shows no such structural deformation. The impacts of strain modulating adsorption energy

(E_{ads}), charge transfer (Q_e), and change in work function ($\Delta\phi$) values are depicted in Figure 3.9. As shown in Figure 3.9(a), the adsorption energies of SO_2 on all PNG monolayers increase as the applied compressive biaxial strains increase. On the contrary, it decreases as the applied tensile biaxial strain increases. Notably, the effect of the applied strain on pysvn2 is more pronounced, whereas the adsorption strength of SO_2 on pysvn1 and pysvn3 is less susceptible to the applied biaxial strains. The adsorption energy of pysvn2 is regulated from -0.51 eV (0%) to -0.76 (-3%) with the maximal regulating amplitude of 0.25 eV. The charge transfer values further support the prominent impact of applied strain on pysvn2, as presented in Figure 3.9(b). Additionally, the average electrostatic potential plots of all three monolayers are represented in Figures A.8-A.10 (Appendix A. Supporting Data) under biaxial strains from -3% to $+3\%$. The work function of the monolayer decreases as compressive strain is applied, whereas the work function is increased by tensile strain. The change in work function before and after the adsorption of gas molecules is shown in Figure 3.9(c), also indicates that the pysvn2 monolayers experience the maximum changes (0.45 eV) when strain is applied.

External Electric Fields

The application of an electric field (E-field) has been considered a key approach to altering the features of low-dimensional materials [176]. Many prior studies suggested that using an external electric field to modify the performance of 2D materials as a gas sensor is an effective method [177, 178]. Electric fields cause changes in the carrier density (E-field causes polarization of charge density) produced in a material by the field at its surface, which further alters the response of the sensor toward the adsorbate. The sensor's response is noted as a variation in drain current when an electric field is applied usually, investigated using field-effect transistors (FETs) [179]. In this section, we analyzed the modulated sensitivity of PNG toward SO_2 detection by examining the impact of the external electric field. The electric field along the z-direction (perpendicular to the surface) and intensity of -0.4 to $+0.4$ V/Å are taken into consideration. As observed in Figure 3.10(a), the adsorption potential of SO_2 on PNG monolayers is E-field dependent. Remarkably, SO_2 adsorption on these monolayers is weakened with positive E-field and then strengthened, while the external electric field decreases from 0 to -0.4 V/Å. Furthermore, as shown in Figure3.10(b), the adsorption distance (d) increases (decreases) with increasing positive

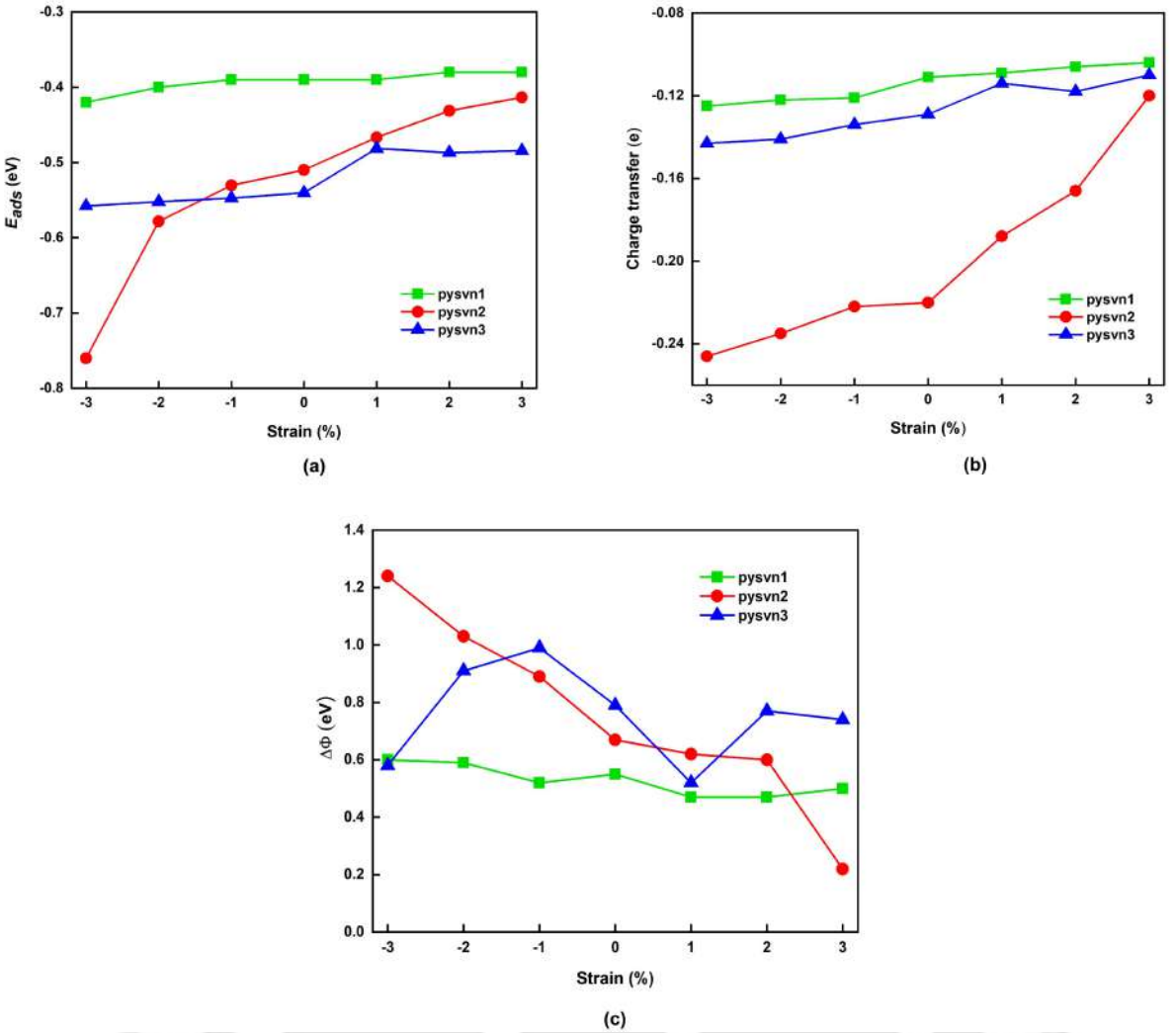

Figure 3.9: Impact of strain on SO_2 adsorbed PNG monolayers. Fluctuation in (a) adsorption energy, (b) charge transfer value, and (c) changes in work function with biaxial strains ranging from -3% to $+3\%$, respectively.

(negative) electric field strength, influencing the strength of interactions as well as the charge transfer values [Figure3.10(c)] between SO_2 and PNG monolayers. The formula for calculating the charge density difference in the PNG monolayers caused by an electric field is given in equation A.3 (Appendix A. Supporting Data). Positive and negative electric fields decrease and increase the electron density, respectively, on the PNG monolayer surface (golden and purple iso-surfaces) as displayed in Figure 3.11(a-b). In the meantime, SO_2 molecules interact with monolayers by accepting upper-surface electrons. Accordingly, the reduced upper surface electron density decreases electron transfer from the PNG monolayer to gas-adsorbed molecules, minimizing their adsorption efficiency as well as the charge transfer value.

We considered the biaxial strain and electric field's range -3.0% to $+3.0\%$ and -0.4 to $+0.4$

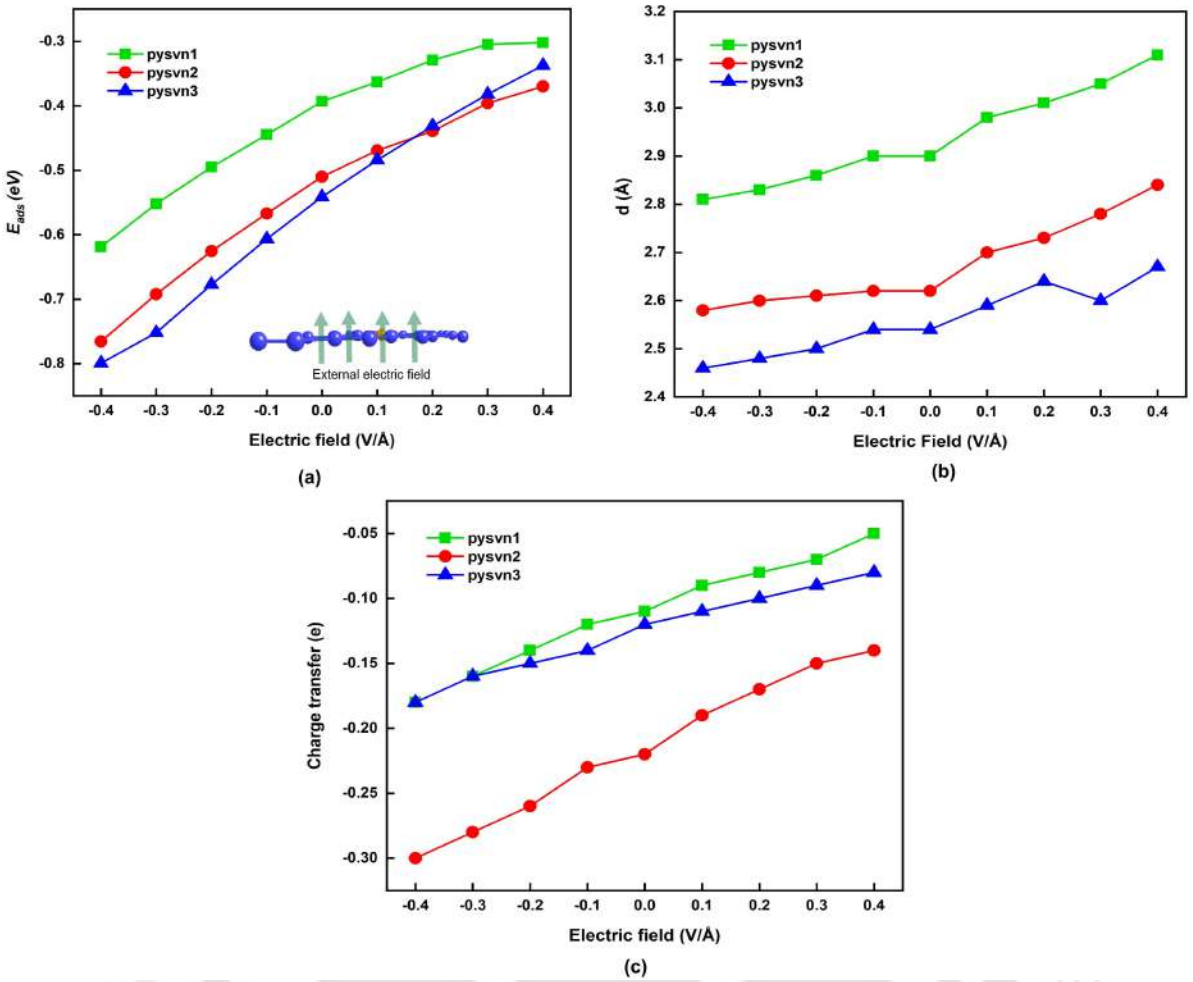

Figure 3.10: Effect of external electric field ranging from −0.4 to 0.4 V/Å (a) adsorption energy (E_{ads}), (b) adsorption distance (d), and (c) charge transfer (Q_e) value. In Figure 10(a), the inset represents the positive E-field.

V/Å, respectively, with respect to the adsorption energy (E_{ads}). The previous report suggests that adsorption energy lies between −0.30 to −0.80 eV, defining the multitime reusability of the sensor [172]. Upon consideration of above mentioned range in the external applied electric field and strain, the adsorption energy does not exceed the threshold of reversibility.

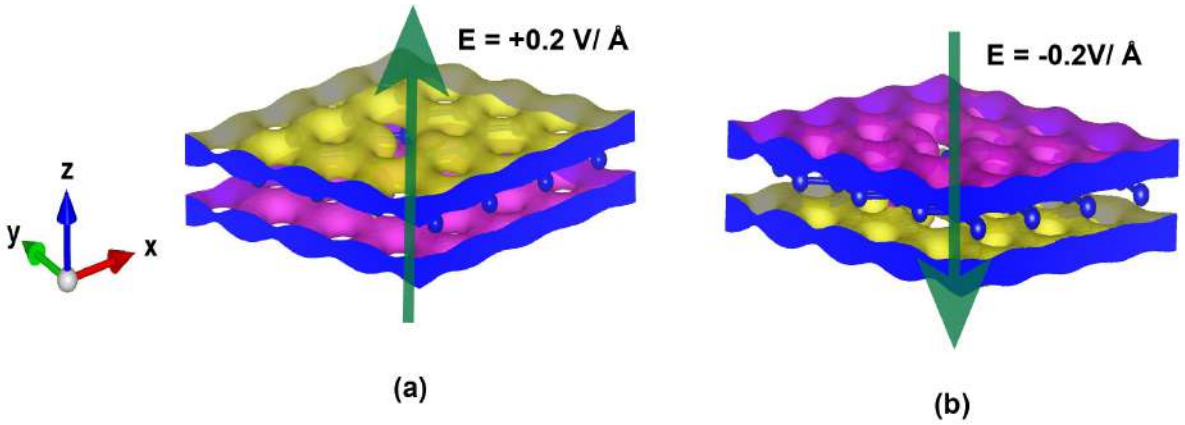

Figure 3.11: Charge density difference (CDD) of pysvn1 monolayer by (a) positive and (b) negative electric fields. The electron density accumulation and depletion is shown in purple and golden isosurfaces, respectively.

3.4 Conclusions

In summary, the interaction between PNG monolayers and SO_2 molecules was investigated using DFT and AIMD in an effort to determine the potential of PNG monolayers as SO_2 gas sensors. Our findings imply that PNG monolayers are suitable SO_2 sensors as they exhibit significant adsorption energy, considerable charge transfer, orbital hybridization near the Fermi-level, and work function variation. The adsorption potential of the PNG monolayers can be ordered as pysvn3 > pysvn2 > pysvn1. The predicted sensor recovery times for pysvn1, pysvn2, and pysvn3 are 0.59 μs, 72 μs, and 24 ms, respectively, which further define the multi-time reusability of the sensor at room temperature. Besides that, our investigation into the thermal stability of the system revealed that pysvn1 is not stable at a temperature of 300 K. Additionally, it has been observed that these monolayers interact with common environmental composites (O_2, N_2, H_2O, and CO_2) in a comparatively weak manner, defining the sensors' selectivity. The results also suggest that PNG monolayers subjected to external compressive strains or negative electric fields provide a higher sensing tendency in the SO_2 gas. Our work with pyridinic dominance N-doped graphene monolayers is a step toward realizing the vision of an efficient gas sensor, and we hope this work validates the sensing capability of these materials as a SO_2 gas sensor.

Chapter 4

Surface Oxygen Functionalized B_2S_2 Monolayer for NO and NO_2 Detection

(This work in this Chapter is published in *Phys. Chem. Chem. Phys.*, 2024, 26, 12386–12396.)

4.1 Introduction

Air pollution is one of the most intractable issues confronting the world in the present era [180]. The continuous upswing in the emission of gaseous contaminants, including carbon monoxide (CO), sulfur dioxide (SO_2), nitrogen oxides (NO_x), and carbon dioxide (CO_2), significantly alters the atmospheric composition and damages the ecosystem as well as human health [27]. NO_2 has recently been discovered to be a major contributor to fine particulate pollution [28]. Furthermore, NO and NO_2 pollutants in the atmosphere generate acid rain, which is extremely detrimental to aquatic life, infrastructure, and vegetation. Apart from contributing to environmental issues, exposure to NO and NO_2 causes respiratory illness ($>$ 50 ppm) and is harmful to the skin even at a low concentration [181]. Thus, finding suitable materials for the next-generation gas sensors that exhibit desirable features such as high selectivity and sensitivity, low detection limits, and operational stability at room temperature presents a significant challenge and has developed into an actively explored research area [182, 183].

In recent years, 2D transition metal dichalcogenides (TMDs) have become an emerging class of materials beyond graphene [184–186]. These materials are highly favorable for fundamental

research on new physical properties and applications in nanoelectronics, nanophotonics, etc. Among various TMDs, molybdenum disulfide (MoS_2) has drawn considerable interest within the sensing domain due to its ability to detect diverse analytes at room temperature, favorable surface-to-volume ratio, and tunable semiconducting characteristics [187]. It also offered significant benefits in developing flexible and wearable sensing devices [43].

Analogous to MoS_2, Tang *et al.* [16] theoretically proposed a B_2S_2 structure due to valence electron analogies between molybdenum (Mo) atoms and B_2-pairs. This boron sulfide monolayer (B_2S_2) has a variety of potential uses in future nano-devices or nano-electronics [188, 189], photo-electrochemical current switching [190], hydrogen storage [191], etc., due to its remarkable thermoelectric [192], high mechanical strength, stability [188], and exceptional electronic properties [193]. Experimental synthesis of this new 2D material B_2S_2 was carried out by Zhang *et al.* [12]. The two possible structural configurations of 2D-B_2S_2 are T-phase (T-B_2S_2) and H-phase (h-B_2S_2) (both are analogous to MoS_2), having indirect band-gap of 4.09 eV and 3.92 eV, respectively. Such wide band gaps will lead to high UV absorption and enable possible implementation in ultra-violet optoelectronic devices [16]. h-B_2S_2 exhibits a fairly high electron mobility of up to 1.21×10^5 $cm^2\ V^{-1}\ s^{-1}$ along the K-Γ direction while T-B_2S_2 exhibits almost two-order of magnitude less electron mobility (2.18×10^3 $cm^2\ V^{-1}\ s^{-1}$) than h-B_2S_2. The carrier mobility of h-B_2S_2 is comparable to other graphene-based two-dimensional materials and is much greater than h-MoS_2 (200 $cm^2\ V^{-1}\ s^{-1}$) [16, 194]. This demonstrates that h-B_2S_2 monolayers are better suited for electronic devices than T-B_2S_2. Meanwhile, the inert surface and a large band gap of 3.92 eV limit the application of h-B_2S_2 in the sensing field [12].

Surface atom functionalization is a viable method to modify the surface chemistry of the materials and broaden their application in various disciplines, including sensors, catalysts, transistors, and batteries [79, 195, 196]. The chemical reactivity of oxygen and its allotropes makes them ideal for surface modification and engineering [197]. Numerous previous studies have demonstrated that surfaces terminated with oxygen molecules substantially impact the gas sensitivity and response time of a sensor [79, 198].

Driven by the effect of surface functionalization in gas-sensing applications, we have functionalized the surface of h-B_2S_2 by introducing oxygen atoms, resulting in the formation of

an oxygen-functionalized h-B_2S_2 monolayer, denoted as Oh-B_2S_2. In this study, we have investigated the gas-sensing properties of the monolayer Oh-B_2S_2 towards a range of potentially hazardous gases such as carbon monoxide (CO), nitrogen monoxide (NO), carbon dioxide (CO_2), nitrogen dioxide (NO_2), nitrous oxide (N_2O), and sulfur dioxide (SO_2). Additionally, we have also examined its response to common atmospheric gases such as oxygen (O_2), nitrogen (N_2), and hydrogen (H_2). To investigate the structural characteristics, stability, most stable adsorption configurations, charge density difference, work function, and electronic properties of the Oh-B_2S_2 monolayer, density functional theory (DFT) was implemented. The non-equilibrium Green's function (NEGF) method was employed to analyze the current-voltage ($I-V$) behavior of the device both before and after gas adsorption. To understand the structural anisotropy, zero-bias transmission spectra of Oh-B_2S_2 monolayer were calculated prior to its adsorption along zigzag (x-axis) and armchair (y-axis) directions. Further, an ab *initio* molecular dynamics (AIMD) simulation was employed to assess the thermal stability of the structures before gas adsorption and their adsorption-desorption dynamics after gas adsorption.

4.2 Computational Details

DFT [199, 200] calculations were performed for analysis of structural relaxation and electronic properties as implemented in the Quantum ESPRESSO software package [147]. The generalized gradient approximation (GGA) based Perdew−Burke−Ernzerhof (PBE) functional [150] was used for approximating the exchange−correlation term. The long-range dispersion correction was described by using the DFT-D3 method [152]. A plane wave cutoff energy of 680 eV and the projector augmented-wave (PAW) pseudo-potential [201] were used to treat the electron−ion core interaction. Brillouin zone sampling [151] of $5\times5\times1$ and $15\times15\times1$ was performed for the structural optimization and density of states (DOS) computation of a $3\times3\times1$ supercell of Oh-B_2S_2. In addition, spin-polarized DFT theory was adopted to deal with the unpaired electrons. A vacuum of 30 Å was considered along the z-direction to avoid inter-layer interaction. The lattice constant and the atomic position were relaxed with energy and Hellmann−Feynman force convergence criteria of 10^{-3} eV/atom and 0.01 eV/Å. Phonon dispersion spectra of the monolayer were calculated using density functional perturbation theory (DFPT) [202] with a grid

of 6×6. Equations B.1 and B.2 (Appendix B. Supporting Data) were implemented to determine the binding energy (E_b) [16] and the cohesive energy (E_{coh}) [163] of Oh-B_2S_2 monolayer. We have used deformation potential theory (DPT) [16, 203] to calculate the electron carrier mobility of the system, as stated in equation 4.1a [16].

$$\mu_{2D} = \frac{e\hbar^3 C_{2D}}{k_B T m^* m^a (E_l^i)^2} \tag{4.1a}$$

$$\frac{E - E_0}{S_0} = \frac{1}{2} \times C_{2D} \times \left(\frac{\Delta l}{l_0}\right)^2 \tag{4.1b}$$

$$E_l^i = \Delta V_i \times \left(\frac{\Delta l}{l_0}\right)^{-1} \tag{4.1c}$$

The parameters in equations (4.1a-4.1c) are the charge of the electron (e), reduced Planck's constant ($\hbar = \frac{h}{2\pi}$), Boltzmann's constant (k_B), and temperature (T). m^* and m^a are the effective and average effective masses along the transport direction. C_{2D} is the elastic modulus that can be calculated using equation 4.1b, where E_0 and E are the total energies of the crystal before and after deformation. S_0 is the lattice volume, Δl and l_0 are variations in the lattice constant and initial lattice constant. E_l^i is the deformation potential constant and can be obtained from equation 4.1c, where ΔV_i is the change in energy in the i^{th} band under strain. However, the DPT method has certain limitations, as it only considers scattering resulting from unit-cell deformation induced by longitudinal acoustic (LA) phonons. In addition, it assumes isotropic electron–phonon coupling (EPC) that is independent of the electron or phonon momentum direction, which may introduce inaccuracies [204]. To overcome these limitations and achieve more accurate estimates of intrinsic mobility, it is necessary to compute the EPC matrix element for each individual scattering process. However, such calculations are computationally expensive [205]. Therefore, in this work, we have chosen to adhere to the DPT approach.

The computed adsorption energy (E_{ads}) of the gas molecules over the Oh-B_2S_2 monolayer was given by equation 4.2 [79, 206]

$$E_{ads} = E_{Oh-B_2S_2+gas} - (E_{gas} + E_{Oh-B_2S_2}) \tag{4.2}$$

Where $E_{Oh-B_2S_2+gas}$, E_{gas}, and $E_{Oh-B_2S_2}$ represent the energies of fully relaxed gas-molecule adsorbed Oh-B_2S_2 monolayer, an individual gas molecule, and Oh-B_2S_2 monolayer, respectively. The Bader charge analysis [207] was performed to understand the charge transfer between the monolayer and the gas molecule. Furthermore, the calculation of the charge density difference (CDD) plot was done using equation 4.3 [79] and visualized using the VESTA software [156].

$$\rho_{cdd} = \rho_{Oh-B_2S_2+gas} - (\rho_{gas} + \rho_{Oh-B_2S_2}) \tag{4.3}$$

Where $\rho_{Oh-B_2S_2+gas}$, ρ_{gas}, and $\rho_{Oh-B_2S_2}$ depict the charge densities of gas-molecule adsorbed on Oh-B_2S_2 monolayer, individual gas molecule, and Oh-B_2S_2 monolayer, respectively.

The thermal stability of the Oh-B_2S_2 monolayer and gas molecule adsorbed monolayer were investigated through AIMD simulations using the CP2K code [157] with the QUICKSTEP module. The DZVP-MOLOPT-SR-GTH basis set in conjunction with the Goedecker–Teter–Hutter (GTH) pseudopotential [98, 158] and a plane wave basis with a kinetic energy cutoff of 500 Ry were used to represent the Kohn-Sham orbitals and total electron density, respectively.

Furthermore, to evaluate the electron transport properties, we have used NEGF formalism [208] implemented in the TranSIESTA software package [112]. For the calculation, a $1 \times 1 \times 100$ grid with GGA-PBE functional at a cutoff of 500 Ry was used. The current through the central region was calculated based on the Landauer-Buttiker formula given as equation 4.4 [209, 210].

$$I(V_b) = \frac{2e^2}{h} \int_{\mu_L}^{\mu_R} T(E,V_b)[f(E-\mu_L) - f(E-\mu_R)]dE \tag{4.4}$$

Here, $T(E,V_b)$ is the transmission coefficient of electrons at energy E and voltage V_b, f is the Fermi function, and $\mu_{R/L}$ is the electrochemical potential of the right (R)/left (L) electrode.

4.3 Results and Discussion

4.3.1 Structural Feature Analysis

Initially, the unit cell of Oh-B_2S_2, as depicted by the black dotted line in Figure 4.1(a), was optimized. The lattice constant of Oh-B_2S_2 was found to be $a = b = 3.05$ Å, and the B−S, B−B, and S−O bond lengths were 1.95, 1.72, and 1.47 Å, respectively, which are consistent with

the h-B_2S_2 monolayer [16]. The dynamic stability of the Oh-B_2S_2 monolayer was established by the absence of imaginary frequency in the phonon dispersion curve and projected density of phonon states, as shown in Figure 4.1(b) and Figure B.1 (Appendix B. Supporting Data), respectively. The AIMD plot in Figure 4.1(c) indicates the thermal stability of the Oh-B_2S_2

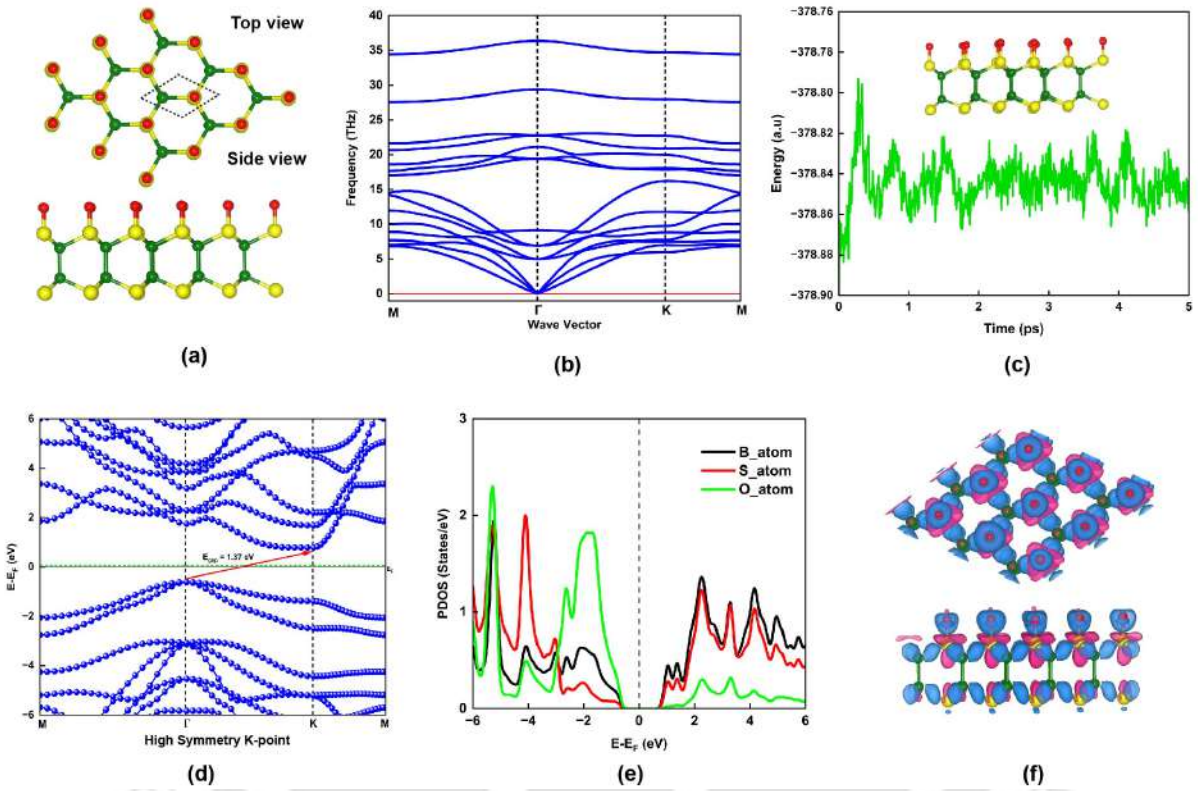

Figure 4.1: (a) Top and side view of Oh-B_2S_2 monolayer (the black dotted line represents the unit cell), (b) Phonon dispersion spectrum plot, (c) AIMD plot at 300 K, (d) Electronic band structure (HSE06 functional), (e) Projected density of states (PDOS), (f) Charge density difference (CDD) plot (blue and pink color indicates the charge accumulation and depletion region, respectively) of oxygen-functionalized B_2S_2 (Oh-B_2S_2) monolayer. Green, yellow, and red balls indicate the boron, sulfur, and oxygen atoms.

structure at 300 K over 5 ps, and we have not observed any structural deformation during the simulations. Furthermore, the electronic properties of the monolayer were analyzed via electronic band structure and density of states plots. Figure 4.1(d) shows that Oh-B_2S_2 is an indirect band gap semiconductor of 1.37 eV, whose valence band maximum (VBM) and conduction band minimum (CBM) are located at high symmetry k-points Γ and K, respectively. The presence of the oxygen atom significantly lowers the band gap of the Oh-B_2S_2 monolayer compared to that of h-B_2S_2 [16]. The band gap was calculated employing the HSE06 functional, as PBE-GGA underestimates the band gap value [211]. Figure 4.1(e) displays the projected

density of states (PDOS) for the monolayer, illustrating the overlapping of the s and p-orbitals of B-atoms, S-atoms, and O-atoms. To get insight into charge redistribution in the surface, we have calculated the charge density difference (CDD) plot, shown in Figure 4.1(f). Figure 4.1(f) shows a charge accumulation region on the Oh-B_2S_2 monolayer, which is absent on the h-B_2S_2 monolayer [Figure B.2(a) of Appendix B. Supporting Data]. This small surface charge density may be responsible for the negligible adsorption potential of the h-B_2S_2 monolayer, as shown in Figure B.2(b) (Appendix B. Supporting Data). Besides, we have carried out electron localization function (ELF) analysis to examine the bonding characteristics between the sulfur (S) and oxygen (O) atoms, as depicted in Figure B.3 (Appendix B. Supporting Data). ELF= 1.0 (red color) indicates complete localization of electrons, while ELF= 0.5 (green color) indicates delocalization [172]. In Figure B.3, the electron localization between S and O atoms is indicated by the ELF within the range of 0.75 to 0.85.

In addition, to understand the experimental feasibility, we have calculated the E_b and E_{coh} of the Oh-B_2S_2 monolayer. The computed E_b value was determined to be -5.28 eV, which is greater as compared to the binding energy of the OT-B_2S_2 monolayer [Table B.1(b) (Appendix B. Supporting Data)]. Furthermore, the E_{coh} of the Oh-B_2S_2 monolayer was found to be 5.54 eV/atom, slightly lower than the h-B_2S_2 monolayer [16]. However, this cohesive energy is higher than that of other experimentally realized 2D materials, such as blue phosphorene (3.48 eV/atom) [212], silicene (4.57 eV/atom) [213], etc. Carrier mobility (electrons/holes) of semiconductors is a crucial parameter that impacts the efficiency of devices, including energy consumption and electrical performance [214]. Since Oh-B_2S_2 is a $p-$type semiconductor with holes as the majority carrier, we have determined the mobility of both holes and electrons. The carrier mobilities of Oh-B_2S_2 were calculated to be 790×10^2 cm^2 V^{-1} s^{-1} for electrons and 32×10^2 cm^2 V^{-1} s^{-1} for holes [Figure B.4 (Appendix B. Supporting Data)], surpassing that of the MoS_2 monolayer [215, 216]. The high carrier mobility of the Oh-B_2S_2 monolayer can be explained using the equation $\mu = \frac{e\tau}{m^*}$ [217]. It has been noted that the carrier mobility of a system varies inversely with the effective masses of electrons and holes. Upon comparing the effective masses of electrons and holes in MoS_2 and Oh-B_2S_2 from Figure B.2 (Appendix B. Supporting Data), we have found that these values are lower for Oh-B_2S_2, resulting in higher carrier mobility [217].

Furthermore, the high elastic modulus and deformation potential ratio are essential parameters influencing the high carrier mobility of the Oh-B_2S_2 monolayer (Figure B.2 of Appendix B. Supporting Data) [218]. For reference, we have also calculated the electron and hole carrier mobilities of MoS_2, which were found to be 280 and 161 $cm^2\ V^{-1}\ s^{-1}$, respectively [194, 214, 219]. Figure B.4(c) (Appendix B. Supporting Data) shows the deformation potential plot for electron and hole mobilities and the elastic modulus plot of MoS_2.

4.3.2 Adsorption Properties of the Oh-B_2S_2 Monolayer

Prior to the investigation, the sensing properties of the Oh-B_2S_2 monolayer were assessed by studying the adsorption of toxic gases CO, NO, CO_2, NO_2, N_2O, and SO_2. These gaseous pollutants were introduced on the Oh-B_2S_2 monolayer at various adsorption orientations at a 3 Å distance. The adsorption energies of the gas molecules with different orientations are shown in Figure 4.2(a) and Figure B.5 (Appendix B. Supporting Data). Figure 4.2(b) depicts the optimized structure of the energetically most favored adsorption configuration, in which the molecules preferentially remain parallel to the surface. The adsorption distance (d) between the gas molecule and the surface was further confirmed by the potential energy curves (PECs) shown in Figure B.6 (Appendix B. Supporting Data). The E_{ads} can be used to quantitatively evaluate the adsorption strength between the gas molecules and the monolayer. All negative values of adsorption energies for each gas molecule indicate that adsorption was an exothermic process with thermodynamic stability, which is favorable for the sensing applications [220]. The most favorable adsorption sites were identified by the highest adsorption energies from an energetically favorable viewpoint, as shown in Table 4.1. The positive charge transfer (CT) values (Table 4.1) indicate that the gas molecules behave as donors.

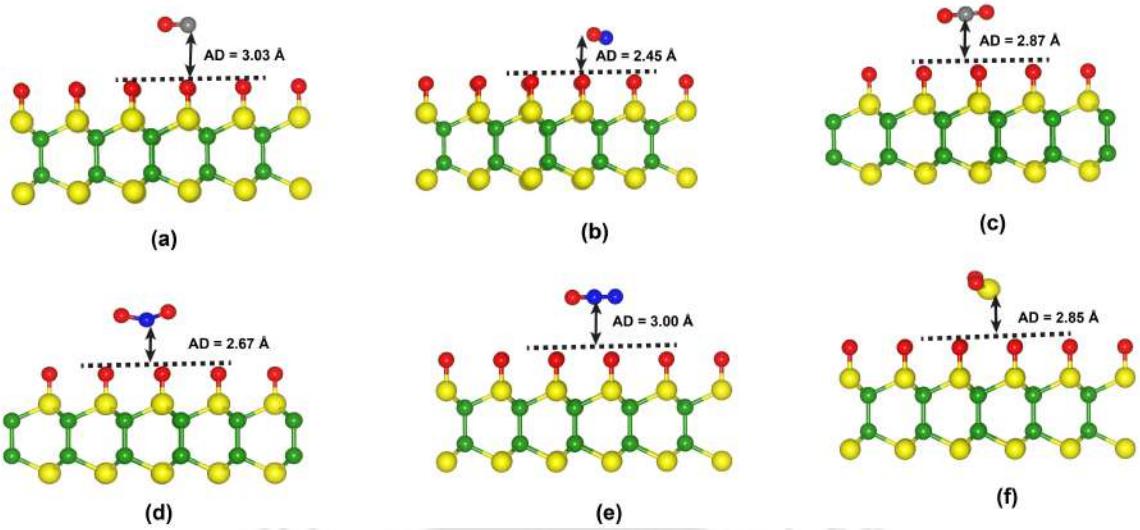

Figure 4.2: (a-f) Top view of preferable optimized geometries of Oh-B_2S_2 monolayer after adsorption of CO, NO, CO_2, NO_2, N_2O, and SO_2, respectively, on their most favorable site. Yellow, green, red, blue, and grey balls represent S, B, O, N, and C atoms. AD = adsorption distance.

Table 4.1: Computed adsorption energy (E_{ads}), charge transfer value (Q_e), adsorption distance (d), bond length (l), and bond angle (Θ) of the gas molecule before and after adsorption on Oh-B_2S_2 monolayer.

Gas-Molecule	E_{ads} (eV)	Q_e	d (Å)	Before-adsorption		After-adsorption	
				l(Å)	Θ(°)	l(Å)	Θ(°)
CO	−0.07	0.006	3.03	1.13	–	1.13	–
NO	−0.56	0.340	2.45	1.16	–	1.13	–
CO_2	−0.10	0.004	2.87	1.17	179.89	1.17	179.89
NO_2	−0.16	0.133	2.67	1.21	133.41	1.20	136.81
N_2O	−0.10	0.009	3.00	1.19/1.15	179.98	1.19/1.14	179.86
SO_2	−0.11	0.009	2.85	1.45	119.42	1.45	118.99

Table 4.1 reveals that the NO molecule interacts with the monolayer with considerable binding energy [172] and charge transfer value among all other molecules. Furthermore, it was worth noting that the adsorption distance of the NO gas molecule exhibits a relatively small value of 2.45 Å compared to the other gases. Additionally, the O−N bond length experienced a reduction of 0.03 Å relative to the length of the isolated NO molecule. The adsorption energy of NO in Oh-B_2S_2 monolayer is higher than many previously reported materials such as graphene [221] (0.02 eV), WS_2 [222] (−0.25 eV), silicene [223] (−0.35 eV), MoS_2 [224] (−0.19 eV), phosphorene [225] (−0.32 eV), etc. Besides, as the gas sensing mechanism is essentially dependent on the charge transfer phenomena, Table 4.1 indicates that the CT value for NO_2 is sufficient enough to

influence the properties of the Oh-B_2S_2 monolayer [225]. This CT value of NO_2 for the Oh-B_2S_2 monolayer is greater than that of graphene [221] (-0.09e), and MoS_2 (0.04e) monolayer [226]. In addition, the adsorption of NO_2 gas molecule onto an Oh-B_2S_2 monolayer occurs at an interfacial distance of 2.67 Å. However, the remaining four gas molecules, CO, CO_2, N_2O, and SO_2, interact weakly due to their longer adsorption distance, resulting in small CT values.

The phenomenon of charge redistribution is visually depicted in Figure 4.3 *via* a charge density difference (CDD) plot. CDD qualitatively reveals the regions of charge accumulation (blue color) and depletion (pink color) in the entire system, providing insight into the charge transfer between the gas molecules and the surface. All six gas molecules (CO, NO, CO_2, NO_2, N_2O, and SO_2) have undergone charge donation to the surface as charge accumulates on them. As depicted in Figure 4.3(a, c, e, f), negligible charge redistributions were observed between molecule-monolayer systems, resulting in relatively weak binding strength. However, in the case of NO and NO_2 adsorbed systems [Figure 4.3(b,d)], there is a noticeable redistribution of charge within the molecule and a significant increase in charge transfer between the molecule and the Oh-B_2S_2 monolayers. This observation highlights the greater sensitivity of the Oh-B_2S_2 monolayer towards NO and NO_2 molecules. In order to gain a more thorough understanding of

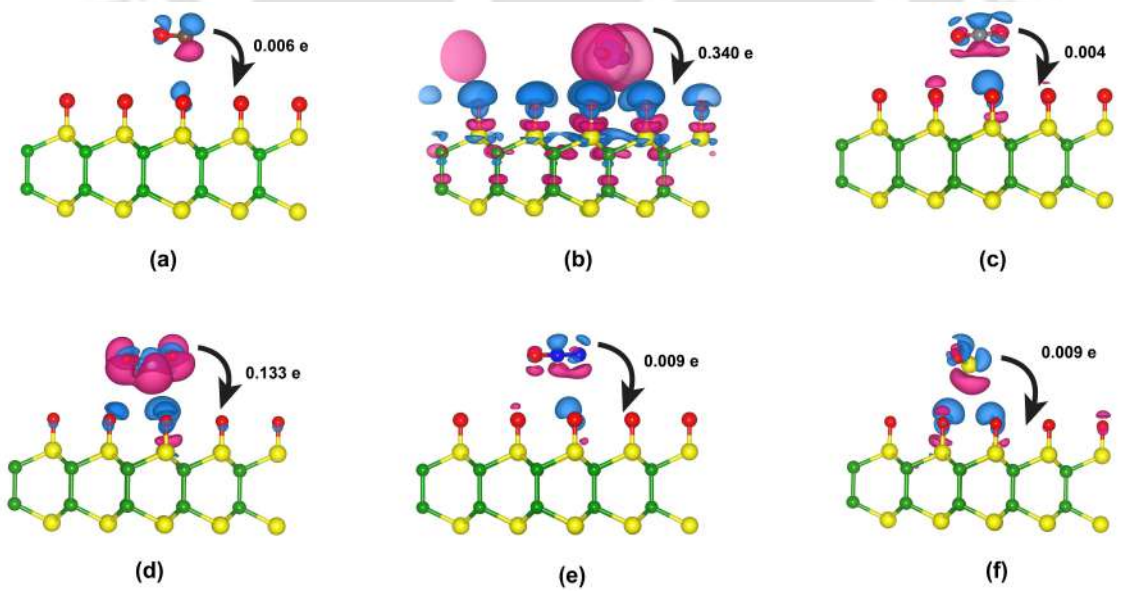

Figure 4.3: Charge density difference (CDD) plot of (a) CO, (b) NO, (c) CO_2, (d) NO_2, (e) N_2O, and (f) SO_2 adsorbed Oh-B_2S_2 monolayer, respectively. Pink and blue colors depict the charge depletion and accumulation region, respectively, at iso-surface value 0.003 e/bohr^3.

the charge redistribution within the system, we have computed the plane-averaged charge density

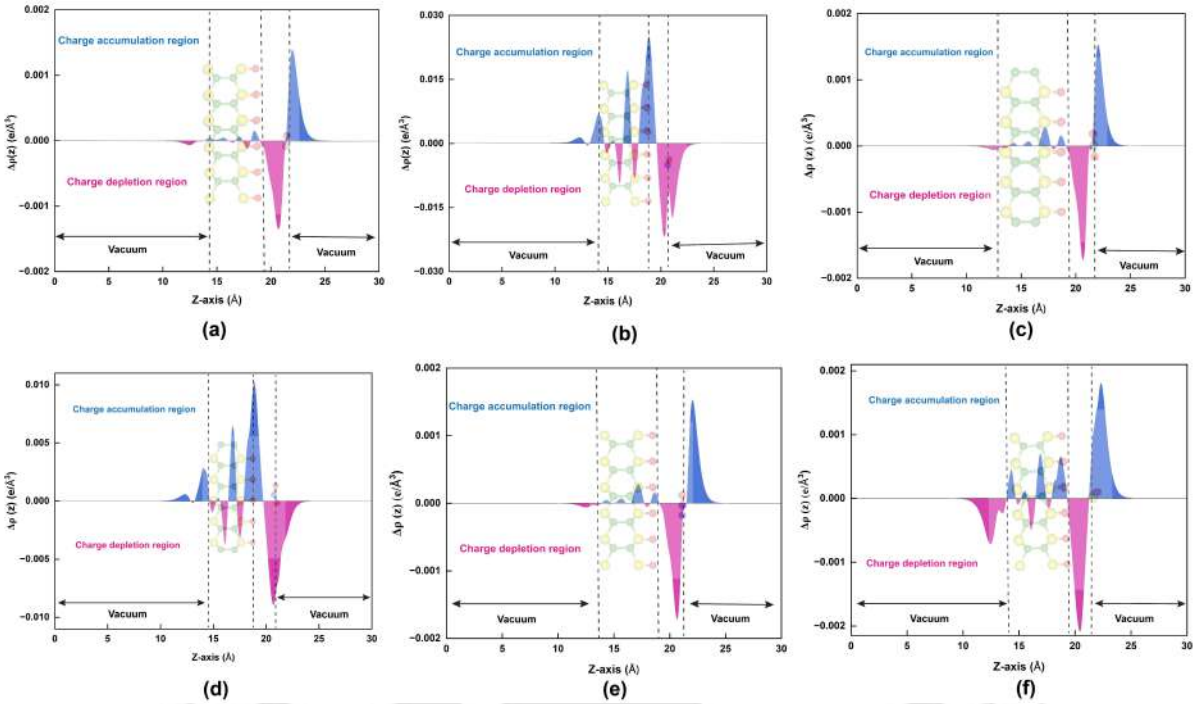

Figure 4.4: Plane-average charge density difference (CDD) plots of (a) CO, (b) NO, (c) CO_2, (d) NO_2, (e) N_2O, and (f) SO_2 adsorbed Oh-B_2S_2 monolayer, respectively. Blue and pink colors depict the charge accumulation and depletion regions, respectively.

difference $\Delta\rho(z)$ over the *xy*-plane according to equation 4.5

$$\Delta\rho(z) = \int_{A_{xy}} \rho_{cdd} dxdy \tag{4.5}$$

Here, A_{xy} denotes the surface area of the supercell, and the function ρ_{cdd} is defined by equation 4.3. Figure 4.3(b,d) indicates the presence of a notable region of charge accumulation on the surface, and the curves' amplitude is high compared to Figure 4.4(a,c,e,f). This finding aligns with our charge density difference and charge transfer value studies (Figure 4.4).

Electronic Properties Analysis

Furthermore, to obtain a reliable depiction of alterations in the electronic structure that occur subsequent to gas molecule adsorption, we have calculated the density of states (DOS) plots before and after the adsorption of each molecule, as shown in Figure 4.5. The overlap of atomic peaks on the DOS curves reveals the hybridization between atomic orbitals and, thus, the extent of interaction between atoms. Meanwhile, this parameter will influence the conductivity change of the system. The total density of states (TDOS) curve rises and declines around the

E_F, influencing the conductivity change of the system. Figure 4.5(b,d) illustrates the existence of novel peaks at the E_F in the Oh-B_2S_2 monolayer upon adsorption of NO and NO_2. The electronic structure modification through adsorption and charge transfer impacts the conductivity of the Oh-B_2S_2 monolayer, which can provide a response signal for the potentially hazardous molecules, as evidenced by prior studies [79]. In contrast, for other gas molecules such as CO, CO_2, N_2O, and SO_2, no such interactions are present at the Fermi level or close to the Fermi level. The above observation can be elucidated by the relatively low adsorption energies and negligible CT values. This finding suggests that the adsorption of these gases causes an insignificant influence on the electronic behaviour of the Oh-B_2S_2 monolayer, as displayed in Figure 4.5(a,c,e,f).

Based on the calculations carried out until now, it was observed that the Oh-B_2S_2 monolayer exhibits remarkable charge transfer values and alteration of the electronic property of the material only when interacting with NO and NO_2 molecules. A possible reason for considerable CT and electronic properties modulation is the presence of unpaired electrons on NO and NO_2. Hence, spin-polarized density functional theory was employed to examine the impact of an unpaired electron. Figure B.3 (Appendix B. Supporting Data) presents the adsorption energies, charge transfer values, and adsorption distances, which show minor variations from the density functional theory calculation results. The spin-polarized density of states (SPDOS) depicted in Figure B.7 (Appendix B. Supporting Data) demonstrates the existence of orbital overlap at the E_F, which profoundly affects the electronic properties of the Oh-B_2S_2 monolayer. Furthermore, to check if the 3×3 supercell is sufficient to describe the adsorption properties of the material towards NO and NO_2, we have extended our calculation to 4×4 and 5×5 supercells, and results are shown in Table B.4 (Appendix B. Supporting Data). From Table B.4, it can be seen that there is a very minimal difference in the E_{ads} and CT values as the size of the supercell increases. Therefore, we can conclude that the sensing potential of the Oh-B_2S_2 monolayer can be well explained by 3×3 supercell.

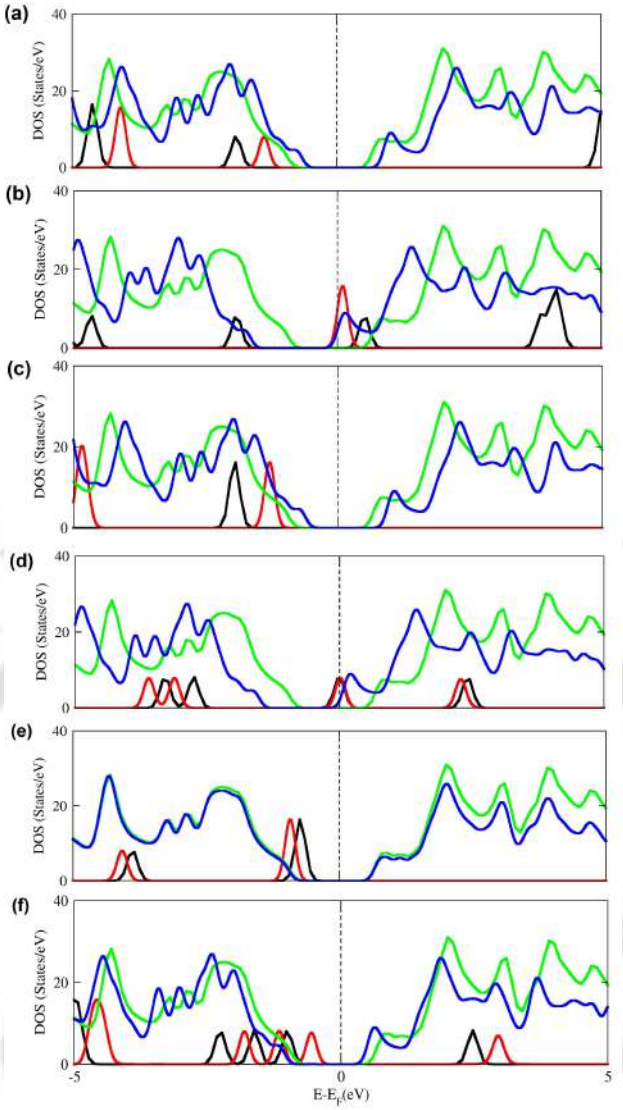

Figure 4.5: Density of states (DOS) plots of a) CO, (b) NO, (c) CO_2, (d) NO_2, (e) N_2O, and (f) SO_2 before and after adsorption upon Oh-B_2S_2 nanosheets. Green and blue indicate the DOS of Oh-B_2S_2 before and after gas adsorption, and black and red colors indicate the DOS of isolated and adsorbed gas molecules. The black dotted line represents the E_F.

4.3.3 Selectivity and Temperature Dependence of NO and NO_2 Adsorption-Desorption Dynamics on Oh-B_2S_2

The term selectivity refers to the potential of gas sensors to distinguish particular gas molecules from various gases [79, 206]. Therefore, to investigate the Oh-B_2S_2 monolayer for its potential application as a practical gas sensor, we have determined the impact of prominent environmental gases along with some other gases (such as O_2, N_2, H_2, H_2O, O_3, and CH_4) [227] on its surface. The H_2O molecule was incorporated into our calculation to determine humidity [175]. Figure

B.8 (Appendix B. Supporting Data) illustrates the optimized geometries associated with the most favorable adsorption configuration for each gas molecule. All stable adsorption has a parallel configuration with a minimum distance between 2.85 and 2.99 Å. The data associated with the adsorption of gas molecules on the Oh-B_2S_2 monolayer are displayed in Table B.5 (Appendix B. Supporting Data). The results reveal that the interaction strength and CT value pertaining to the NO and NO_2 molecules on Oh-B_2S_2 are higher compared to those of the other gases. The E_{ads} for NO and NO_2 were -0.56 and -0.16 eV, respectively, and the corresponding CT values were 0.34 and 0.13e. In contrast, the E_{ads} for other atmospheric gases range from -0.03 to -0.12 eV, and the CT values range from 0.004 to 0.08e as shown in Figure B.9 (Appendix B. Supporting Data). This demonstrated the considerable preference for NO and NO_2 gases with high selectivity in the presence of other environmental gases.

The working features of a sensor can undergo significant changes when exposed to finite temperatures. Hence, it is crucial to ascertain the fundamental dynamics, i.e., the adsorption-desorption behavior of the sensor at various temperatures, before implementation [228]. The underlying dynamic behavior of NO and NO_2 on the Oh-B_2S_2 monolayer was studied using AIMD simulations at T = 300 K, 350 K, and 400 K for 10 picoseconds (ps) based on the constant particle number-volume-temperature (NVT) canonical ensemble with the Nosé thermostat [159]. Figure 4.6 presents the AIMD plots alongside the atomic structure of the system at various temperatures after simulation. The findings of our AIMD simulations demonstrated the room temperature stability of the NO-adsorbed Oh-B_2S_2 monolayer [Figure 4.6(a)], where variations in energy over time remain stable around a given constant. However, an increase in temperature to 350 K leads to changes in the adsorption structure. Consequently, the molecule begins to desorb from the surface, demonstrating a time scale in the femtosecond (fs) range throughout the simulation. The atomic structure of the NO_2-adsorbed Oh-B_2S_2 monolayer attains equilibrium at different temperatures, as depicted in Figure 4.6(b). The observed configuration indicates that during the simulations, the NO_2 molecule remains close to the surface up to a temperature of 350 K. Nevertheless, as the temperature increases to 400 K, the NO_2 molecule was observed to undergo desorption from the surface within a time frame of 0.2 ps. In summary, the AIMD results indicate that the desorption temperatures for NO and NO_2 over Oh-B_2S_2 monolayer

were between $300-350$ K and $350-400$ K, respectively. Therefore, it may be inferred that the Oh-B_2S_2 monolayer demonstrates favorable gas sensing capabilities for NO and NO_2 molecules at ambient temperature. The room temperature functioning of the Oh-B_2S_2 nanosensor towards NO and NO_2 eliminates the requirement for a heat source in high-temperature applications, streamlining device production and lowering operating costs [229].

Furthermore, we have determined the desorption time (τ) of the gas molecule at a temperature of 300 K. It refers to the minimum amount of time needed for a sensor to remove the adsorbed gases from its surface. The value of τ can be theoretically determined by using the transition state theory and van't-Hoff-Arrhenius equation [206, 230] as follows:

$$\tau = A^{-1} exp \frac{-E_{ads}}{k_B T} \tag{4.6}$$

Here A is the attempt frequency (10^{12} s^{-1}, for visible light), T is the temperature, and k_B is the Boltzmann constant [231]. The E_{ads} examined at a temperature of 300 K corresponds to the adsorption configuration of NO and NO_2 after the simulations of 10 ps. The corresponding energies for NO and NO_2 are -0.54 and -0.13 eV. Thus, the estimated desorption times for NO and NO_2 were 0.80 milliseconds (ms) and 0.15 nanoseconds (ns) under visible light irradiation and at ambient temperature (300 K).

4.3.4 Work function of the sensor

The expression for the work function (ϕ) of a 2D material can be represented as, $\phi = E_{vac} - E_F$ [232]. Here, E_F is the energy associated with the Fermi level of the material from which the electron is extracted and E_{vac} is the energy required to overcome the surface dipole barrier, which approaches a constant at a significant distance from the surface [232]. We have estimated the work functions of the Oh-B_2S_2 monolayer before and after NO and NO_2 adsorption. An inherent polarisation electric field exists owing to the asymmetry of the Oh-B_2S_2 monolayer [233]. Hence, a dipole correction was implemented while calculating the average electrostatic potential plot, as depicted in Figure B.10 (Appendix B. Supporting Data). Figure B.10 shows that the electrostatic potential difference (U) decreases after the adsorption of gas molecules ($U_{Oh-B_2S_2}$: 4.19 eV $>$ $U_{Oh-B_2S_2+NO_2}$: 3.13 eV $>$ $U_{Oh-B_2S_2+NO}$: 2.34 eV). This phenomenon can be ascribed to

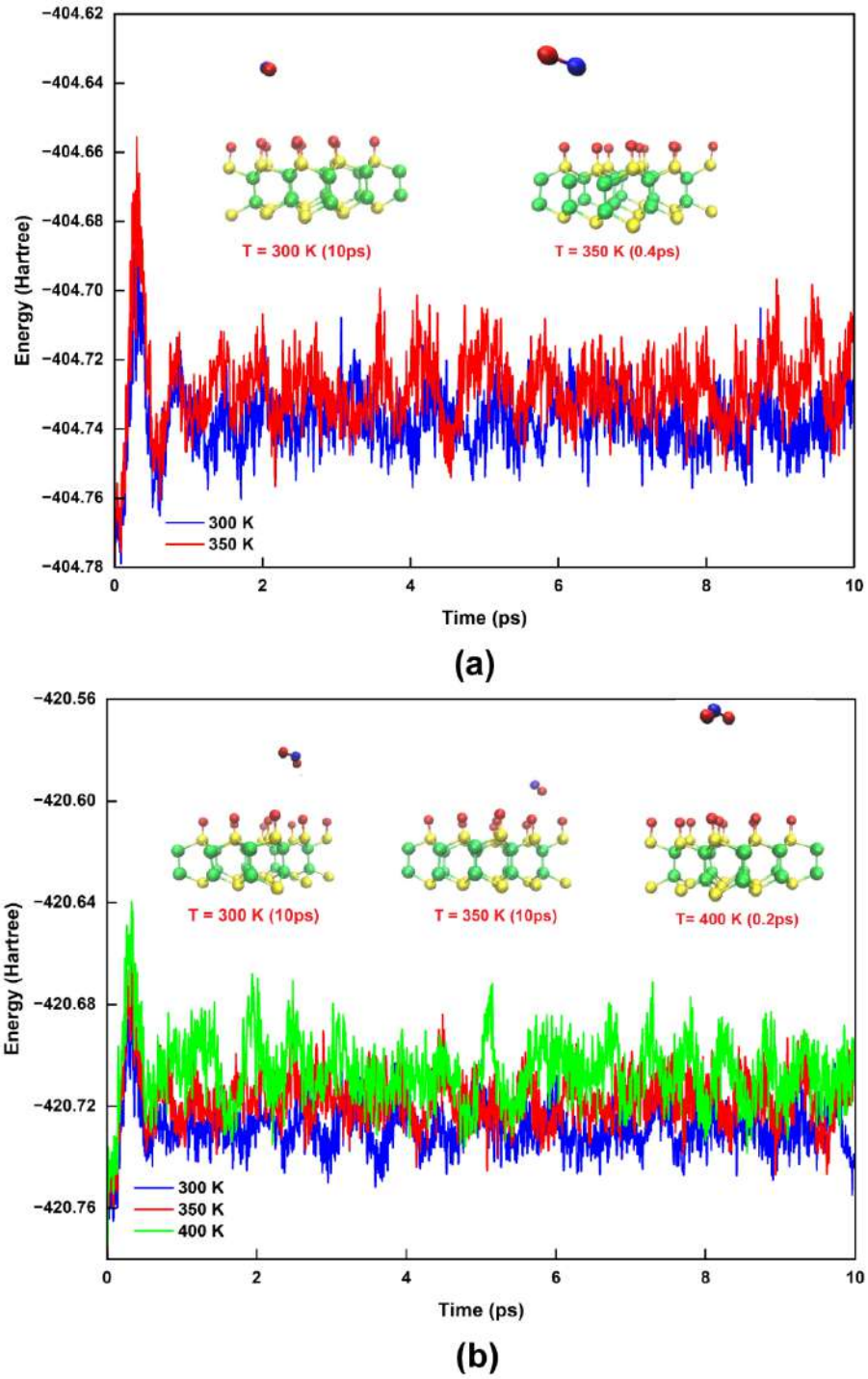

Figure 4.6: AIMD simulation plots of (a) NO and (b) NO_2 adsorbed Oh-B_2S_2 monolayers for 10 ps at T = 300 K, 350 K, and 400 K with their final geometries.

the intrinsic dipole moment of the gas molecules and the charge transfer between the two interfaces. The work functions of Oh-B_2S_2 monolayer, Oh-B_2S_2+NO, and Oh-B_2S_2+NO_2 were determined to be 6.92, 4.74, and 5.82 eV, respectively. As the gas molecules act as donors, the work function of the monolayer decreases after adsorption. Figure 4.7 illustrates the pictorial depiction of alterations in the work function of the Oh-B_2S_2 monolayer with adsorbed with NO and NO_2 compared to the pristine system. Experimentally, the change in work function due to gas adsorption is estimated *via* scanning Kelvin probe, which has led to the realization gas sensors that rely on work function measurements [231].

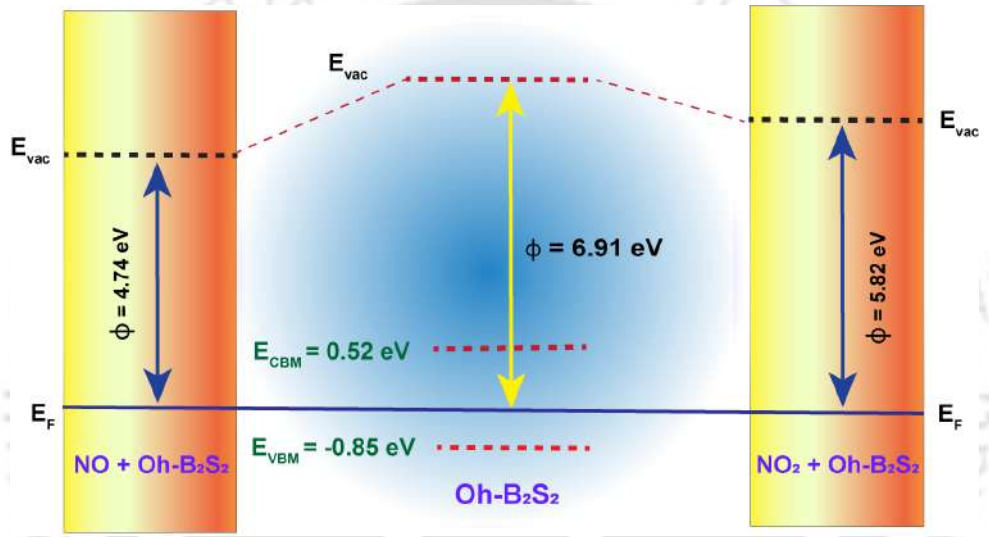

Figure 4.7: Pictorial depiction of alterations in the work function of the Oh-B_2S_2 nanosheets when adsorbed NO and NO_2 compared to the pristine system.

4.3.5 I-V Characteristic Plots

It is essential to explore the possibility of the Oh-B_2S_2 monolayer to be used as a gas sensing tool from a device point of view [79, 130]. Despite some gas molecules altering the electronic structure around the E_F, the charge transfer generated by the adsorption of the gas molecules on the monolayer can produce varied sensitivities for resistivity measurements [130, 172]. Therefore, the efficacy of the Oh-B_2S_2 monolayer as a potential gas sensor can be specifically assessed by applying the NEGF method [79, 172] to calculate the transmission properties and current–voltage ($I-V$) characteristics. Two semi-infinite electrodes were considered during the investigation, which are the periodic extensions of the pristine monolayer termed "pseudoelectrodes". A similar simplified device model has been extensively used in previous publications [130, 234,

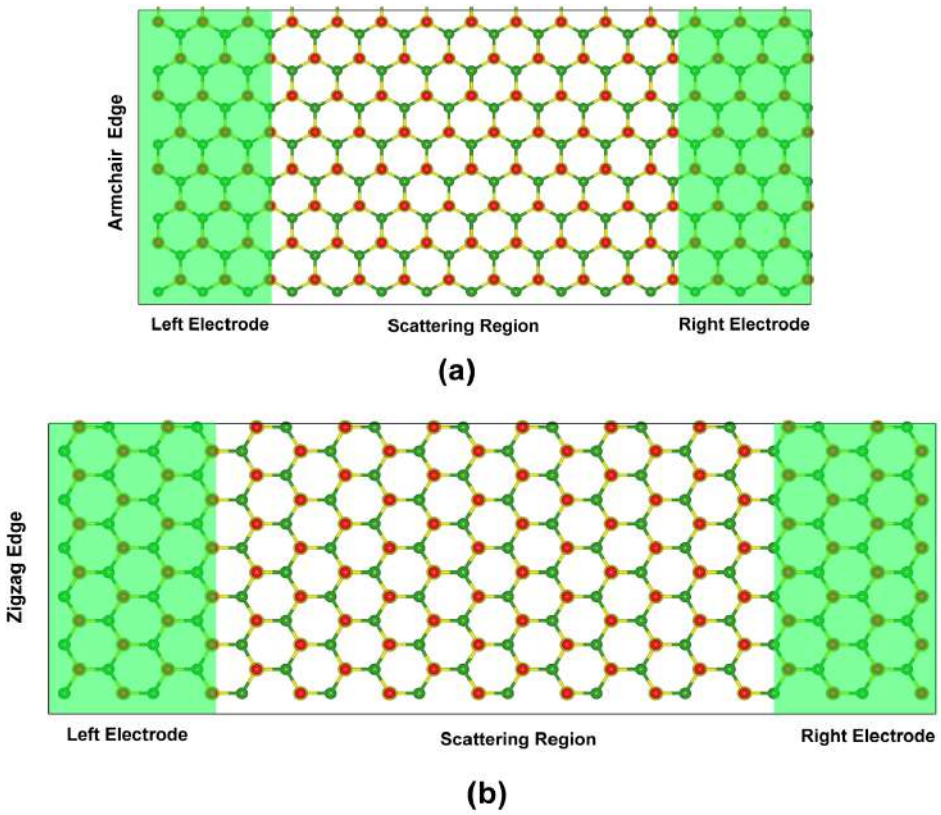

Figure 4.8: Schematic representation of the electron transport model of Oh-B_2S_2 monolayer along the (a) armchair direction and (b) zigzag direction. The device setup consists of a left electrode, a right electrode, and a central scattering region.

235]. Two transport models were computed for the direction of the current flow, namely the x-direction (zigzag) and the y-direction (armchair), due to the structural anisotropy of the Oh-B_2S_2 monolayer (Figure 4.8). Because the zero-bias transmission was higher along the zigzag direction [Figure 4.9(a)], we have considered the transport along that direction. A transmission gap around the E_F was observed in both directions due to the semiconductor nature of the material. To analyze the qualitative sensitivity of the Oh-B_2S_2 monolayer towards NO and NO_2 gases, we have simulated the current-voltage relationships before and after gas adsorption using a model as shown in Figure 4.8(b). The $I-V$ characteristic plots of the bare Oh-B_2S_2 and gas-adsorbed Oh-B_2S_2 monolayers are shown in Figure 4.9(b). From the $I-V$ plots, it can be seen that there is no current flow up to 1.0 bias voltage in all cases (bare Oh-B_2S_2 surface and gas-adsorbed Oh-B_2S_2). Introducing a bias voltage causes the shifting of the left electrode's E_F in accordance with the right electrode. Thus, the current begins to flow only when the left electrode's VBM crosses over into the right electrode's CBM [236]. Figure 4.9(b) demonstrates that the current through a device based on Oh-B_2S_2 monolayer decreases when the device is exposed to gas

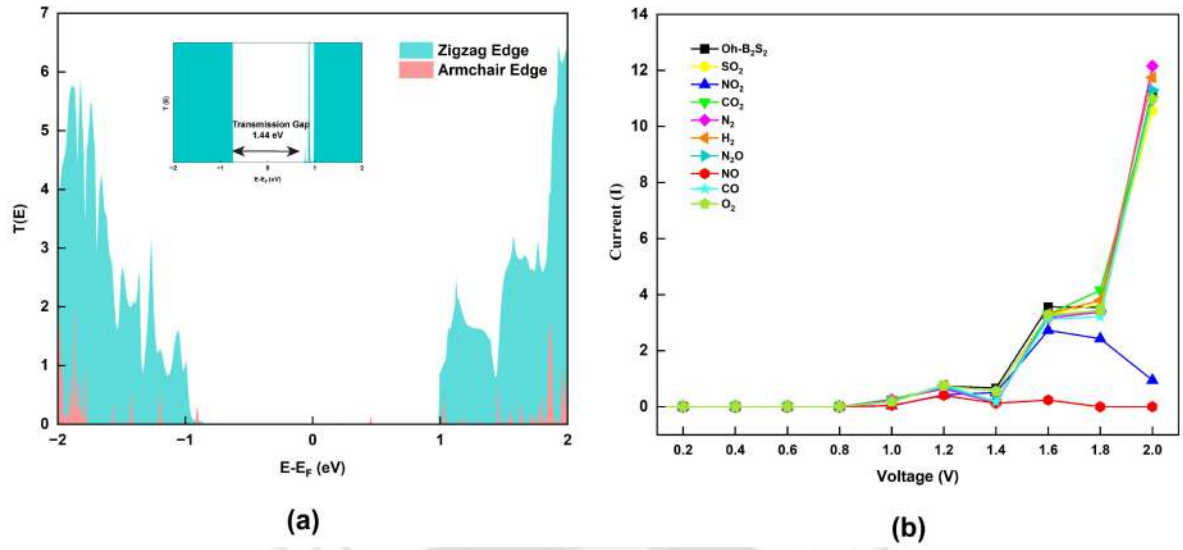

Figure 4.9: (a) Zero bias transmission spectra T(E) plots along zigzag and armchair directions, (b) $I-V$ characteristic plots for the Oh-B_2S_2 monolayer and gas-adsorbed Oh-B_2S_2 nanosheets (gases: CO, NO, CO_2, NO_2, N_2O, SO_2, H_2, N_2, and O_2).

molecules NO and NO_2. The presence of an unpaired electron in the NO and NO_2 molecules induces the localization of the wavefunction and may lead to pronounced back-scattering and the subsequent suppression of conductive pathways [130, 236, 237]. At biases of 1.2 and 1.4 V, the NO-adsorbed Oh-B_2S_2 monolayer experiences a reduction in current flow to 45% and 81%, respectively. This outcome suggests that the material exhibits a favorable sensitivity towards NO in 1.2 and 1.4 V bias voltage regions. Nevertheless, with increased voltage, there was a major decrease in the magnitude of current flow within the range of 10^{-15} to 10^{-16} nA. Moreover, it has been identified that the sensitivity towards NO_2 reaches its maximum at bias voltage 2 V, resulting in a corresponding decrease in the current by 91%. In contrast, the $I-V$ characteristic plots of several environmental gases (including O_2, N_2, and H_2) and toxic gases (such as CO, CO_2, N_2O, and SO_2) are almost comparable to the Oh-B_2S_2 monolayer. This observation reveals the weak bonding characteristics between the gas molecules and the substrate, which we have previously discussed.

Furthermore, it was noted from the individual plots [Figure 4.9(b)] that there is no monotonic increase in the current with respect to the voltage. In the case of bare Oh-B_2S_2, the current increases from 0.74 to 11 nA as the bias voltage is raised from 1.2 to 2.0 V. However, a minor reduction in the current was noticed at a bias voltage of 1.4 V. For NO-adsorbed Oh-B_2S_2, a marginal rise in current was observed at 1.2 V, followed by a sharp decline in current as the

voltage is increased from 1.4 to 2.0 V. Similarly, NO_2-adsorbed Oh-B_2S_2 monolayer causes a rise in current to 2.72 nA at 1.6 V, which further reduces to 0.94 nA at 2.0 V. The decrease in the current with an increase in the voltage can be explained by the negative differential resistance (NDR) phenomenon [238, 239]. Such NDR behaviors in *para*-SiC_3 [240], boron-phosphorus [172], and defect-borophene monolayers [120] have been reported recently. The origin of the NDR phenomenon of Oh-B_2S_2 and gas-adsorbed Oh-B_2S_2 can be explained by transmission spectra [T(E)] at different biases [241, 242]. In the case of Oh-B_2S_2, an NDR phenomenon was observed at 1.4 V bias voltage. Upon comparing the T(E) at bias voltages 1.2, 1.4, and 1.6 V, the amplitude of the transmission peak at 1.4 V was comparatively small within the bias window (Figure B.11 of Appendix B. Supporting Data), and hence the current drops at that bias. Similarly, for NO and NO_2 adsorbed Oh-B_2S_2 monolayers, the transmission spectra are shown in Figure B.12 to Figure B.13 (Appendix B. Supporting Data) The low magnitude of the transmission peak was observed in the bias window from the voltage 1.4 V (for NO-adsorbed Oh-B_2S_2) and after 1.6 V (NO_2-adsorbed Oh-B_2S_2), leading to the suppression of current. Transmission spectra are generated as a result of the conductance channels that are accessible within different energy bands. The decrease in conductance channels at certain biases results in a corresponding decrease in the flow of electrical current [236], which is consistent with the previously proposed NDR mechanisms [241].

4.3.6 Comparative Analysis of Oh-B_2S_2 Monolayer and MoS_2 Monolayer Towards NO and NO_2 Detection

Low carrier mobility in the MoS_2 monolayer demands high bias voltage for resistance measurement [227]. Similar to MoS_2, but with a B_2-ion pair in place of the Mo ions, we believe that the B_2S_2 monolayer can overcome the shortcomings of the MoS_2 monolayer. It was determined that the Oh-B_2S_2 monolayer, which has been functionalized with oxygen atoms, exhibits charge carrier mobility of 790×10^2 cm^2 V^{-1} s^{-1} and 32×10^2 cm^2 V^{-1} s^{-1} for electrons and holes. This high mobility is attributed to the fast operation of the device. On the contrary, the MoS_2 monolayer demonstrates an electron mobility of 280 cm^2 V^{-1} s^{-1} and hole mobility of 161 cm^2 V^{-1} s^{-1}. Meanwhile, a comparison was made between the E_{ads} and CT values of NO and NO_2 adsorption on Oh-B_2S_2 and MoS_2. Although the E_{ads} of NO_2 was found to be slightly higher in

MoS_2, the gas sensing mechanism primarily relies on the charge transfer value. Table 4.2 reveals that Oh-B_2S_2 exhibited relatively higher adsorption potential towards NO and NO_2 compared to the MoS_2 monolayer [44, 224, 226, 243].

Table 4.2: Theoretical prediction of E_{ads} and CT values of NO and NO_2-adsorption upon MoS_2 and Oh-B_2S_2 (vdW: van der Waals correction).

Material	Gas	E_{ads} (eV)	CT (e)	Methods	Reference
MoS_2	NO	−0.03	0.02	GGA-PBE	[44]
		−0.19	-	GGA-PBE	[224]
		−0.17	-	GGA-PBE (vdW)	[243]
	NO_2	−0.01	0.11	GGA-PBE	[44]
		−0.20	0.04	GGA-PBE (vdW)	[226]
		−0.17	−0.03	GGA-PBE (vdW)	[243]
Oh-B_2S_2	NO	−0.56	0.34	GGA-PBE (vdW)	This work
	NO_2	−0.16	0.13	GGA-PBE (vdW)	This work

4.4 Conclusions

In a nutshell, we have investigated the structure, stability, and electronic properties of oxygen-functionalized B_2S_2 (Oh-B_2S_2) monolayer *via* DFT and AIMD simulations. The monolayer was observed to be stable and ideal for experimental fabrication with an indirect band gap of 1.37 eV. Our findings show that the Oh-B_2S_2 monolayer has high sensitivity and selectivity for NO and NO_2 gas molecules, even in the presence of common ambient gases like O_2, N_2, H_2, H_2O, O_3, and CH_4 as well as harmful pollutants, including CO, CO_2, N_2O, and SO_2. To further confirm the adsorption behaviors of Oh-B_2S_2 towards gaseous molecules, charge transfer, work function, and electronic property studies were carried out. The presence and absence of gas molecules (functioning as ON and OFF states) are further demonstrated by the current-voltage ($I-V$) characteristics plot for device application. Our results unambiguously show negative differential resistance (NDR) in the presence of NO and NO_2 molecules after a 1.2 and 1.6 V bias voltage, respectively. We hope our findings presented in this study may help to explain the sensing properties of the material and subsequently aid in the development of boron-based functionalized nanosensors for the detection of hazardous gases.

Chapter 5

DEFECT-INDUCED BILAYER BOROPHENE FOR CHARGE CONTROLLED CO_2 ACTIVATION

(This work in this Chapter is published in *J. Phys. Chem. C* 2025, 129, 13939-13953.)

5.1 Introduction

Carbon dioxide (CO_2) is a potent greenhouse gas that is becoming more prevalent in the atmosphere due to the excessive reliance on fossil fuels [244]. Catalytic conversion of CO_2 into organic fuels and other industrial raw materials is a crucial measure towards increasing energy efficiency and lowering global CO_2 levels. Preceding its catalytic reformation or decomposition, activation, and dissociation of the greenhouse gas CO_2 is necessary [244–247]. Nevertheless, the fundamental challenge in CO_2 reduction lies in the activation of CO_2 molecules, as they possess a very stable nature with dissociation energy exceeding 750 kJ mol^{-1} [248–250]. Thus, research has focused on developing materials and effective ways to boost CO_2 activation [250, 251].

A new approach, known as charge-modulated CO_2 activation, involves modifying the charge state of nanomaterials, offering a highly selective, clean, and controlled method for capturing CO_2 [252]. The charge states of nanomaterials can be easily regulated using techniques such as electrospray, electron beams, gate voltage, or electrochemical methods [253, 254]. The emergence of mechanically exfoliated graphene sparked significant interest in two-dimensional (2D) nanomaterials in CO_2 activation and conversion [255, 256]. Boron, the next neighboring

element to carbon, shows more bonding possibilities compared to carbon [14]. Sun et al. shows that uncharged hexagonal boron nitride (h-BN) nanosheet and CO_2 molecules have weak van der Waals interactions. However, adding extra electrons to this nanomaterial substantially improved the binding strength. This electron-rich nanomaterial strongly interacts with CO_2 because of its Lewis acid nature. However, the effective injection of the necessary electrons is greatly hindered by the high band gap of h-BN (around 5.8 eV) [254]. Borophene, a 2D sheet of boron, has entered into this horizon and enriched the understanding of the physics and chemistry of boron [257]. These boron sheets consist of a combination of triangular and hexagonal patterns. The stability of these sheet structures is achieved by the equilibrium between two-center bonding in the hexagonal regions and three-center bonding in the triangular regions. Thus, the hexagonal triangle ratio, i.e.,"hexagonal hole density," is a major factor that affects the stability of the borophene [258–260]. The presence of the hexagonal holes makes the borophene structure more stable due to the π-σ self-doping mechanism [261]. Borophene polymorphisms, including the β_{12} [254] and $\chi 3$ sheets [262], have drawn significant interest in charge-modulated CO_2 activation as its charge state can be easily modified experimentally owing to its metallic properties with high electronic conductivity. However, several studies show that the open-shell configuration of borophene leads to its reactivity and susceptibility to oxidation upon exposure to air. This limits the integration of borophene into practical applications [263, 264].

Recently, bilayer borophene (BL-B) grown on single-crystal Ag (111) or Cu (111) substrates has drawn attention to its potential in electronic and energy applications [19, 265]. The BL-B exhibits superior thermal stability and is less susceptible to oxidation compared to its monolayer counterparts due to the presence of covalently linked interlayers[23, 266]. There have been numerous proposed BL-B polymorphs, including metal to Dirac semimetal to semiconductors, depending on the stacking pattern, substrate interaction, hole density, etc. [20, 267, 268]. The BL-B considered in this study corresponds to the α-phase with a vacancy concentration (v) of $\frac{1}{12}$. The two layers are connected via interlayer B-B covalent bonds ($\sim$2 Å) in an AB stacking configuration. The presence of interlayer covalent bonding between B-B results in weaker interaction between BL-B and the Ag(111) substrate, as evidenced by reduced adsorption energy and interfacial charge transfer. This weak coupling facilitates the detachment of BL-B from the

substrate, supporting the existence of a free-standing BL-B [24, 269]. Furthermore, the structural parameters of the BL-B, such as the lattice periodicity (5.71 × 5.71 Å), show excellent agreement with experimentally observed α-phase BL-B. Simulated atomic force microscopy (AFM) images also replicate key experimental features, including B atoms with coordination numbers of 5 and 6, moiré pattern, and topography[13, 270–272]. In addition, Ma *et al.* [22] reported that both AA and AB-stacked BL-B have the same interlayer bonding density ($u = \frac{1}{4}$), involving three B-B σ-bonds that connect six inward-buckled atoms per unit cell. In the AB stacked structure, the charge density associated with the 12c-12e π-bond network shifts subtly along one-third of the long diagonal. This breaks the mirror symmetry present in the AA stacking, which is centered around the hexagonal vacancies [22, 273]. They also help to focus the metallic out-of-plane orbitals (localization of the multicenter bonding states), creating a new 2D semiconductor with a bandgap of 1.13 eV.

A further significant approach for enhancing CO_2 capture and conversion in 2D materials involves maximizing the exposure of active sites and optimizing the intrinsic activity of each site [245, 274]. The unavoidable atomic defects, as well as engineered defects (point defect, vacancy defect, grain boundary, substitution, etc.), are considered an efficient way to attain these goals [275]. These defects could serve as carrier donors, scattering, trapping, active sites, etc., at different conditions and tailor the performance of 2D materials [276, 277]. Thus, the controlled inclusion of defects in 2D materials becomes crucial for the advancement of new materials for energy conversion and storage.

Inspired by charge-induced CO_2 activation and engineered defects in 2D nanostructures, we have explored the possibility of pristine and defect-induced BL-B as a material for charge-modulated CO_2 activation. Density functional theory (DFT) was employed to investigate the stability of various monovacancy structures along with the adsorption properties of CO_2 on both neutral and negatively charged BL-B. The temperature-dependent dissociation and desorption behaviour of the adsorbed CO_2 was studied using ab *initio* molecular dynamics (AIMD) simulations. In addition, various coverages were employed to ascertain the maximum adsorption capacity of CO_2 on the BL-B nanosheet. Furthermore, the selectivity of the negatively charged BL-B for CO_2 was investigated by analyzing its mixtures with CH_4, N_2, and H_2 gases.

5.2 Computational Details

All the calculations were performed using the DFT implemented in the Quantum ESPRESSO (QE) [147] software package. Projector-augmented wave (PAW) pseudopotentials [100] describe the interactions between valence electrons and ionic cores with the explicit treatment of the valence electrons. We have used a generalized gradient approximation of Perdew-Burke-Ernzerhof (GGA-PBE) [150] for the exchange-correlation functional. A vacuum region of 25 Å is implemented along the z-axis to avoid interlayer interactions, and the DFT-D3 [152] method is used to treat the dispersion interaction. The threshold criteria for energy and force are set at 10^{-6} eV and 10^{-2} eV/Å, respectively, with an energy cutoff of 600 eV. Using the Monkhorst-Pack [151] grid, the Brillouin zones are sampled with $5 \times 5 \times 1$ k-points for optimization and $15 \times 15 \times 1$ for density of states (DOS) calculation. A 2×2 BL-B supercell with 88 boron atoms was used for the calculation. In the upper layer of the BL-B, we have identified three (3) distinct boron atoms that generate discrete monovacancy point defect structures. Equations A.1 and A.2 (Appendix A. Supporting Data) define the formation energy (E_{form}) and cohesive energies (E_{coh}), respectively, which were used to analyze the stability of these systems. The carrier mobilities of electrons and holes ($\mu_{e/h}$) of the system have been determined using the deformation potential theory (DPT), as shown in Equation 4.1a-4.1c. The adsorption energy (E_{ads}) of CO_2, N_2, CH_4, and H_2 on the adsorbent material has been investigated by introducing excess electrons using equation 5.1 [278, 279].

$$E_{ads}(q) = E_{surface+CO_2}(q) - [E_{surface}(q) + E_{CO_2}(0)] \tag{5.1}$$

The terms $E_{surface+CO_2}(q)$, $E_{surface}(q)$, and $E_{CO_2}(0)$ represent the total energies of the CO_2 adsorbed surface at charge q, the surface at charge q, and the isolated neutral gas molecule, respectively. The charge density difference (CDD) was determined from the charge density of the optimized CO_2 adsorbed surface, isolated surface, and CO_2 molecule using equation 5.2 and plotted using the VESTA code [156].

$$\rho_{CDD} = \rho_{surface+gas} - \rho_{surface} - \rho_{gas} \tag{5.2}$$

Here, $\rho_{surface+gas}$, $\rho_{surface}$, and ρ_{gas} stand for charge densities of CO_2-adsorbed surface, surface, and CO_2 molecule, respectively.

The Löwdin charge analysis is employed to examine the charge transfer [280, 281]. Further, the charge density (ρ) of the investigated system was determined by $\rho = Q/S$ [252]. Here, Q and S are the total charge and the surface area of the supercell. S can be calculated from $S = \frac{\sqrt{3}}{2}a^2$; a is the lattice constant.

AIMD simulations were carried out in CP2K code [157] with QUICKSTEP module to understand the dynamics of the CO_2 adsorbed structure that vary on temperature. We have used the norm-conserving Goedecker-Teter-Hutter (GTH) pseudopotentials [98] with DZVP-MOLOPT-SR-GTH basis sets. The simulations were conducted using an NVT ensemble with a Nose-Hoover thermostat [159] at 300 K for 10 ps.

5.3 Results and Discussion

5.3.1 Structure-Stability of BL-B and Defect Induced BL-B

The unit cell of the BL-B nanosheet was optimized using DFT calculations, as illustrated in Figure 5.1. This exhibits a hexagonal geometry, with the lattice constant a=b=5.7 Å which aligns with the previous experimental [13] and theoretical periodicity [24]. The dynamic stability of the BL-B was investigated by examining the phonon dispersion spectrum, as illustrated in Figure 5.1(b). The highest measured frequency is 40 THz, and the absence of imaginary frequencies in the phonon spectrum demonstrates the dynamic stability of the BL-B nanosheet. The electronic characteristics of BL-B are further investigated with the PBE functional. BL-B was found to be an indirect band-gap semiconductor with an energy gap of 0.70 eV [Figure 5.1(c,d)], supporting earlier data [24]. The presence of interlayer bonds is the key parameter for inducing the bandgap opening in BL-B, influencing its electronic properties.

Since precisely arranging defects at the atomic level enhances the adsorption efficiency by altering the structural characteristics and surface functioning, we have introduced point defect into an extended 2×2 supercell of BL-B. In the upper layer of the BL-B, we have identified three distinct boron atoms (depending on their chemical environment), each contributing to the creation of a unique mono-vacancy defect structure denoted as BL-B-Def-1, BL-B-Def-2,

and BL-B-Def-3, as shown in Figure 5.2. To assess the probability of forming various defect configurations in BL-B (as described above), we computed their formation energies (E_{form}) and cohesive energies (E_{coh}), as shown in Figure 5.3. The negative E_{form} in all structures indicates that the existence of these defects is thermodynamically favorable. Additionally, the control of E_{form} is primarily dependent on parameters such as pressure, temperature, and feedstock [146]. The calculated E_{coh} of the defect-introduced structure was found to be comparable with the pristine BL-B and higher than the E_{coh} of phosphorene (-3.48 eV/atom) [282], silicene (-4.57 eV/atom) [213], borophene (-5.99 eV/atom) [213], etc. It is worth noting that BL-B-Def-1 has easily formed among other defects, with a lower E_{form} of -0.108 eV and a maximum E_{coh} of -6.23 eV/atom. [213, 283]. Post-growth treatments, such as electron beam irradiation, ion bombardment, plasma, chemical treatment, etc., are more commonly used for defect engineering than synthesis methods due to their greater versatility and practicality [284]. E-beams not only tune the structure in a controllable manner but also allow in situ visualization of defect dynamics during engineering processes [55, 58]. Further, thermal annealing is a widely employed and straightforward technique for inducing defects in materials. In addition, various experimental techniques, including scanning tunneling microscopy (STM) and scanning tunneling spectroscopy (STS), have been employed to confirm the presence of defects in the materials [284, 285]. In BL-B, the covalent bonding between the two layers acts like a strong framework, giving stability to the structure, even when defects appear on the surface.

5.3.2 Interaction of a CO_2 on Neutral and Negatively Charged Pristine and Defect-Induced BL-B Nanosheets

Prior to the investigation of the CO_2 activation over charge-induced BL-B, we performed the calculation in 2×2 supercells of neutral BL-B nanosheets (pristine and defect-induced). The CO_2 molecule was initially positioned at 3 Å distance from the surface before optimization at two adsorption sites, A and B (Figure 5.2). The results demonstrate the weak interaction between uncharged BL-B nanosheets and CO_2, with an adsorption distance (AD) exceeding 3.2 Å. Then, we have calculated the E_{ads} of the CO_2 molecule that varies with charge state at pristine and defect-induced BL-B nanosheets, shown in Figure 5.4. The negatively charged BL-B nanosheet can give electrons, and Lewis acid CO_2 tends to acquire electrons during reactions;

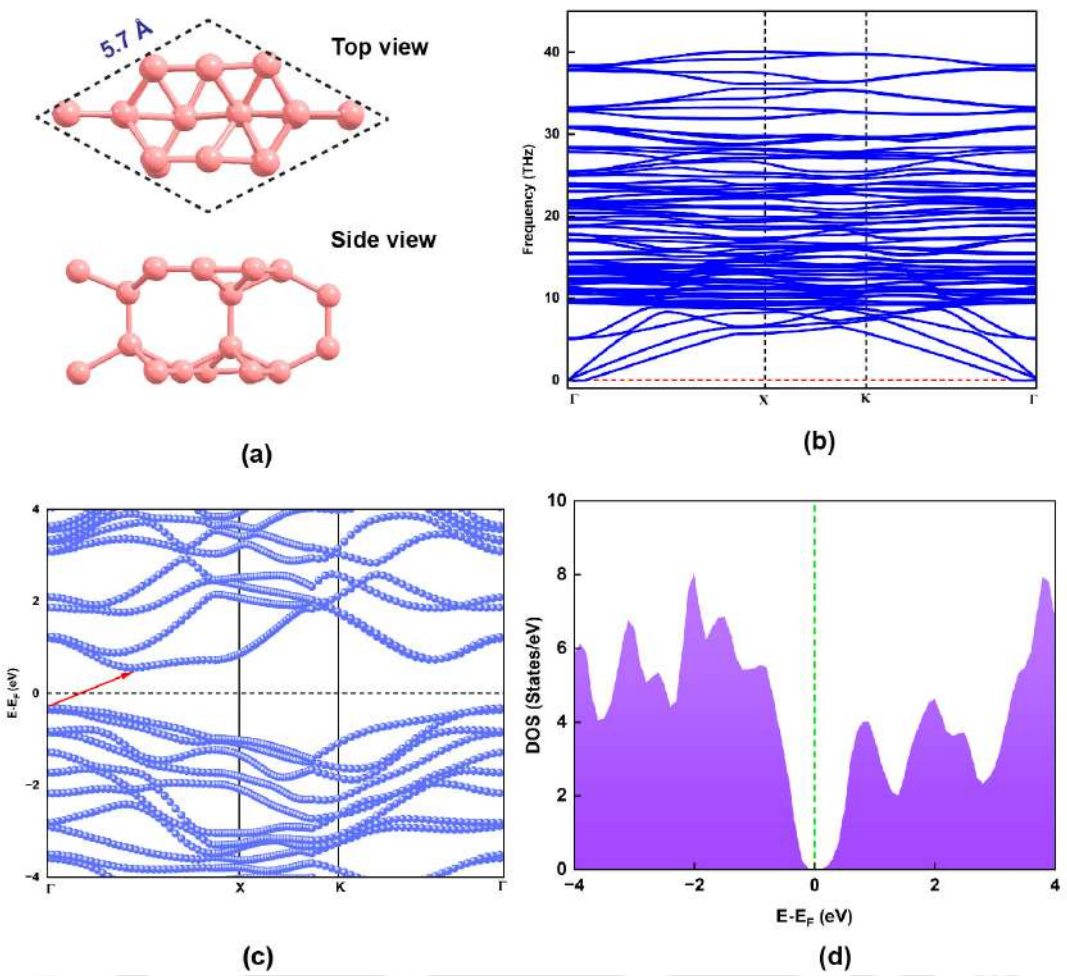

Figure 5.1: (a) Top view and side view of the unit cell of bilayer borophene (BL-B), (b) phonon dispersion spectra, (c) electronic band structure, and (d) density of states (DOS) of bilayer borophene (BL-B).

this leads to a strong interaction between the two. Figure 5.4 displays that the most favorable CO_2 activation configuration is at site B of the $6e^-$ BL-B-Def-1 nanosheet with an E_{ads} -1.89 eV. The remaining all involve physisorption with a very weak interaction despite charge injection. To confirm the CO_2 interaction on a 2×2 supercell (pristine and defect-induced system), we have also calculated the E_{ads} with 3×3 supercells, as shown in Table C.1 (Appendix C. Supporting Data), and structures were displayed in Figure C.1 (Appendix C. Supporting Data). The minimal difference in E_{ads} across varying supercell sizes suggests that the 2×2 supercell of BL-B is adequate to describe the CO_2 adsorption potential.

To elucidate the underlying process of CO_2 activation on charge-induced BL-B-Def-1 nanosheet, two key parameters have been used: (a) electron density profile [254] and (b) p-band center. The electron density profile for the frontier molecular orbitals (FMOs) of neutral BL-B

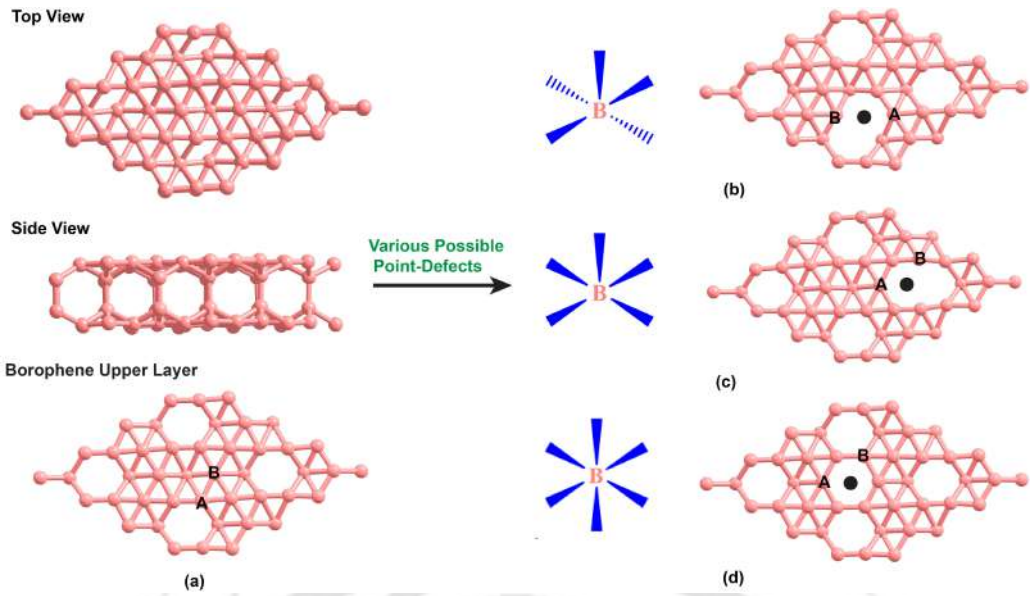

Figure 5.2: (a) Top view, side view, and upper layer of BL-B, (b) BL-B-Def-1, (c) BL-B-Def-2, and (d) BL-B-Def-3. The pink ball denotes the B atom; the black dot represents the location of the B-atom that has been removed while creating the vacancy; A and B are two different binding sites.

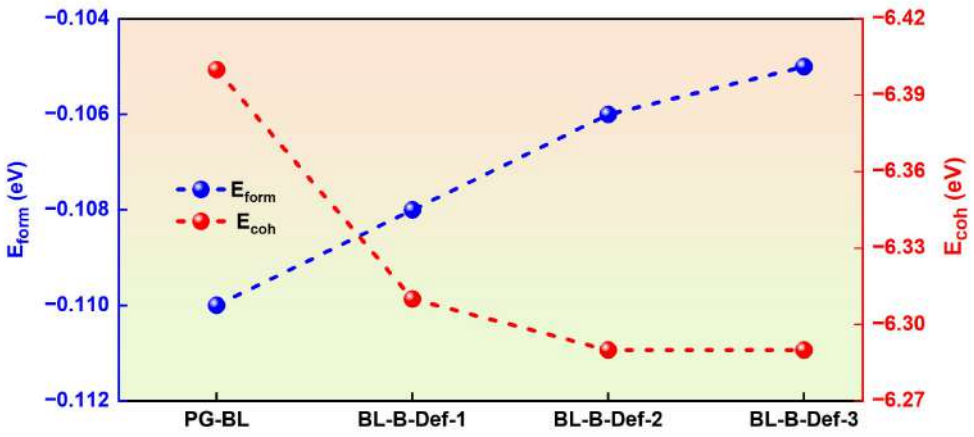

Figure 5.3: E_{form} (blue) and E_{coh} (red) energies plots of BL-B and defect-induced BL-B.

nanosheets, that is, the lowest unoccupied molecular orbital (LUMO), LUMO+1, and LUMO+2, has been presented in Figure 5.5 and Figure C.2 (Appendix C. Supporting Data). Figure 5.5(a-c) demonstrates that the LUMOs of BL-B-Def-1 are primarily localized on the B-atoms at site B, indicating that any additional electrons introduced to the nanosheet will occupy its p-orbitals. In addition, we have also explored the FMOs of BL-B, BL-B-Def-2, and BL-B-Def-3 (Figure C.2 (Appendix C. Supporting Data), which reveals that the MOs are not localized in a specific region. Therefore, the presence of additional electrons does not improve the adsorption efficiency

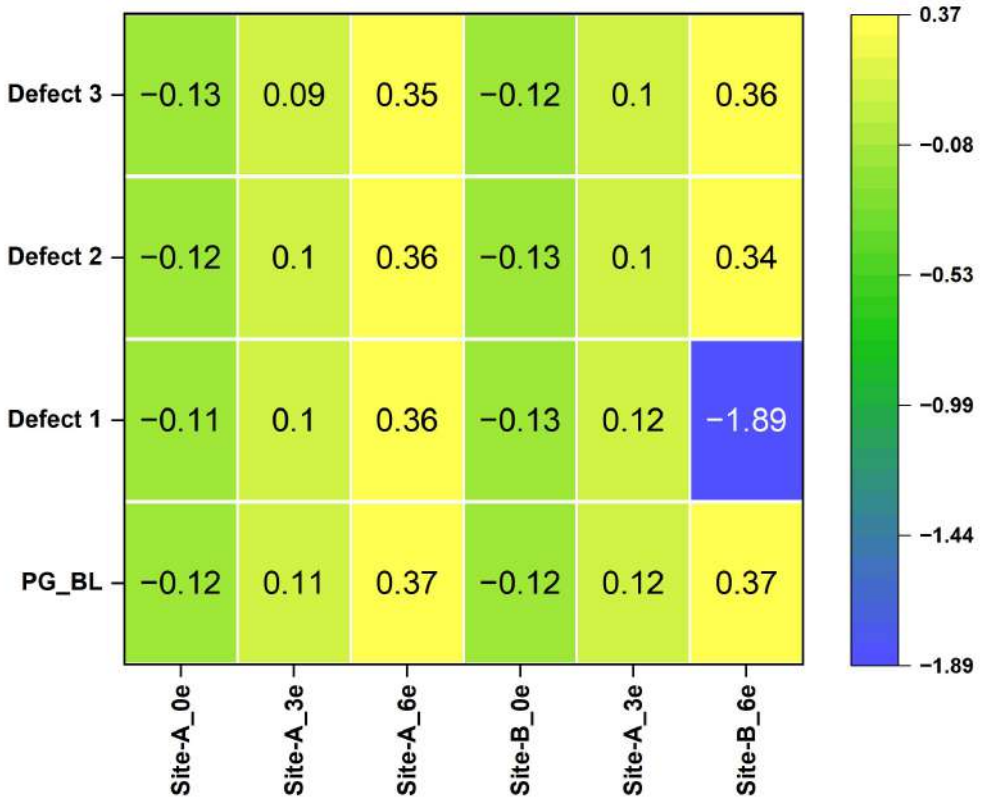

Figure 5.4: Heatmap plot that shows E_{ads} (eV) of CO_2 at various BL-B structures as a function of charge states.

of the system. Further, the CDD between the neutral and the negatively charged ($1e^-$, $3e^-$, and $6e^-$) BL-B-Def-1 is shown in Figure 5.5(d-f). The CDD profiles display an increase in the electron density at site B (marked in a black circle) as charge states increase, leading to strong CO_2 adsorption. We have further used the p-band center as a parameter for electron injection at the antibonding states. The p-band center of BL-B is the centroided of the boron p-orbitals density of states, generally elucidating the bond formation and reactivity patterns of the p-block element [286]. We have shown the p-band centers of all the nanosheets in Figure 5.6(a). Figure 5.6(b) illustrates the bonding and antibonding states of all nanosheets. As seen in Figure 5.6(b), the p-band center moves to a higher position, and the filling of anti-bonding states decreases because these states have been pushed above the E_F, making them empty [287]. It is evident that the antibonding energy of the BL-B-Def-1 nanosheet is lower compared to the other nanosheet. Reducing the energy level of the antibonding orbitals enhances the likelihood of electrons occupying the antibonding orbital (AO) to a greater extent [288]. Moreover, the AOs of BL-B-Def-1 are highly populated, resulting in a comparatively lower number of electrons

filling the antibonding states.

Since BL-B-Def-1 facilitated the CO_2 activation upon charge injection, the latter part of this work predominantly centers on investigating the BL-B-Def-1 nanosheet. Further, the presence of the p-band center at a lower energy level indicates the stability of BL-B-Def-1 as compared to the other systems.

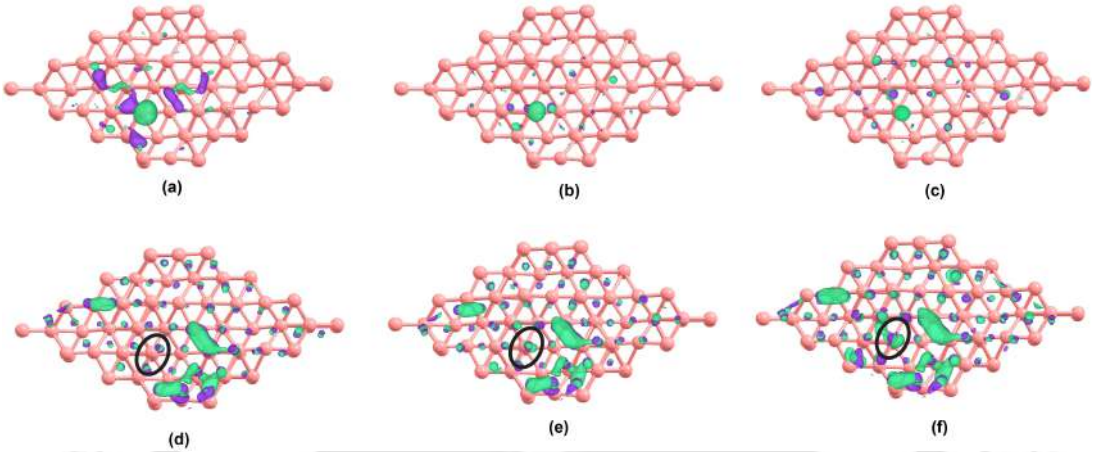

Figure 5.5: Frontier Molecular Orbital (FMO) plots (a) LUMO, (b) LUMO+1, (c) LUMO+2 of BL-B-Def-1 nanosheet. Charge density difference (CDD) plots (d) 0^- and $1e^-$, (e) 0^- and $3e^-$, and (f) $0e^-$ and $6e^-$ of BL-B-Def-1 nanosheet. Green and purple colors represent the charge accumulation and depletion region at isosurface 0.003 bohr/e^-.

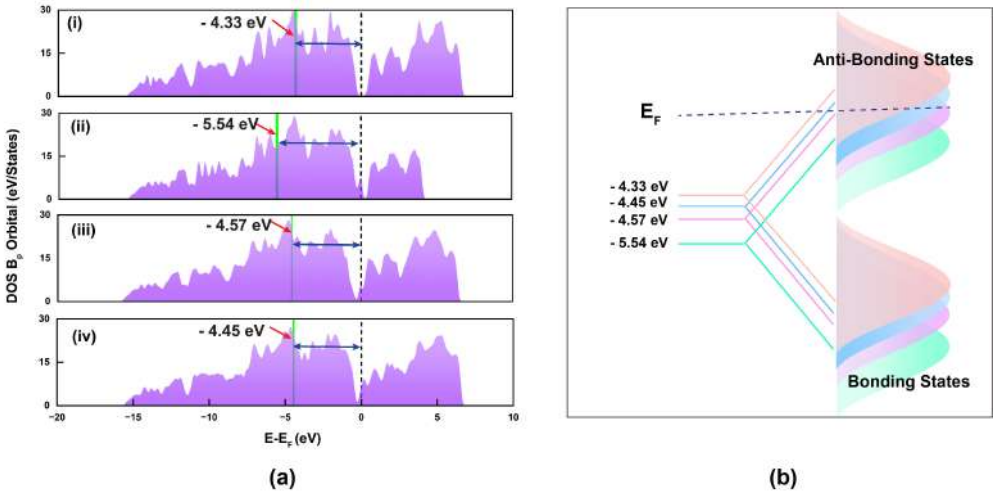

Figure 5.6: (a) Density of states (DOS) of B_p-orbitals of (i) BL-B, (ii) BL-B-Def-1, (iii) BL-B-Def-2, and (iv) BL-B-Def-3 with its p-band center. (b) Schematic representation of bonding and anti-bonding states of BL-B and defect-induced BL-B.

5.3.3 CO_2 Activation on Charge-Induced BL-B-Def-1 Nanosheet

The BL-B-Def-1 is identified as an indirect band-gap semiconductor with 0.35 eV band gap (Figure C.3 of Appendix C. Supporting Data), lower than the pristine BL-B. The higher conductivity of BL-B-Def-1 than its pristine counterpart greatly enhances the injection of excess electrons for charge-modulated CO_2 capture [254]. The presence of defects reduces the band gap by introducing new electronic states near the valence band (VB). This, in turn, causes the valence band maximum (VBM) to be uplifted [289]. Further, the presence of defects lowered the carrier mobility (μ) of the BL-B-Def-1, which was found to be 1.68×10^3 cm^2 V^{-1} S^{-1} for electrons and 240 cm^2 V^{-1} S^{-1} for holes (Table C.2 of Appendix C. Supporting Data). However, the μ of BL-B-Def-1 is still higher than many nanosheets that show good catalytic activity [290–292]. Figure C.4 (Appendix C. Supporting Data) displays elastic modulus and deformation potential calculation details.

We have explored the influence of charge density on CO_2 capture efficiency using the charge-modulated switchable method, with a specific focus on negatively charged BL-B-Def-1. The CT values between the surface and the CO_2 were assessed via Löwdin charge analyses. This indicates the generation of negatively charged species ($CO_2{}^{\delta-}$) as the CO_2 molecule accepts electrons into its LUMO. The E_{ads} and CT values of CO_2 on BL-B-Def-1 as a function of charge densities are presented in Figure 5.7(a). To treat the unpaired electrons in BL-B-Def-1, we have also used spin-polarized density functional theory (SPDFT) calculations. Figure 5.7(a) shows that the E_{ads} values of CO_2 on BL-B-Def-1 vary between -0.15 and $+0.35$ eV for negative charge densities up to 4.43×10^{14} e^-/cm^2. For charge densities exceeding 4.43×10^{14} e^-/cm^2, the molecules strongly bind to the surface, resulting in significantly large E_{ads} (-1.89 to -1.81 eV) and CT (0.62 to 0.63e) values. The energetically favorable configuration of a CO_2 interaction at site B of the neutral and ρ = 5.32 $\times10^{14}$ e^-/cm^2 BL-B-Def-1 nanosheet was presented in Figure 5.7(b) and (d). Additional evidence of the optimal adsorption distance (AD) between the nanosheet and CO_2 molecule was provided by potential energy curves (PECs) in Figure C.5 (Appendix C. Supporting Data). The adsorption of CO_2 on the charge-neutral nanosheet [Figure 5.7(b-c)] indicates physisorption as evidenced by AD of 3.12 Å, small CT value of 0.009e, and the E_{ads} of -0.12 eV. The molecule aligns parallel to the nanosheet and undergoes a minimal

structural change, resembling an isolated CO_2 molecule. The O−C−O bond angle and C-O bond length of the absorbed CO_2 molecule are measured at 179.70° and 1.17 Å, respectively. Figure 5.7(d-e) shows that the B-atom of the nanosheet forms a chemical binding with the CO_2 molecule at a distance of 1.67 Å (with carbon) and 1.62 Å (with oxygen) from the adsorption site. The CO_2 molecule has a non-linear geometry, with an O−C−O bond angle of 119.87°, and the two double bonds are elongated from 1.17 Å to 1.23 Å and 1.37 Å, respectively. In the $6e^-$ charge state, the E_{ads} were increased to −1.89 eV, with a CT value of 0.62e. The structural parameters, E_{ads}, and CT values highlight the superior ability of BL-B-Def-1 to activate CO_2 molecule, which is in line with previous investigations [293–295]. In addition, Figure C.6 (Appendix C. Supporting Data) reveals that the E_{coh} energy of BL-B-Def-1 undergoes minimal changes upon injecting the extra charge density. We have also examined the DOS for isolated CO_2, CO_2 adsorbed

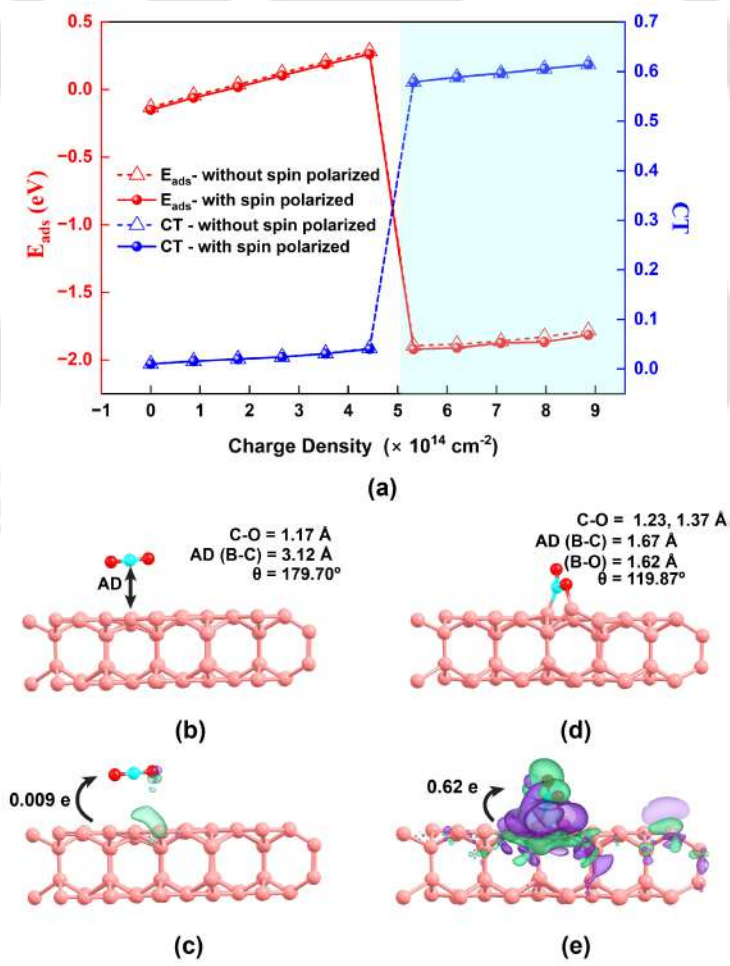

Figure 5.7: (a) E_{ads} and CT plots of BL-B-Def-1 as a function of charge density along with the spin-polarized calculation. The blue-shaded region indicates the chemisorption region. Structure of stable adsorption configuration and CDD plots at $0e^-$ [(b) and (c)] and $6e^-$ [(d) and (e).]

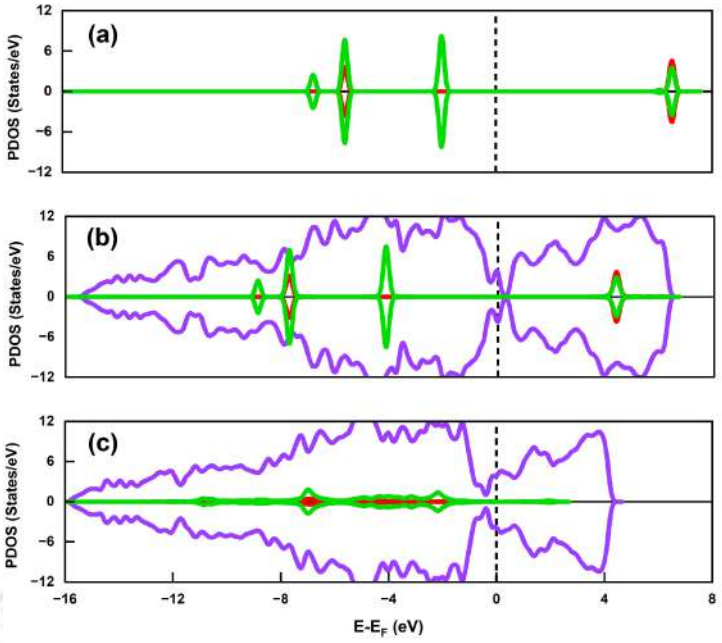

Figure 5.8: Projected density of states (PDOS) plots of (a) isolated CO_2, (b) CO_2-adsorbed defect-induced bilayer borophene (BL-B-Def-1) at $0e^-$, and (c) CO_2-adsorbed defect-induced bilayer borophene (BL-B-Def-1) at $6e^-$. Purple, green, and red colors represent the DOS of $B_{p-orbital}$, $O_{p-orbital}$, and $C_{p-orbital}$, respectively.

in $0e^-$, and $6e^-$ charge states in order to identify the active mode in CO_2 molecule, shown in Figure 5.8. The DOS calculations found that the highest occupied molecular orbital (HOMO) for an isolated CO_2 gas molecule is $1\pi_g$ bonding orbital, whereas the LUMO contains a $2\pi_u$ antibonding orbital [Figure 5.8(a)]. These findings align well with previous theoretical studies [247, 296]. The DOS plot at $0e^-$ charge state [Figure 5.8(b)] indicates no alterations in the states of CO_2 due to its minimal adsorption and negligible structural changes. The DOS of CO_2 adsorbed BL-B-Def-1 at $6e^-$ states (i.e., charge density (ρ) = 5.32×10^{14} e^-/cm^2) indicates that the molecule adopts a bent structure, resulting in the splitting of degenerate $1\pi_g$ bonding and $2\pi_u$ antibonding orbitals [Figure 5.8(c)]. This process occurs as the C=O bond in the CO_2 molecule is activated. Furthermore, we have seen that the chemisorption of CO_2 on the nanosheet caused the total orbital levels of CO_2 to undergo a downshift, which supports earlier findings [297, 298].

5.3.4 Dissociation of CO_2 into CO^*+O^*

Once CO_2 is activated, dissociation is a key step in its chemical conversion into valuable organic feedstock [299]. Figure 5.9 presents the AIMD simulation plot of CO_2 adsorption on BL-B-Def-1 and the change in bond length C-O along with time. At 300 K, the C-O bond dissociation is

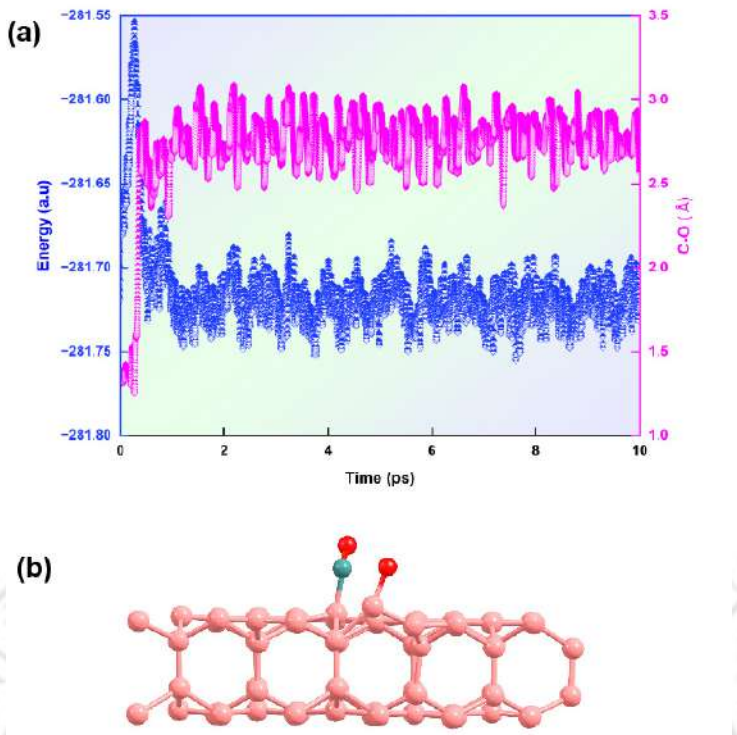

Figure 5.9: (a) AIMD simulations plots of CO_2-adsorbed Def-1-BL-B nanosheet at charge density 5.32×10^{14} e^-/cm^2 for 10 ps at 300 K, (b) Structure of CO_2 at 335 ps.

observed after 335 ps. The final structure after the simulation of 335 ps is shown in Figure 5.9(b). It has been shown that $CO_2^{\delta-}$ species, formed when an electron attaches to CO_2, spontaneously break apart into CO^* and O^* at 300 K. The presence of dative bonds induced by B vacancies, which create adsorption sites for O atoms, leads to the spontaneous dissociation of the CO_2 molecule [300].

Further, the desorption of the CO_2 molecule was studied by removing the extra charge from the nanosheet and enabling the system to stabilize. It has been observed that the CO_2 molecule remains bound to the surface, even after the charge is removed due to the strong bonding between the C and O atoms with the nanosheet, as displayed in Figure C.7 (Appendix C. Supporting Data).

5.3.5 CO_2 Capture Capacity and its Selectivity

One of the most important parameters for assessing the effectiveness of BL-B-Def-1 nanosheet is its CO_2 adsorption capacity. We have computed the E_{ads} of CO_2 on the surface of the material at various coverages with preloaded additional charges. As the number of defects increases to incorporate more CO_2, we have first estimated the E_{coh} and E_{form} energies of the BL-B-Def-1

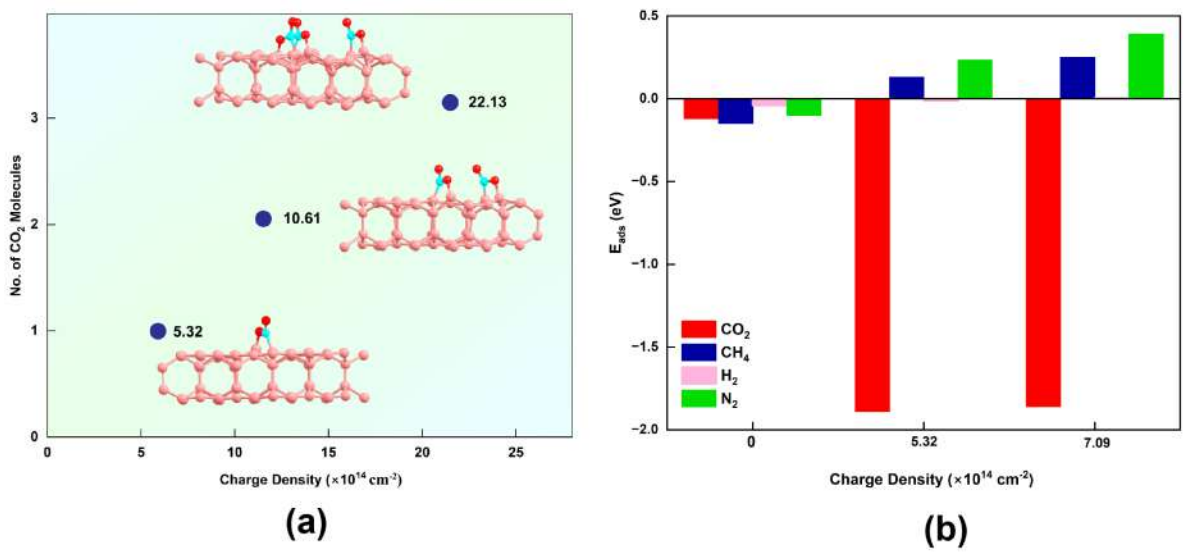

Figure 5.10: (a) Schematic plot of CO_2 adsorption capacity over BL-B-Def-1. (b) Selectivity: E_{ads} plot of CO_2, CH_4, H_2, and N_2 at charge densities 5.32×10^{14} e^-/cm^2 and 7.09×10^{14} e^-/cm^2.

with an increase in defect concentration (2.32 and 3.52 %, respectively) and added charge and tabulated in Table C.3 (Appendix C. Supporting Data) The occurrence of a negative E_{form} and a high E_{coh} indicates that the system is prone to include a considerable number of defects due to the presence of the second borophene layer that is stabilized by the covalent bond. The maximum adsorption capacity of CO_2 on a 2×2 supercell was found to be three CO_2 molecules at a charge density of 2.21×10^{15} e^-/cm^2 as shown in Figure 5.10(a). An increase in CO_2 molecules beyond three causes some to move significantly away from the adsorbent during relaxation, even with an increased charge density of the nanosheet. Further, the previous report demonstrates that the maximum charge density injection through the electrochemical gating technique is 3.50×10^{15} e^-/cm^2 [301]. Thus, the maximal adsorption capacity of our defect BL-B-Def-1 can be experimentally determined. The capacity of the nanosheet to activate CO_2 molecules (X_{cap}) can be defined as $X_{cap} = n/S$. Here, n is the total adsorbed CO_2, and S is the surface area of the nanosheet [302]. Hence, the adsorption capacity of the BL-B-Def-1 is calculated to be 2.66×10^{14} cm^{-2}, which is comparable with previously reported C_3N monolayer (2.16×10^{14} cm^{-2}) [303], C_6N_2 (2.37×10^{14} cm^{-2}) [253].

CO_2 capture technologies are primarily interested in three types of gas mixtures: natural gas sweetening (CO_2/CH_4), pre-combustion (CO_2/H_2), and post-combustion (CO_2/N_2) [304]. Therefore, we have analyzed the CH_4, H_2, and N_2 adsorption on the nanosheets in both neutral and

negatively charged states (at $\rho = 5.32 \times 10^{14}$ e^-/cm^2 and 7.09×10^{14} e^-/cm^2) and compared them with CO_2 [Figure 5.10(b)]. It has been observed that the adsorption of CH_4, H_2, and N_2 on neutral and charged BL-B-Def-1 nanosheets is physisorption in nature. The E_{ads} of CH_4, H_2, and N_2 on neutral and charge states vary from -0.02 to -0.3 eV, whereas the CO_2 from a chemical bond with an E_{ads} of -1.89 eV at a charge density of 5.32×10^{14} e^-/cm^2. Hence, it illustrates that BL-B-Def-1, with a negative charge state, exhibits exceptional selectivity in collecting CO_2 from H_4, H_2, and N_2 mixtures. The optimized structure of all the gas molecules (CH_4, H_2, and N_2) at 5.32×10^{14} e^-/cm^2 is shown in Figure C.8 (Appendix C. Supporting Data). To explore the origin of the physisorption of CH_4, H_2, and N_2 and the chemisorption of CO_2 on BL-B-Def-1 [305], we have plotted the DOS of the system and gas molecules in Figure C.9 (Appendix C. Supporting Data). In Figure C.9, the DOS of CO_2 is near the E_F of BL-B-Def-1 compared to CH_4, H_2, and N_2, indicating that the CO_2 molecule exhibits greater reactivity towards BL-B-Def-1 with increased charge density.

5.4 Conclusions

This work explores the CO_2 activation potential of pristine and atomic-point defect bilayer borophene (BL-B) using first-principles simulations incorporating DFT-D3 dispersion correction. The study illustrates the thermodynamic viability of generating different point defects in BL-B through defect calculations. At a charge density of 5.12×10^{14} e^-/cm^2, the BL-B-Def-1 nanosheet exhibits chemisorption of CO_2, which is subsequently dissociated into CO^* and O^* species. The high electrical conductivity of BL-B-Def-1 allows for easy injection of negative charges. A substantial amount of these injected negative charges accumulates at the defect site. Additionally, the high carrier mobility ($\mu_{e/h}$) of BL-B-Def-1 is well-suited for charge-discharge applications. The CO_2 coverage at BL-B-Def-1 reaches saturation at charge densities of 2.21×10^{15} e^-/cm^2, yielding CO_2 capture capacities of up to 2.66×10^{14} e^-/cm^2. Experimental approaches such as electrochemical gating can generate 3.15×10^{15} e^-/cm^2 charge density on a 2D surface. Thus, we believe that charge-modulated CO_2 activation on defect-induced BL-B is experimentally plausible. The AIMD simulations reveal the desorption of CO_2 from the Def-1-BL-B at 350 K after 280 ps. Moreover, the BL-B-Def-1 nanosheets with negative charge densities

exhibit remarkable selectivity for separating CO_2 from mixtures with CO_2/CH_4, CO_2/H_2, and CO_2/N_2. Overall, we have proposed point defects in 2D semiconducting BL-B nanosheet as a suitable charge-induced material for CO_2 capture. Our results offer valuable insights into the development of experimentally possible, controlled, highly selective, and high-capacity CO_2 activation materials.

Chapter 6

CO_2 Reduction on Defective Bilayer Borophene: Charge Neutral Method vs. Constant Potential Method

(This work in this Chapter is published in *J. Phys. Chem. C* 2025, 129, 13939-13953.)

6.1 Introduction

The utilization of fossil fuels in various human activities, such as power generation, transportation, industrial revolution, etc., is the most significant contributor to CO_2 emissions. CO_2 is a major component of greenhouse gases and becomes a threat to the global climate [306, 307]. Thus, CO_2 activation and conversion of CO_2 into valuable chemicals and fuels have significant potential to minimize environmental pollution and address global energy demand [308]. The electrochemical CO_2 reduction reaction (ECRR) is the most promising approach to CO_2 conversion due to its cost-effectiveness, controllability through the applied electrode potential, and operation at ambient temperature and pressure [309–311]. Further, the ECRR shows precise control over generated products and reaction pathways based on electrocatalysts and electrolytes with energy sources such as wind and solar power [293, 312].

Figure 6.1 illustrates the ECRR and the possible product generated in the reaction cell [313, 314]. The electrochemical reaction cell is composed of a cathode, an anode, an aqueous electrolyte

solution, and an ion-exchange membrane. The anode promotes an oxygen evolution reaction (OER) that produces O_2. During this reaction, H^+ ions and e^- are also produced, where e^- flow through the external circuit to the cathode, and the H^+ ions are transferred to the ion-exchange membrane. The interaction of protons and electrons in the cathode, which is coated with the appropriate catalyst, results in the reduction of CO_2 or the generation of H_2. The electrolyte present in the electrochemical cell dissolves CO_2 and acts as a medium for the transfer of charged species (e^-/H^+) [313, 315]. Depending on multiple proton-coupled electron transfer (PCET),

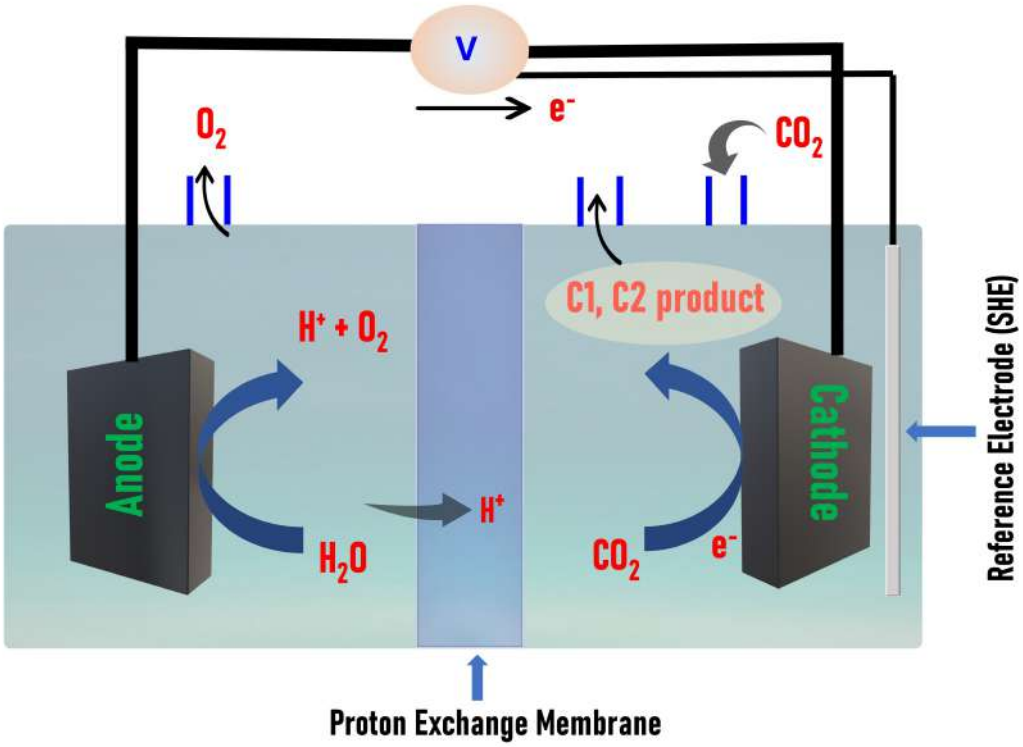

Figure 6.1: Schematic representation of CO_2 reduction in an electrochemical cell.

CO_2 reduction produces different C1 and C2 products, including CO, HCOOH, C_2H_5OH, CH_4, CH_3OH, etc., via various routes [316]. Figure 6.2 and Table 6.1 illustrate the potential pathways for generating different C1 products [317, 318]. Among these, CH_3OH is a crucial product with a high volume-specific energy density [319], serving as a fuel in direct methanol fuel cells (DMFCs), an intermediate for various chemical products, and facilitating easy storage and transport [315].

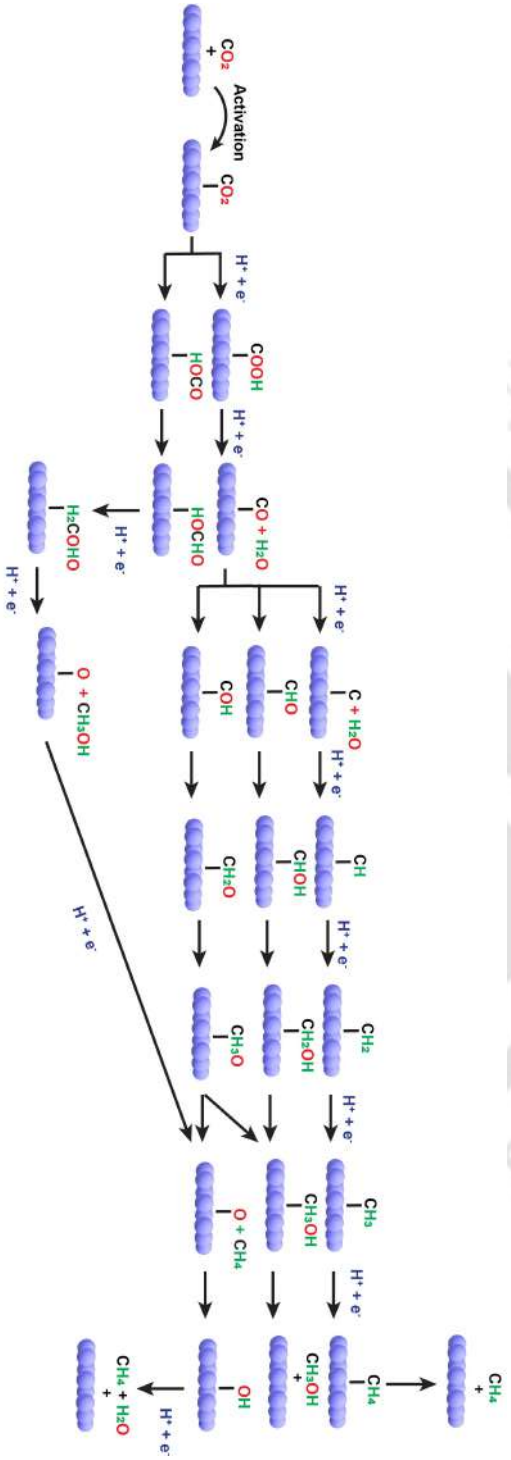

Figure 6.2: Depicting possible electrochemical CO_2 reduction roadmaps to form various C1/C2 products.

Table 6.1: Equations used to calculate the free energy at each elementary step for electrocatalytic CO_2 reduction reaction (ECRR).

Elementary steps	
Reaction	Activation
$* + CO_2 \rightarrow *CO_2$	
$*+ CO_2 + 1H^+ + 1e^- \rightarrow *COOH$	$1e^-$
$* CO_2 + 1H^+ + 1e^- \rightarrow *COOH$	
$* + CO_2 + 2H^+ + 2e^- \rightarrow *CO + H_2O$	$2e^-$
$* + CO_2 + 2H^+ + 2e^- \rightarrow *HOCOH$	
$* + CO_2 + 3H^+ + 3e^- \rightarrow *CHO + H_2O$	$3e^-$
$* + CO_2 + 3H^+ + 3e^- \rightarrow *COH + H_2O$	
$* + CO_2 + 4H^+ + 4e^- \rightarrow *CHOH + H_2O$	$4e^-$
$* + CO_2 + 4H^+ + 4e^- \rightarrow *CH.O + H_2O$	
$* + CO_2 + 4H^+ + 4e^- \rightarrow *C+2H_2O$	
$* + CO_2 + 5H^+ + 5e^- \rightarrow *CH_2O + H_2O$	$5e^-$
$* + CO_2 + 5H^+ + 5e^- \rightarrow *CH_2OH + H_2O$	
$* + CO_2 + 5H^+ + 5e^- \rightarrow *CH_2OH + H_2O$	
$* + CO_2 + 5H^+ + 5e^- \rightarrow *CH_22H_2O$	
$* + CO_2 + 6H^+ + 6e^- \rightarrow *CH_3OH + H_2O$	$6e^-$
$* + CO_2 + 6H^+ + 6e^- \rightarrow *CH_3OH + + H_2O$	
$*CH_3OH \rightarrow * + CH_3OH$ (l)	
$* + CO_2 + 6H^+ + 6e^- \rightarrow *O + CH_4(g) + H_2O$	
$* + CO_2 + 6H^+ + 6e^- \rightarrow *CH_4+2H_2O$	
$* + CO_2 + 7H^+ + 7e^- \rightarrow *OH + CH_4(g) + H_2O$	$7e^-$
$* + CO_2 + 7H^+ + 7e^- \rightarrow *CH_4+2H_2O$	
$* + CO_2 + 8H^+ + 8e^- \rightarrow *+2H_2O+CH_4(g)$	$8e^-$
$* + CO_2 + 8H^+ + 8e^- \rightarrow *CH_4+2H_2O$	
$*CH_4 \rightarrow * + CH_4(g)$	

A suitable and efficient electrocatalyst is one of the major components for achieving controllable product selectivity and reaction channels. Selective production of oxygenates, like methanol (CH_3OH), is significantly dependent on the adsorption energy (E_{ads}) and the geometry of intermediates. The stabilization of the C-O bond, which is caused by the preferential adsorption of oxygen over carbon atoms of intermediates, could enhance the selectivity for methanol. Hence, the catalyst surface should have oxophilic characteristics to promote CH_3OH production by reducing the probability of oxygen loss and allowing intermediates to be absorbed partially or completely through oxygen atoms [320]. In addition, another limitation in ECRR is the high overpotential (η) and the prominent hydrogen evolution reaction (HER), which significantly competes with the CO_2 electroreduction process [312].

Atomically thin 2D electrocatalysts are promising materials as they provide surface-active sites with high density and uniformity, with the ease of tweaking their atomic structure in several ways [321]. Most of these studies focus mainly on metal-based electrocatalysts [322, 323] since metal-free materials exhibit inadequate electronic conductivities and fail to activate CO_2 molecules effectively [169, 324]. Nonetheless, metal-free electrocatalysts have several benefits, including environmental safety, low cost, unaffected by the poisoning effect, and good durability [325, 326]. Thus, developing metal-free electrocatalysts with both high activity and selectivity for ECRR is crucial.

In recent years, bilayer borophene (BL-B) synthesized on Ag(111) and Cu(111) substrates has garnered interest for its potential in electrical and energy applications [24]. Since the two layers are linked *via* a covalent bond, the BL-B demonstrates enhanced thermal stability and reduced susceptibility to oxidation compared to its monolayer counterpart [19, 24]. In the previous chapter, we have thoroughly discussed the activation and the challenges related to the activation of the CO_2 molecule (i.e., to produce the CO_2^- intermediate) over 2D pristine and defect-induced bilayer borophene (BL-B). Hence, this chapter solely focuses on the reduction of CO_2 into valuable feedstock to realize carbon neutrality [320, 327]. Since boron exhibits oxophilic behavior [328], the BL-B surface can form chemical bonds with both C and O atoms [as shown in Figure 5.7(b] and may therefore show selective reduction toward CH_3OH. The electrocatalytic activity of the pristine and defect-induced BL-B was evaluated using quantum

mechanical calculations, which typically assumes that the catalyst is charge-neutral, known as the charge-neutral method (CNM). Further, to evaluate the charge effect of the catalyst for a more realistic scenario, a constant potential model (CPM) is applied [329]. Thus, our findings are helpful in understanding the ECRR mechanism in BL-B and the influence of potential in an actual electrochemical reaction.

6.2 Computational Details

Density Functional Theory (DFT) [330] calculations incorporating spin-polarization were performed via Vienna Ab initio Simulation Package (VASP) [331] with GGA-PBE functional [150] to generate the free energy diagram for ECRR. To describe the interaction between electrons and ions, the projector-augmented wave approach was employed with a kinetic energy cutoff of 400 eV [100]. DFT-D3 dispersion correction [152] was used to treat the interaction between the ECRR intermediate and the catalyst with the energy tolerance of 10^{-5} eV to optimise the atomic structures. The Monkhorst-Pack approach with a $5 \times 5 \times 1$ k-point grid was used for Brillouin zone integration [151]. In this work, a 2×2 supercell of BL-B was considered with a vacuum of 25 Å in the z-direction to avoid the interaction of periodic images.

The electrocatalytic efficiency of the defect-induced BL-B was analyzed using a computational hydrogen electrode (CHE) model proposed by Nørskov et al. The idea of the CHE model is that at the reference relative hydrogen electrode (RHE), the chemical potentials of a proton-electron pair [$\mu(H^+ + e^-)$] and a hydrogen molecule [$\mu(H_2)$] are equivalent. Therefore, the free energy of H_2-molecule can be used as a reference for the $H^+ + e^-$ free energy in the PCET process. The overall chemical potential of a $H^+ + e^-$ pair is equivalent to H_2, and can be expressed as [318]

$$\mu(H^+ + e^-) = \mu\frac{1}{2}(H_2) \tag{6.1}$$

The free energy change of the $H^+ + e^-$ with respect to potential is defined by the linear correlation between electron energy and potential where the electron energy is shifted by $-eU$. Here, U is the applied bias, and e is the elemental positive charge. The change in free energy for an

electrocatalytic reduction reaction $^* + A + H^+ + e^- = AH^*$ can be written as [318]

$$\Delta G = G(AH^*) - G(^*) - G(A) - \frac{1}{2}G(H_2) - eU \tag{6.2}$$

Here, $G(AH^*)$, $G(^*)$, and $G(A)$ are the free energies of catalyst+intermediate, catalyst, and intermediate. The free energy of each reduction intermediate can be determined according to the equation 6.3 [333]

$$G = E_{elec} + E_{ZPE} - TS \tag{6.3}$$

Where E_{elec} is the calculated electronic energy, E_{ZPE} is the zero-point energy, T is the temperature (298.15 K), and S is the entropy. E_{ZPE} and S are calculated from the vibrational frequencies analysis with the VASPKIT [334].

The CO_2 to CH_3OH and CH_4 reduction is $6e^-$ and $8e^-$ process, respectively. The path involved in each elementary step is shown in Table 6.1. Theoretical limiting potential (U_L) is an important factor in evaluating catalyst performance, which can be defined as the maximum change in free energy (ΔG_{max}) throughout all elementary steps across the lowest energy path using the equation $U_L = \frac{-\Delta G_{max}}{e}$. Further, the overpotential (η) of an ECRR can be calculated as $\eta = U_{eq} - U_L$. U_{eq} is the equilibrium potential (0.016 V for CH_3OH and 0.169 V for CH_4) [335].

The conventional CHE model is a CNM that ignores the change in charge effect during the catalytic cycle (i.e., the electron is constant). The CPM deals with the more realistic approach in an electrocatalytic cycle. According to the CPM, the electrode potential (U) relative to the (standard hydrogen electrode) SHE is expressed as

$$U = \frac{-\mu(e^-) - \phi_{SHE}}{e} \tag{6.4}$$

Here, ϕ_{SHE} and $\mu(e^-)$ denote the work function of the referenced electrode and the chemical potential of the electron, respectively [329, 336]. Here, we have considered ϕ_{SHE} to be 4.44 eV (4.44 $\pm$ 0.02 eV), determined by the experiment. The CPM model maintains a constant potential/bias (U) by changing the number of electrons (N_e) to modify the Fermi Level (E_F) of the system in relation to the SHE, i.e., E_F(reactant-Q1) = E_F(reactant-Q2) =μ_e. The grand canonical electronic energy (Ω) is determined if the two slab models have the same μ_e but

different N_e.

$$\Omega = E_{DFT} - N_e \mu_e \tag{6.5}$$

E_{DFT} denotes the electronic energy of the system in a charged state. The free energy profile is derived by applying correction to thermal energy correction to Ω [337]. CNM and CPM approximated the solvation effect using the self-consistent continuum solvation model, which uses a continuum medium and a spatially variable dielectric function. The dielectric constant of water is considered to be 78.35 [338].

6.3 Results and Discussion

6.3.1 Geometrical Structure of BL-B and CO_2@BL-B-Def-1

The unit cell of the BL-B nanosheet was optimized through DFT calculations, as illustrated in Figure 6.3(a). This exhibits a hexagonal geometry, with the lattice constant a=b=5.71 Å which aligns with previous experimental [13] and theoretical periodicity [24] along with the Quantum ESPRESSO (QE) results. The E_{ads}, the structural configuration, and the charge density difference (CDD) of CO_2 adsorbed BL-B-Def-1 were shown in Figure 6.3(b,c), and the results are comparable with the QE results.

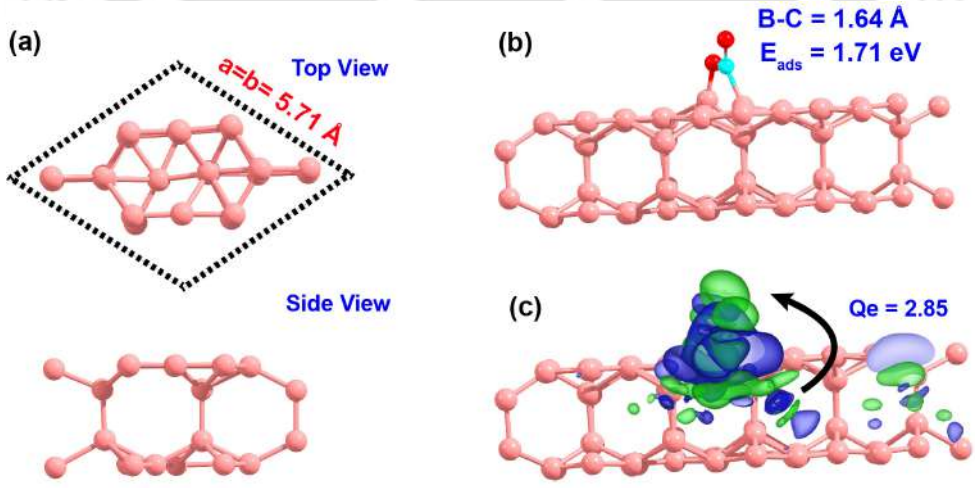

Figure 6.3: (a) Unit cell of BL-B shown from the side and top views. (b) CO_2 adsorbed on BL-B-Def-1 at a charge state of $6e^-$. (c) CDD plot, where green and blue represent charge accumulation and depletion regions, respectively. Pink, red, and cyan indicate boron, oxygen, and carbon atoms, respectively.

6.3.2 Electrocatalytic Reduction of CO_2

Following the CO_2 molecule activation, the reduction of CO_2 into various industrially important chemicals, including formic acid and methanol (CH_3OH), or light hydrocarbons such as methane (CH_4), represents a highly advantageous transformation due to the extensive applications in diverse fields. Among these, CH_3OH is a crucial product with a high volume-specific energy density [319], serving as an organic fuel in direct methanol fuel cells (DMFCs), an intermediate for several chemical compounds and facilitating easy storage and transport [315]. Therefore, we have demonstrated the significant potential of the BL-B-Def-1 surface for the selective reduction of CO_2 into valuable organic fuels.

Electrocatalytic CO_2 Reduction Reaction (ECRR) to CO and HCOOH

CO and HCOOH are generated via the $2e^-$ reduction in ECRR. $H^+ + e^-$ transfer is involved in each step. In the first protonation step, two possible intermediates are formed due to the two distinct hydrogenation sites (on the carbon or oxygen atom), namely *COOH and *OCHO, which are crucial for the initiation of the ECRR process. Then, *COOH or *OCHO continues to be reduced to *CO or *HCOOH. These can be reduced further as a chemical intermediate or released from the catalyst surface to yield CO and HCOOH, respectively. The probable reduction pathways are shown below [325]:

$$Pathway1 : CO_2 \rightarrow {}^*CO_2 \rightarrow {}^*COOH \rightarrow {}^*CO + H_2O \rightarrow {}^* + CO \tag{6.6}$$

$$Pathway2 : CO_2 \rightarrow {}^*CO_2 \rightarrow {}^*OCOH \rightarrow {}^*HCOOH \rightarrow {}^* + HCOOH \tag{6.7}$$

Figure 6.4 shows the free energy change across the reaction pathways at charge $0e^-$ and $6e^-$. Figure 6.4(a) illustrates that CO_2 activation is an uphill process, consistent with our finding that no molecule is activated at zero charge. Further, as presented in Figure 6.4(a), *COOH to *CO and *OCHO to *HCOOH are two potential determining steps (PDS) with theoretical limiting potentials (U_L) of -0.63 and -0.72 V in pathways 1 and 2, respectively. The exothermic nature of CO_2 adsorption is seen in Figure 6.4(b), suggesting that CO_2 activation and subsequent reduction are feasible. After the activation, the hydrogenation/reduction of $^*CO_2$ to produce *CO or *HCOOH has a thermodynamically uphill free energy shift. In pathway 1, the transformation

from *COOH to *CO exhibited a maximum free energy change of 0.62 eV. In contrast, pathway 2 (*OCHO to *HCOOH) involves a higher barrier height of 1.57 eV, suggesting that pathway 1 on charge-induced BL-B-Def-1 is more favorable. The results further corroborate our AIMD findings, demonstrating the dissociation or breakdown of CO_2 into *CO and *O [Figure 5.9]. Furthermore, given that the CO adsorption energy is relatively moderate (-1.12 eV), the process favors further reduction over desorption. In comparing pathways 1 and 2 at $0e^-$ and $6e^-$ BL-B-Def-1, it was observed that pathway 1 is more probable at $6e^-$ BL-B-Def-1, exhibiting a relatively lower U_L of -0.62 V among all.

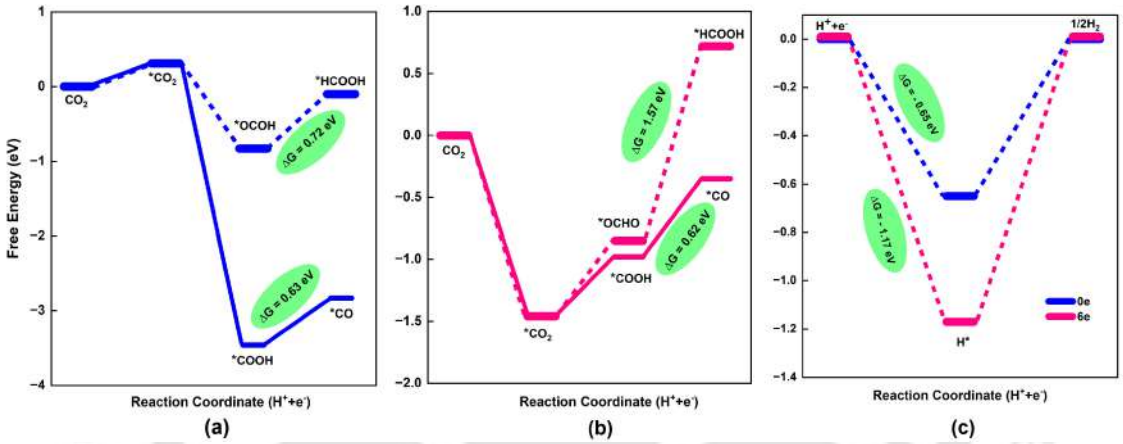

Figure 6.4: Reaction-free energy profiles of CO_2 to *CO (pathway 1: solid lines) and *HCOOH (pathway 2: dashed lines) reduction on (a) BL-B-Def-1 ($0e^-$) and (b) charge-induced BL-B-Def-1 ($6e^-$).(c) HER profile at $0e^-$ and $6e^-$.

Selectivity for Electrocatalytic CO_2 Reduction Reaction (ECRR) vs. Hydrogen Evolution Reaction (HER)

In aqueous electrolytes, HER ($H^+ + e^- \rightarrow \frac{1}{2} H_2$) is frequently a competing reaction with the ECRR, as the evolution of hydrogen would consume the $H^+ + e^-$ and hinders the catalytic activity of the ECRR [325, 334]. The initial elementary step in ECRR involves the activation of CO_2 ($^*CO_2$) on the catalyst, exhibiting free energy values of 0.32 eV and -1.46 eV for the $0e^-$ and $6e^-$ BL-B-Def-1 nanosheet, respectively [Figure 6.4(a,b)]. Further, the free energy barrier for the HER is measured at -0.65 eV for the $0e^-$ and -1.17 eV for the $6e^-$ BL-B-Def-1 structure, as illustrated in Figure 6.4(c). For the studied structures, the findings revealed that at $0e^-$, BL-B-Def-1 exhibits a significant energetic downhill for the adsorption of H*, suggesting an improvement in thermodynamic conditions for the HER. On the contrary, at $6e^-$, the activation

of CO_2 demonstrates a greater downhill in free energy relative to H^*, indicating a resistance to HER. Further, the predicted η of charge-induced BL-B-Def-1 for ECRR was determined to be 0.63 V, which is 0.54 V lower than the η of HER, significantly suppressing HER.

Selective Electrocatalytic CO_2 Reduction Reaction (ECRR) to CH_3OH using Charge Neutral Method (CNM)

Our earlier results show that the charge-induced BL-B-Def-1 exhibits selectivity for ECRR in the presence of HER. Thus, we have continued with the analysis of the subsequent reduction of CO into various industrially valuable feedstocks (CH_3OH and CH_4) with this system. The most preferable path is pathway 1, which generates $^*CO$, as seen in Figure 6.4(b). Figure 6.5 illustrates that the hydrogenation of the intermediate $^*CO$ results in the formation of the intermediates $^*CHO$ or $^*COH$. The generation of $^*CHO$ occurs with a lower free energy barrier, indicating a favorable process. $^*CO$ reduction to $^*CHO$ is in a constant state of competitiveness with the kinetically rapid process of $^*CO$ desorption to CO. Figure 6.5 and Figure 6.4(b) demonstrate that the conversion of $^*CO$ to $^*CHO$ yields a reduced energy barrier compared to $^*CO$ desorption, hence significantly favoring further CO reduction [339]. Furthermore, the bond length of B−C between BL-B-Def-1 and CHO measures 1.58 Å, associated with an adsorption energy of −3.25 eV. This suggests that $^*CHO$ exhibits a favorable tendency to interact with the BL-B-Def-1, facilitating the acceptance of an electron and a proton to yield $^*CH_2O$ or $^*CHOH$. In step 4, between the two potential intermediate structures, $^*CH_2O$ demonstrates exothermic properties and shows a preference for the formation of the $^*CH_2O$ intermediate. It was observed that $^*CHO$ to $^*OCH_2$ conversion shows a flipping mechanism coupled with the reduction process, which is consistent with the mechanism previously proposed [340]. The thermodynamically favorable pathway flipping mechanism is shown in Figure 6.6. Figure 6.6 shows that the formation of two possible intermediates (a) one arising from the direct hydrogenation of $^*CHO$ and (b) the $^*CHO$ flipping mechanism, with a notable difference in free energy. Among these, the intermediate generated via structural flipping displays a lower free energy, suggesting it is the more thermodynamically favorable pathway for CO_2 reduction. Further, $^*OCH_2$ is reduced to yield $^*CH_3O$ or $^*CH_2OH$, with the barrier energy for $^*CH_2OH$ formation being lower (−1.30 eV) compared to that of $^*CH_3O$ (−1.01 eV). $^*CH_2OH$ is subsequently reduced to produce

$^*CH_3OH$, and since the adsorption energy of $^*CH_3OH$ is very small, it prefers to be desorbed from the surface, leading to CH_3OH (l) generation and catalyst regeneration ($*$). The complete CH_3OH generation process is governed by the formation of $^*CO$, which is likely the PDS with a maximum Gibbs free energy change (ΔG_{max}) of 0.62 eV. Selective production of oxygenates, like methanol (CH_3OH), is significantly dependent on the E_{ads} and the geometry of intermediates. The stabilization of the C−O bond, which results from the preferred adsorption of oxygen over carbon atoms of intermediates, could enhance the selectivity for methanol. Hence, the catalyst surface should have oxophilic characteristics to promote CH_3OH production by reducing the probability of oxygen loss and allowing intermediates to be absorbed partially or wholly through oxygen atoms [320]. Since boron exhibits oxophilic behavior [328], the BL-B surface, through chemical bonding with the C and O atoms [Figure 6.3(b)], shows selective reduction toward CH_3OH. Figure 6.7 shows the energy profile diagram for the generation of CH_4 at $6e^-$. The preferred CH_4 generation pathway, which is an $8e^-$ process, is shown below.

$$^*CO_2 \rightarrow {}^*COOH \rightarrow {}^*CO + H_2O \rightarrow {}^*CHO \rightarrow {}^*CH_2O \rightarrow {}^*CH_3O \rightarrow {}^*O + CH_4$$
$$\rightarrow {}^*OH + CH_4 \rightarrow {}^* + CH_4 + H_2O$$

which is an $8e^-$ process. Production of CH_4 demanded a greater η of 2.54 V, with $^*OH \rightarrow {}^* + CH_4 + H_2O$ serving as a PDS, which is also influenced by the HER. All our calculations indicate that the predicted η for the reduction of CO_2 to CH_4 is greater compared to the reduction of CO_2 to CH_3OH, suggesting a preference for CH_3OH formation. Thus, the preferred pathway for selective methanol production is predicted to be

$$^*CO_2 \rightarrow {}^*COOH \rightarrow {}^*CO + H_2O \rightarrow {}^*CHO \rightarrow {}^*OCH_2 \rightarrow {}^*CH_2OH \rightarrow {}^*CH_3OH$$
$$\rightarrow {}^* + CH_3OH$$

with a η of 0.63 V. The determined η of charge-induced BL-B-Def-1 shows a better/comparable performance to several previously observed electrocatalysts, including Ni-supported C_2N, which has a value of 0.9 V [341], molybdenum-based metal carbide catalyst (1.1 V) [320], Ni-N_4-C (almost equal to 1.6 V) [342], Cu (1 V) [343] etc.

Figure 6.8 displays the electrocatalytic reduction pathway of CO_2 at $0e^-$, demonstrating selective

reduction to CH_4 at a η of 2.07 V with a different reduction

$$^*CO_2 \rightarrow {}^*COOH \rightarrow {}^*CO + H_2O \rightarrow {}^*CHO \rightarrow {}^*CH_2O \rightarrow {}^*CH_3O \rightarrow {}^*O + CH_4$$
$$\rightarrow {}^*OH \rightarrow {}^* + H_2O + CH_4$$

pathway. Thus, it was observed that the lowering of the η of a catalyst results from the incorporation of charge states, which also influences product selectivity [344, 345]. The charge state of 2D materials has a pronounced influence on electrochemical reactions. This phenomenon can be understood as the charge-induced modification in the occupation of energy levels being more pronounced due to the low density of states inherent to 2D materials [344].

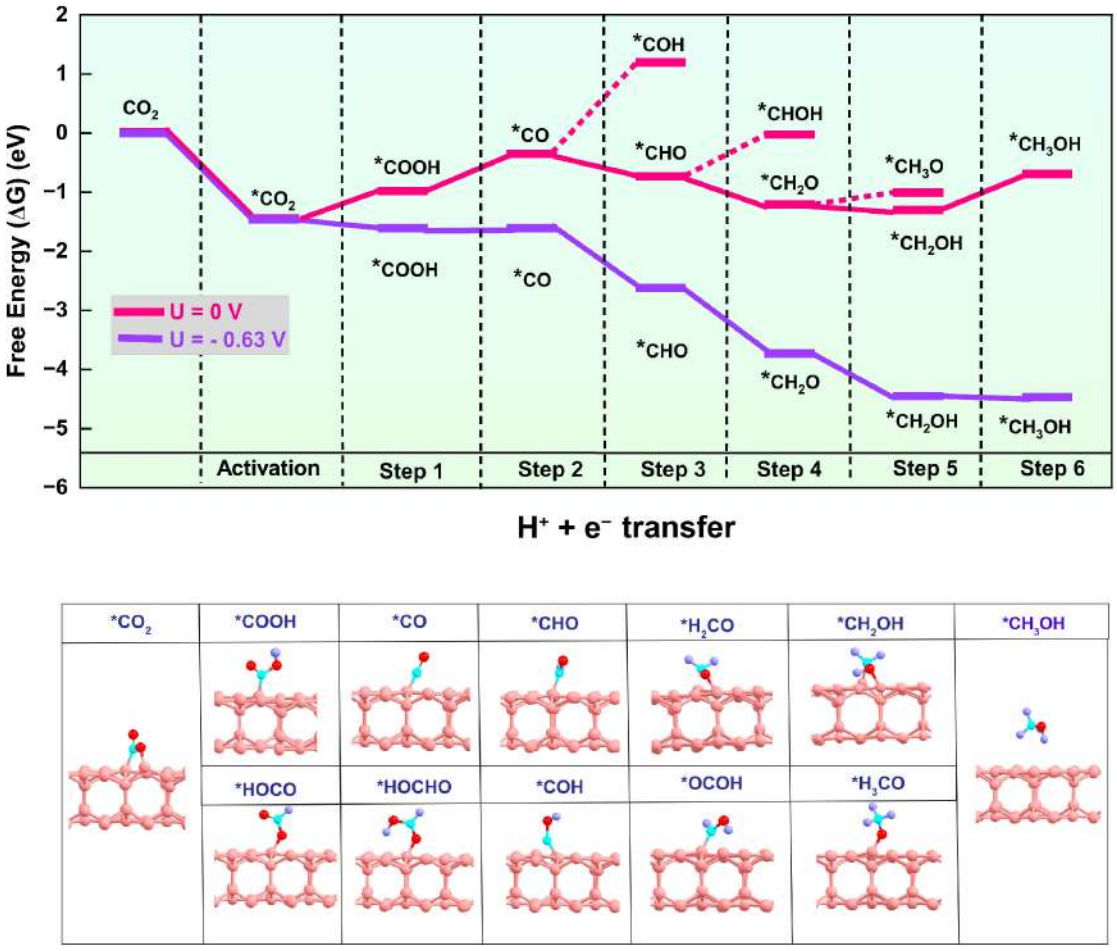

Figure 6.5: Reaction free energy profile at U= 0 V and −0.63 V with CNM along with the structures of various reaction intermediates.

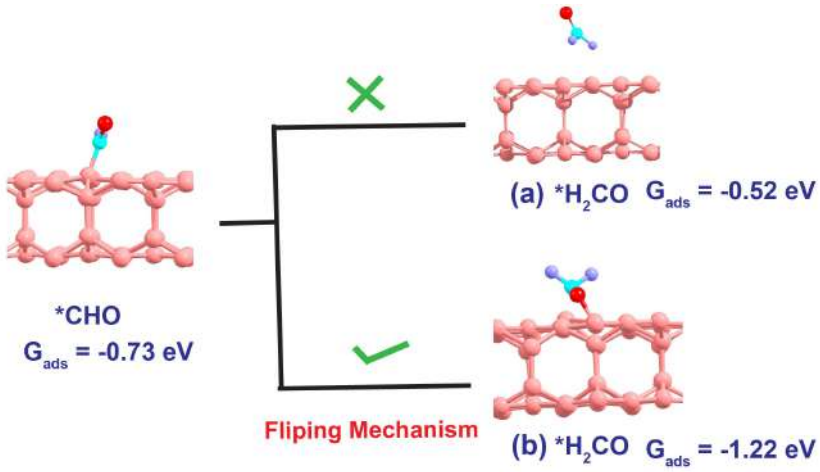

Figure 6.6: Structure of $^*CH_2O$ (a) direct hydrogenation of $^*CHO$ and (b) $^*CHO$ undergoes flipping.

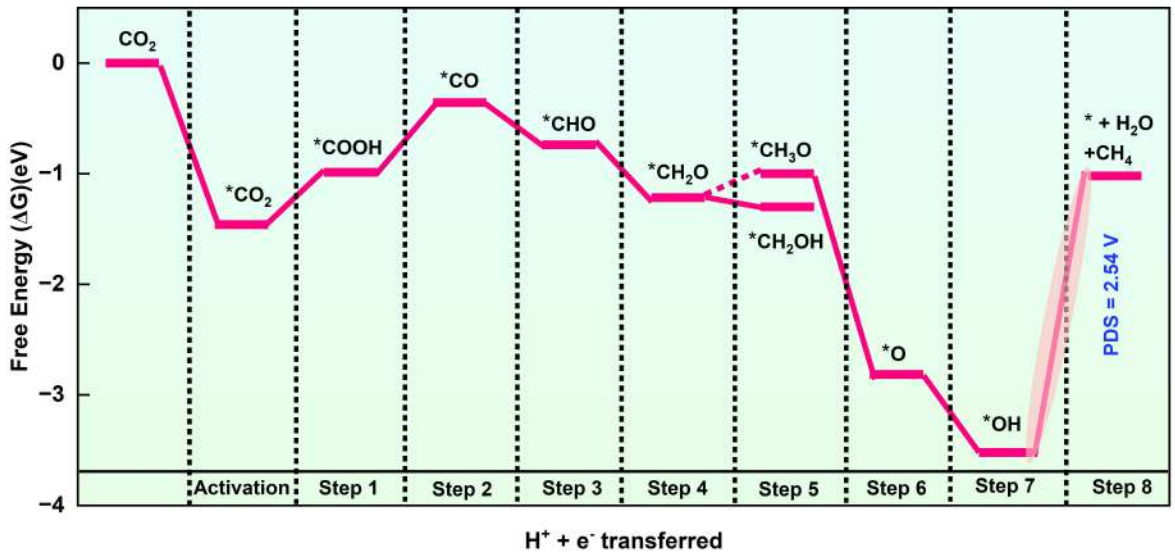

Figure 6.7: Free energy profile of electrocatalytic CO_2 reduction reaction (ECRR) to CH_4 using the charge neutral method (CNM) at $6e^-$.

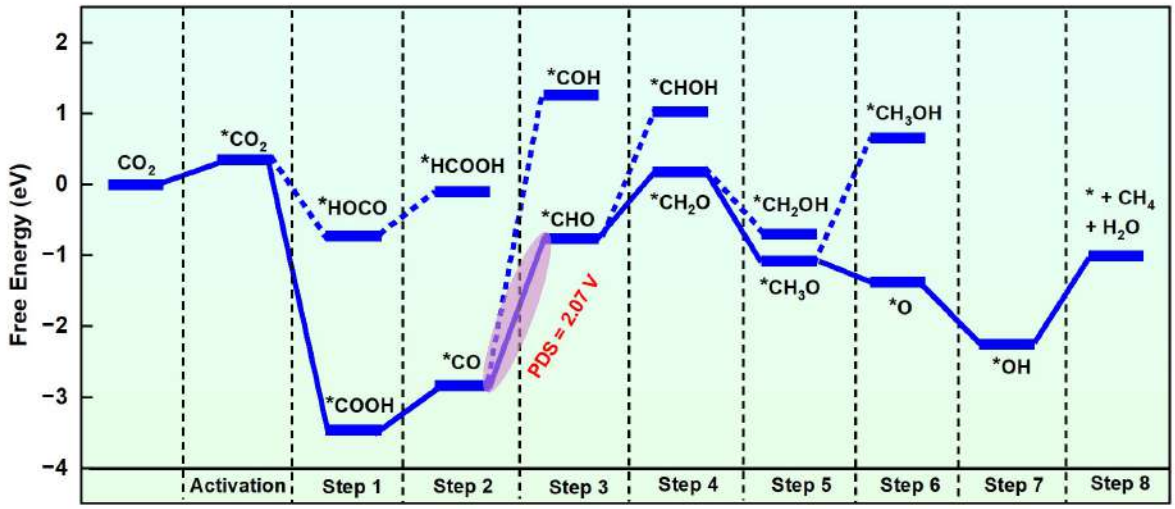

Figure 6.8: Free energy profile of electrocatalytic CO_2 reduction reaction (ECRR) to CH_4 using the charge neutral method (CNM) at $0e^-$.

Electrocatalytic CO_2 Reduction Reaction (ECRR) using Constant Potential Method (CPM)

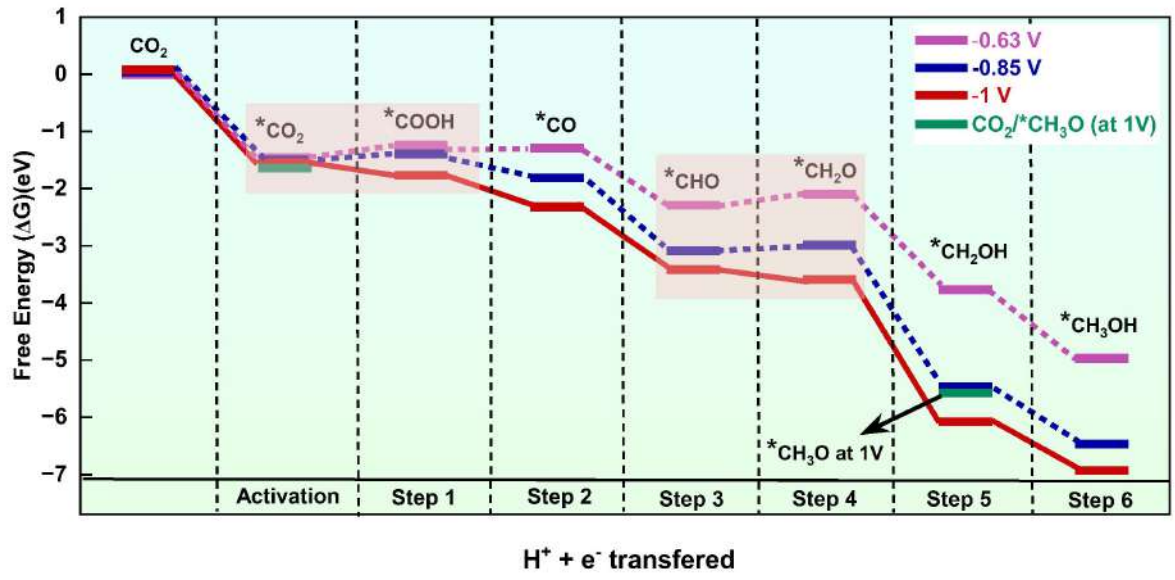

Figure 6.9: Reaction free energy profiles at U= −0.63, −0.85, and −1.0 V using the constant potential method (CPM).

The free energy plot in Figure 6.5 presents the energy profile diagram obtained at a constant charge of $6e^-$, ignoring the influence of the applied voltage. In an actual scenario of an electrochemical reaction, the reactive site of an electrochemical interface does not sustain a steady charge over the catalytic cycle. The electrons constantly travel between the catalyst and the electrode to maintain the established equilibrium [336]. We have generated the potential-

dependent free energy reaction profile for ECRR at 0.63 V by applying the CPM model (Figure 6.9; violet color). Figure 6.9 illustrates that all PCET processes are exothermic except for $^*COOH$ and $^*CH_2O$ formation at U=−0.63 V. The formation of $^*COOH$ is an uphill process by 0.22 eV, and the $^*CH_2O$ is by 0.14 eV. This finding signifies that CO_2 conversion will be hindered by the generation of $^*COOH$ and $^*CH_2O$ at an applied potential of −0.63 V, indicating that a higher negative potential is required to promote this reaction. The estimated free energies of $^*COOH$, $^*CO$, $^*CHO$ $^*CH_2O$, and $*CH_3O$ lie above the predicted free energies from the CHE model. Since $^*COOH$ is a PDS as predicted by the CPM, to facilitate CO_2 reduction, an additional potential of 0.22 V needs to be applied. Therefore, a potential of −0.85 V was applied to the free energy reaction profile diagram that shows the $^*CO_2 \rightarrow {}^*COOH$ and $^*CHO \rightarrow {}^*CH_2O$ reactions remain thermodynamically unfavorable, as illustrated in Figure 6.9 (blue color). Additionally, an extra potential of 0.15 V was introduced to the reaction, leading to the natural spontaneity of all the reactions. According to the CPM, the adsorption energy of CH_3OH is significantly lower, suggesting desorption of CH_3OH instead of further reduction. The adsorption of CO_2 is a non-redox process and remains unaffected by the applied potential throughout the CHE model [345]. Therefore, we have assumed that the activation energy of CO_2 molecule takes place at $6e^-$ and that subsequent reduction occurs in accordance with the CPM method. In contrast, the CPM model shows CO_2 adsorption free energies of −1.72 (green color in Figure 6.9) in Def-1-BL-B at U = −1.0 V. The CPM model predicts greater negative CO_2 adsorption-free energies, indicating a considerable stabilization of $^*CO_2$ from the CHE model validated by the prior work [345]. Further, the activation of CO_2 at a charge state of $6e^-$ is not only a spontaneous process but also demonstrates selectivity for CH_3OH production in competition with HER.

The simulation potential of −1 V vs. SHE is determined using the CPM, which provides a more realistic representation of the electrocatalytic cycle by maintaining equilibrium between the electrode and the catalyst. However, the efficiency of ECRR is highly sensitive to pH and electrolyte composition, as these factors influence proton availability in the solution, thereby impacting both the thermodynamics and kinetics of the reaction [346, 347]. For example, at neutral pH (pH = 7), a potential of −1 V vs. SHE corresponds to approximately −0.59 V

vs. RHE. This highlights the importance of pH-dependent potential shifts when interpreting the activity and selectivity trends in CO_2 reduction under realistic electrochemical conditions. However, scaling up or implementing practical electrochemical setups for ECRR depends not only on the applied potential and pH but also on several other factors that must be carefully optimized to ensure stable and efficient operation. It includes the type of electrolyte, flow rate, and form of CO_2 feedstock, which can all be adjusted to improve performance. For industrial use, the cell should ideally reach a Faradaic efficiency above 90 % and operate at a voltage between 2.5 and 3 V [348].

Further, ECRR may be limited by other possible side reactions, such as CO poisoning and carbonate formation along with HER. CO poisoning is a well-known issue in many catalytic systems, where CO binds strongly to active sites, thereby inhibiting further catalytic activity by blocking access to reactants [349]. However, in our system, CO poisoning is unlikely to be a limiting factor. Our calculations reveal that at an applied potential of -1 V, the transformation from adsorbed *CO to *CHO is thermodynamically favorable and occurs spontaneously. This indicates that *CO does not accumulate on the surface, as it is rapidly converted into downstream intermediates. As a result, the active sites remain accessible, and the catalytic cycle is maintained. In an alkaline case, CO_2 is bound to react with OH^- ($2OH^- + CO_2 = {CO_3}^{2-} + H_2O$), which is present in the electrolyte and produces carbonate (${CO_3}^{2-}$). Along with carbonate formation, high pH causes a huge waste of CO_2 [350]. However, ECRR in acidic media offers a promising route to suppress CO_3^{2-} formation, as any CO_3^{2-} formed is rapidly converted back to CO_2 due to high bulk acidity [350].

6.3.3 Density of States (DOS) calculation

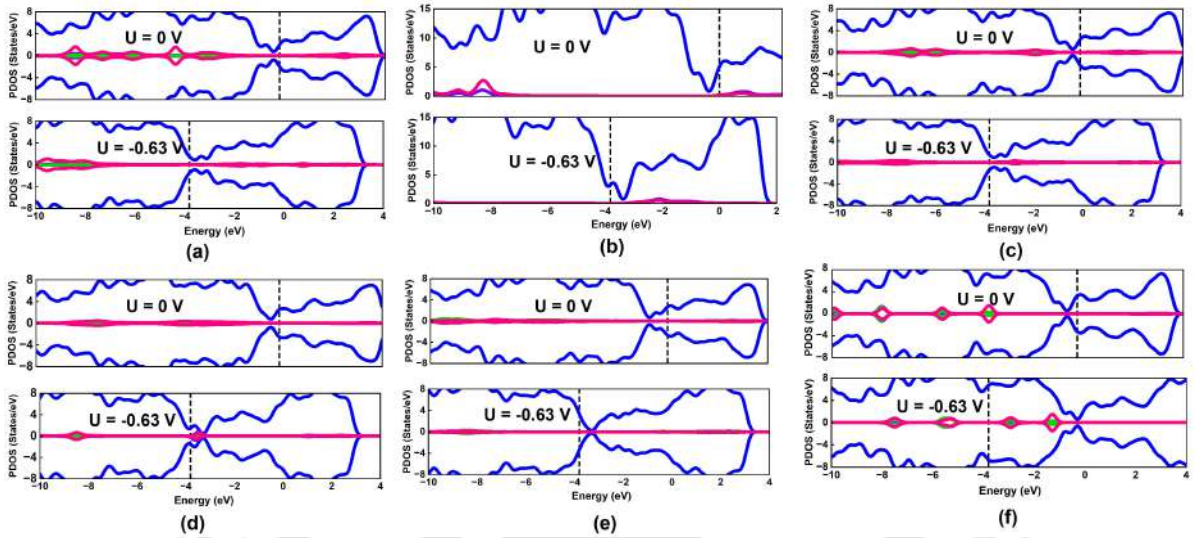

Figure 6.10: Density of states (DOS) plots of different reaction intermediate (a) *COOH, (b) *CO, (c) *CHO, (d) *CH_2O, (e) *CH_2OH, and (f) *CH_3OH applying charge neutral method (CNM) and constant potential method (CPM) (−0.63 V). Blue, pink, purple, and green colors denote the DOS of B, C, O, and H-atoms, respectively.

The electronic structures of all intermediate configurations allowed us to investigate the underlying cause of the potential effects observed. The observed ΔG_{CPM}-ΔG_{CNM} results from a significant modification of the DOS plot at the fixed potential of the intermediates. The key difference between the DOS plots generated from CNM and CPM lies in the placement of the E_F, as shown in Figure 6.10. However, in some cases, we have observed alterations in both the shape and the position of the intermediate-surface interaction in these two models. In the scenario of *COOH [Figure 6.10(a)], the interaction of the intermediate COOH at the VB region is significantly distanced from the E_F in contrast to the CHE model. In the case of the CB region, the hybridization in both instances is within 2-3 eV. The DOS of *CO displayed in Figure 6.9(b) shows that the interaction of the molecule at CNM is closer to the E_F than the fixed potential model. In contrast, for *CHO,*CH_2O, *CH_3O, and *CH_3OH [Figure 6.10(c-f)], it has been observed that the interaction of intermediates with the surface is closer to the E_F compared to the CNM model. Based on the calculated DOS, it appears that changes in electronic structures, rather than charging-induced electrostatic contact, are the primary source of the potential effects [338].

6.4 Conclusions

This work explores the CO_2 electrocatalytic reduction potential of atomic point defect bilayer borophene (BL-B-Def-1) using first-principles simulations incorporating DFT-D3 dispersion correction. The ECRR catalyzed by BL-B-Def-1 was investigated from both CNM and CPM, where the CPM gives a more realistic description of the system with the effect of applied potential on the catalyst. The CNM predicts the $^*COOH \rightarrow {}^*CO$ as a PDS with an η of 0.63 V, while the CPM found $^*CO_2 \rightarrow {}^*COOH$ as a PDS with an η of 1.0 V. Further, it was also found that the CH_4 formation required a higher η of 2.54 V, indicating the selectivity towards CH_3OH formation. Moreover, the charge-induced BL-B-Def-1 suppresses HER, along with the remarkable selectivity for separating CO_2 from mixtures with CO_2/CH_4, CO_2/H_2, and CO_2/N_2. In a nutshell, we have proposed point defects in 2D semiconducting BL-B nanosheet as a suitable charge-induced material for CO_2 selective reduction. Thus, this study provides new insight to improve our understanding of the charge state on catalytic activity and the importance of incorporating the applied potential on an electrocatalytic cycle.

Chapter 7

CONCLUSIONS

The extraction of graphene from graphite in 2004 was marked as a major breakthrough for the emergence of a new era in two-dimensional (2D) materials. Their distinctive electronic, optical, and mechanical properties, with large surface-to-volume ratios, make them promising candidates for integration into advanced energy and environmental-related applications.

In this thesis, we have explored the potential of graphene, h-B_2S_2, and bilayer borophene (BL-B) for gas sensing and catalytic applications that offer promising solutions for efficient gas detection and conversion, contributing to cleaner and more sustainable technologies. The sheet of a one-layer thin carbon atom, "Graphene," exhibited a unique linear energy-momentum relationship, resembling the behavior of massless relativistic fermions, high carrier mobilities and electrical conductivity, excellent mechanical and thermal stability, and a high surface-to-volume ratio. h-B_2S_2 is a lighter addition to the family of TMD-like 2D materials that possess tunable electronic properties and high-charge carrier mobility, making it well-suited for sensing devices. Further, the 2D BL-B, with remarkable electronic conductivity, better stability, and higher oxidation resistance than its monolayer counterpart, has the potential to exhibit excellent electrocatalytic properties.

However, pristine 2D materials with inherent properties may not fully satisfy the demands of emerging multifunctional applications. Thus, precise property tuning is crucial for optimizing their performance in advanced functional devices. The atomic thickness and huge, extensive surface area of 2D materials make them highly desirable for unparalleled control over their properties through atomic-scale structural (ASS) modification. The various ASS techniques discussed in this thesis are single vacancy defects, substitutional doping, surface functionalization, and

strain engineering. They play a crucial role in tailoring the electronic properties and the charge density over the surface of the materials and show their applicability in gas sensing devices and electrocatalysis.

Computational methodologies play a crucial role in designing high-performance gas sensors and electrocatalysts with improved sensitivity, selectivity, and efficiency. These approaches help predict material properties, reaction mechanisms, and sensor performance before experimental validation. In our work, we utilize various computational techniques, including density functional theory (DFT) with periodic boundary conditions (PBC), plane-wave basis sets, pseudo-potentials, ab initio molecular dynamics (AIMD) simulations, and the non-equilibrium Green's function (NEGF) method.

In work 1 (**Chapter 3**), we investigated the gas sensing performance of pyridinic dominance N-doped graphene (PNG). PNG contained both doping and defect, which effectively modified the zero-band gap graphene into a p-type semiconductor with good thermal stability at 300 K. The calculated adsorption energy, charge transfer, and orbital overlapping show that the PNG monolayer with two and three nitrogen doping shows good SO_2 sensing potential with high selectivity, good recovery time, and thermal stability. Furthermore, the adsorption potential of SO_2 on PNG can be strengthened or weakened by applying external strains or electric fields, which is highly desirable to control the sensing performance of the monolayers. This work is a step toward the vision of developing efficient gas sensors for the detection of toxic gas molecules in the environment.

In work 2 (**Chapter 4**), we have functionalized the h-phase boron sulfide monolayer with an oxygen atom, creating a new material called Oh-B_2S_2 nanosheet with unique structural and electrical properties. In-depth analysis of the structure, stability, and sensing potential of the newly designed Oh-B_2S_2 nanosheet was carried out through DFT, AIMD, density functional perturbation theory (DFPT), and NEGF modelling. The Oh-B_2S_2 nanosheet has an electron carrier mobility of 789.90×10^2 $cm^{-2}V^{-1}s^{-1}$, significantly higher than the mobility of the MoS_2 monolayer (200 $cm^{-2}V^{-1}s^{-1}$). The findings of our study suggest that the Oh-B_2S_2 nanosheet exhibits superior performance compared to graphene and MoS_2 in the selective sensing of NO and NO_2. The *I-V* characteristic plots provide evidence supporting the selective detection of NO

and NO_2 molecules in the presence of other toxic gases and common environmental composites. Further, the observed negative difference resistance (NDR) of the Oh-B_2S_2 nanosensor after the adsorption of gases can be elucidated through the analysis of transmission spectra plots obtained under different biases. Our research shows that future gas-sensing nanoelectronics could make use of materials similar to transition metal dichalcogenides (TMDs), which are based on lighter elements.

Work 3 (**Chapter 5**) presents the investigation of the activation of highly stable CO_2 on pristine and defect-induced bilayer borophene (BL-B) nanosheets with varying charge states using DFT calculations. Our findings reveal that the adsorption capacity of CO_2 is significantly enhanced by the addition of an extra negative charge (5.12×10^{14} e^-/cm^2) at defect-engineered BL-B. Our AIMD simulation shows the dissociation of the CO_2 molecule into CO^* and O^*, which is crucial for the further reduction of CO_2 to industrially important fuels. Furthermore, these negatively charged defect-induced BL-B exhibit strong selectivity in separating CO_2 from CH_4, H_2, and N_2 mixtures. Our findings highlight defect-induced BL-B as a highly efficient material for tunable, selective, and efficient CO_2 activation.

Following the CO_2 activation in work 4 (**Chapter 6**), we have studied the electrochemical reduction of CO_2 into C1-organic fuels such as CH_3OH and CH_4. The electrocatalytic activity of the nanosheet was studied using the charge neutral method (CNM) and constant potential method (CPM). The CPM model gives a more realistic description of a catalytic cycle by incorporating applied potential as the catalyst is charged when it exchanges electrons with the electrode to reach an equilibrium. The predicted overpotential (η) for the selective conversion of CO_2 into CH_3OH was found to be 0.63 V and 1.0 V under CNM and CPM, respectively. Thus, our results highlight the impact of the induced charge on the electrocatalytic performance of catalytic reduction, thereby offering a basis for developing new materials and approaches for catalytic activity.

In conclusion, this thesis highlights the advancements in gas-sensing and electrocatalytic performance of two-dimensional (2D) materials through strategic structural engineering. Introducing targeted surface modifications, we have successfully optimized their intrinsic properties and demonstrated their potential for practical implementation in toxic gas detection and the con-

version of toxic gases into organic fuels. Thus, this thesis is an effort toward energy and environmental sustainability, addressing global air pollution.

Comparison tables summarizing the performance of different 2D material systems reported in the literature for SO_2 detection, NO and NO_2 sensing, and CO_2 activation and reduction, alongside the results obtained in this thesis

Table 7.1: Comparison of performance of various 2D material systems for SO_2 detection with the results obtained in this thesis.

Materials	**E_{ads} (eV)**	**Q_e**	References
PNG (pysvn2 & pysvn3)	-0.51 & -0.54	-0.22 & -0.12	Our Work [206]
$MoTe_2$	-0.34	-0.15	[351]
MoS_2	-0.22	0.06	[352]
BeS_2	-0.24	-0.02	[353]
WSe_2	-0.36	-0.18	[354]

SO_2 Detection: The table clearly shows that pyridinic-dominance N-doped graphene (pysvn2 and pysvn3) exhibit superior sensing potential for SO_2 compared to many previously reported 2D monolayer materials.

Table 7.2: Comparison of performance of various 2D material systems for NO and NO_2 detection with the results obtained in this thesis.

Materials	Gas-Molecule	**E_{ads} (eV)**	**Q_e**	References
Oh-B_2S_2	NO	-0.56	0.34	Our Work [355]
	NO_2	-0.16	0.13	
MoS_2	NO	-0.03	0.02	[44]
	NO_2	-0.01	0.11	
WSe_2	NO	-0.02	0.03	[356]
	NO_2	-0.06	0.11	
Graphene	NO	-0.02	0.01	[221]
	NO_2	-0.06	0.10	

NO_2 and NO Detection: The table clearly shows that Oh$-B_2S_2$ exhibits superior sensing potential for NO and NO_2 compared to many previously reported 2D monolayer materials.

CO_2 Activation: The table reveals that defect-induced bilayer borophene requires an additional $6e^-$ for CO_2 activation, a value comparable to those reported for other 2D materials, highlighting its competitive performance.

Table 7.3: Comparison of performance of various 2D material systems for CO_2 activation with the results obtained in this thesis.

Materials	Charge-States for Activation	References
Defect-induced bilayer borophene	$6e^-$	Our Work [357]
h-BN	$1e^-$	[252]
Penta graphene	$5e^-$	[358]
BeN_4 with beryllium vacancy	$6e^-$	[278]
N-doped graphene (C site)	$6e^-$	[359]

Table 7.4: Comparison of performance of various 2D material systems for CO_2 activation with the results obtained in this thesis.

Materials	η in CHE (V)	η in CPM (V)	References
Defect-induced bilayer borophene	0.63	1	Our Work [357]
Cu (111)	0.87 & 0.85	-	[360, 361]
$Cu_3@C_2N$ (Co) and $Co_3@C_2N$	0.51-0.67 V	-	[341]
Mo_2C/N-CNT	1.1	-	[320]
$(FeO)_4$/Cu(100)	0.49	0.89	[345]

CO_2 Reduction: The table indicates that the overpotential for CO_2 reduction on defect-induced bilayer borophene is lower than that of many metal-based electrocatalysts calculated via the CHE method, and is comparable to metal-based catalysts evaluated using the CPM approach, showcasing its promising electrocatalytic efficiency.

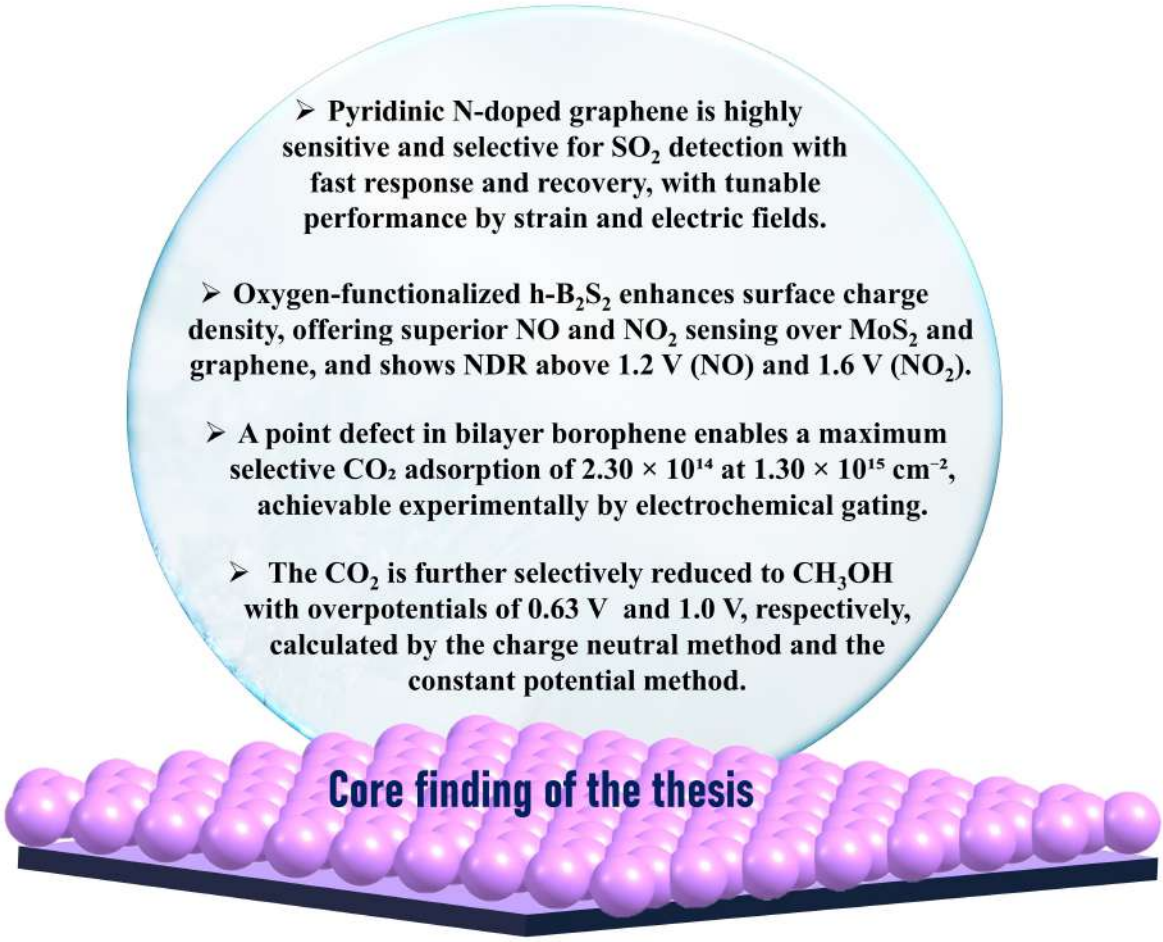

Figure 7.1: Figure presents the core finding of this thesis.

Appendix A

SUPPORTING DATA

Equation A1: Equation for defect formation energy (E_f) [362]

$$E_f = \frac{E_d - x\mu_c - y\mu_n}{x+y} \tag{A.1}$$

This is the equation of defect formation energy (E_f). Here, E_d is the energy of the doped system, x is the number of C-atoms, and y is the number of N-atoms. μ_c and μ_n are the chemical potentials of C and N-atoms taken as the total energy of graphene per C-atom and half of the energy of the nitrogen molecule, respectively.

Equation A2: Equation for the cohesive energies (E_{coh}) [228]

$$E_{coh} = \frac{(xE_c + yE_n) - E_{tot}}{x+y} \tag{A.2}$$

x and y are the total numbers of C and N atoms in the system. E_{tot} is the energy of the system. E_c and E_n are the energies of the isolated C and N atoms, respectively.

Equation A3: Equation for charge density difference under applied electric field ($\Delta\rho_{elec}$).

$$\Delta\rho_{elec} = \rho^{PNG}_{UnderEF} - \rho^{PNG} \tag{A.3}$$

where $\rho^{PNG}_{UnderEF}$ is the charge density under electric field and ρ^{PNG} is without electric field [178].

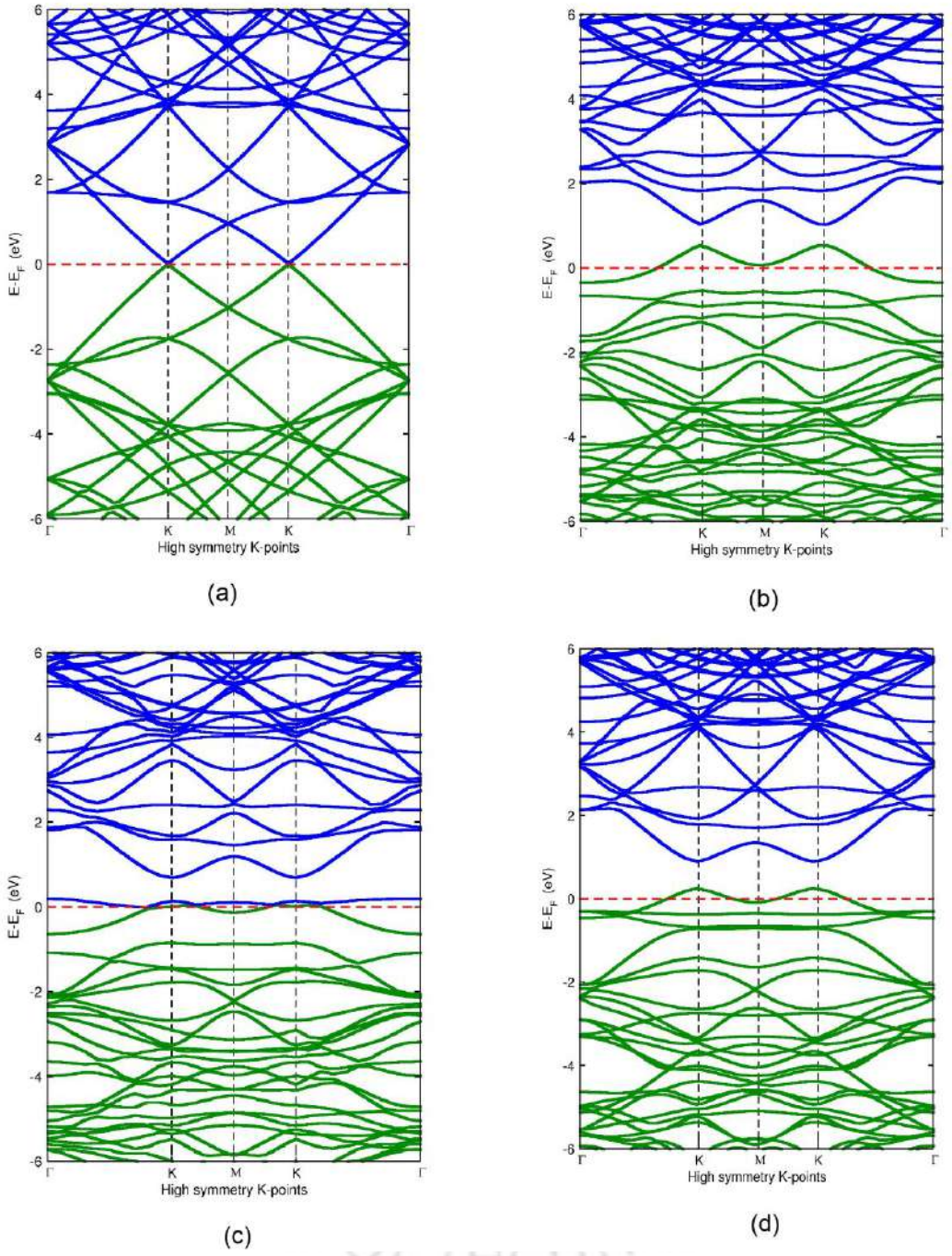

Figure A.1: Band structure of (a) pristine graphene, (b) pysvn1, (c) pysvn2, and (d) pysvn3.

Table A.1: Computed bandgap (E_g), work function (ϕ), and doping effect of PG and PNG monolayers.

System	E_g (eV)	ϕ (eV)	Doping effect
PG	0	4.29	Zero band gap
pysvn1	0.46	4.79	p-type
pysvn2	0.14	4.55	p-type
pysvn3	0.64	4.77	p-type

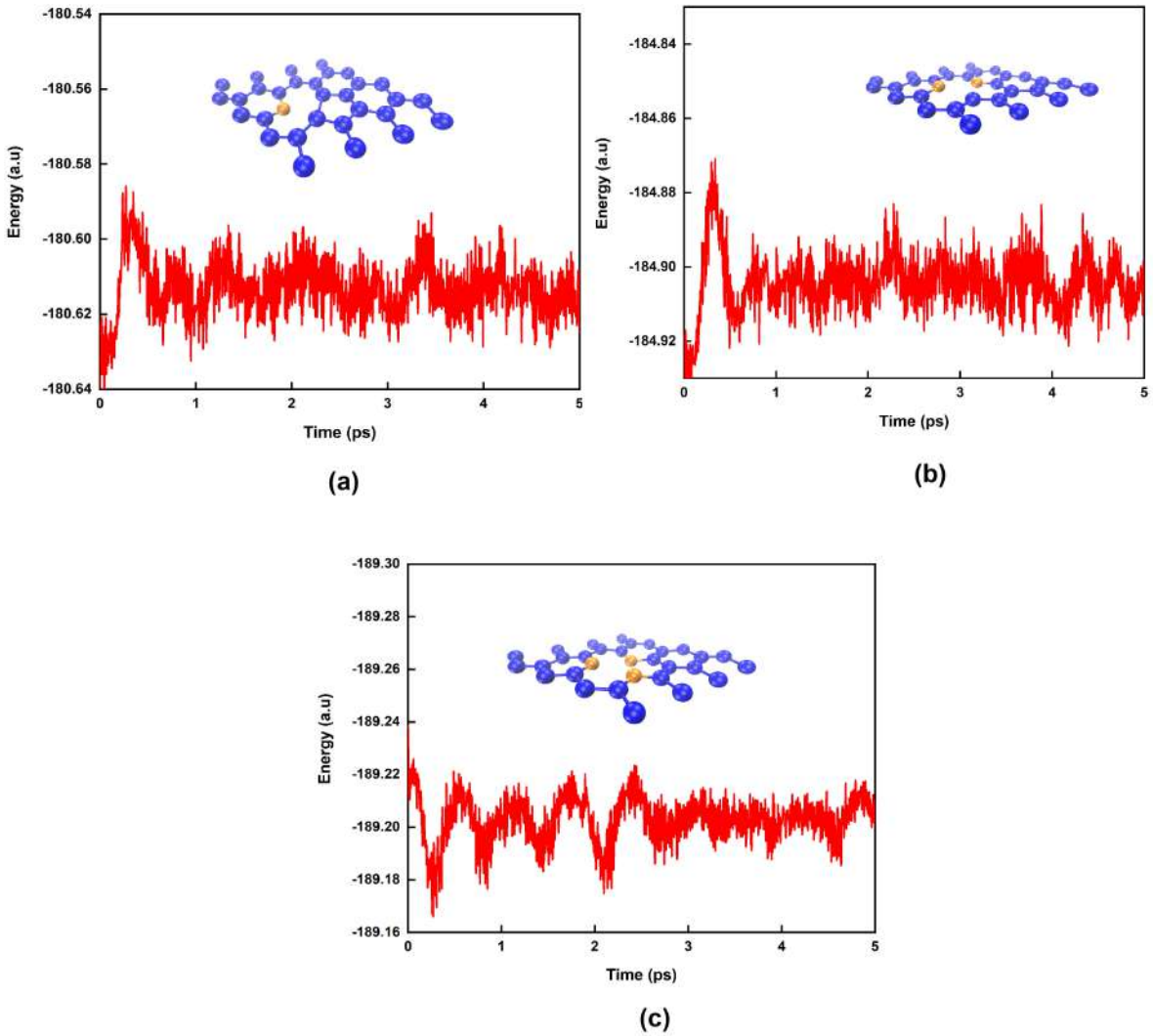

Figure A.2: Snapshots after 5 ps and AIMD plots (a) pysvn1, (b) pysvn2, and (c) pysvn3 at T = 300 K.

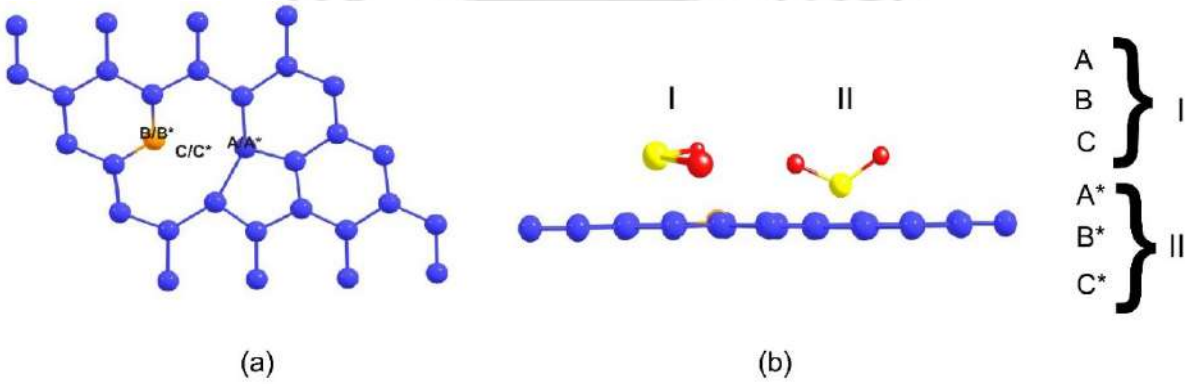

Figure A.3: Schematic representation of possible adsorption (a) sites (through C, through N, and through vacancy) and (b) orientation (horizontal and vertical) of the gas molecules.

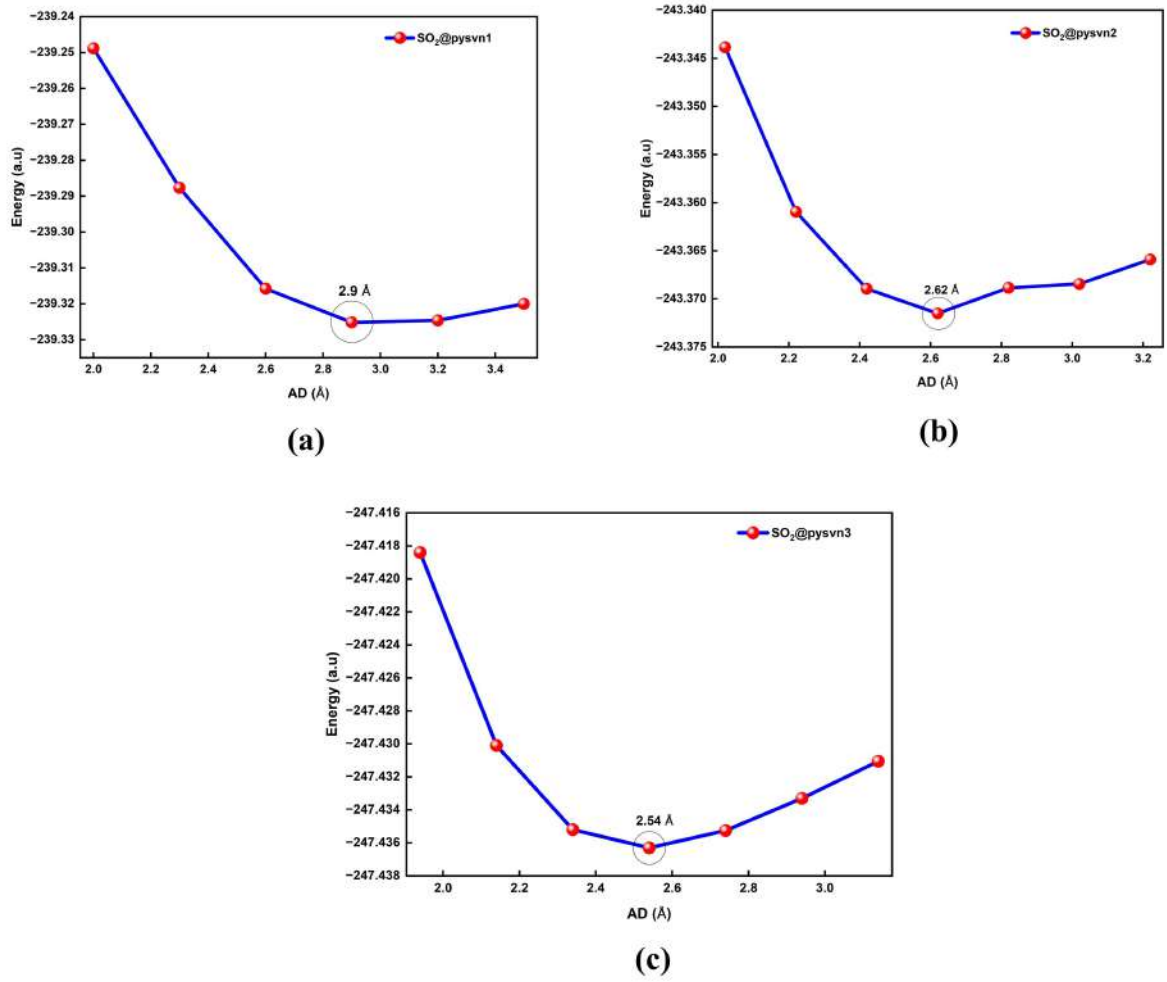

Figure A.4: The potential energy curve for SO_2 molecules on the PNG monolayers. (a) pysvn1, (b) pysvn2, and (c) pysvn3.

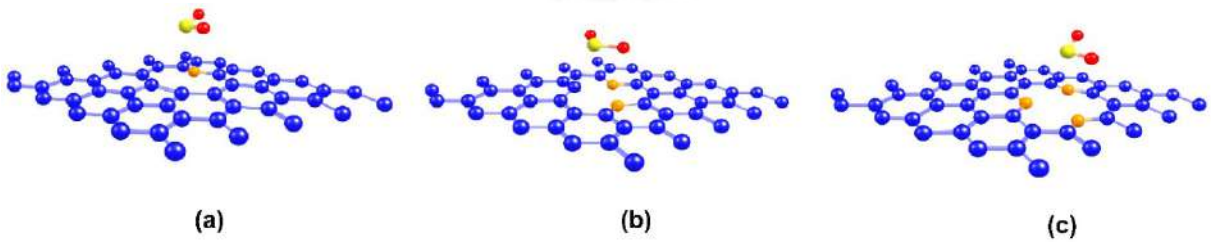

Figure A.5: Most preferable adsorption configuration of SO_2 adsorbed on 5×5 supercell of (a) pysvn1, (b) pysvn2, and (c) pysvn3 monolayers.

Table A.2: Computed adsorption energy (E_{ads}) and charge transfer (Q_e) value of SO_2 adsorbed on 4×4 and 5×5 supercells of PNG monolayers.

System	Supercell size	E_{ads} (eV)	Q_e
pysvn1	4×4	−0.39	-0.11
	5×5	−0.39	-0.11
pysvn2	4×4	−0.51	-0.22
	5×5	−0.54	-0.22
pysvn3	4×4	−0.54	-0.12
	5×5	−0.56	-0.13

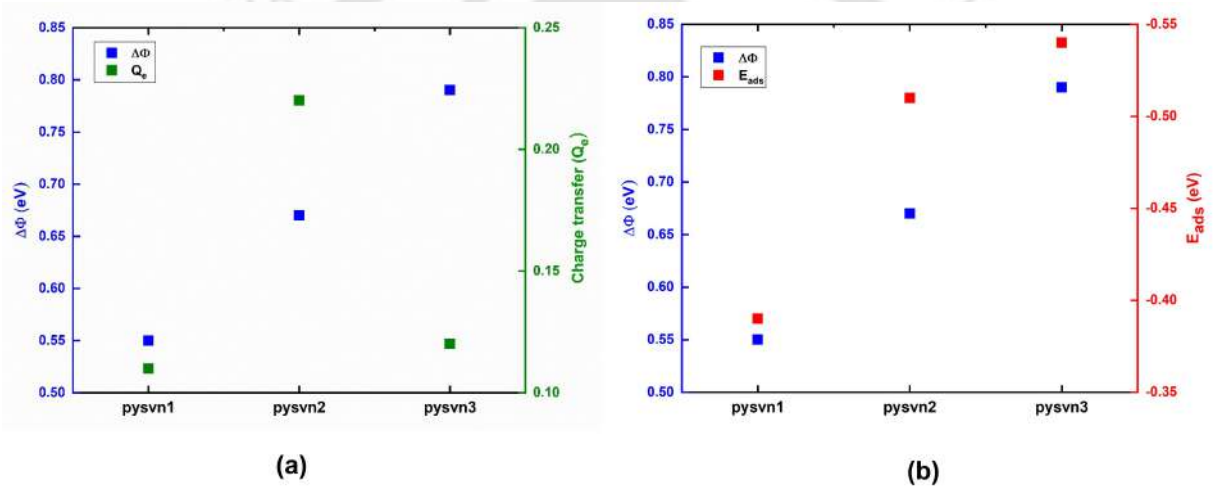

Figure A.6: Correlation plot between (a) work function (ϕ) and charge transfer value (Q_e) (b) work function (ϕ) and adsorption energy (E_{ads}).

Table A.3: Energies of non-magnetic and magnetic (at various initial magnetization values) solutions.

Specification	**Energies (Ry)**	**Total Magnetization (μ_B)**
Non-magnetic	-486.7433	-
Magnetic (0.1)	-486.7433	0.07
Magnetic (0.2)	-486.7433	0.07
Magnetic (0.3)	-486.7433	0.07
Magnetic (0.4)	-486.7433	0.07
Magnetic (0.5)	-486.7433	0.07

Table A.4: Adsorption energy (E_{ads}) and charge transfer (Q_e) values for SO_2, CO_2, H_2O, N_2, and O_2 on PNG monolayers are presented. Negative and positive Q_e values indicate the electron-accepting and electron-donating nature of the gas molecules, respectively.

System	Gas Molecules	E_{ads} (eV)	Q_e
pysvn1	SO_2	−0.39	-0.11
	CO_2	−0.17	-0.014
	N_2O	−0.23	-0.019
	N_2	−0.12	-0.07
	O_2	−0.04	-0.024
pysvn2	SO_2	−0.51	-0.22
	CO_2	−0.21	-0.016
	N_2O	−0.01	-0.02
	N_2	−0.009	-0.005
	O_2	−0.04	-0.006
pysvn3	SO_2	−0.54	-0.12
	CO_2	−0.27	-0.016
	N_2O	−0.43	-0.028
	N_2	−0.16	-0.007
	O_2	−0.08	-0.028

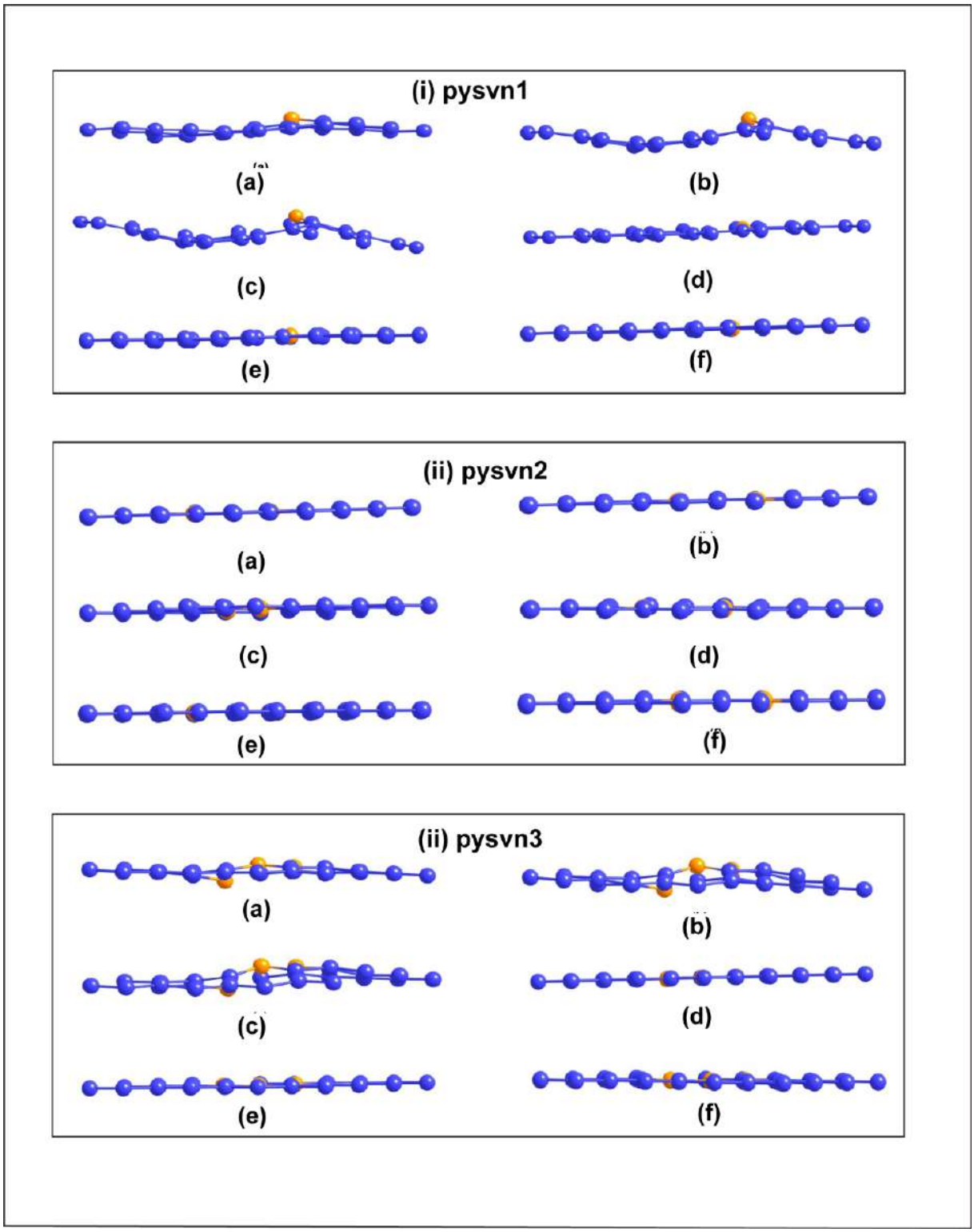

Figure A.7: Structures of (i) pysvn1, (ii) pysvn2, and (iii) pysvn3 after applying biaxial strain (a) compression strain (-1 %), (b) compression strain (-2%), (c) compression strain (-3%), (d) tensile strain (1%), (e) tensile strain (2%), and (f) tensile strain (3%), respectively.

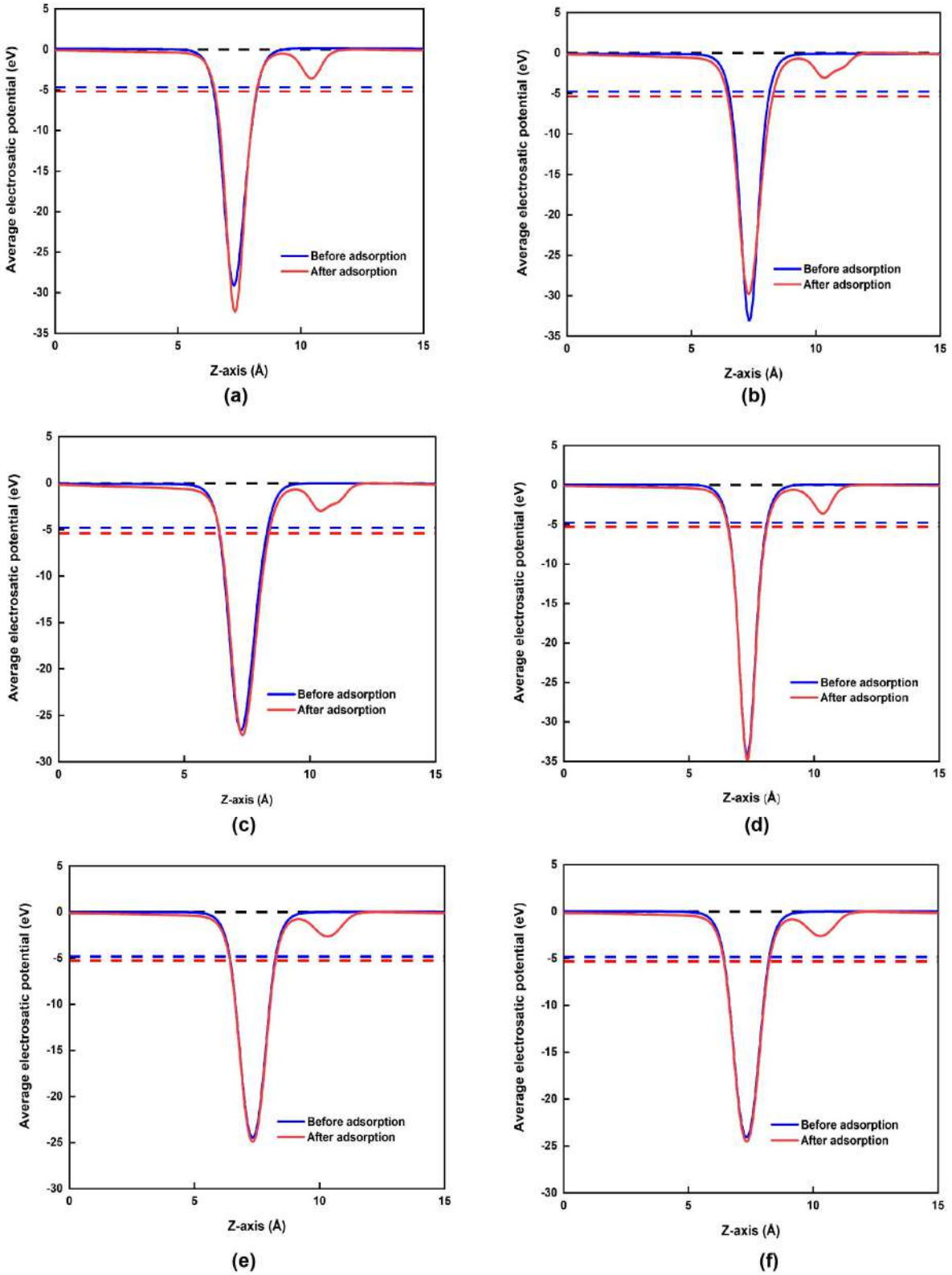

Figure A.8: Average electrostatic potential plots of pysvn1 after applying biaxial strain (a) compression strain (-1%), (b) compression strain (-2%), (c) compression strain (-3%), (d) tensile strain (1%), (e) tensile strain (2%), and (f) tensile strain (3%), respectively. The vacuum level is set to zero.

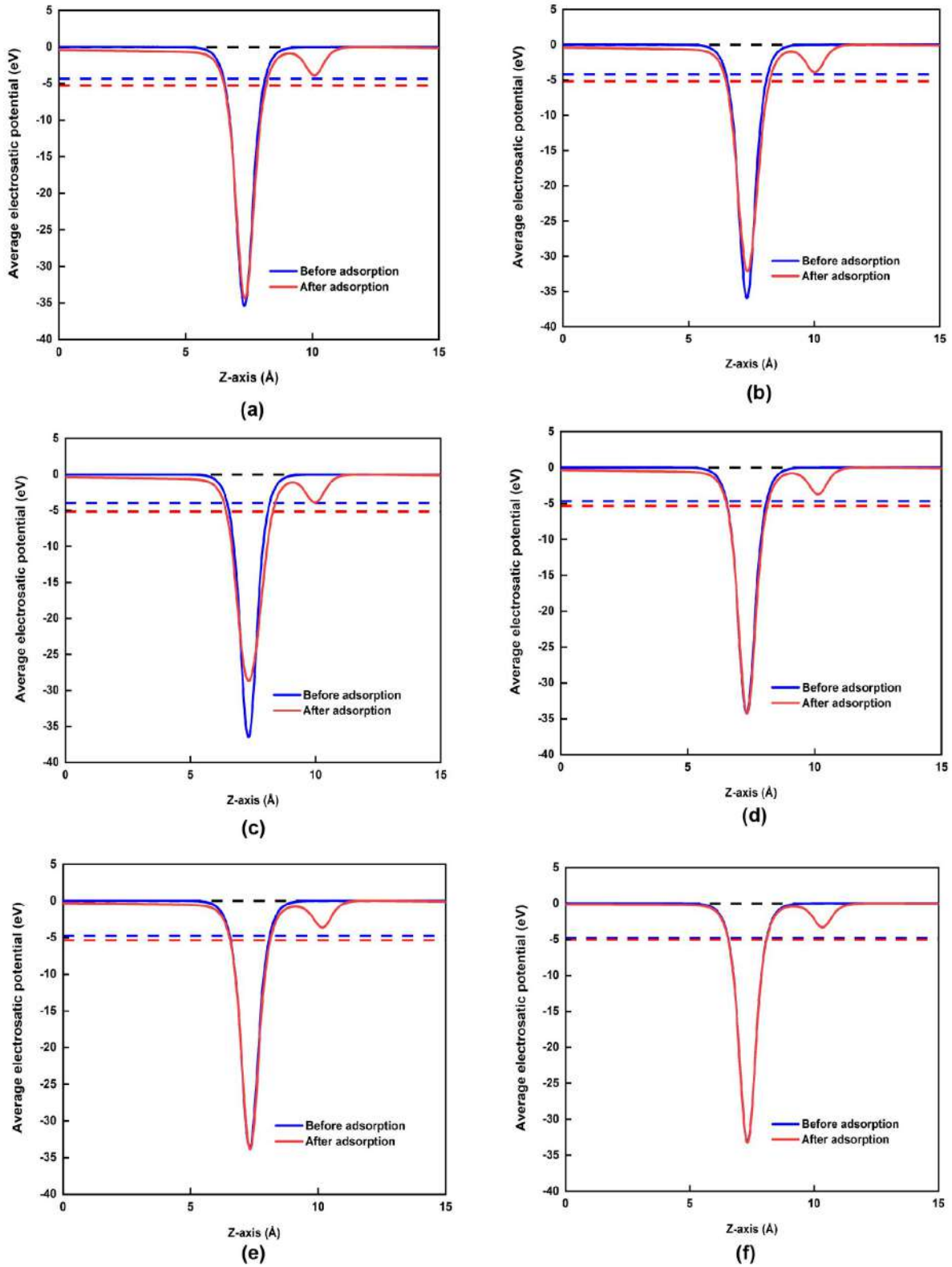

Figure A.9: Average electrostatic potential plots of pysvn2 after applying biaxial strain (a) compression strain (-1%), (b) compression strain (-2%), (c) compression strain (-3%), (d) tensile strain (1%), (e) tensile strain (2%), and (f) tensile strain (3%), respectively. The vacuum level is set to zero.

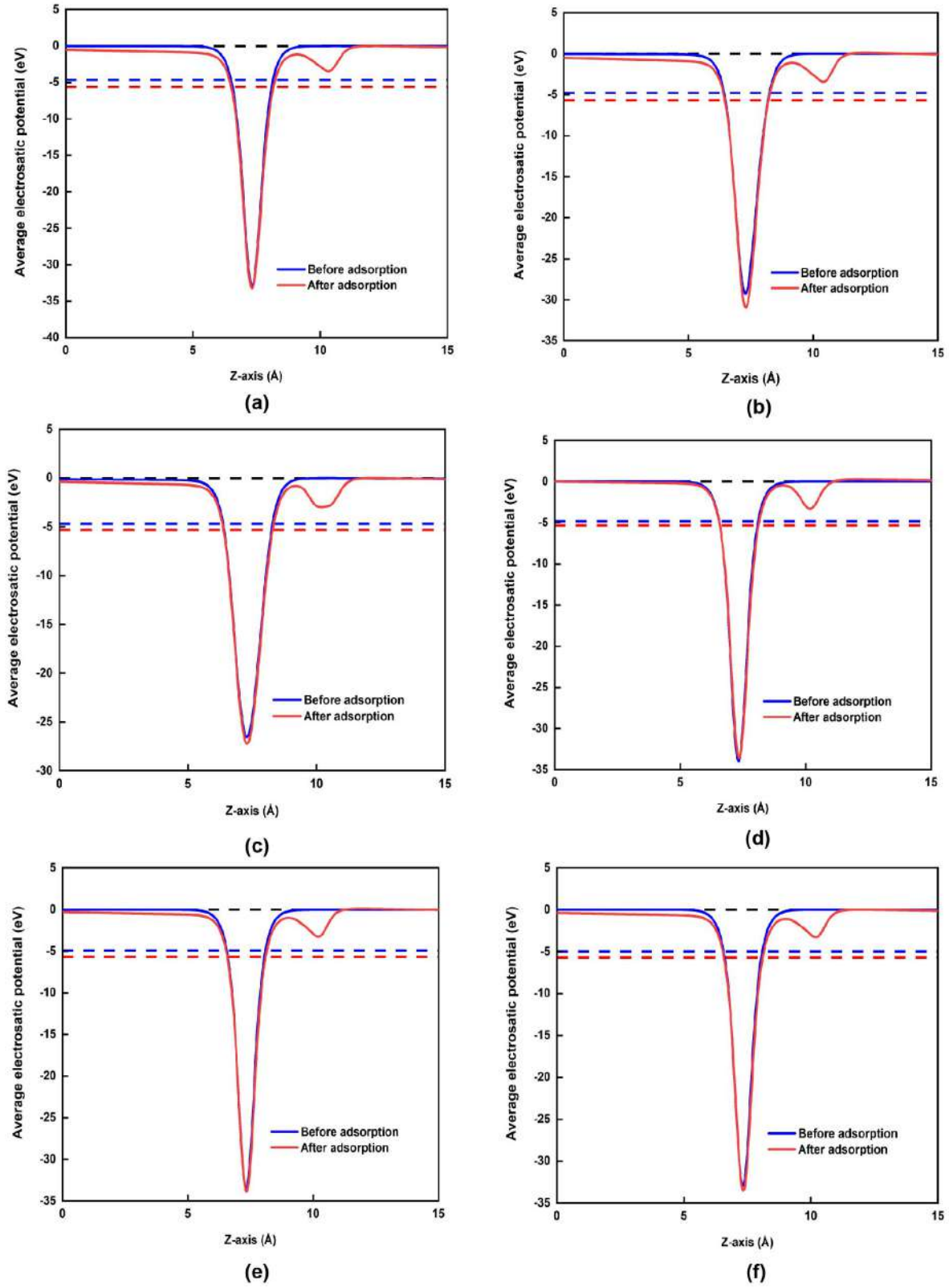

Figure A.10: Average electrostatic potential plots of pysvn3 after applying biaxial strain (a) compression strain (-1%), (b) compression strain (-2%), (c) compression strain (-3%), (d) tensile strain (1%), (e) tensile strain (2%), and (f) tensile strain (3%), respectively. The vacuum level is set to zero.

Appendix B

SUPPORTING DATA

Equation B1: Calculation of binding energy (E_b) [12]

$$E_b = E_{Oh-B_2S_2} - E_{h-B_2S_2} - E_O \tag{B.1}$$

$E_{Oh-B_2S_2}$, $E_{h-B_2S_2}$, and E_O indicates the total energy of oxygen functionalized h-B_2S_2, h-B_2S_2 and O-atom.

Equation B2: Equation for the cohesive energies (E_{coh}) [228]

$$E_{coh} = \frac{(2E_B + 2E_S + E_O) - E_{Oh-B_2S_2}}{5} \tag{B.2}$$

E_B, E_S, and E_O are the energies of individual B-atom, S-atom, and O-atom, respectively. and $E_{Oh-B_2S_2}$ is the energy of the oxygen functionalized h-B_2S_2 monolayer.

Table B.1: Binding energy (E_b) and S-O bond length of OT-B_2S_2 monolayer were calculated using the PBE-GGA functional.

Parameters	Calculated (Our Result)	Reported (Previous work) [12]
Binding Energy (eV)	−4.42	−4.01
S-O bond length (Å)	1.47	1.48

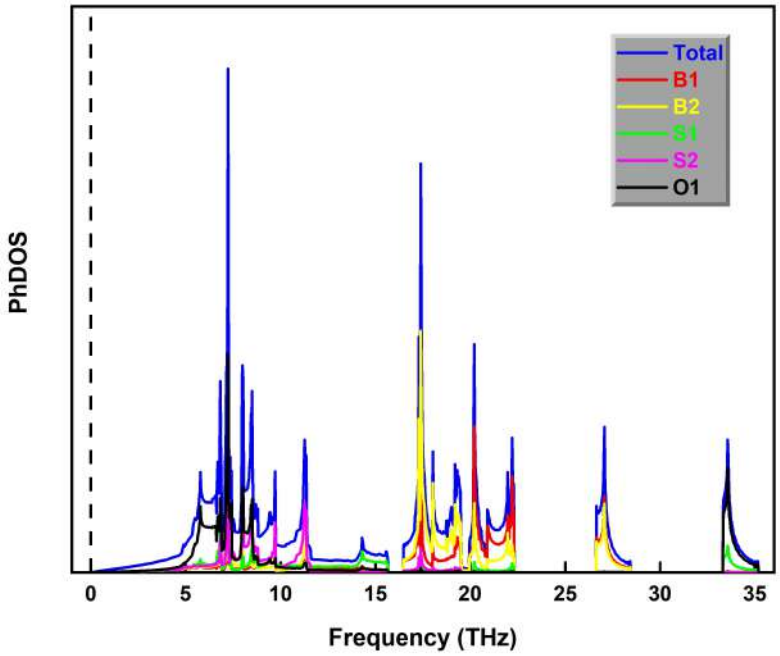

Figure B.1: Projected density of phonon states (PhDOS) plot of Oh-B_2S_2 monolayer.

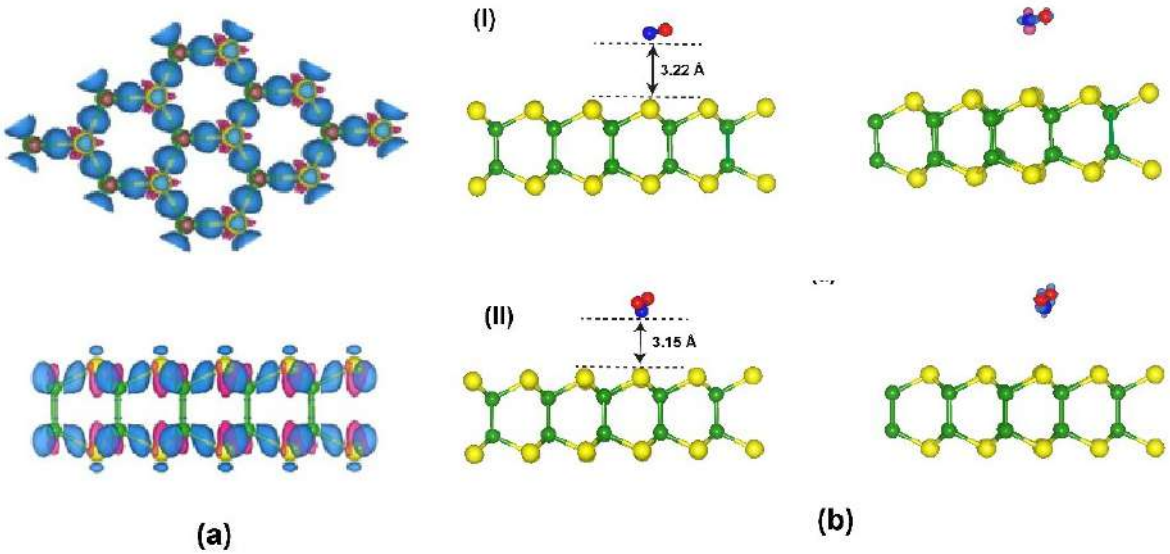

Figure B.2: (a) Charge density difference (CDD) plot of h-B_2S_2 monolayer (blue and pink colors indicate the charge accumulation and depletion region, respectively) and (b) most preferable adsorption configuration and CDD plots of (I) NO and (II) NO_2 adsorbed h-B_2S_2 monolayer.

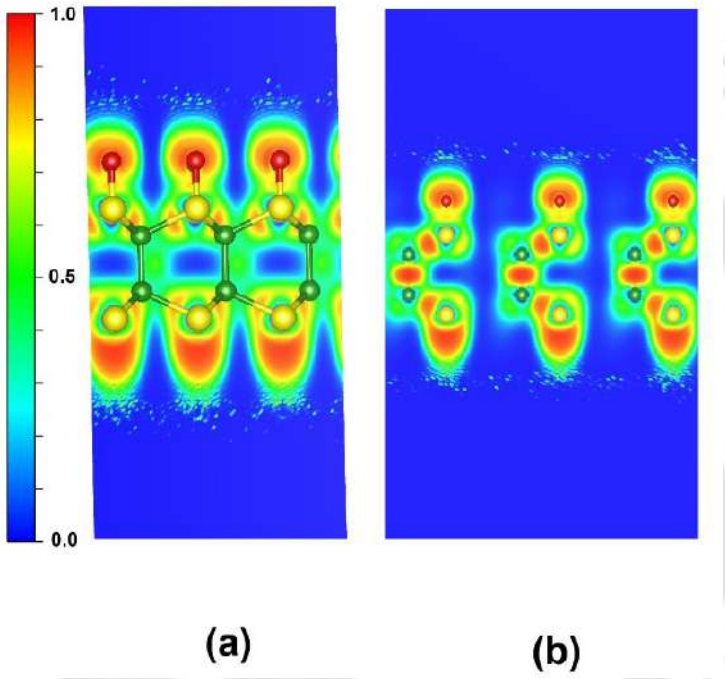

Figure B.3: Electron localization functions of oxygen functionalized h-B_2S_2 (Oh-B_2S_2) monolayer. ELF=1.0 (red color) indicates complete localization of electrons, while ELF=0.5 (green color) indicates delocalization. (a) 100-plane and (b) 110-plane.

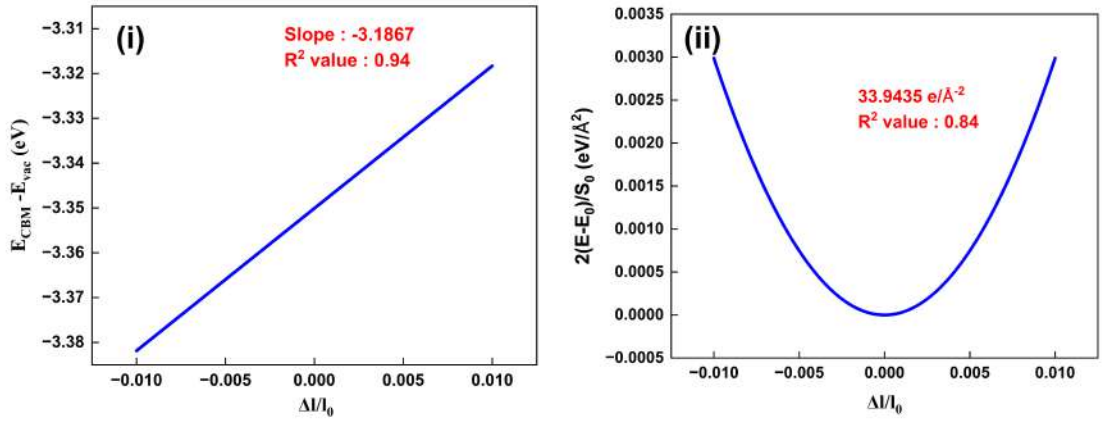

(a) (i) Linear fitting of deformation potential and (ii) curve fitting of elastic modulus of h-B_2S_2 monolayer. **Electron mobility:** μ(K-Γ): 1152.25 $\times$ 10^2 cm^2 V^{-1} s^{-1} **(Calculated)**, μ(K-Γ): 1211.67 $\times$ 10^2 cm^2 V^{-1} s^{-1} **(Reported)**.

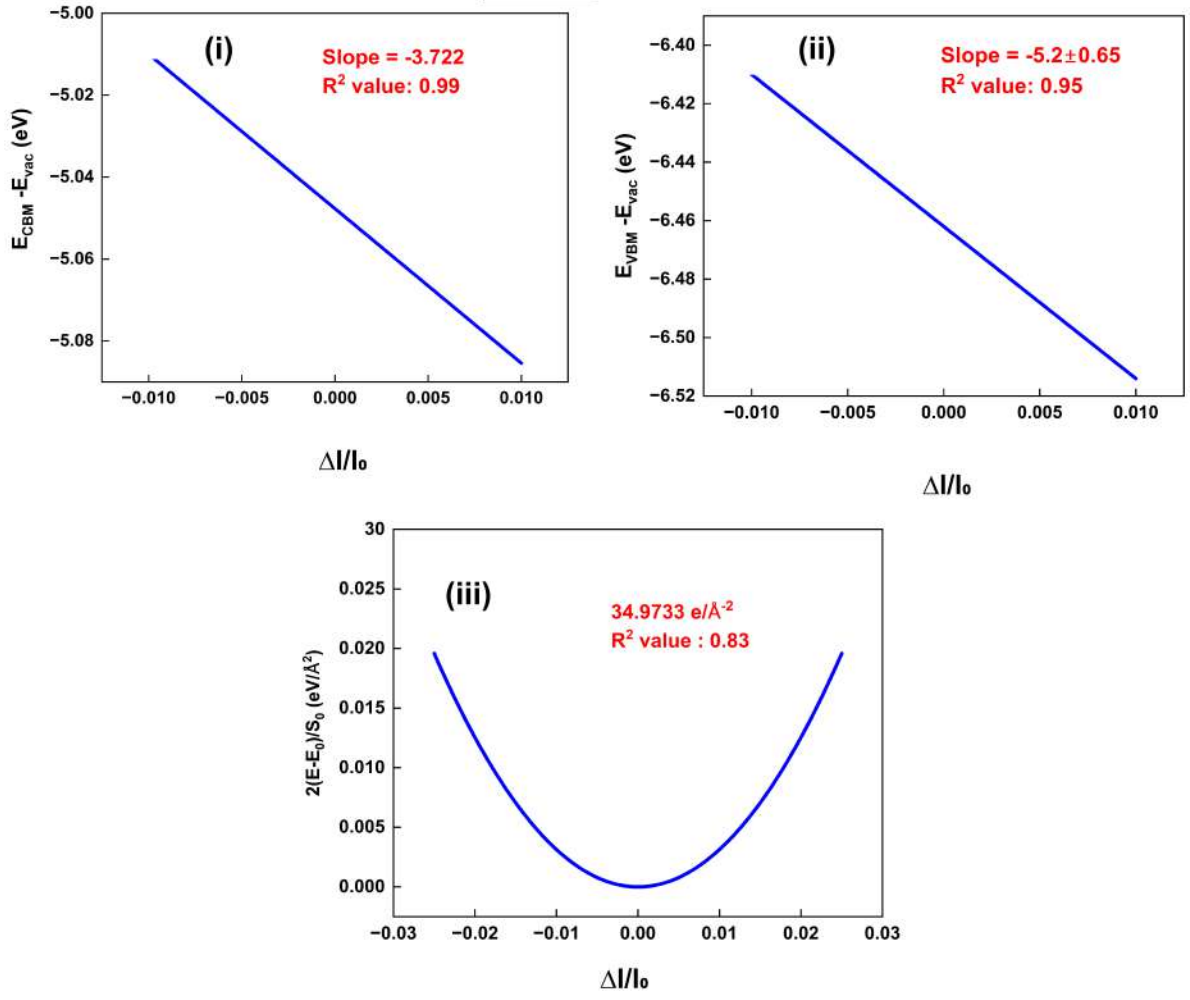

(b) Linear fitting of deformation potential for the electron, (b) Linear fitting of deformation potential for the hole, and (c) curve fitting of elastic modulus of Oh-B_2S_2 monolayer.
Electron mobility: μ(K-Γ): 790 $\times$ 10^2 cm^2 V^{-1} s^{-1}, **Hole mobility**, μ(K-Γ): 32 $\times$ 10^2 cm^2 V^{-1} s^{-1} [**Calculated**]

.

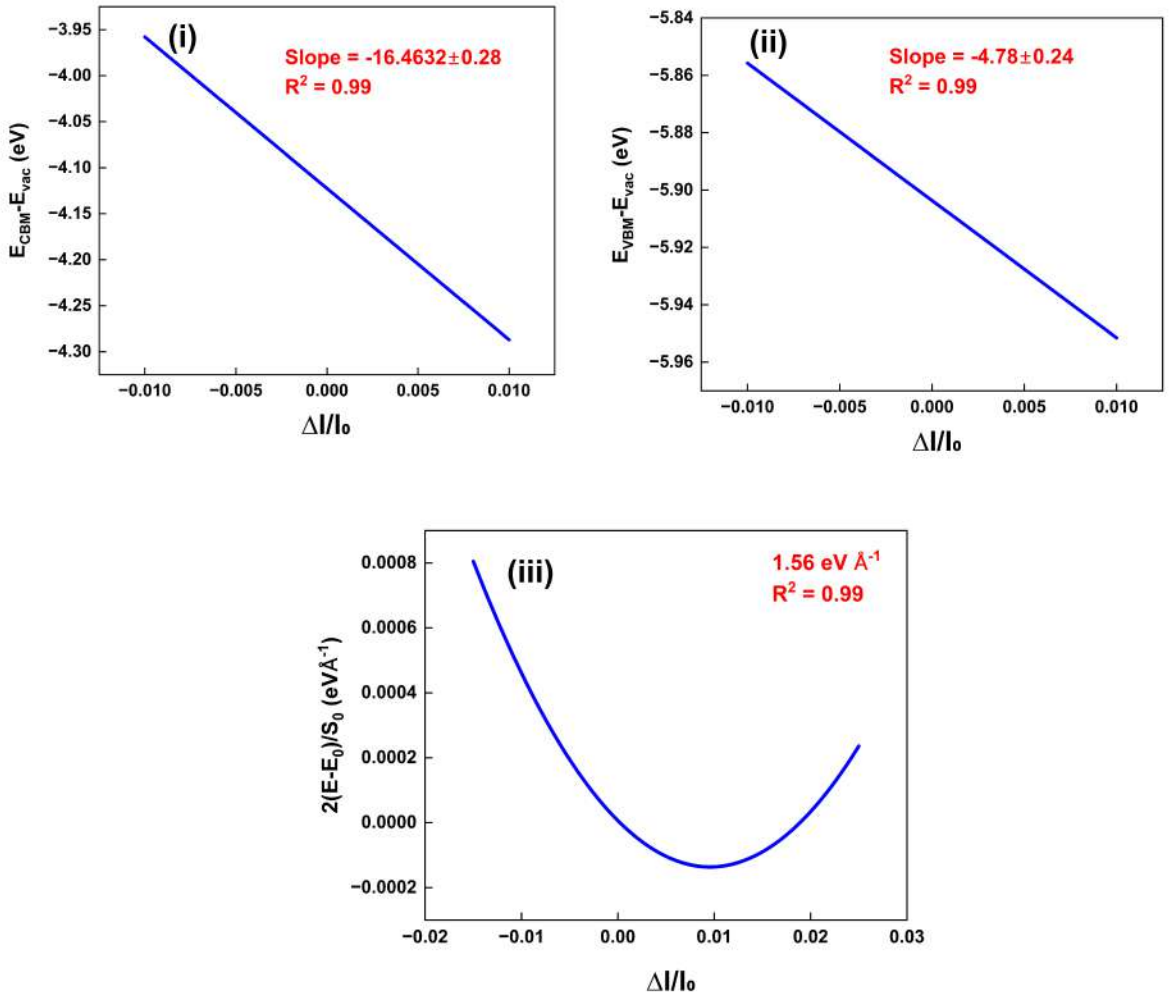

(c) Linear fitting of deformation potential for the electron, (b) Linear fitting of deformation potential for the hole, and (c) curve fitting of elastic modulus of MoS_2 monolayer.
Electron mobility: μ(K-M): 280 $cm^2\ V^{-1}\ s^{-1}$, **Hole mobility**, μ(K-M): 161 $cm^2\ V^{-1}\ s^{-1}$ [**Calculated**]
.

Figure B.4: Linear fitting deformation potential and curve fitting elastic modulus plots of h-B_2S_2, Oh-B_2S_2, and MoS_2.
[For curve fitting, we have used the quadratic equation $y = Ax^2$.]

Table B.2: Comparison of Effective mass, Deformation potential, and Elastic modulus (J m^{-2}).

Systems	**Effective mass (in the unit of m_0)**		**Deformation potential**		**Elastic modulus**
	electron	**hole**	**electron**	**hole**	
MoS_2	0.45 (Reported) [363] 0.31 (Calculated)	0.62 (Reported) [363] 0.43 (Calculated)	16.46	4.78	246.60
Oh-B_2S_2	0.11	0.31	3.72	5.2	559.15

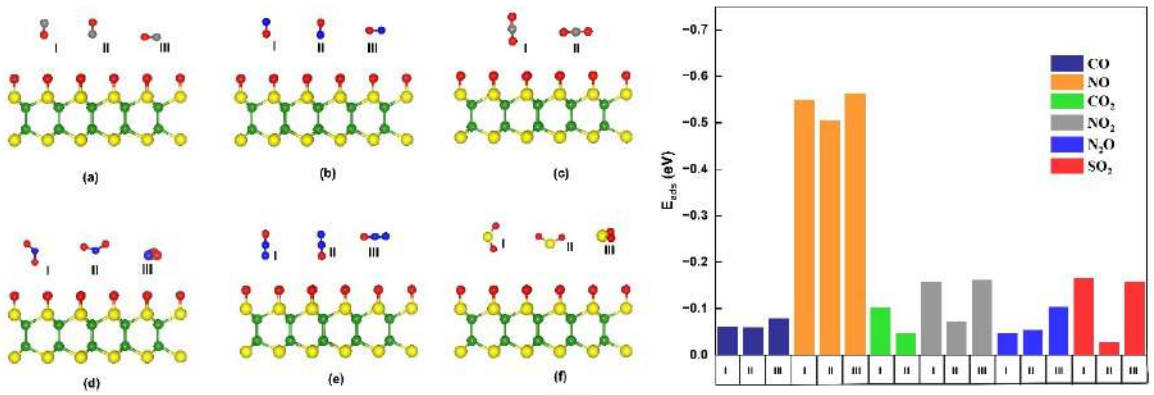

Figure B.5: Different orientations of (a) CO, (b) NO, (c) CO_2, (d) NO_2, (e) N_2O, and (f) SO_2 molecules on Oh-B_2S_2 monolayer.

Table B.3: Results obtained from spin-polarized density functional theory (SPDFT).

Molecule/Supercell	**E_{ads} (eV)**	**AD (Å)**	**Q_e**
NO	-0.50	2.45	0.29
NO_2	-0.12	2.67	0.11

Table B.4: Adsorption energies (E_{ads}), adsorption distances (AD), and charge transfer (Q_e) values of NO and NO_2-adsorbed Oh-B_2S_2 monolayer for 4× 4 and 5× 5 supercells.

Molecule/Supercell	***E_{ads} (eV)***	**AD (Å)**	**Q_e**
NO (3×3)	-0.56	2.45	0.34
NO (4×4)	-0.57	2.45	0.34
NO (5×5)	-0.60	2.46	0.33
NO (3×3)	-0.16	2.65	0.13
NO_2 (4×4)	-0.17	2.65	0.15
NO_2 (5×5)	-0.17	2.67	0.14

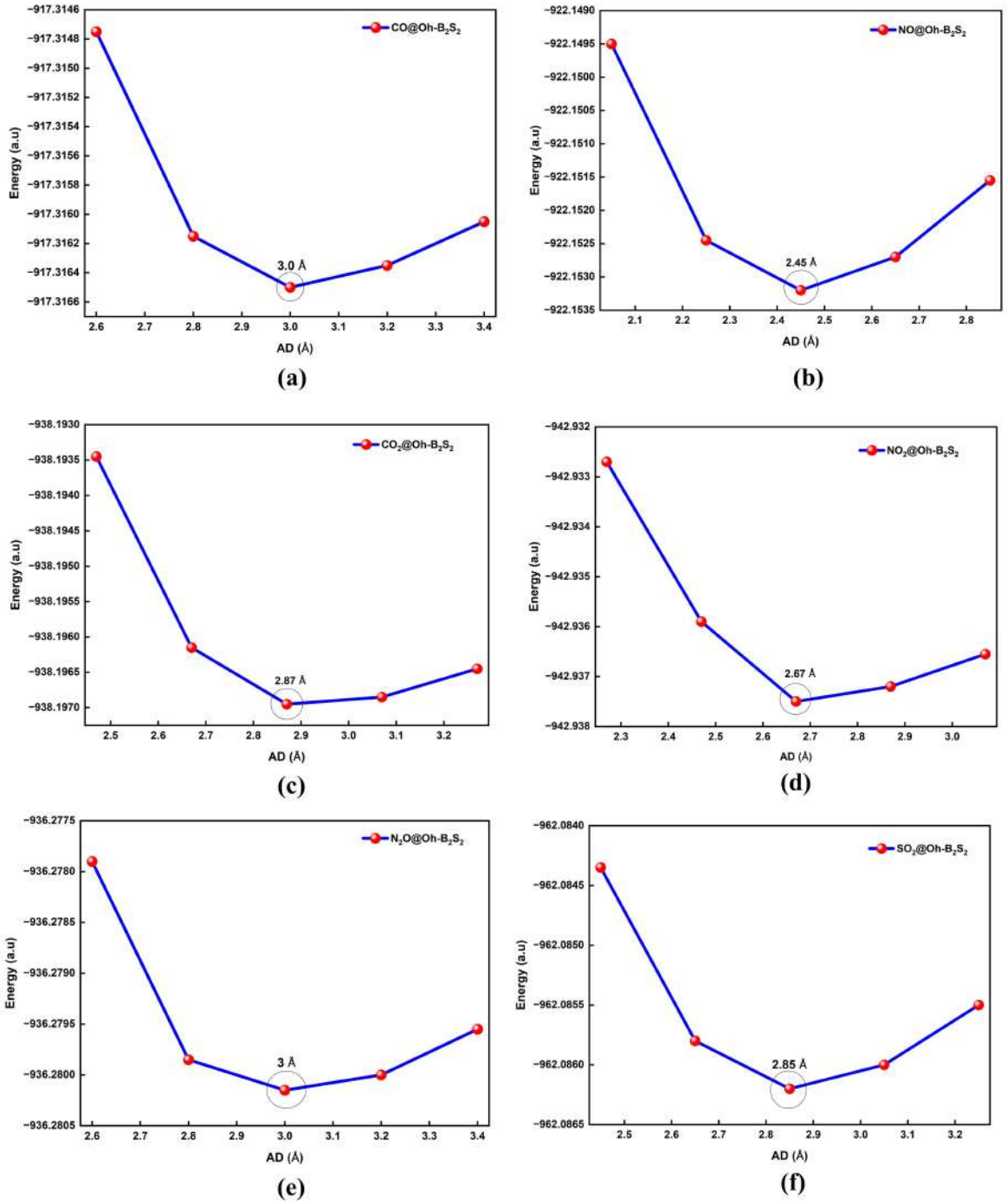

Figure B.6: Potential energy curves (PECs) of (a) CO, (b) NO, (c) CO_2, (d) NO_2, (e) N_2O, and (f) SO_2 molecules on Oh-B_2S_2 monolayer.

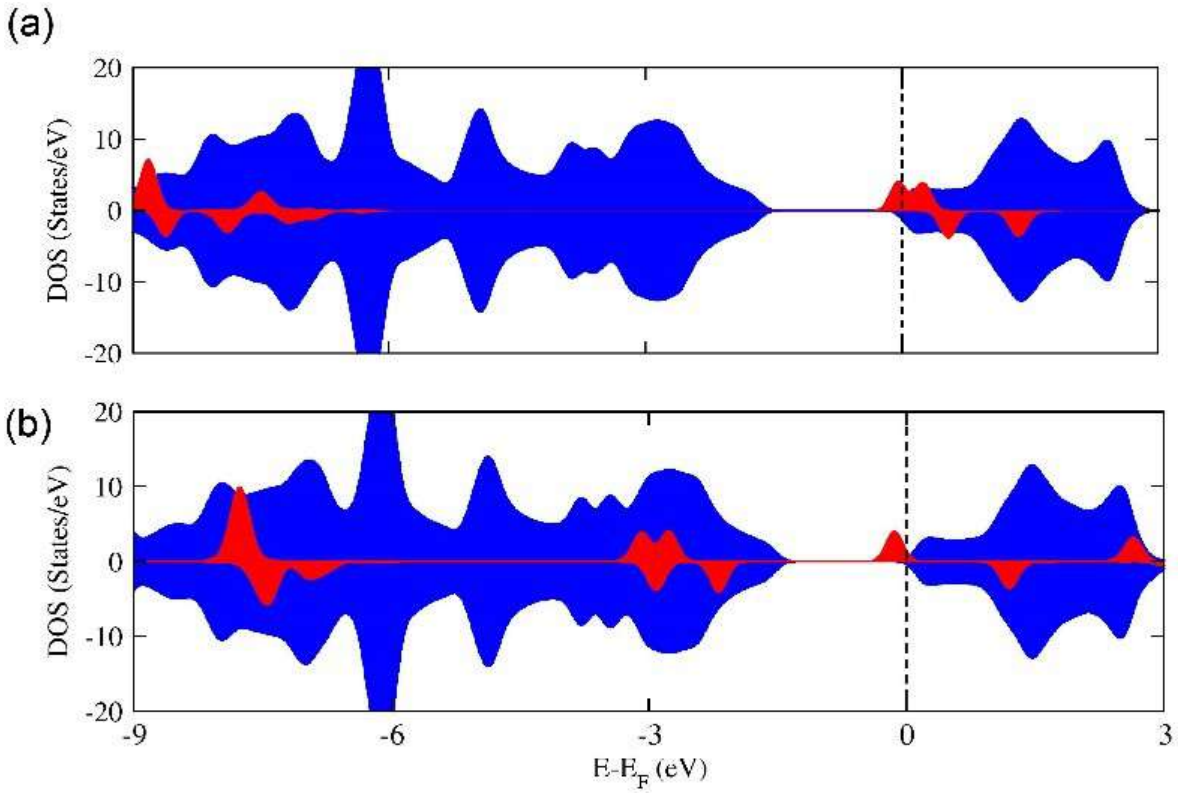

Figure B.7: Spin-polarized density of states (SPDOS) (a) NO and (b) NO_2 -adsorbed Oh-B_2S_2 monolayer. Blue and red are the density of states (DOS) of Oh-B_2S_2 monolayer and gas molecules, respectively.

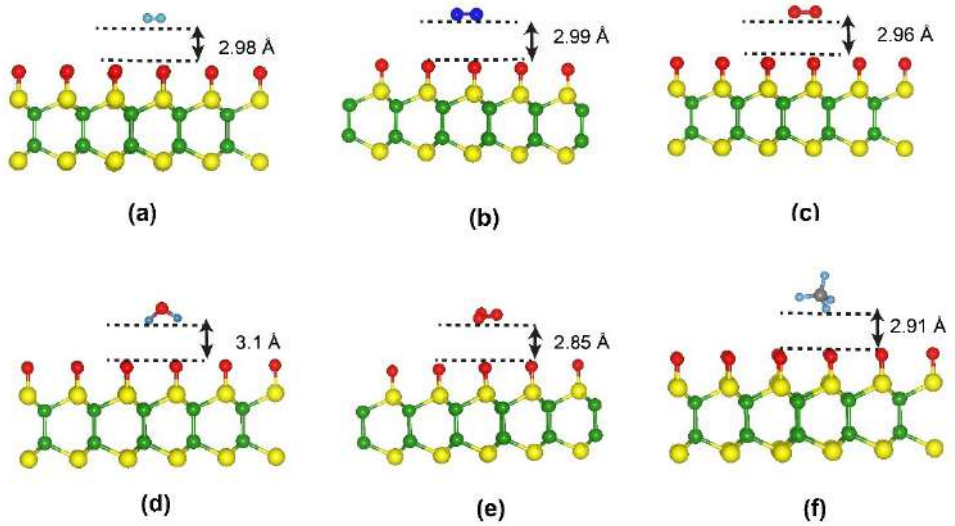

Figure B.8: The optimized geometries associated with the favorable adsorption configuration for (a) H_2, (b) N_2, (c) O_2, (d) H_2O, (e) O_3, and (f) CH_4 on the Oh-B_2S_2 monolayer.

Table B.5: Adsorption energies (E_{ads}) and charge transfer (Q_e) for different gas molecules in various orientations.

Gas Molecule	Orientation	E_{ads} (eV)	Q_e
NO	Parallel	-0.56	0.34
	Through N	-0.50	-
	Through O	-0.54	-
NO_2	Parallel	-0.16	0.13
	Through N	-0.08	-
	Through O	-0.15	-
H_2	Parallel	-0.03	0.004
	Perpendicular	-0.03	-
N_2	Parallel	-0.07	0.007
	Perpendicular	-0.05	-
O_2	Parallel	-0.09	0.08
	Perpendicular	-0.07	-
H_2O	Parallel	-0.12	0.05
	Through O	-0.11	-
	Through H	-0.08	-
O_3	Parallel	-0.10	0.02
	Perpendicular	-0.06	-
CH_4	Parallel	-0.10	0.02
	Perpendicular	-0.10	-

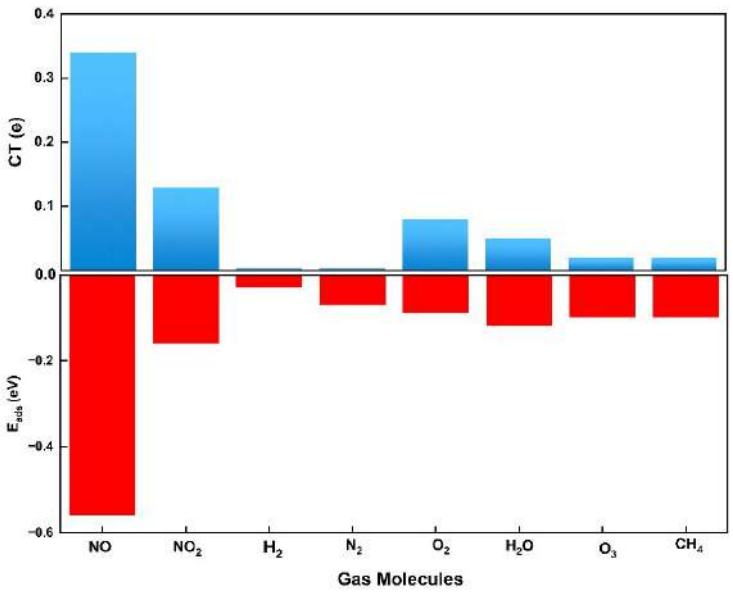

Figure B.9: Adsorption energies (E_{ads}) and charge transfer (Q_e) plots of NO, NO_2, H_2, N_2, O_2, H_2O, O_3, and CH_4 on Oh-B_2S_2 monolayer.

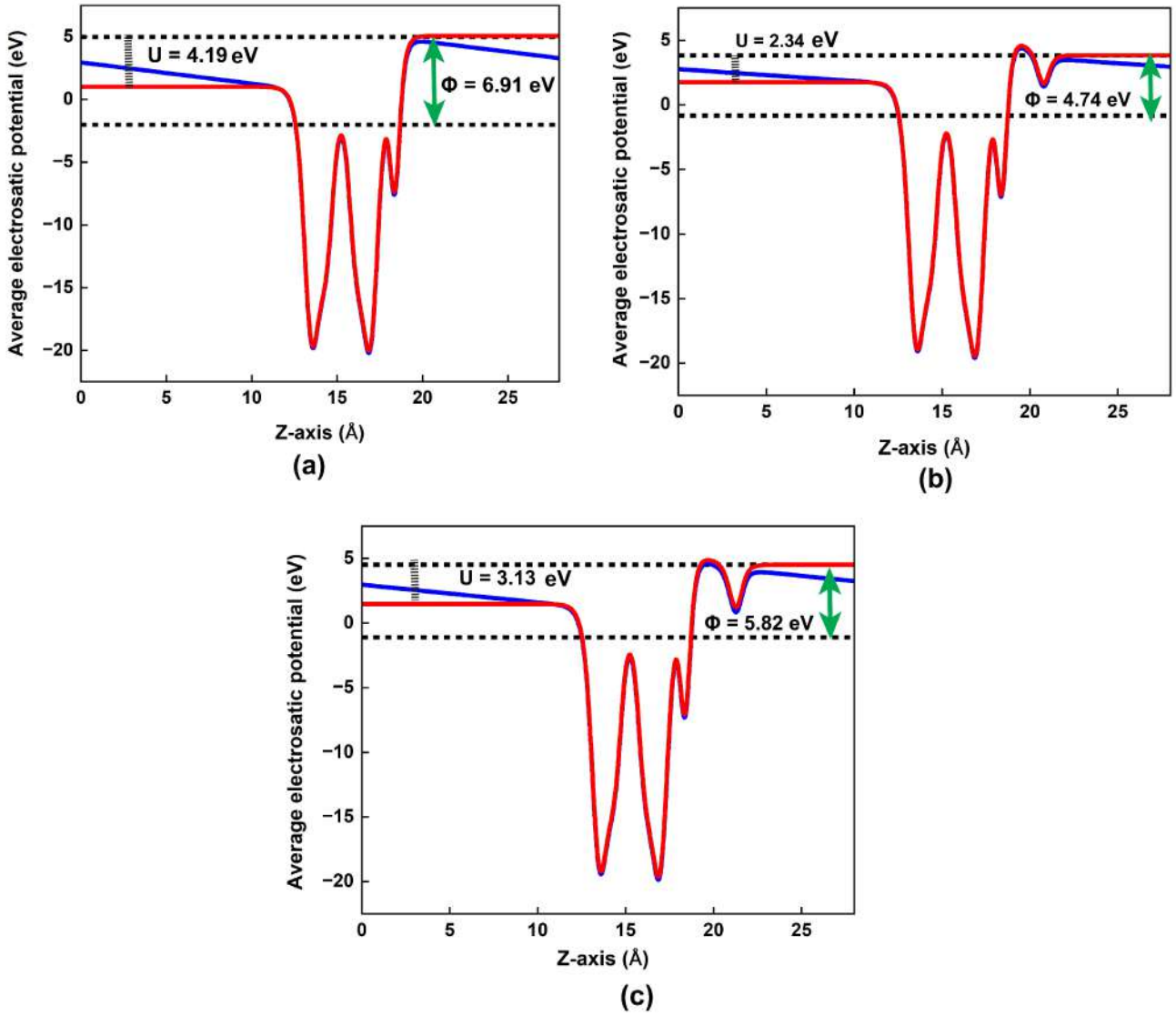

Figure B.10: Average electrostatic potential plots of (a) Oh-B_2S_2, (b) NO-adsorbed Oh-B_2S_2, and (c) NO_2-adsorbed Oh-B_2S_2 monolayers. The blue and red curves represent the results without and with dipole correction, respectively.

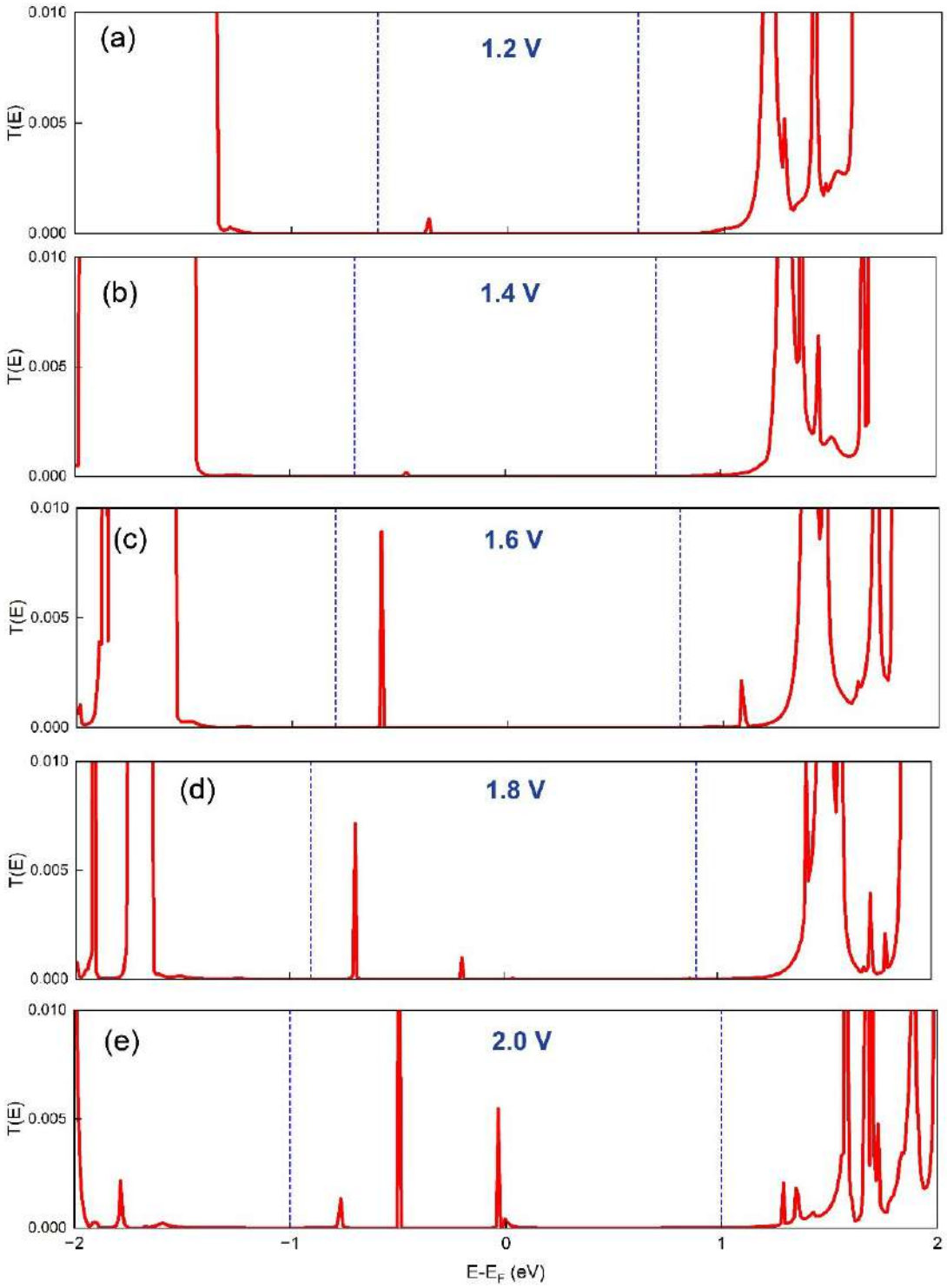

Figure B.11: Transmission spectra T(E) plots of Oh-B_2S_2 at different bias voltages.

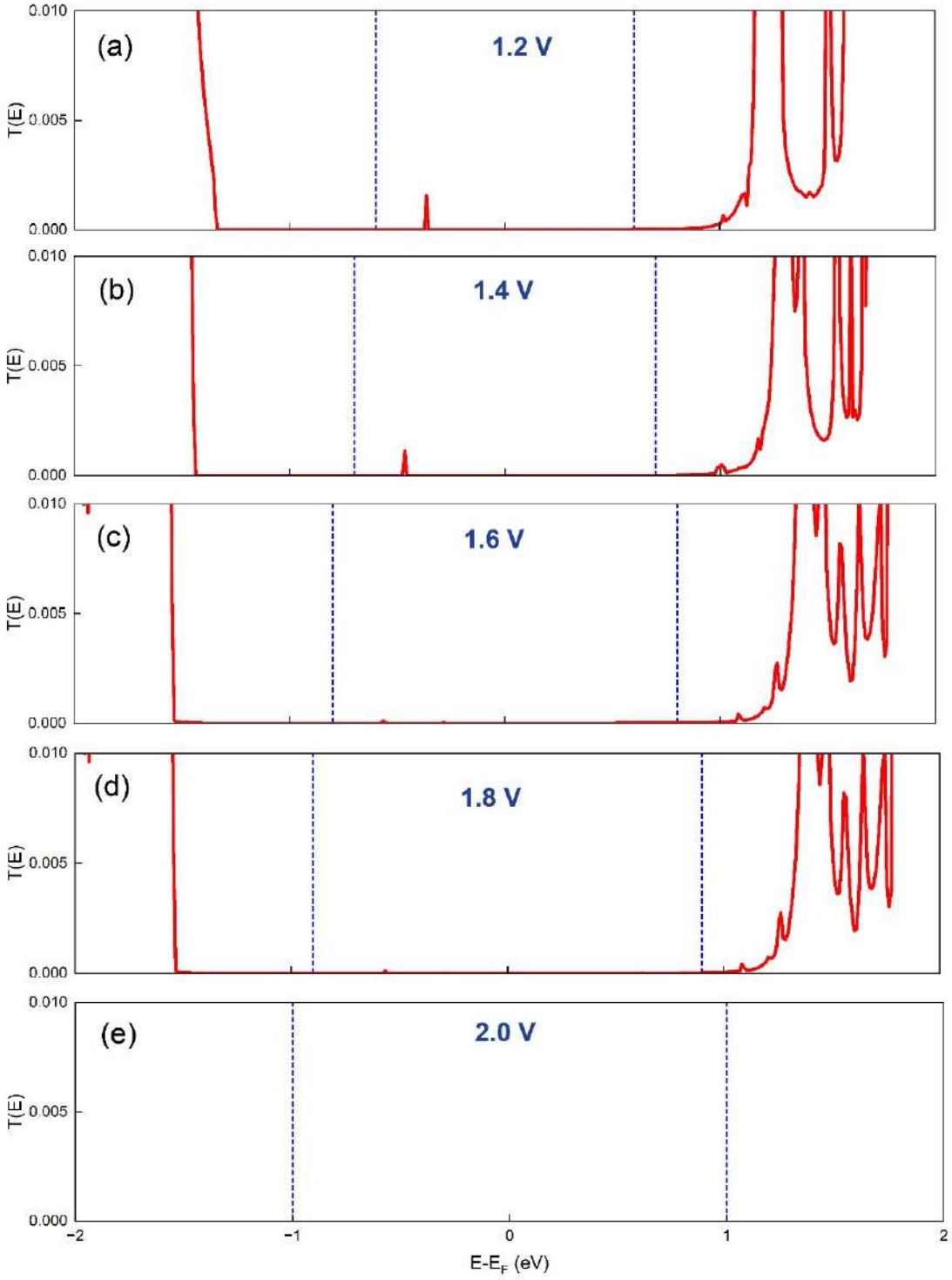

Figure B.12: Transmission spectra T(E) plots of NO-adsorbed Oh-B_2S_2 at different bias voltages.

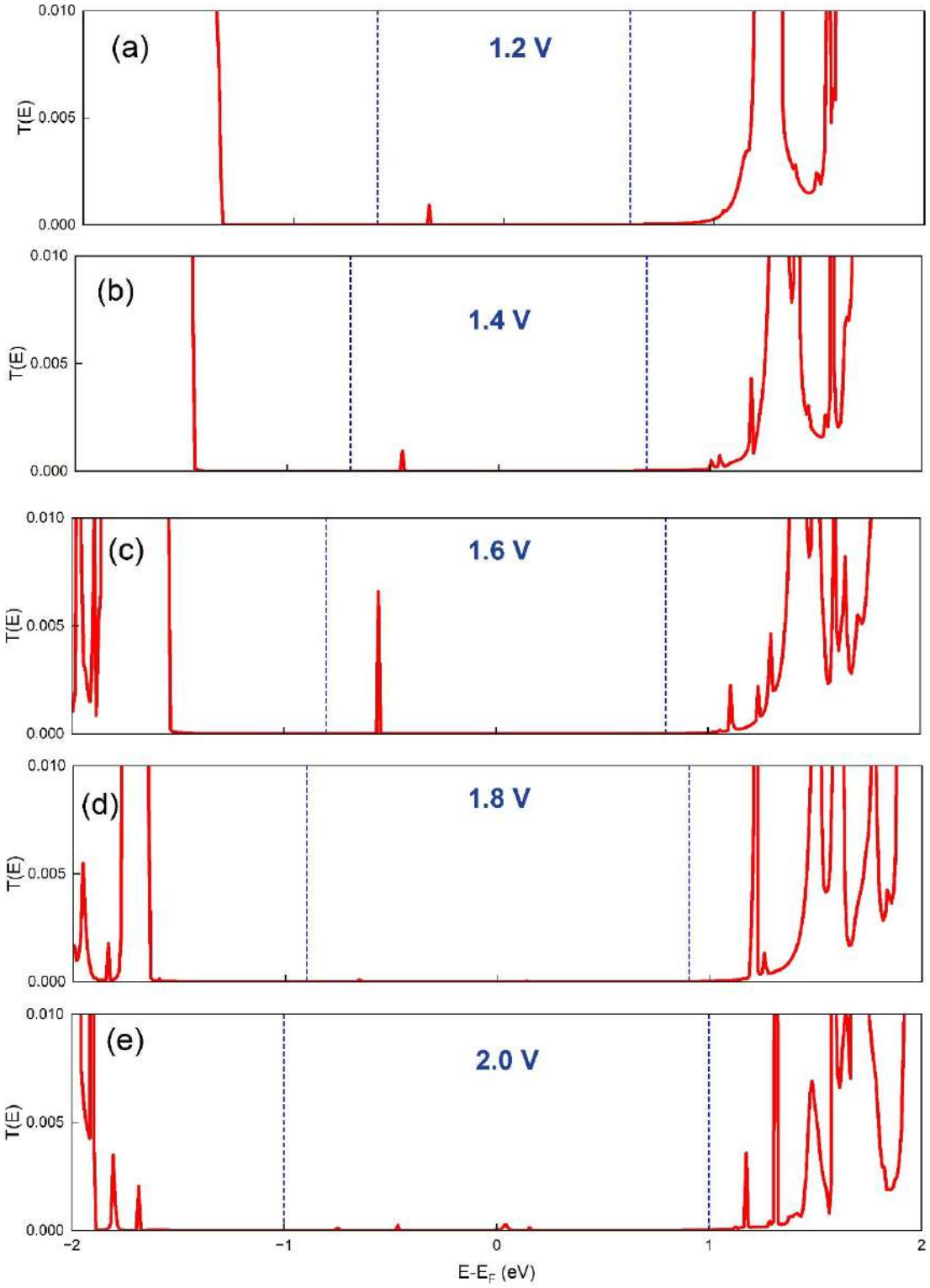

Figure B.13: Transmission spectra T(E) plots of NO_2-adsorbed Oh-B_2S_2 at different bias voltages.

Appendix C

SUPPORTING DATA

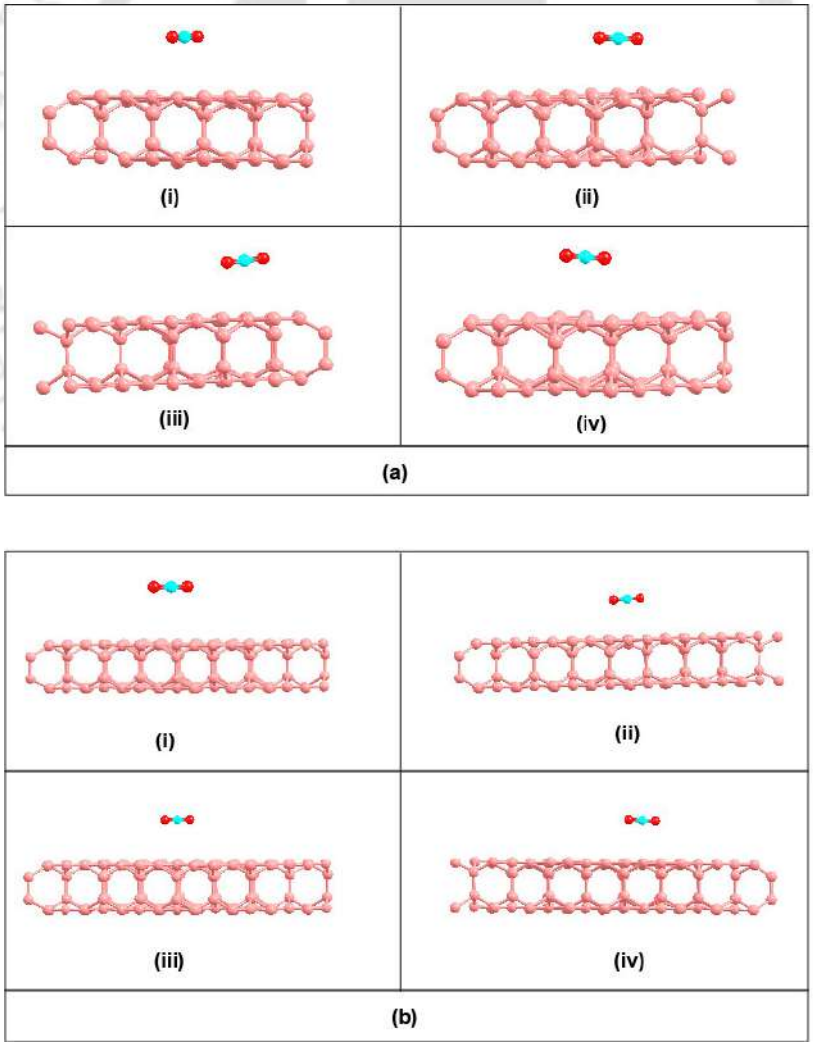

Figure C.1: Structure of CO_2 adsorption at (a) 2×2 and (b) 3×3 supercells of bilayer borophene (BL-B) and defect-induced bilayer borophene (BL-B-Def-1) at $0e^-$ charge state.

Table C.1: Adsorption energies (E_{ads}) of CO_2 at 2×2 and 3×3 supercells of bilayer borophene (BL-B) and defect-induced bilayer borophene.

System	Size	E_{ads} (eV)
BL-B	2×2	-0.12
	3×3	-0.13
BL-B-Def-1	2×2	-0.11
	3×3	-0.12
BL-B-Def-2	2×2	-0.12
	3×3	-0.13
BL-B-Def-3	2×2	-0.13
	3×3	-0.13

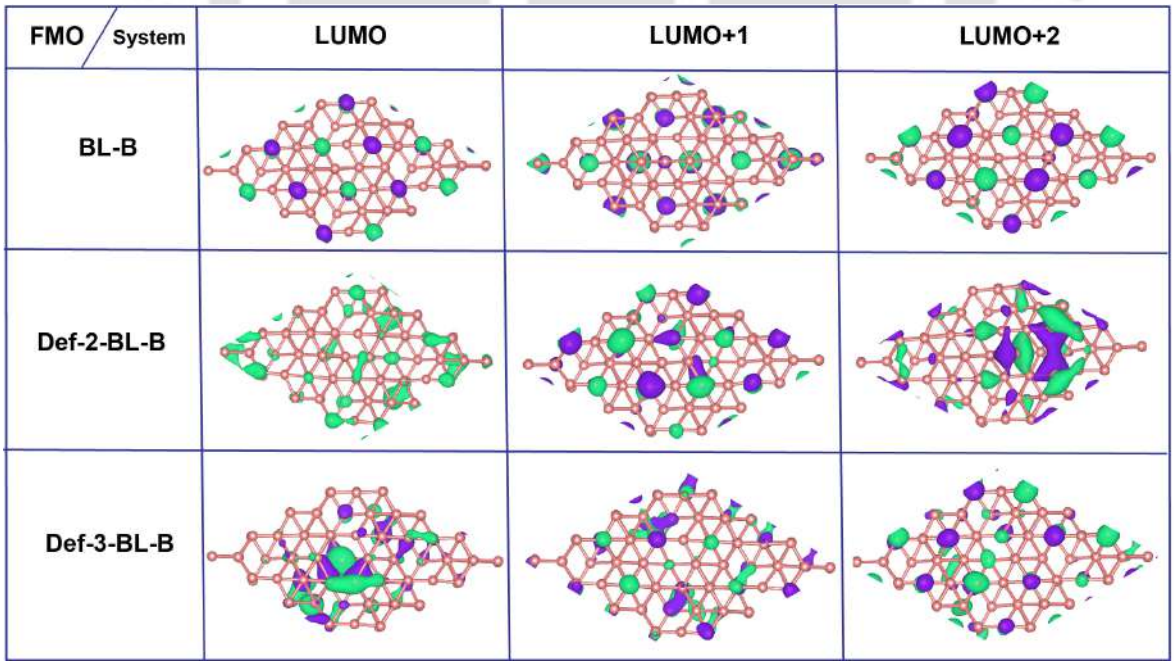

Figure C.2: Frontier molecular orbitals (FMOs) of bilayer borophene (BL-B) and defect-induced bilayer borophene (BL-B-Def-2 and BL-B-Def-3). Green and purple colors represent the charge accumulation and depletion region.

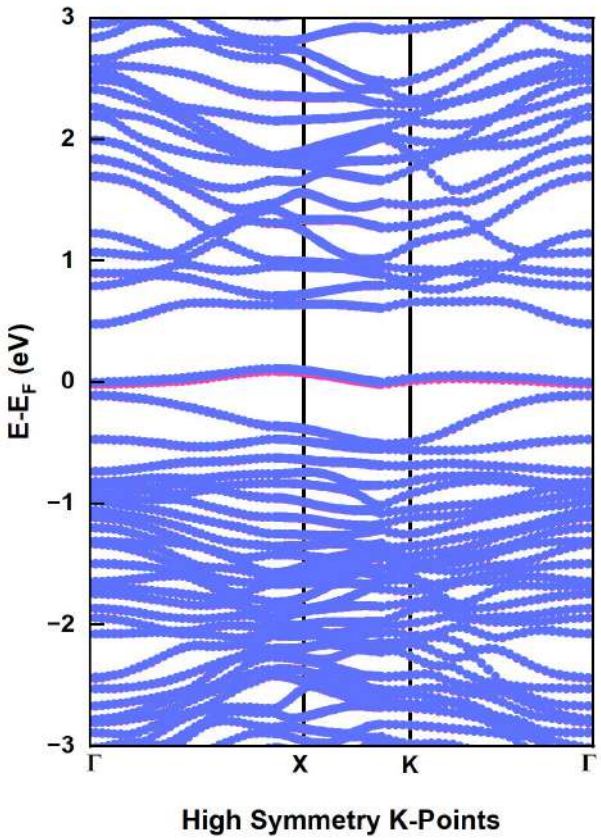

Figure C.3: Electronic band structure of defect-induced bilayer borophene (BL-B-Def-1). Blue and pink colors determine the spin-up and spin-down of the channels, respectively.

Table C.2: Electron and hole mobility values for different systems.

System	**Electron mobility** (μ_e) ($cm^2V^{-1}s^{-1}$)	**Hole mobility** (μ_h) ($cm^2V^{-1}s^{-1}$)
BL-B	2.10×10^4 (Reported) [260] 3.25×10^4 (Current study)	9.66×10^2 (Reported) [260] 6.8×10^2 (Current study)
BL-B-Def-1	1.69×10^3	240

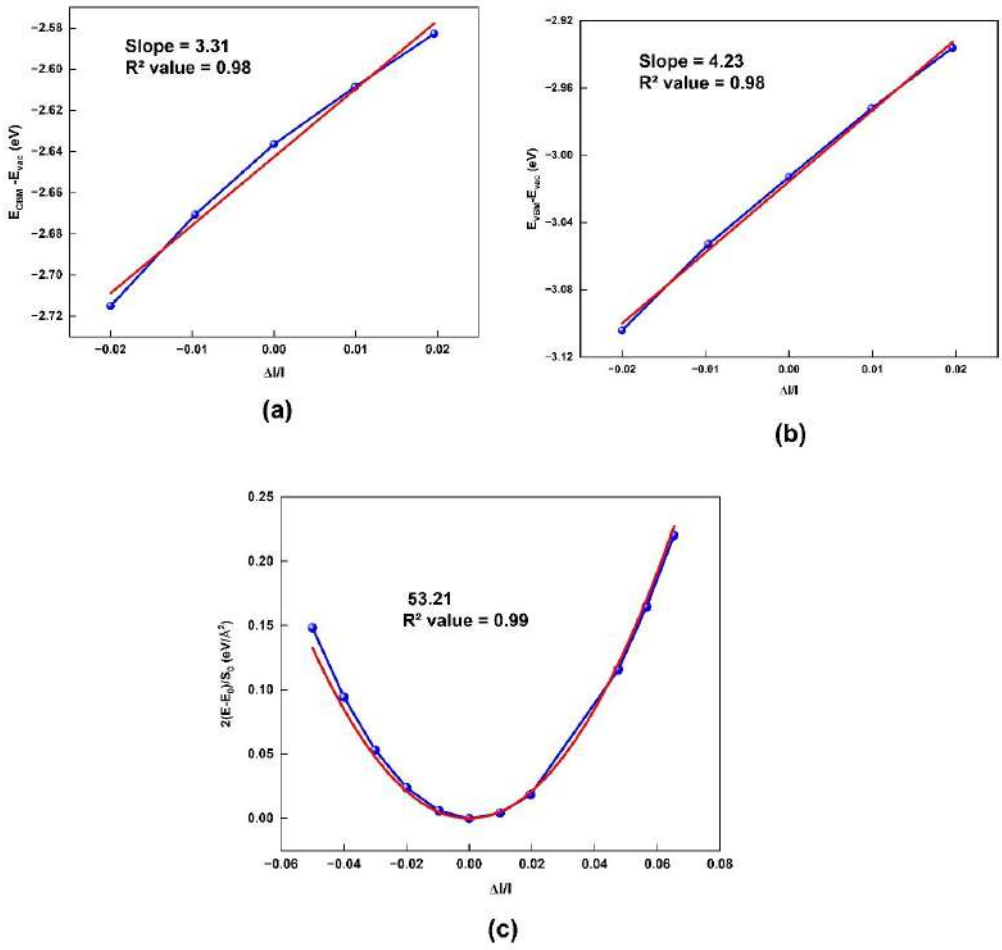

Figure C.4: (a) Linear fitting plot of deformation potential for the electron, (b) linear fitting plot of deformation potential for the hole, and (c) curve fitting plot of elastic modulus of bilayer defect-induced bilayer borophene (BL-B-Def-1) nanosheet. [For curve fitting, we have used the quadratic equation $y = Ax^2$.]

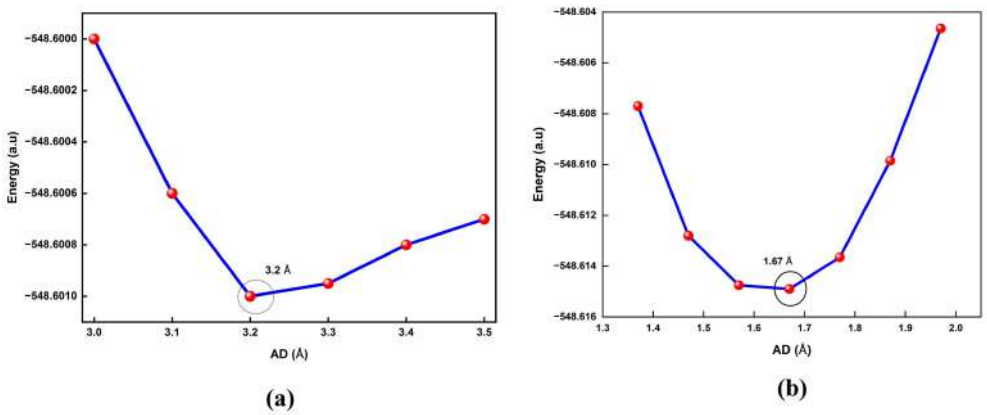

Figure C.5: Potential energy curves (PECs) of optimum adsorption distance (AD) of CO_2 adsorption on bilayer defect-induced bilayer borophene (BL-B-Def-1) on (a) $0e^-$ and (b) $6e^-$.

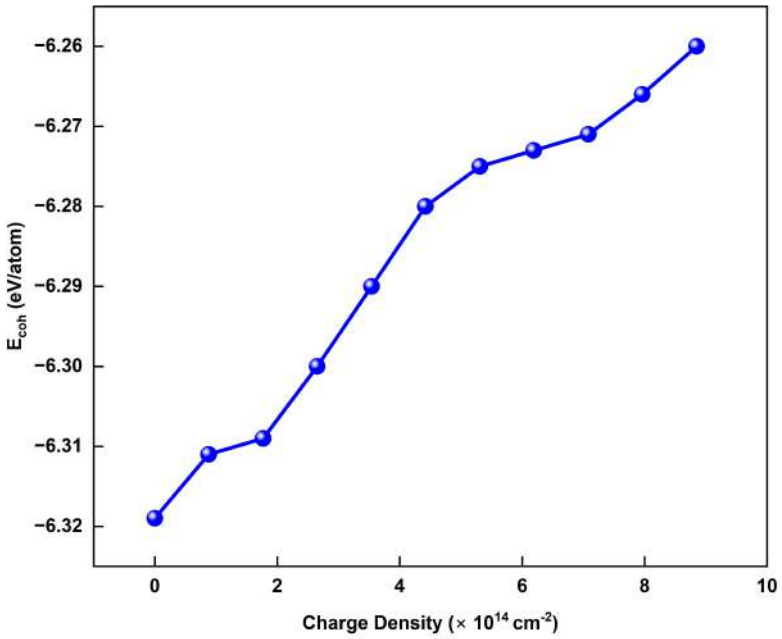

Figure C.6: Cohesive Energy (E_{coh}) at different charge density of BL-B-Def-1.

Table C.3: Formation energy (E_{form}) and cohesive energy (E_{coh}) of defect-induced bilayer borophene (BL-B-Def-1) at various defect concentrations and charge densities.

System	**Charge density** (10^{15} cm^{-2})	E_{form} **(eV)**	E_{coh} **(eV)**
BL-B-Def-1(Defect concentration 2.32%)	0	-0.103	6.28
	1.06	-	6.25
BL-B-Def-1(Defect concentration 3.52%)	0	-0.102	6.26
	2.04	-	6.20

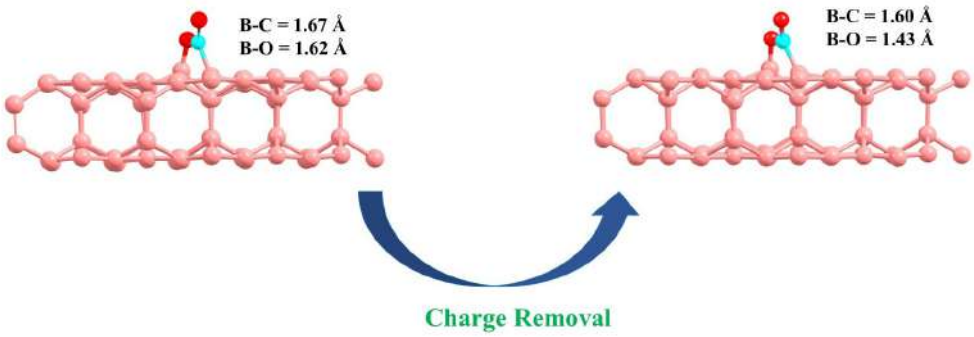

Figure C.7: Change in the structure after removing charge density from CO_2 adsorbed structure.

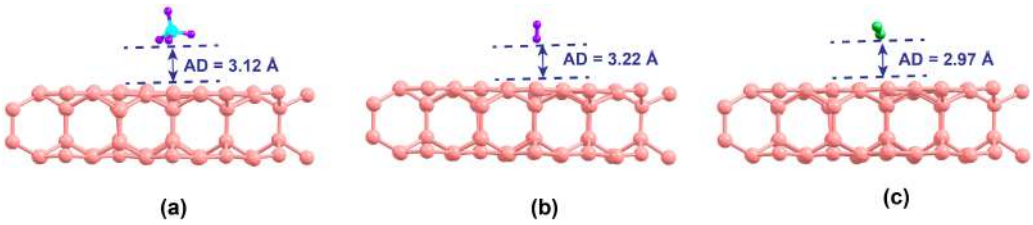

Figure C.8: Most stable adsorption configuration of (a) CH_4, (b) H_2, and (C) N_2 defect-induced bilayer borophene (BL-B-Def-1) at charge density 5.32×10^{14} $e^{-}cm^{-2}$.

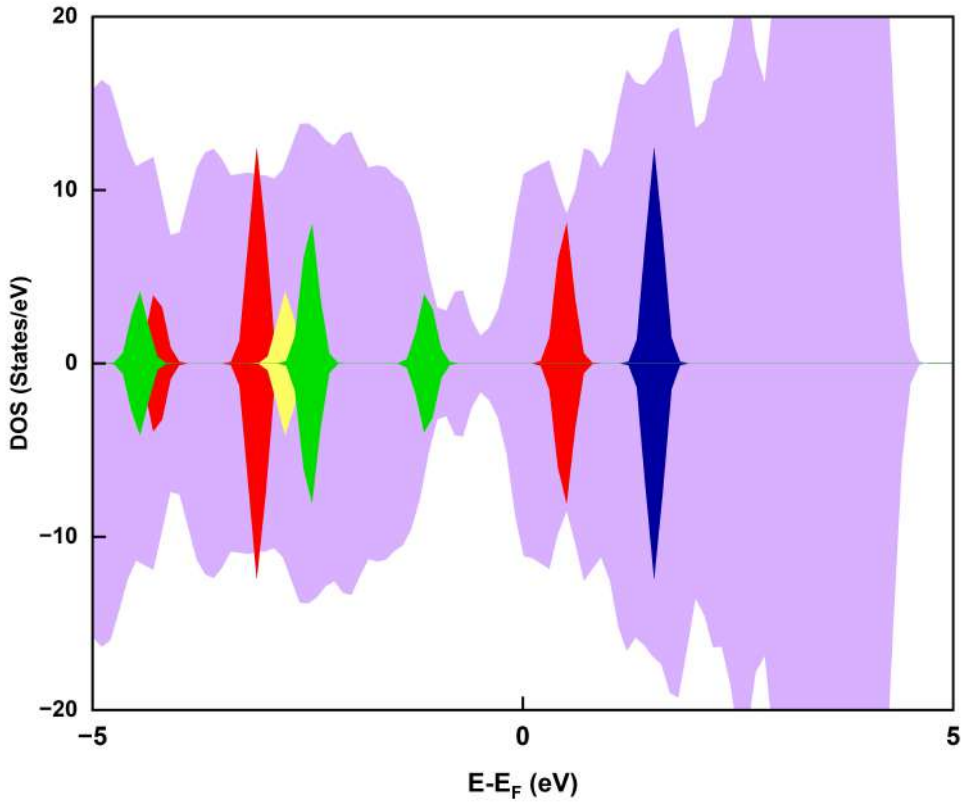

Figure C.9: Density of states (DOS) of defect-induced bilayer borophene (BL-B-Def-1) at charge density 5.32×10^{14} e^{-}/cm^2 (purple). CO_2 (red), CH_4 (blue), H_2 (yellow), and N_2 (green). The positive and negative values represent spin-up and spin-down states, respectively. The Fermi level (E_F) of BL-B-Def-1 is set to zero, and other molecules are referenced to the vacuum level of BL-B-Def-1.

Bibliography

(1) Geim, A. K.; Novoselov, K. S. The Rise of Graphene, *Nat. Mater.* **2007**, *6*, 183–191.

(2) Miró, P.; Audiffred, M.; Heine, T. An Atlas of Two-Dimensional Materials, *Chem. Soc. Rev.* **2014**, *43*, 6537–6554.

(3) Castro Neto, A. H.; Guinea, F.; Peres, N. M.; Novoselov, K. S.; Geim, A. K. The Electronic Properties of Graphene, *Rev. Mod. Phys.* **2009**, *81*, 109–162.

(4) Manna, A. K.; Pati, S. K. Stability and Electronic Structure of Carbon Capsules with Superior Gas Storage Properties: A Theoretical Study, *Chem. Phys.* **2013**, *426*, 23–30.

(5) Zeng, M.; Xiao, Y.; Liu, J.; Yang, K.; Fu, L. Exploring Two-Dimensional Materials Toward the Next-Generation Circuits: From Monomer Design to Assembly Control, *Chem. Rev.* **2018**, *118*, 6236–6296.

(6) Geim, A. K. Graphene: Status and Prospects, *Science* **2009**, *324*, 1530–1534.

(7) Brown, M. A.; Crosser, M. S.; Leyden, M. R.; Qi, Y.; Minot, E. D. Measurement of High Carrier Mobility in Graphene in an Aqueous Electrolyte Environment, *Appl. Phys. Lett.* **2016**, *109*, 093104 (1–4).

(8) Balandin, A. A.; Ghosh, S.; Bao, W.; Calizo, I.; Teweldebrhan, D.; Miao, F.; Lau, C. N. Superior Thermal Conductivity of Single-Layer Graphene, *Nano Lett.* **2008**, *8*, 902–907.

(9) Nag, A.; Raidongia, K.; Hembram, K. P.; Datta, R.; Waghmare, U. V.; Rao, C. Graphene Analogues of BN: Novel Synthesis and Properties, *ACS Nano* **2010**, *4*, 1539–1544.

(10) Xu, M.; Liang, T.; Shi, M.; Chen, H. Graphene-Like Two-Dimensional Materials, *Chem. Rev.* **2013**, *113*, 3766–3798.

(11) Bhimanapati, G. R.; Lin, Z.; Meunier, V.; Jung, Y.; Cha, J.; Das, S.; Xiao, D.; Son, Y.; Strano, M. S.; Cooper, V. R., et al. Recent Advances in Two-Dimensional Materials Beyond Graphene, *ACS Nano* **2015**, *9*, 11509–11539.

(12) Zhang, Y.; Zhou, M.; Yang, M.; Yu, J.; Li, W.; Li, X.; Feng, S. Experimental Realization and Computational Investigations of B_2S_2 as a New 2D Material with Potential Applications, *ACS Appl. Mater. Inter.* **2022**, *14*, 32330–32340.

(13) Liu, X.; Li, Q.; Ruan, Q.; Rahn, M. S.; Yakobson, B. I.; Hersam, M. C. Borophene Synthesis Beyond the Single-Atomic-Layer Limit, *Nat. Mater.* **2022**, *21*, 35–40.

(14) Kulish, V. V. Surface Reactivity and Vacancy Defects in Single-Layer Borophene Polymorphs, *Phys. Chem. Chem. Phys.* **2017**, *19*, 11273–11281.

(15) Kaneti, Y. V.; Benu, D. P.; Xu, X.; Yuliarto, B.; Yamauchi, Y.; Golberg, D. Borophene: Two-Dimensional Boron Monolayer: Synthesis, Properties, and Potential Applications, *Chem. Rev.* **2021**, *122*, 1000–1051.

(16) Tang, C.; Ma, F.; Zhang, C.; Jiao, Y.; Matta, S. K.; Ostrikov, K.; Du, A. 2D Boron Dichalcogenides from the Substitution of Mo with Ionic B_2 Pair in MoX_2 (X= S, Se and Te): High Stability, Large Excitonic Effect and High Charge Carrier Mobility, *J. Mater. Chem. C* **2019**, *7*, 1651–1658.

(17) Long, M.; Tang, L.; Wang, D.; Li, Y.; Shuai, Z. Electronic Structure and Carrier Mobility in Graphdiyne Sheet and Nanoribbons: Theoretical Predictions, *ACS Nano* **2011**, *5*, 2593–2600.

(18) Sun, Y.; Bai, H.; Huang, Y. Structures, Electronic Properties and Charge Carrier Mobility of Graphdiyne-Like BN Nanoribbons, *RSC Adv.* **2015**, *5*, 8965–8973.

(19) Chen, C.; Lv, H.; Zhang, P.; Zhuo, Z.; Wang, Y.; Ma, C.; Li, W.; Wang, X.; Feng, B.; Cheng, P., et al. Synthesis of Bilayer Borophene, *Nat. Chem.* **2022**, *14*, 25–31.

(20) Gao, N.; Wu, X.; Jiang, X.; Bai, Y.; Zhao, J. Structure and Stability of Bilayer Borophene: The Roles of Hexagonal Holes and Interlayer Bonding, *FlatChem* **2018**, *7*, 48–54.

(21) Yang, R.; Sun, M. Borophenes: Monolayer, Bilayer and Heterostructures, *J. Mater. Chem. C* **2023**, *11*, 6834–6846.

(22) Ma, Y.-Y.; Zhao, X.-Y.; Zan, W.; Mu, Y.; Zhang, Z.; Li, S.-D. Prediction of Freestanding Semiconducting Bilayer Borophenes, *Nano Res.* **2022**, *15*, 5752–5757.

(23) Niu, T.; Zhou, M. Bilayer Borophene Prevails Over Monolayer Counterpart, *Nano Today* **2022**, *46*, 101608 (1–5).

(24) Xu, Y.; Xuan, X.; Yang, T.; Zhang, Z.; Li, S.-D.; Guo, W. Quasi-Freestanding Bilayer Borophene on Ag (111), *Nano Lett.* **2022**, *22*, 3488–3494.

(25) Saxena, P.; Shukla, P. A Review on Recent Developments and Advances in Environmental Gas Sensors to Monitor Toxic Gas Pollutants, *Environ. Prog. Sustain. Energy.* **2023**, *42*, e14126 (1–18).

(26) Barea, E.; Montoro, C.; Navarro, J. A. Toxic Gas Removal–Metal–Organic Frameworks for the Capture and Degradation of Toxic Gases and Vapours, *Chem. Soc. Rev.* **2014**, *43*, 5419–5430.

(27) Manisalidis, I.; Stavropoulou, E.; Stavropoulos, A.; Bezirtzoglou, E. Environmental and Health Impacts of Air Pollution: A Review, *Front. Public Health* **2020**, *8*, 1–13.

(28) Anenberg, S. C.; Miller, J.; Minjares, R.; Du, L.; Henze, D. K.; Lacey, F.; Malley, C. S.; Emberson, L.; Franco, V.; Klimont, Z., et al. Impacts and Mitigation of Excess Diesel-Related NO_x Emissions in 11 Major Vehicle Markets, *Nature* **2017**, *545*, 467–471.

(29) Hossain, M. D.; Huang, Y.; Yu, T. H.; Goddard III, W. A.; Luo, Z. Reaction Mechanism and Kinetics for CO_2 Reduction on Nickel Single Atom Catalysts from Quantum Mechanics, *Nat. Commun.* **2020**, *11*, 2256 (1–14).

(30) Ren, Y.; Sun, X.; Qi, K.; Zhao, Z. Single Atom Supported on MoS_2 as Efficient Electrocatalysts for the CO_2 Reduction Reaction: A DFT Study, *Appl. Surf. Sci.* **2022**, *602*, 154211 (1–8).

(31) Singh, S.; Goswamy, J. K.; Sapra, G.; Sharma, P. Sensitivity and Selectivity Analysis of Toxic Gases NO_2, SO_2, O_3, Cl_2,$(CH_3)_2NH$, CH_3NH_2, NH_3, HCl, CH_2CHCl and ClO_2 on GO Sheet Platform for Environmental Sustainability: A DFT Prediction, *Sens. Actuators A: Phys.* **2022**, *347*, 113899 (1–10).

(32) Sohrabi, H.; Ghasemzadeh, S.; Ghoreishi, Z.; Majidi, M. R.; Yoon, Y.; Dizge, N.; Khataee, A. Metal-Organic Frameworks (MOF)-Based Sensors for Detection of Toxic Gases: A Review of Current Status and Future Prospects, *Mater. Chem. Phys.* **2023**, *299*, 127512 (1–14).

(33) Sreejyothi, P.; Mandal, S. K. From CO_2 Activation to Catalytic Reduction: A Metal-Free Approach, *Chem. Sci.* **2020**, *11*, 10571–10593.

(34) Qi, G.; Yang, R. T. A Superior Catalyst for Low-Temperature NO Reduction with NH_3, *Chem. Commun.* **2003**, 848–849.

(35) Ottaviano, L.; Mastrippolito, D. The Future Ahead Gas Sensing with Two-Dimensional Materials, *Appl. Phys. Lett.* **2023**, *123*, 050502 (1–8).

(36) Yang, S.; Jiang, C.; Wei, S. Gas Sensing in 2D Materials, *Appl. Phys. Rev.* **2017**, *4*, 021304 (1–34).

(37) Donarelli, M.; Ottaviano, L. 2D Materials for Gas Sensing Applications: A Review on Graphene Oxide, MoS_2, WS_2 and Phosphorene, *Sensors* **2018**, *18*, 3638 (1–45).

(38) Dey, A. Semiconductor Metal Oxide Gas Sensors: A Review, *Mater. Sci. Eng. B* **2018**, *229*, 206–217.

(39) Chai, H.; Zheng, Z.; Liu, K.; Xu, J.; Wu, K.; Luo, Y.; Liao, H.; Debliquy, M.; Zhang, C. Stability of Metal Oxide Semiconductor Gas Sensors: A Review, *IEEE Sens. J* **2022**, *22*, 5470–5481.

(40) Sringamprom, S.; Thanasarnsurapong, T.; Watcharatharapong, T.; Hirunpinyopas, W.; Sirisaksoontorn, W.; Prasongkit, J.; Boonchun, A. Monolayer Penta-$BeAs_2$: A Promising 2D Materials for Toxic Gas Sensor with High Selectivity, *ACS Appl. Mater. Inter.* **2024**, *16*, 56387–56395.

(41) Kim, Y.; Sohn, I.; Shin, D.; Yoo, J.; Lee, S.; Yoon, H.; Park, J.; Chung, S.-m.; Kim, H. Recent Advances in Functionalization and Hybridization of Two-Dimensional Transition Metal Dichalcogenide for Gas Sensor, *Adv. Eng. Mater.* **2024**, *26*, 2301063 (1–26).

(42) Tang, X.; Du, A.; Kou, L. Gas Sensing and Capturing Based on Two-Dimensional Layered Materials: Overview from Theoretical Perspective, *Wiley Interdiscip. Rev. Comput. Mol. Sci.* **2018**, *8*, e1361 (1–20).

(43) Cho, B.; Hahm, M. G.; Choi, M.; Yoon, J.; Kim, A. R.; Lee, Y.-J.; Park, S.-G.; Kwon, J.-D.; Kim, C. S.; Song, M., et al. Charge-Transfer-Based Gas Sensing Using Atomic-Layer MoS_2, *Sci. Rep.* **2015**, *5*, 8052 (1–6).

(44) Yue, Q.; Shao, Z.; Chang, S.; Li, J. Adsorption of Gas Molecules on Monolayer MoS_2 and Effect of Applied Electric Field, *Nanoscale Res. Lett.* **2013**, *8*, 1–7.

(45) Jin, H.; Guo, C.; Liu, X.; Liu, J.; Vasileff, A.; Jiao, Y.; Zheng, Y.; Qiao, S.-Z. Emerging Two-Dimensional Nanomaterials for Electrocatalysis, *Chem. Rev.* **2018**, *118*, 6337–6408.

(46) Yu, Q.; Luo, Y.; Mahmood, A.; Liu, B.; Cheng, H.-M. Engineering Two-Dimensional Materials and Their Heterostructures as High-Performance Electrocatalysts, *Electrochem. Energy Rev.* **2019**, *2*, 373–394.

(47) Tao, H.; Gao, Y.; Talreja, N.; Guo, F.; Texter, J.; Yan, C.; Sun, Z. Two-Dimensional Nanosheets for Electrocatalysis in Energy Generation and Conversion, *J. Mater. Chem. A* **2017**, *5*, 7257–7284.

(48) Fan, F. R.; Wang, R.; Zhang, H.; Wu, W. Emerging Beyond-Graphene Elemental 2D Materials for Energy and Catalysis Applications, *Chem. Soc. Rev.* **2021**, *50*, 10983–11031.

(49) Wang, Y.; Zhang, Z.; Mao, Y.; Wang, X. Two-Dimensional Nonlayered Materials for Electrocatalysis, *Energy Environ. Sci.* **2020**, *13*, 3993–4016.

(50) Ruan, Y.; He, Z.-H.; Liu, Z.-T.; Wang, W.; Hao, L.; Xu, L.; Robertson, A. W.; Sun, Z. Emerging Two-Dimensional Materials for the Electrocatalytic Nitrogen Reduction Reaction to Yield Ammonia, *J. Mater. Chem. A* **2023**, *11*, 22590–22607.

(51) Mei, X.; Xu, W. Recent Advances in Two-Dimensional Materials as Catalysts for the Electrochemical Reduction of Carbon Dioxide, *Iscience* **2023**, *26*, 108499 (1–15).

(52) Xiao, Y.; Zhou, M.; Zeng, M.; Fu, L. Atomic-Scale Structural Modification of 2D Materials, *Adv. Sci.* **2019**, *6*, 1801501 (1–15).

(53) Lei, Y.; Zhang, T.; Lin, Y.-C.; Granzier-Nakajima, T.; Bepete, G.; Kowalczyk, D. A.; Lin, Z.; Zhou, D.; Schranghamer, T. F.; Dodda, A., et al. Graphene and Beyond: Recent Advances in Two-Dimensional Materials Synthesis, Properties, and Devices, *ACS Nanosci. Au* **2022**, *2*, 450–485.

(54) Subrahmanyam, K.; Manna, A. K.; Pati, S. K.; Rao, C. A Study of Graphene Decorated with Metal Nanoparticles, *Chem. Phys. Lett.* **2010**, *497*, 70–75.

(55) Ngome Okello, O. F.; Yang, D.-H.; Chu, Y.-S.; Yang, S.; Choi, S.-Y. Atomic-Level Defect Modulation and Characterization Methods in 2D Materials, *APL Mater.* **2021**, *9*, 100902 (1–20).

(56) Wang, D.; Li, X.-B.; Sun, H.-B. Modulation Doping: A Strategy for 2D Materials Electronics, *Nano Lett.* **2021**, *21*, 6298–6303.

(57) Dastider, A. G.; Rasul, A.; Rahman, E.; Alam, M. K. Effect of Vacancy Defects on the Electronic and Mechanical Properties of Two-Dimensional $MoSi_2N_4$, *RSC Adv.* **2023**, *13*, 5307–5316.

(58) Jiang, J.; Xu, T.; Lu, J.; Sun, L.; Ni, Z. Defect Engineering in 2D Materials: Precise Manipulation and Improved Functionalities, *Research* **2019**, *2019*, 1–14.

(59) Li, H.; Du, M.; Mleczko, M. J.; Koh, A. L.; Nishi, Y.; Pop, E.; Bard, A. J.; Zheng, X. Kinetic Study of Hydrogen Evolution Reaction over Strained MoS_2 with Sulfur Vacancies using Scanning Electrochemical Microscopy, *J. Am. Chem. Soc.* **2016**, *138*, 5123–5129.

(60) Yin, Y.; Han, J.; Zhang, Y.; Zhang, X.; Xu, P.; Yuan, Q.; Samad, L.; Wang, X.; Wang, Y.; Zhang, Z., et al. Contributions of Phase, Sulfur Vacancies, and Edges to the Hydrogen Evolution Reaction Catalytic Activity of Porous Molybdenum Disulfide Nanosheets, *J. Am. Chem. Soc.* **2016**, *138*, 7965–7972.

(61) Zhu, K.; Shi, F.; Zhu, X.; Yang, W. The Roles of Oxygen Vacancies in Electrocatalytic Oxygen Evolution Reaction, *Nano Energy* **2020**, *73*, 104761 (1–18).

(62) Jelmy, E.; Thomas, N.; Mathew, D. T.; Louis, J.; Padmanabhan, N. T.; Kumaravel, V.; John, H.; Pillai, S. C. Impact of Structure, Doping and Defect-Engineering in 2D Materials on CO_2 Capture and Conversion, *React. Chem. Eng.* **2021**, *6*, 1701–1738.

(63) Ma, J.; Zhang, M.; Dong, L.; Sun, Y.; Su, Y.; Xue, Z.; Di, Z. Gas Sensor Based on Defective Graphene/Pristine Graphene Hybrid Towards High Sensitivity Detection of NO_2, *AIP Adv.* **2019**, *9*, 075207 (1–6).

(64) Liu, H.; Liu, Y.; Zhu, D. Chemical Doping of Graphene, *J. Mater. Chem.* **2011**, *21*, 3335–3345.

(65) Sharma, P. P.; Wu, J.; Yadav, R. M.; Liu, M.; Wright, C. J.; Tiwary, C. S.; Yakobson, B. I.; Lou, J.; Ajayan, P. M.; Zhou, X.-D. Nitrogen-Doped Carbon Nanotube Arrays for High-Efficiency Electrochemical Reduction of CO_2: On the Understanding of Defects, Defect Density, and Selectivity, *Angew. Chem.* **2015**, *127*, 13905–13909.

(66) Dai, J.; Yuan, J.; Giannozzi, P. Gas Adsorption on Graphene Doped with B, N, Al, and S: A Theoretical Study, *Appl. Phys. Lett.* **2009**, *95*, 232105 (1–3).

(67) Pham, K. D.; Hoang, T.-D.; Nguyen, Q.-T.; Hoang, D.-Q. Fe-doped SnSe Monolayer: A Promising 2D Material for Reusable SO_2 Gas Sensor with High Sensitivity, *J. Alloys Compd.* **2023**, *940*, 168919 (1–9).

(68) Panigrahi, P.; Hussain, T.; Karton, A.; Ahuja, R. Elemental Substitution of Two-Dimensional Transition Metal Dichalcogenides ($MoSe_2$ and $MoTe_2$): Implications for Enhanced Gas Sensing, *ACS Sensors* **2019**, *4*, 2646–2653.

(69) Parey, V.; Abraham, B. M.; Gaur, N. K.; Thapa, R. First-Principles Study of Two-Dimensional B-Doped Carbon Nanostructures for Toxic Phosgene Gas Detection, *ACS Appl. Nano Mater.* **2022**, *5*, 12737–12745.

(70) Ma, W.; Yao, J.; Xie, F.; Wang, X.; Wan, H.; Shen, X.; Zhang, L.; Jiao, M.; Zhou, Z. Optimizing Electronic Structure Through Point Defect Engineering for Enhanced Electrocatalytic Energy Conversion, *Green Energy Environ.* **2025**, *10*, 109–131.

(71) Martín, N.; Tagmatarchis, N.; Wang, Q. H.; Zhang, X. Chemical Functionalization of 2D Materials, *Chem. Eur. J.* **2020**, *26*, 6292–6295.

(72) Zhou, S.; Liu, C.-C.; Zhao, J.; Yao, Y. Monolayer Group-III Monochalcogenides by Oxygen Functionalization: A Promising Class of Two-Dimensional Topological Insulators, *npj Quantum Mater.* **2018**, *3*, 16 (1–7).

(73) Garrido, M.; Naranjo, A.; Pérez, E. M. Characterization of Emerging 2D Materials After Chemical Functionalization, *Chem. Sci.* **2024**, *15*, 3428–3445.

(74) Weng, K.; Peng, J.; Shi, Z.; Arramel, A.; Li, N. Highly NH_3 Sensitive and Selective $Ti_3C_2O_2$-Based Gas Sensors: A Density Functional Theory-NEGF Study, *ACS Omega* **2023**, *8*, 4261–4269.

(75) Alzate-Carvajal, N.; Luican-Mayer, A. Functionalized Graphene Surfaces for Selective Gas Sensing, *ACS Omega* **2020**, *5*, 21320–21329.

(76) Qi, Y.; Sadi, M. A.; Hu, D.; Zheng, M.; Wu, Z.; Jiang, Y.; Chen, Y. P. Recent Progress in Strain Engineering on van der Waals 2D Materials: Tunable Electrical, Electrochemical, Magnetic, and Optical Properties, *Adv. Mater.* **2023**, *35*, 2205714 (1–18).

(77) Pandey, M.; Pandey, C.; Ahuja, R.; Kumar, R. Straining Techniques for Strain Engineering of 2D Materials Towards Flexible Straintronic Applications, *Nano Energy* **2023**, *109*, 108278 (1–37).

(78) Beniwal, P.; Kumar, T. D. Modulation of H_2 Adsorption in C_9N_4 Monolayer via Biaxial Strain for Hydrogen Storage, *Appl. Surf. Sci.* **2025**, *690*, 162472.

(79) Ma, S.; Yuan, D.; Jiao, Z.; Wang, T.; Dai, X. Monolayer Sc_2CO_2: A Promising Candidate as a SO_2 Gas Sensor or Capturer, *J. Phys. Chem. C* **2017**, *121*, 24077–24084.

(80) Ghosh, B.; Puri, S.; Agarwal, A.; Bhowmick, S. SnP_3: A Previously Unexplored Two-Dimensional Material, *J. Phys. Chem. C* **2018**, *122*, 18185–18191.

(81) Sun, X.; Yang, Q.; Meng, R.; Tan, C.; Liang, Q.; Jiang, J.; Ye, H.; Chen, X. Adsorption of Gas Molecules on Graphene-Like InN Monolayer: A First-Principle Study, *Appl. Surf. Sci.* **2017**, *404*, 291–299.

(82) Rhrissi, I.; Bouhmouche, A.; Abdelrhafor, I.; Moubah, R. Strain-Engineered 2D h-BC_2N Monolayer as a Potential Gas Sensor with Exceptional Sensitivity and Selectivity for NO_2 Gas Detection, *Mat. Sci. Semicon. Proc.* **2024**, *182*, 108707 (1–12).

(83) Beniwal, P.; Chakraborty, B.; Kumar, T. D. Effect of N-doping and Biaxial Compressive Strain on H_2 Adsorption of 2D Holey Graphyne Monolayer via First-Principles Study, *Int. J. Hydrogen Energy* **2025**, *115*, 186–197.

(84) Martin, R. M. Electronic Structure: Basic Theory and Practical Methods, *Cambridge, Cambridge University Press* **2020**.

(85) Koch, W.; Holthausen, M. C. A Chemist's Guide to Density Functional Theory**, 2015**.

(86) Nagy, Á. Density Functional. Theory and Application to Atoms and Molecules, *Phys. Rep.* **1998**, *298*, 1–79.

(87) Becke, A. D. Perspective: Fifty Years of Density-Functional Theory in Chemical Physics, *J. Chem. Phys.* **2014**, *140*, 18A301 (1–18).

(88) Sahni, V.; Sahni, V. The Hohenberg-Kohn Theorems and Kohn-Sham Density Functional Theory, *Quantal Density Functional Theory* **2004**, 99–123.

(89) Sharma, B. I. Basic Concepts of Density Functional Theory: Electronic Structure Calculation, *J. Phys.: Conf. Ser.* **2016**, *765*, 012004 (1–4).

(90) Nomura, Y.; Akashi, R. Density Functional Theory**, 2022**.

(91) Harbola, M. K.; Sahni, V. Quantum-Mechanical Interpretation of the Exchange-Correlation Potential of Kohn-Sham Density-Functional Theory, *Phys. Rev. Lett.* **1989**, *62*, 489–492.

(92) Kohn, W.; Sham, L. J. Self-Consistent Equations Including Exchange and Correlation Effects, *Phys. Rev.* **1965**, *140*, A1133–A1138.

(93) Heyd, J.; Scuseria, G. E.; Ernzerhof, M. Hybrid Functionals Based on a Screened Coulomb Potential, *J. Chem. Phys.* **2003**, *118*, 8207–8215.

(94) Paier, J.; Marsman, M.; Hummer, K.; Kresse, G.; Gerber, I. C.; Ángyán, J. G. Screened Hybrid Density Functionals Applied to Solids, *J. Chem. Phys.* **2006**, *124*, 154709 (1–13).

(95) Garoz, D.; Gilabert, F.; Sevenois, R.; Spronk, S.; Van Paepegem, W. Consistent Application of Periodic Boundary Conditions in Implicit and Explicit Finite Element Simulations of Damage in Composites, *Compos. B Eng.* **2019**, *168*, 254–266.

(96) Kratzer, P.; Neugebauer, J. The Basics of Electronic Structure Theory for Periodic Systems, *Front. Chem.* **2019**, *7*, 106 (1–18).

(97) Marx, D.; Hutter, J. Ab Initio Molecular Dynamics: Basic Theory and Advanced Methods**, 2009**.

(98) VandeVondele, J.; Hutter, J. Gaussian Basis Sets for Accurate Calculations on Molecular Systems in Gas and Condensed Phases, *J. Chem. Phys.* **2007**, *127*, 114105 (1–9).

(99) Grimme, S. Semiempirical GGA-type Density Functional Constructed with a Long-Range Dispersion Correction, *J. Comput. Chem.* **2006**, *27*, 1787–1799.

(100) Kresse, G.; Joubert, D. From Ultrasoft Pseudopotentials to the Projector Augmented-Wave Method, *Phys. Rev. B* **1999**, *59*, 1758–1775.

(101) Schwerdtfeger, P. The Pseudopotential Approximation in Electronic Structure Theory, *ChemPhysChem* **2011**, *12*, 3143–3155.

(102) Migdal, K.; Yanilkin, A. Cold and Hot Uranium in DFT Calculations: Investigation by the GTH Pseudopotential, PAW, and APW+lo Methods, *Comput. Mater. Sci.* **2021**, *199*, 110665 (1–16).

(103) Lu, J.-B.; Cantu, D. C.; Xu, C.-Q.; Nguyen, M.-T.; Hu, H.-S.; Glezakou, V.-A.; Rousseau, R.; Li, J. Norm-Conserving Pseudopotentials and Basis Sets to Explore Actinide Chemistry in Complex Environments, *J. Chem. Theory Comput.* **2021**, *17*, 3360–3371.

(104) Li, G.; Stenlid, J. H.; Ahlquist, M. S.; Brinck, T. Utilizing the Surface Electrostatic Potential to Predict the Interactions of Pt and Ni Nanoparticles with Lewis Acids and Bases—σ-Lumps and σ-Holes Govern the Catalytic Activities, *J. Phys. Chem. C* **2020**, *124*, 14696–14705.

(105) Gerhorst, C.-R.; Neukirchen, A.; Klüppelberg, D. A.; Bihlmayer, G.; Betzinger, M.; Michalicek, G.; Wortmann, D.; Blügel, S. Phonons from Density-Functional Perturbation Theory using the All-Electron Full-Potential Linearized Augmented Plane-Wave Method FLEUR, *Electron. Struct.* **2024**, *6*, 017001.

(106) Peng, X.; Chen, L.; Liu, Y.; Liu, C.; Huang, H.; Fan, J.; Xiong, P.; Zhu, J. Strain Engineering of Two-Dimensional Materials for Energy Storage and Conversion Applications, *Chem. Synth.* **2023**, *3*, 47.

(107) Burdett, J. K.; McCormick, T. A. Electron Localization in Molecules and Solids: The Meaning of ELF, *J. Phys. Chem. A* **1998**, *102*, 6366–6372.

(108) Iftimie, R.; Minary, P.; Tuckerman, M. E. Ab Initio Molecular Dynamics: Concepts, Recent Developments, and Future Trends, *Proc Natl Acad Sci U S A* **2005**, *102*, 6654–6659.

(109) Hairer, E.; Lubich, C.; Wanner, G. Geometric Numerical Integration Illustrated by the Störmer–Verlet Method, *Acta Numer.* **2003**, *12*, 399–450.

(110) Brandbyge, M.; Mozos, J.-L.; Ordejón, P.; Taylor, J.; Stokbro, K. Density-Functional Method for Nonequilibrium Electron Transport, *Phys. Rev. B* **2002**, *65*, 165401 (1–17).

(111) Lee, S. U.; Kawazoe, Y. Nanodesign and Simulation Toward Nanoelectronic Devices**,** **2011**.

(112) Papior, N.; Lorente, N.; Frederiksen, T.; García, A.; Brandbyge, M. Improvements on Non-Equilibrium and Transport Green Function Techniques: The Next-Generation Transiesta, *Comput. Phys. Commun.* **2017**, *212*, 8–24.

(113) Stokbro, K.; Taylor, J.; Brandbyge, M.; Ordejon, P. TranSIESTA: A Spice for Molecular Electronics, *Ann. N.Y. Acad. Sci.* **2003**, *1006*, 212–226.

(114) Camsari, K. Y.; Chowdhury, S.; Datta, S. The Nonequilibrium Green Function (NEGF) Method**,** **2022**, 1583–1599.

(115) Thakur, A.; Sarkar, N. A Tutorial on the NEGF Method for Electron Transport in Devices and Defective Materials, *Eur. Phys. J. B* **2023**, *96*, 113–128.

(116) Datta, S. Quantum Transport: Atom to Transistor**,** **2005**.

(117) Wang, J.-S.; Agarwalla, B. K.; Li, H.; Thingna, J. Nonequilibrium Green's Function Method for Quantum Thermal Transport, *Front. Phys.* **2014**, *9*, 673–697.

(118) Datta, S. Nanoscale Device Modeling: The Green's Function Method, *Superlattices Microstruct.* **2000**, *28*, 253–278.

(119) Choudhuri, I.; Sadhukhan, D.; Garg, P.; Mahata, A.; Pathak, B. Lewis Acid–Base Adducts for Improving the Selectivity and Sensitivity of Graphene Based Gas Sensors, *ACS Sens.* **2016**, *1*, 451–459.

(120) Yu, X.; Chen, F.; Yu, Z.; Li, Y. Computational Study of Borophene with Line Defects as Sensors for Nitrogen-Containing Gas Molecules, *ACS Appl. Nano Mater.* **2020**, *3*, 9961–9968.

(121) Kumar, S. Acid Rain-the Major Cause of Pollution: Its Causes, Effects**,** **2017**, *13*, 53–58.

(122) Chen, T.-M.; Kuschner, W. G.; Gokhale, J.; Shofer, S. Outdoor Air Pollution: Nitrogen Dioxide, Sulfur Dioxide, and Carbon Monoxide Health Effects, *Am. J. Med. Sci.* **2007**, *333*, 249–256.

(123) Faye, O.; Eduok, U.; Szpunar, J. A. Boron-Decorated Graphitic Carbon Nitride (g-C_3N_4): An Efficient Sensor for H_2S, SO_2, and NH_3 Capture, *J. Phys. Chem. C* **2019**, *123*, 29513–29523.

(124) Xu, H.; Li, J.; Fu, Y.; Li, P.; Luo, W.; Tian, Y. Ag/Ag_2S Nanoparticle-Induced Sensitization of Recovered Sulfur-Doped SnO_2 Nanoparticles for SO_2 Detection, *ACS Appl. Nano Mater.* **2020**, *3*, 8075–8087.

(125) Zhao, J.; Liu, H.; Yu, Z.; Quhe, R.; Zhou, S.; Wang, Y.; Liu, C. C.; Zhong, H.; Han, N.; Lu, J., et al. Rise of Silicene: A Competitive 2D Material, *Prog. Mater. Sci.* **2016**, *83*, 24–151.

(126) Choudhuri, I.; Patra, N.; Mahata, A.; Ahuja, R.; Pathak, B. B–N@ Graphene: Highly Sensitive and Selective Gas Sensor, *J. Phys. Chem. C* **2015**, *119*, 24827–24836.

(127) Sahithi, A.; Sumithra, K. Adsorption and Sensing of CO and NH_3 on Chemically Modified Graphene Surfaces, *RSC Adv.* **2020**, *10*, 42318–42326.

(128) Shukri, M.; Saimin, M.; Yaakob, M.; Yahya, M.; Taib, M. Structural and Electronic Properties of CO and NO Gas Molecules on Pd-doped Vacancy Graphene: A First Principles Study, *Appl. Surf. Sci.* **2019**, *494*, 817–828.

(129) Schedin, F.; Geim, A. K.; Morozov, S. V.; Hill, E. W.; Blake, P.; Katsnelson, M. I.; Novoselov, K. S. Detection of Individual Gas Molecules Adsorbed on Graphene, *Nat. Mater.* **2007**, *6*, 652–655.

(130) Shukla, V.; Warna, J.; Jena, N. K.; Grigoriev, A.; Ahuja, R. Toward the Realization of 2D Borophene Based Gas Sensor, *J. Phys. Chem. C* **2017**, *121*, 26869–26876.

(131) Baby, A.; Di Valentin, C. Gas Sensing by Metal and Nonmetal Co-Doped Graphene on a Ni Substrate, *J. Phys. Chem. C* **2021**, *125*, 24079–24095.

(132) Usachov, D.; Vilkov, O.; Gruneis, A.; Haberer, D.; Fedorov, A.; Adamchuk, V.; Preobrajenski, A.; Dudin, P.; Barinov, A.; Oehzelt, M., et al. Nitrogen-Doped Graphene: Efficient Growth, Structure, and Electronic Properties, *Nano Lett.* **2011**, *11*, 5401–5407.

(133) Wang, H.; Maiyalagan, T.; Wang, X. Review on Recent Progress in Nitrogen-Doped Graphene: Synthesis, Characterization, and its Potential Applications, *ACS Catal.* **2012**, *2*, 781–794.

(134) Srivastava, S.; Kashyap, P. K.; Singh, V.; Senguttuvan, T.; Gupta, B. K. Nitrogen Doped High Quality CVD Grown Graphene as a Fast Responding NO_2 Gas Sensor, *New J. Chem.* **2018**, *42*, 9550–9556.

(135) Zhou, Q.; Ju, W.; Liu, Y.; Li, J.; Zhang, Q. Influence of Defects and Dopants on the Sensitivity of Arsenene Towards HCN, *Appl. Surf. Sci.* **2020**, *506*, 144936–144947.

(136) Hussain, T.; Kaewmaraya, T.; Chakraborty, S.; Ahuja, R. Defect and Substitution-Induced Silicene Sensor to Probe Toxic Gases, *J. Phys. Chem. C* **2016**, *120*, 25256–25262.

(137) Liu, X.-Y.; Zhang, J.-M.; Xu, K.-W.; Ji, V. Improving SO_2 Gas Sensing Properties of Graphene by Introducing Dopant and Defect: A First-Principles Study, *Appl. Surf. Sci.* **2014**, *313*, 405–410.

(138) Tit, N.; Said, K.; Mahmoud, N. M.; Kouser, S.; Yamani, Z. H. Ab-Initio Investigation of Adsorption of CO and CO_2 Molecules on Graphene: Role of Intrinsic Defects on Gas Sensing, *Appl. Surf. Sci.* **2017**, *394*, 219–230.

(139) Qin, Y.; Shen, X.; Bai, Y. First-Principles Prediction of Strain-Induced Gas-Sensing Tuning in Tin Sulfide, *Phys. Chem. Chem. Phys.* **2021**, *23*, 18712–18723.

(140) Schiros, T.; Nordlund, D.; Palo, L.; Prezzi, D.; Zhao, L.; Kim, K. S.; Wurstbauer, U.; Gutierrz, C.; Delongchamp, D.; Jaye, C., et al. Connecting Dopant Bond Type with Electronic Structure in N-doped Graphene, *Nano Lett.* **2012**, *12*, 4025–4031.

(141) Haile, A. S.; Hansen, H. A.; Yohannes, W.; Mekonnen, Y. S. Pyridinic-Type N-Doped Graphene on Cobalt Substrate as Efficient Electrocatalyst for Oxygen Reduction Reaction in Acidic Solution in Fuel Cell, *J. Phys. Chem. Lett.* **2021**, *12*, 3552–3559.

(142) Ghosh, D.; Pati, S. K. Trapping of Gaseous Pollutants on Defective N-doped Graphene, *Phys. Chem. Chem. Phys.* **2017**, *19*, 636–643.

(143) Ma, C.; Shao, X.; Cao, D. Nitrogen-doped Graphene as an Excellent Candidate for Selective Gas Sensing, *Sci. China Chem.* **2014**, *57*, 911–917.

(144) Wang, Q.; Ji, Y.; Lei, Y.; Wang, Y.; Wang, Y.; Li, Y.; Wang, S. Pyridinic-N-Dominated Doped Defective Graphene as a Superior Oxygen Electrocatalyst for Ultrahigh-Energy-Density Zn–Air Batteries, *ACS Energy Lett.* **2018**, *3*, 1183–1191.

(145) Guo, D.; Shibuya, R.; Akiba, C.; Saji, S.; Kondo, T.; Nakamura, J. Active Sites of Nitrogen-Doped Carbon Materials for Oxygen Reduction Reaction Clarified using Model Catalysts, *Science* **2016**, *351*, 361–365.

(146) Bu, S.; Yao, N.; Hunter, M. A.; Searles, D. J.; Yuan, Q. Design of Two-Dimensional Carbon-Nitride Structures by Tuning the Nitrogen Concentration, *npj Comput. Mater.* **2020**, *6*, 1–8.

(147) Giannozzi, P.; Baroni, S.; Bonini, N.; Calandra, M.; Car, R.; Cavazzoni, C.; Ceresoli, D.; Chiarotti, G. L.; Cococcioni, M.; Dabo, I., et al. QUANTUM ESPRESSO: A Modular and Open-Source Software Project for Quantum Simulations of Materials, *J. Phys. Condens. Matter.* **2009**, *21*, 395502.

(148) Yan, P.; Shu, S.; Zou, L.; Liu, Y.; Li, J.; Wei, F. Density Functional Theory Study of Active Sites on Nitrogen-Doped Graphene for Oxygen Reduction Reaction, *R. Soc. Open Sci.* **2021**, *8*, 210272–210282.

(149) Vanderbilt, D. Soft Self-Consistent Pseudopotentials in a Generalized Eigenvalue Formalism, *Phys. Rev. B* **1990**, *41*, 7892–7895.

(150) Perdew, J. P.; Burke, K.; Ernzerhof, M. Generalized Gradient Approximation Made Simple, *Phys. Rev. Lett.* **1996**, *77*, 3865–3868.

(151) Monkhorst, H. J.; Pack, J. D. Special Points for Brillouin-Zone Integrations, *Phys. Rev. B* **1976**, *13*, 5188–5191.

(152) Moellmann, J.; Grimme, S. DFT-D3 Study of Some Molecular Crystals, *J. Phys. Chem. C* **2014**, *118*, 7615–7621.

(153) Yutomo, E. B.; Noor, F. A.; Winata, T. Effect of the Number of Nitrogen Dopants on the Electronic and Magnetic Properties of Graphitic and Pyridinic N-Doped Graphene–A Density-Functional Study, *RSC Adv.* **2021**, *11*, 18371–18380.

(154) Tang, W.; Sanville, E.; Henkelman, G. A Grid-Based Bader Analysis Algorithm Without Lattice Bias, *J. Phys. Condens. Matter* **2009**, *21*, 084204 (1–7).

(155) Henkelman, G.; Arnaldsson, A.; Jónsson, H. A Fast and Robust Algorithm for Bader Decomposition of Charge Density, *Comput. Mater. Sci.* **2006**, *36*, 354–360.

(156) Momma, K.; Izumi, F. VESTA: A Three-Dimensional Visualization System for Electronic and Structural Analysis, *J. Appl. Crystallogr.* **2008**, *41*, 653–658.

(157) Kühne, T. D.; Iannuzzi, M.; Del Ben, M.; Rybkin, V. V.; Seewald, P.; Stein, F.; Laino, T.; Khaliullin, R. Z.; Schütt, O.; Schiffmann, F., et al. CP2K: An Electronic Structure and Molecular Dynamics Software Package-Quickstep: Efficient and Accurate Electronic Structure Calculations, *J. Chem. Phys.* **2020**, *152*, 194103 (1–47).

(158) Goedecker, S.; Teter, M.; Hutter, J. Separable Dual-Space Gaussian Pseudopotentials, *Phys. Rev. B* **1996**, *54*, 1703–1710.

(159) Evans, D. J.; Holian, B. L. The Nose–Hoover Thermostat, *J. Chem. Phys.* **1985**, *83*, 4069–4074.

(160) Neto, A. C.; Guinea, F.; Peres, N. M.; Novoselov, K. S.; Geim, A. K. The Electronic Properties of Graphene, *Rev. Mod. Phys.* **2009**, *81*, 109–162.

(161) Pham, T. T.; Pham, T. N.; Chihaia, V.; Vu, Q. A.; Trinh, T. T.; Pham, T. T., et al. How do the Doping Concentrations of N and B in Graphene Modify the Water Adsorption?, *RSC Adv.* **2021**, *11*, 19560–19568.

(162) Hou, Z.; Wang, X.; Ikeda, T.; Terakura, K.; Oshima, M.; Kakimoto, M.-a.; Miyata, S. Interplay Between Nitrogen Dopants and Native Point Defects in Graphene, *Phys. Rev. B* **2012**, *85*, 165439 (1–9).

(163) Shin, H.; Kang, S.; Koo, J.; Lee, H.; Kim, J.; Kwon, Y. Cohesion Energetics of Carbon Allotropes: Quantum Monte Carlo Study, *J. Chem. Phys* **2014**, *140*, 114702 (1–6).

(164) Wang, X.; Sun, G.; Routh, P.; Kim, D.-H.; Huang, W.; Chen, P. Heteroatom-Doped Graphene Materials: Syntheses, Properties and Applications, *Chem. Soc. Rev.* **2014**, *43*, 7067–7098.

(165) Jalili, S.; Vaziri, R. Study of the Electronic Properties of Li-Intercalated Nitrogen Doped Graphite, *Mol. Phys.* **2011**, *109*, 687–694.

(166) Purser, G. H. The Significance of the Bond Angle in Sulfur Dioxide, *J. Environ. Chem. Eng.* **1989**, *66*, 710–713.

(167) Kumar, V.; Bano, A.; Roy, D. R. First-Principles Calculations of SiBi Nanosheets as Sensors for Oxygen-Containing Gases, *ACS Appl. Nano Mater.* **2021**, *4*, 2440–2451.

(168) Meng, R.-S.; Cai, M.; Jiang, J.-K.; Liang, Q.-H.; Sun, X.; Yang, Q.; Tan, C.-J.; Chen, X.-P. First Principles Investigation of Small Molecules Adsorption on Antimonene, *IEEE Elec. Dev. Lett.* **2016**, *38*, 134–137.

(169) Qin, H.; Feng, C.; Luan, X.; Yang, D. First-Principles Investigation of Adsorption Behaviors of Small Molecules on Penta-Graphene, *Nanoscale Res. Lett.* **2018**, *13*, 1–7.

(170) Feng, C.; Qin, H.; Yang, D.; Zhang, G. First-Principles Investigation of the Adsorption Behaviors of CH_2O on BN, AlN, GaN, InN, BP, and P Monolayers, *Mater.* **2019**, *12*, 676 (1–8).

(171) Oprea, A.; Bârsan, N.; Weimar, U. Work Function Changes in Gas Sensitive Materials: Fundamentals and Applications, *Sens. Actuators B Chem.* **2009**, *142*, 470–493.

(172) Thomas, S.; Kumar, V.; Roy, D. R.; Zaeem, M. A. Two-Dimensional Boron–Phosphorus Monolayer for Reversible NO_2 Gas Sensing, *ACS Appl. Nano Mater.* **2020**, *3*, 10073–10081.

(173) Xiong, H.; Zhang, H.; Gan, L. A New Bifunctional C_3N Nanosheet of NO_2, SO_2 Gas Sensor and CO_2 Separation: A First-Principles Study, *Physica E Low Dimens. Syst. Nanostruct.* **2021**, *126*, 114463 (1–7).

(174) Hussain, T.; Singh, D.; Gupta, S. K.; Karton, A.; Sonvane, Y.; Ahuja, R. Efficient and Selective Sensing of Nitrogen-Containing Gases by Si_2BN Nanosheets Under Pristine and Pre-Oxidized Conditions, *Appl. Surf. Sci.* **2019**, *469*, 775–780.

(175) Fan, X.; Elgammal, K.; Smith, A. D.; Östling, M.; Delin, A.; Lemme, M. C.; Niklaus, F. Humidity and CO_2 Gas Sensing Properties of Double-Layer Graphene, *Carbon* **2018**, *127*, 576–587.

(176) Jia, Y.; Zhuang, G.; Wang, J. Electric Field Induced Silicon Carbide Nanotubes: A Promising Gas Sensor for Detecting SO_2, *J. Phys. D: Appl. Phys.* **2012**, *45*, 065305 (1–8).

(177) Xiao, M.; Zhang, B.; Song, H.; Lv, Y.; Xiao, B. Effects of External Electric Field on Adsorption Behavior of Organic Molecules on Stanene: Highly Sensitive Sensor Devices, *Solid State Commun.* **2021**, *338*, 114459 (1–7).

(178) Pham, K. D.; Dinh, P. C.; Vu, T. V.; Luong, H. L.; Hoang, D.-Q.; Khyzhun, O.; Van Ngoc, H., et al. Effects of Electric Field and Biaxial Strain on the (NO_2, NO, O_2, and SO_2) Gas Adsorption Properties of Sc_2CO_2 Monolayer, *Micro and Nanostr.* **2022**, *163*, 107135 (1–12).

(179) Weintrub, B. I.; Hsieh, Y.-L.; Kovalchuk, S.; Kirchhof, J. N.; Greben, K.; Bolotin, K. I. Generating Intense Electric Fields in 2D Materials by Dual Ionic Gating, *Nat. Commun.* **2022**, *13*, 1–6.

(180) Srivastava, S.; Pal, P.; Sharma, D. K.; Kumar, S.; Senguttuvan, T.; Gupta, B. K. Ultrasensitive Boron–Nitrogen-Codoped CVD Graphene-Derived NO_2 Gas Sensor, *ACS Mater.* **2022**, *2*, 356–366.

(181) Singh, A. K.; Yen, C.-C.; Wen, C.-F.; Horng, R.-H.; Wuu, D.-S. Growth and Characterization of Sputtered ZnO: $ZnGa_2O_4$ Dual-Phase Films on Sapphire Substrates for NO Gas-Sensing Applications, *ACS Appl. Elec. Mater.* **2023**, 2574–2582.

(182) Yu, L.; Li, F. Metal Dimers Embedded Vertically in Defect-Graphene as Gas Sensors: A First-Principles Study, *Phys. Chem. Chem. Phys.* **2022**, *24*, 9842–9847.

(183) Qin, D.; Chen, T.; Xie, L.; Yang, N.; Luo, C.; Zhou, G. Design and Analysis of a 2D Grapheneplus (G+)-Based Gas Sensor for the Detection of Multiple Organic Gases, *Phys. Chem. Chem. Phys.* **2023**, *25*, 29315–29326.

(184) Fiori, G.; Bonaccorso, F.; Iannaccone, G.; Palacios, T.; Neumaier, D.; Seabaugh, A.; Banerjee, S. K.; Colombo, L. Electronics Based on Two-Dimensional Materials, *Nat. Nanotech.* **2014**, *9*, 768–779.

(185) Li, R.; Cheng, Y.; Huang, W. Recent Progress of Janus 2D Transition Metal Chalcogenides: From Theory to Experiments, *Small* **2018**, *14*, 1802091 (1–11).

(186) Babariya, B.; Raval, D.; Gupta, S. K.; Gajjar, P. Selective and Sensitive Toxic Gas-Sensing Mechanism in a 2D Janus MoSSe Monolayer, *Phys. Chem. Chem. Phys.* **2022**, *24*, 15292–15304.

(187) Pham, T.; Li, G.; Bekyarova, E.; Itkis, M. E.; Mulchandani, A. MoS_2-Based Optoelectronic Gas Sensor with Sub-Parts-Per-Billion Limit of NO_2 Gas Detection, *ACS Nano* **2019**, *13*, 3196–3205.

(188) Fan, D.; Lu, S.; Chen, C.; Jiang, M.; Li, X.; Hu, X. Versatile Two-Dimensional Boron Monosulfide Polymorphs with Tunable Bandgaps and Superconducting Properties, *Appl. Phys. Lett.* **2020**, *117*, 013103 (1–5).

(189) Demirci, S.; Avazlı, N.; Durgun, E.; Cahangirov, S. Structural and Electronic Properties of Monolayer Group III Monochalcogenides, *Phys. Rev. B* **2017**, *95*, 115409 (1–8).

(190) Kusaka, H.; Ishibiki, R.; Toyoda, M.; Fujita, T.; Tokunaga, T.; Yamamoto, A.; Miyakawa, M.; Matsushita, K.; Miyazaki, K.; Li, L., et al. Crystalline Boron Monosulfide Nanosheets with Tunable Bandgaps, *J. Mater. Chem. A* **2021**, *9*, 24631–24640.

(191) Mishra, P.; Singh, D.; Sonvane, Y.; Ahuja, R. Metal-Functionalized 2D Boron Sulfide Monolayer Material Enhancing Hydrogen Storage Capacities, *J. Appl. Phys.* **2020**, *127*, 184305 (1–10).

(192) Mishra, P.; Singh, D.; Sonvane, Y.; Ahuja, R. Two-Dimensional Boron Monochalcogenide Monolayer for Thermoelectric Material, *Sustain. Energy Fuels* **2020**, *4*, 2363–2369.

(193) Mortazavi, B.; Rabczuk, T. Boron Monochalcogenides; Stable and Strong Two-Dimensional Wide Band-Gap Semiconductors, *Energies* **2018**, *11*, 1573–1583.

(194) Radisavljevic, B.; Radenovic, A.; Brivio, J.; Giacometti, V.; Kis, A. Single-Layer MoS_2 Transistors, *Nat. Nanotechnol.* **2011**, *6*, 147–150.

(195) Zhao, H.; Ye, J.; Song, W.; Zhao, D.; Kang, M.; Shen, H.; Li, Z. Insights into the Surface Oxygen Functional Group-Driven Fast and Stable Sodium Adsorption on Carbon, *ACS Appl. Mater. Interfaces* **2020**, *12*, 6991–7000.

(196) Ostadhossein, A.; Guo, J.; Simeski, F.; Ihme, M. Functionalization of 2D Materials for Enhancing OER/ORR Catalytic Activity in Li–Oxygen Batteries, *Commun. Chem.* **2019**, *2*, 95(1–11).

(197) Guo, Y.; Guo, W. Magnetism in Oxygen-Functionalized Hexagonal Boron Nitride Nanosheet on Copper Substrate, *J. Phys. Chem. C* **2015**, *119*, 873–878.

(198) Zaki, S. E.; Basyooni, M. A.; Shaban, M.; Rabia, M.; Eker, Y. R.; Attia, G. F.; Yilmaz, M.; Ahmed, A. M. Role of Oxygen Vacancies in Vanadium Oxide and Oxygen Functional Groups in Graphene Oxide for Room Temperature CO_2 Gas Sensors, *Sens. Actuator A Phys.* **2019**, *294*, 17–24.

(199) Hohenberg, P.; Kohn, W. Inhomogeneous Electron Gas, *Phys. Rev. B* **1964**, *136*, 864–871.

(200) Burke, K. Perspective on Density Functional Theory, *J. Chem. Phys.* **2012**, *136*, 150901 (1–9).

(201) Blöchl, P. E. Projector Augmented-Wave Method, *Phys. Rev. B* **1994**, *50*, 17953–19979.

(202) Baroni, S.; De Gironcoli, S.; Dal Corso, A.; Giannozzi, P. Phonons and Related Crystal Properties from Density-Functional Perturbation Theory, *Rev. Mod. Phys.* **2001**, *73*, 515–562.

(203) Xie, J.; Zhang, Z.; Yang, D.; Xue, D.; Si, M. Theoretical Prediction of Carrier Mobility in Few-Layer BC_2N, *J. Phys. Chem. Lett.* **2014**, *5*, 4073–4077.

(204) Gupta, S.; Zhang, J.-J.; Lei, J.; Yu, H.; Liu, M.; Zou, X.; Yakobson, B. I. Two-Dimensional Transition Metal Dichalcogenides: A Theory and Simulation Perspective, *Chem. Rev.* **2025**, *125*, 786–834.

(205) Cheng, L.; Liu, Y. What Limits the Intrinsic Mobility of Electrons and Holes in Two Dimensional Metal Dichalcogenides?, *J. Am. Chem. Soc.* **2018**, *140*, 17895–17900.

(206) Nath, U.; Sarma, M. Pyridinic Dominance N-Doped Graphene: A Potential Material for SO_2 Gas Detection, *J. Phys. Chem. A* **2023**, *127*, 1112–1123.

(207) Sanville, E.; Kenny, S. D.; Smith, R.; Henkelman, G. Improved Grid-Based Algorithm for Bader Charge Allocation, *J. Comput. Chem.* **2007**, *28*, 899–908.

(208) Do, V.-N. Non-Equilibrium Green Function Method: Theory and Application in Simulation of Nanometer Electronic Devices, *Adv. Nat. Sci.: Nanosci. Nanotechnol.* **2014**, *5*, 033001 (1–21).

(209) Ou, P.; Song, P.; Liu, X.; Song, J. Superior Sensing Properties of Black Phosphorus as Gas Sensors: A Case Study on the Volatile Organic Compounds, *Adv. Theory Simul.* **2019**, *2*, 1800103 (1–9).

(210) Haidar, E.-A.; Tawfik, S. A.; Stampfl, C.; Hirao, K.; Yoshizawa, K.; El-Demerdash, S. H.; Nakajima, T.; El-Nahas, A. M. Electronic Transport Investigation of Redox-Switching of Azulenequinones/Hydroquinones via First-Principles Studies, *Phys. Chem. Chem. Phys.* **2019**, *21*, 17859–17867.

(211) Morales-García, Á.; Valero, R.; Illas, F. An Empirical, Yet Practical way to Predict the Band Gap in Solids by using Density Functional Band Structure Calculations, *J. Phys. Chem. C* **2017**, *121*, 18862–18866.

(212) Wang, C.; You, Y.; Choi, J.-H. First-Principles Study of Defects in Blue Phosphorene, *Mater. Res. Express* **2019**, *7*, 015005 (1–8).

(213) Peng, B.; Zhang, H.; Shao, H.; Xu, Y.; Zhang, R.; Zhu, H. The Electronic, Optical, and Thermodynamic Properties of Borophene from First-Principles Calculations, *J. Mater. Chem. C* **2016**, *4*, 3592–3598.

(214) Ji, L.; Shi, J.; Zhang, Z.; Wang, J.; Zhang, J.; Tao, C.; Cao, H. Theoretical Prediction of High Electron Mobility in Multilayer MoS_2 Heterostructured with $MoSe_2$, *J. Chem. Phys.* **2018**, *148*, 014704 (1–8).

(215) Guo, F.; Liu, Z.; Zhu, M.; Zheng, Y. Electron–Phonon Scattering Limited Hole Mobility at Room Temperature in a MoS_2 Monolayer: First-Principles Calculations, *Phys. Chem. Chem. Phys.* **2019**, *21*, 22879–22887.

(216) Jin, Z.; Li, X.; Mullen, J. T.; Kim, K. W. Intrinsic Transport Properties of Electrons and Holes in Monolayer Transition-Metal Dichalcogenides, *Phys. Rev. B* **2014**, *90*, 045422 (1–7).

(217) Mir, S. H.; Yadav, V. K.; Singh, J. K. Recent Advances in the Carrier Mobility of Two-Dimensional Materials: A Theoretical Perspective, *ACS Omega* **2020**, *5*, 14203–14211.

(218) Xiao, J.; Long, M.; Li, X.; Xu, H.; Huang, H.; Gao, Y. Theoretical Prediction of Electronic Structure and Carrier Mobility in Single-Walled MoS_2 Nanotubes, *Sci. Rep.* **2014**, *4*, 4327–4334.

(219) Ju, L.; Bie, M.; Shang, J.; Tang, X.; Kou, L. Janus Transition Metal Dichalcogenides: A Superior Platform for Photocatalytic Water Splitting, *J. Phys.: Mater.* **2020**, *3*, 022004–022015.

(220) Kadhim, M. M.; Sadoon, N.; Gheni, H. A.; Hachim, S. K.; Majdi, A.; Abdullaha, S. A.; Rheima, A. M. Application of B_3O_3 Monolayer as an Electrical Sensor for Detection of Formaldehyde Gas: A DFT Study, *Comput. Theor. Chem.* **2023**, *1219*, 113941–113947.

(221) Leenaerts, O.; Partoens, B.; Peeters, F. Adsorption of H_2O, NH_3, CO, NO_2, and NO on Graphene: A First-Principles Study, *Phys. Rev. B* **2008**, *77*, 125416 (1–6).

(222) Bui, V. Q.; Pham, T. T.; Le, D. A.; Thi, C. M.; Le, H. M. A First-Principles Investigation of Various Gas (CO, H_2O, NO, and O_2) Adsorptions on a WS_2 Monolayer: Stability and Electronic Properties, *J. Phys.: Condens. Matter* **2015**, *27*, 305005 (1–11).

(223) Feng, J. W.; Liu, Y. J.; Wang, H. X.; Zhao, J. X.; Cai, Q. H.; Wang, X. Z. Gas Adsorption on Silicene: a Theoretical Study, *Comput. Mater. Sci.* **2014**, *87*, 218–226.

(224) Wang, Z.; Zhang, Y.; Ren, Y.; Wang, M.; Zhang, Z.; Zhao, W.; Yan, J.; Zhai, C.; Yun, J. NO Gas Adsorption Properties of MoS_2 from Monolayer to Trilayer: A First-Principles Study, *Mater. Res. Express* **2021**, *8*, 015024 (1–9).

(225) Cai, Y.; Ke, Q.; Zhang, G.; Zhang, Y.-W. Energetics, Charge Transfer, and Magnetism of Small Molecules Physisorbed on Phosphorene, *J. Phys. Chem. C* **2015**, *119*, 3102–3110.

(226) Bermudez, V. Computational Study of the Adsorption of NO_2 on Monolayer MoS_2, *J. Phys. Chem. C* **2020**, *124*, 15275–15284.

(227) Chakraborty, D.; Johari, P. First-Principles Investigation of the 1T-$HfTe_2$ Nanosheet for Selective Gas Sensing, *ACS Appl. Nano Mater.* **2020**, *3*, 5160–5171.

(228) Liang, X.; Ng, S.-P.; Ding, N.; Wu, C.-M. L. Thermal Stability of NO on Ga-Doped Graphene and Effect of External Electric Field, *Comput. Mater. Sci.* **2018**, *151*, 214–221.

(229) Zhang, J.; Liu, X.; Neri, G.; Pinna, N. Nanostructured Materials for Room-Temperature Gas Sensors, *Adv. Mater.* **2016**, *28*, 795–831.

(230) Aasi, A.; Javahersaz, R.; Mehdi Aghaei, S.; Panchapakesan, B. Novel Green Phosphorene as a Superior Gas Sensor for Dissolved Gas Analysis in Oil Transformers: Using DFT Method, *Mol. Simul.* **2022**, *48*, 541–550.

(231) Reji, R. P.; Balaji, S. K. C.; Sivalingam, Y.; Kawazoe, Y.; Velappa Jayaraman, S. First-Principles Density Functional Theory Calculations on the Potential of Sc_2CO_2 MXene Nanosheets as a Dual-Mode Sensor for Detection of Volatile Organic Compounds in Exhaled Human Breath, *ACS Appl. Nano Mater.* **2023**, *6*, 5345–5356.

(232) Hu, G.; Fung, V.; Huang, J.; Ganesh, P. Work Function Engineering of 2D Materials: The Role of Polar Edge Reconstructions, *J. Phys. Chem. Lett.* **2021**, *12*, 2320–2326.

(233) Wenna, H.; Xuefeng, C.; Minglei, J.; Fengzhu, R.; Chengxiao, P.; Haigang, Y.; Qinfen, G.; Bing, W.; Huabing, Y. A Direct Z-Scheme g-C_6N_6/InP van der Waals Heterostructure: A Promising Photocatalyst for High-Efficiency Overall Water Splitting, *J. Phys. D: Appl. Phys.* **2022**, *55*, 264001 (1–9).

(234) Zhao, J.; Huang, X.; Yin, Y.; Liao, Y.; Mo, H.; Qian, Q.; Guo, Y.; Chen, X.; Zhang, Z.; Hua, M. Two-Dimensional Gallium Oxide Monolayer for Gas-Sensing Application, *J. Phys. Chem. Lett.* **2021**, *12*, 5813–5820.

(235) Yang, N.; Chen, T.; Xu, Z.; Liu, G.; Dong, X.; Yu, Y.; Xiao, X. Studying the Adsorption of Gas Molecules and Defects on Modulating the Electronic Transport Characteristics of Monolayer Penta-BN_2-Based Devices, *Langmuir* **2023**, *39*, 15507–15516.

(236) Kou, L.; Frauenheim, T.; Chen, C. Phosphorene as a Superior Gas Sensor: Selective Adsorption and Distinct I-V Response, *J. Phys. Chem. Lett.* **2014**, *5*, 2675–2681.

(237) Ran, X.; Hou, P.; Song, J.; Song, H.; Zhong, X.; Wang, J. Negative Differential Resistance Effect in Resistive Switching Devices Based on h-$LuFeO_3$/$CoFe_2O_4$ Heterojunctions, *Phys. Chem. Chem. Phys.* **2020**, *22*, 5819–5825.

(238) Ren, H.; Li, Q.-X.; Luo, Y.; Yang, J. Graphene Nanoribbon as a Negative Differential Rsistance Device, *Appl. Phys. Lett.* **2009**, *94*, 173110 (1–3).

(239) Nguyen, P. D.; Nguyen, T. C.; Hossain, F. M.; Huynh, D. H.; Evans, R.; Skafidas, E. Negative Differential Resistance Effect in Planar Graphene Nanoribbon Break Junctions, *Nanoscale* **2015**, *7*, 289–293.

(240) Babar, V.; Sharma, S.; Schwingenschlogl, U. New Paradigm for Gas Sensing by Two-Dimensional Materials, *J. Phys. Chem. C* **2019**, *123*, 13104–13109.

(241) Shaheen, A.; Ali, M.; Othman, W.; Tit, N. Origins of Negative Differential Resistance in N-Doped ZnO Nano-Ribbons: Ab-Initio Investigation, *Sci. Rep.* **2019**, *9*, 9914 (1–13).

(242) Tiwari, D. L.; Sivasankaran, K. Nitrogen-Doped NDR Behavior of Double Gate Graphene Field Effect Transistor, *Superlattices Microstruct.* **2019**, *136*, 106308.

(243) Zhao, S.; Xue, J.; Kang, W. Gas Adsorption on MoS_2 Monolayer from First-Principles Calculations, *Chem. Phys. Lett.* **2014**, *595*, 35–42.

(244) Kunkel, C.; Vines, F.; Illas, F. Transition Metal Carbides as Novel Materials for CO_2 Capture, Storage, and Activation, *Energy Environ. Sci.* **2016**, *9*, 141–144.

(245) Parey, V.; Abraham, B. M.; Mir, S. H.; Singh, J. K. High-Throughput Screening of Atomic Defects in MXenes for CO_2 Capture, Activation, and Dissociation, *ACS Appl. Mater. Interfaces* **2021**, *13*, 35585–35594.

(246) Ye, J.; Liu, C.; Ge, Q. DFT Study of CO_2 Adsorption and Hydrogenation on the In_2O_3 Surface, *J. Phys. Chem. C* **2012**, *116*, 7817–7825.

(247) Xiao, J.; Frauenheim, T. Theoretical Insights into CO_2 Activation and Reduction on the Ag (111) Monolayer Supported on a ZnO (0001) Substrate, *J. Phys. Chem. C* **2013**, *117*, 1804–1808.

(248) Di, J.; Song, P.; Zhu, C.; Chen, C.; Xiong, J.; Duan, M.; Long, R.; Zhou, W.; Xu, M.; Kang, L., et al. Strain-Engineering of $Bi_{12}O_{17}Br_2$ Nanotubes for Boosting Photocatalytic CO_2 Reduction, *ACS Mater. Lett.* **2020**, *2*, 1025–1032.

(249) Chen, M.; Zhuo, Z.; Lv, H.; Wu, X. Enhanced Activation of CO_2 on h-BN Nanosheets via Forming a Donor–Acceptor Heterostructure with 2D M_2X Electrenes, *J. Phys. Chem. C* **2021**, *125*, 18762–18769.

(250) Kuriakose, N.; Mondal, K.; Ghosh, P., et al. CO_2 Capture, Activation and Dissociation on the Ti_2C Surface and Ti_2C MXene: The Role of Surface Structure, *Phys. Chem. Chem. Phys.* **2020**, *22*, 14599–14612.

(251) Jiao, Y.; Du, A.; Zhu, Z.; Rudolph, V.; Lu, G. Q. M.; Smith, S. C. A Density Functional Theory Study on CO_2 Capture and Activation by Graphene-Like Boron Nitride with Boron Vacancy, *Catal. Today* **2011**, *175*, 271–275.

(252) Sun, Q.; Li, Z.; Searles, D. J.; Chen, Y.; Lu, G.; Du, A. Charge-Controlled Switchable CO_2 Capture on Boron Nitride Nanomaterials, *J. Am. Chem. Soc.* **2013**, *135*, 8246–8253.

(253) He, C.; Wang, R.; Xiang, D.; Li, X.; Fu, L.; Jian, Z.; Huo, J.; Li, S. Charge-Regulated CO_2 Capture Capacity of Metal Atom Embedded Graphyne: A First-Principles Study, *Appl. Surf. Sci.* **2020**, *509*, 145392–145399.

(254) Tan, X.; Tahini, H. A.; Smith, S. C. Borophene as a Promising Material for Charge-Modulated Switchable CO_2 Capture, *ACS Appl. Mater. Interfaces* **2017**, *9*, 19825–19830.

(255) He, H.; Sekoulopoulos, S.; Zygmunt, S. Single-Electron Activation of CO_2 on Graphene-Supported ZnO Nanoclusters: Effects of Doping in the Support, *J. Phys. Chem. C* **2016**, *120*, 16732–16740.

(256) Zhang, H.; Li, J.; Xi, S.; Du, Y.; Hai, X.; Wang, J.; Xu, H.; Wu, G.; Zhang, J.; Lu, J., et al. A Graphene-Supported Single-Atom FeN_5 Catalytic Site for Efficient Electrochemical CO_2 Reduction, *Angew. Chem. Int. Ed.* **2019**, *131*, 15013–15018.

(257) Mannix, A. J.; Zhou, X.-F.; Kiraly, B.; Wood, J. D.; Alducin, D.; Myers, B. D.; Liu, X.; Fisher, B. L.; Santiago, U.; Guest, J. R., et al. Synthesis of Borophenes: Anisotropic, Two-Dimensional Boron Polymorphs, *Science* **2015**, *350*, 1513–1516.

(258) Tang, H.; Ismail-Beigi, S. First-Principles Study of Boron Sheets and Nanotubes, *Phys. Rev. B* **2010**, *82*, 115412–115431.

(259) Qiu, L.; Zhang, X.; Kong, X.; Mitchell, I.; Yan, T.; Kim, S. Y.; Yakobson, B. I.; Ding, F. Theory of Sigma Bond Resonance in Flat Boron Materials, *Nat. Commun.* **2023**, *14*, 1804–1811.

(260) Yan, X.; Wang, S.; Sun, Y.; Liu, Y.; Wang, Y.; Yang, G. Semiconducting Bilayer Borophene with High Carrier Mobility, *J. Phys. Chem. Lett.* **2023**, *14*, 9698–9704.

(261) Tang, H.; Ismail-Beigi, S. Self-Doping in Boron Sheets from First Principles: A Route to Structural Design of Metal Boride Nanostructures, *Phys. Rev. B* **2009**, *80*, 134113–134120.

(262) Luo, W.; Wang, H.; Wang, Z.; Liu, G.; Liu, S.; Ouyang, C. First-Principles Study of χ 3-Borophene for Charge-Modulated Switchable CO_2 Capture, *Phys. Chem. Chem. Phys.* **2020**, *22*, 8864–8869.

(263) Li, Q.; Kolluru, V. S. C.; Rahn, M. S.; Schwenker, E.; Li, S.; Hennig, R. G.; Darancet, P.; Chan, M. K.; Hersam, M. C. Synthesis of Borophane Polymorphs Through Hydrogenation of Borophene, *Science* **2021**, *371*, 1143–1148.

(264) Mu, Y.; Li, S.-D. First-Principles Study on the Oxidation of Supported β_{12}-Borophene, *J. Phys. Chem. C* **2020**, *124*, 28145–28151.

(265) Ebrahimi, M. The Birth of Bilayer Borophene, *Nat. Chem.* **2022**, *14*, 3–4.

(266) Li, L.; Schultz, J. F.; Mahapatra, S.; Liu, X.; Zhang, X.; Hersam, M. C.; Jiang, N. Atomic-Scale Insights into the Interlayer Characteristics and Oxygen Reactivity of Bilayer Borophene, *Angew. Chem. Int. Ed.* **2023**, *62*, e202306590.

(267) Nakhaee, M.; Ketabi, S.; Peeters, F. Dirac Nodal Line in Bilayer Borophene: Tight-Binding Model and Low-Energy Effective Hamiltonian, *Phys. Rev. B* **2018**, *98*, 115413–115421.

(268) Mozvashi, S. M.; Givi, M. R.; Tagani, M. B. The Effects of Substrate and Stacking in Bilayer Borophene, *Sci. Rep.* **2022**, *12*, 13661–13670.

(269) Tang, H.; Ismail-Beigi, S. Novel Precursors for Boron Nanotubes: The Competition of Two-Center and Three-Center Bonding in Boron Sheets, *Phys. Rev. Lett.* **2007**, *99*, 115501 (1–4).

(270) Qureshi, A. H.; Sun, Y.; Wang, L.; Wang, Y.; Yao, X.; Zhang, X. Bilayer Borophene Allotropes: Structural Stabilities and Electronic Properties, *ACS Appl. Nano Mater.* **2024**, *7*, 15685–15692.

(271) Roy, P.; Ghoshal, S.; Pramanik, A.; Sarkar, P. Single B-vacancy Enriched α1-Borophene Sheet: An Efficient Metal-Free Electrocatalyst for CO_2 Reduction, *Phys. Chem. Chem. Phys.* **2023**, *25*, 25018–25028.

(272) Ghosh, A.; Goswami, B.; Pal, S.; Sarkar, P. How the Stacking Pattern Influences the Charge Transfer Dynamics of van der Waals Heterostructures: An Answer from a Time-Domain *Ab initio* Study, *J. Phys. Chem. Lett.* **2023**, *14*, 7672–7679.

(273) Wu, X.; Dai, J.; Zhao, Y.; Zhuo, Z.; Yang, J.; Zeng, X. C. Two-Dimensional Boron Monolayer Sheets, *ACS Nano* **2012**, *6*, 7443–7453.

(274) Xiong, J.; Di, J.; Xia, J.; Zhu, W.; Li, H. Surface Defect Engineering in 2D Nanomaterials for Photocatalysis, *Adv. Funct. Mater.* **2018**, *28*, 1801983–1802001.

(275) Zhang, H.; Lv, R. Defect Engineering of Two-Dimensional Materials for Efficient Electrocatalysis, *J. Materiomics* **2018**, *4*, 95–107.

(276) Sun, T.; Zhang, G.; Xu, D.; Lian, X.; Li, H.; Chen, W.; Su, C. Defect Chemistry in 2D Materials for Electrocatalysis, *Mater. Today Energy* **2019**, *12*, 215–238.

(277) Hu, Z.; Wu, Z.; Han, C.; He, J.; Ni, Z.; Chen, W. Two-Dimensional Transition Metal Dichalcogenides: Interface and Defect Engineering, *Chem. Soc. Rev.* **2018**, *47*, 3100–3128.

(278) Mahmoudi, M.; Tan, X.; Smith, S. C. Enhanced Charge-Modulated Switchable CO_2 Capture on Graphene-like BeN_4 with Beryllium Vacancy, *J. Phys. Chem. C* **2022**, *126*, 18189–18197.

(279) Bal, K. M.; Neyts, E. C. Overcoming Old Scaling Relations and Establishing New Correlations in Catalytic Surface Chemistry: Combined Effect of Charging and Doping, *J. Phys. Chem. C* **2019**, *123*, 6141–6147.

(280) Löwdin, P.-O. On the Non-Orthogonality Problem Connected with the Use of Atomic Wave Functions in the Theory of Molecules and Crystals, *J. Chem. Phys.* **1950**, *18*, 365–375.

(281) Molavi, R.; Safaiee, R.; Sheikhi, M. Oxygen Adsorption Properties of Small Cobalt Oxide Clusters: Application Feasibility as Oxygen Gas Sensors, *Phys. Chem. Chem. Phys.* **2020**, *22*, 14889–14899.

(282) Hu, W.; Yang, J. Defects in Phosphorene, *J. Phys. Chem. C* **2015**, *119*, 20474–20480.

(283) Dhakal, R.; Nepal, S.; Ray, R.; Paudel, R.; Kaphle, G. Effect of Doping on SGS and Weak Half-Metallic Properties of Inverse Heusler Alloys, *J. Magn. Magn. Mater.* **2020**, *503*, 166588–166591.

(284) Jiang, J.; Yang, P.; Liou, J. J.; Liao, W.; Chai, Y. Defect Engineering of Two-Dimensional Materials Towards Next-Generation Electronics and Optoelectronics, *Nano Res.* **2023**, *16*, 3104–3124.

(285) Qin, H.; Sorkin, V.; Pei, Q.-X.; Liu, Y.; Zhang, Y.-W. Failure in Two-Dimensional Materials: Defect Sensitivity and Failure Criteria, *J. Appl. Mechanics* **2020**, *87*, 030802 (1–11).

(286) Fang, D.; Zhang, L.; Niu, Y.; Wang, Y.; Su, Q.; Wang, J.; Wang, C. Elevating the p-Band Centre of SnO_2 Nanosheets Through W Incorporation for Promoting CO_2 Electroreduction, *Dalton Trans.* **2022**, *51*, 541–552.

(287) Huang, B.; Zhuang, L. Fermi Softness: A Local Perspective on Surface Activity, Conceptual Density Functional Theory: Towards a New Chemical Reactivity Theory **2022**, *2*, 573–586.

(288) Hou, C.; Ming, S.; Chen, K.; Rong, J.; Yu, X.; Yu, L.; Hou, H. Mechanism of Nitrogen Coordination Modulation of Fe_Nx@ BP System Catalysts on the Activity of Oxygen Reduction Reaction, *J. Phys. Chem. C* **2024**, *128*, 3204–3213.

(289) Guo, X.; Zheng, H.; King, S.; Afanas' ev, V.; Baklanov, M.; de Marneffe, J.-F.; Nishi, Y.; Shohet, J. Defect-Induced Bandgap Narrowing in Low-k Dielectrics, *Appl. Phys. Lett.* **2015**, *107*, 082903–082906.

(290) Kumar, K.; Jamnuch, S.; Majidi, L.; Misal, S.; Ahmadiparidari, A.; Dato, M. A.; Sterbinsky, G. E.; Wu, T.; Salehi-Khojin, A.; Pascal, T. A., et al. Active States During the Reduction of CO_2 by a MoS_2 Electrocatalyst, *J. Phys. Chem. Lett.* **2023**, *14*, 3222–3229.

(291) Rawat, A.; Jena, N.; De Sarkar, A., et al. A Comprehensive Study on Carrier Mobility and Artificial Photosynthetic Properties in Group VI B Transition Metal Dichalcogenide Monolayers, *J. Mater. Chem. A* **2018**, *6*, 8693–8704.

(292) Xiang, H.; Zheng, Y.; Chen, Y.; Xu, Y.; Hu, T. S.; Feng, Y.; Zhou, Y.; Liu, S.; Chen, X. Self-Gating Enhanced Carrier Transfer in Semiconductor Electrocatalyst Verified in Microdevice, *Chin. Chem. Lett.* **2022**, *33*, 3221–3226.

(293) Ju, L.; Tan, X.; Mao, X.; Gu, Y.; Smith, S.; Du, A.; Chen, Z.; Chen, C.; Kou, L. Controllable CO_2 Electrocatalytic Reduction via Ferroelectric Switching on Single Atom Anchored In_2Se_3 Monolayer, *Nat. Commun.* **2021**, *12*, 5128–5137.

(294) Silveri, F.; Quesne, M. G.; Viñes, F.; Illas, F.; Catlow, C. R. A.; de Leeuw, N. H. Catalytic Reduction of Carbon Dioxide on the (001),(011), and (111) Surfaces of TiC and ZrC: A Computational Study, *J. Phys. Chem. C* **2022**, *126*, 5138–5150.

(295) Lou, Z.; Li, W.; Yuan, H.; Hou, Y.; Yang, H.; Wang, H. Structural Rule of N-Coordinated Single-Atom Catalysts for Electrochemical CO_2 Reduction, *J. Mater. Chem. A* **2022**, *10*, 3585–3594.

(296) González, S.; Illas, F.; Fierro, J. L., et al. Evidence for Spontaneous CO_2 Activation on Cobalt Surfaces, *Chem. Phys. Lett.* **2008**, *454*, 262–268.

(297) Wang, S.-G.; Liao, X.-Y.; Cao, D.-B.; Huo, C.-F.; Li, Y.-W.; Wang, J.; Jiao, H. Factors Controlling the Interaction of CO_2 with Transition Metal Surfaces, *J. Phys. Chem. C* **2007**, *111*, 16934–16940.

(298) Ko, J.; Kim, B.-K.; Han, J. W. Density Functional Theory Study for Catalytic Activation and Dissociation of CO_2 on Bimetallic Alloy Surfaces, *J. Phys. Chem. C* **2016**, *120*, 3438–3447.

(299) Lee, J.; Sorescu, D. C.; Deng, X. Electron-Induced Dissociation of CO_2 on TiO_2 (110), *J. Am. Chem. Soc.* **2011**, *133*, 10066–10069.

(300) Liu, L.; Zhao, C.; Li, Y. Spontaneous Dissociation of CO_2 to CO on Defective Surface of Cu(I)/TiO_{2-x} Nanoparticles at Room Temperature, *J. Phys. Chem. C* **2012**, *116*, 7904–7912.

(301) Daghero, D.; Paolucci, F.; Sola, A.; Tortello, M.; Ummarino, G.; Agosto, M.; Gonnelli, R.; Nair, J. R.; Gerbaldi, C. Large Conductance Modulation of Gold Thin Films by Huge Charge Injection via Electrochemical Gating, *Phys. Rev. Lett.* **2012**, *108*, 066807–066811.

(302) Guo, Y.; Kang, X.; Gao, S.; Duan, X. Charge-Controlled Switchable CO_2 Capture and Gas Separation using BC_3 Nanosheets, *Phys. Chem. Chem. Phys.* **2023**, *25*, 12420–12425.

(303) Li, X.; Guo, T.; Zhu, L.; Ling, C.; Xue, Q.; Xing, W. Charge-Modulated CO_2 Capture of C_3N Nanosheet: Insights From DFT Calculations, *Chem. Eng, J.* **2018**, *338*, 92–98.

(304) Tan, X.; Kou, L.; Tahini, H. A.; Smith, S. C. Conductive Graphitic Carbon Nitride as an Ideal Material for Electrocatalytically Switchable CO_2 Capture, *Sci. Rep.* **2015**, *5*, 17636–17643.

(305) Xia, W.; Hu, W.; Li, Z.; Yang, J. A First-Principles Study of Gas Adsorption on Germanene, *Phys. Chem. Chem. Phys.* **2014**, *16*, 22495–22498.

(306) Zayed, M. E. et al. Electrochemical Reduction of Carbon Dioxide to Methanol on Defective Graphene Supported Cu Based Single-Atom Catalysts: A First Principles Approach**, 2022**.

(307) Zhang, L.; Zhao, Z.-J.; Gong, J. Nanostructured Materials for Heterogeneous Electrocatalytic CO_2 Reduction and Their Related Reaction Mechanisms, *Angew. Chem. Int. Ed.* **2017**, *56*, 11326–11353.

(308) Fonseca, H. A.; Verga, L. G.; Da Silva, J. L. Theoretical Tuning of the Cu/S Ratio on Two-Dimensional CuS_x Materials for the CO_2 Electrochemical Reduction Reaction, *J. Phys. Chem. C* **2023**, *127*, 24118–24128.

(309) Nascimento, G. R.; Neto, M. M.; Da Silva, J. L.; Galvão, B. R. Influence of Co Doping on Copper Nanoclusters for CO_2 Electroreduction, *ACS Omega* **2024**, *9*, 47114–47121.

(310) Pawar, A. A.; Bandal, H. A.; Rajkamal, A.; Kim, H. Understanding the Impact of Reaction Parameters on Electrochemical Reduction of CO_2 to Methanol: Activity Relationship of Cuprite@ Polyaniline Electrodes, *J. Electroanal. Chem.* **2023**, *946*, 117721–117732.

(311) Lu, Q.; Jiao, F. Electrochemical CO_2 Reduction: Electrocatalyst, Reaction Mechanism, and Process Engineering, *Nano Energy* **2016**, *29*, 439–456.

(312) Zhao, S.; Li, S.; Guo, T.; Zhang, S.; Wang, J.; Wu, Y.; Chen, Y. Advances in Sn-Based Catalysts for Electrochemical CO_2 Reduction, *Nanomicro Lett.* **2019**, *11*, 1–19.

(313) Yang, Z.; Oropeza, F. E.; Zhang, K. H. P-block Metal-Based (Sn, In, Bi, Pb) Electrocatalysts for Selective Reduction of CO_2 to Formate, *APL Mater.* **2020**, *8*, 060901(1–26).

(314) Kumar, B.; Muchharla, B.; Dikshit, M.; Dongare, S.; Kumar, K.; Gurkan, B.; Spurgeon, J. M. Electrochemical CO_2 Conversion Commercialization Pathways: A Concise Review on Experimental Frontiers and Technoeconomic Analysis, *Environ. Sci. Technol. Lett.* **2024**, *11*, 1161–1174.

(315) Wiranarongkorn, K.; Eamsiri, K.; Chen, Y.-S.; Arpornwichanop, A. A Comprehensive Review of Electrochemical Reduction of CO_2 to Methanol: Technical and Design aspects, *J. CO_2 Util.* **2023**, *71*, 102477–102493.

(316) Liu, L.; Wang, C.; Xue, F.; Li, J.; Zhang, H.; Lu, S.; Su, X.; Cao, B.; Huo, W.; Fang, T. DFT Investigation of CO_2 Hydrogenation to Methanol Over Ir-Doped Cu Surface, *Mol. Catal.* **2022**, *528*, 112460–112469.

(317) Farooqi, S. A.; Farooqi, A. S.; Sajjad, S.; Yan, C.; Victor, A. B. Electrochemical Reduction of Carbon Dioxide into Valuable Chemicals: A Review, *Environ. Chem. Lett.* **2023**, *21*, 1515–1553.

(318) Nie, X.; Luo, W.; Janik, M. J.; Asthagiri, A. Reaction Mechanisms of CO_2 Electrochemical Reduction on Cu(1 1 1) Determined with Density Functional Theory, *J. Catal.* **2014**, *312*, 108–122.

(319) Liu, Y.; Li, F.; Zhang, X.; Ji, X. Recent Progress on Electrochemical Reduction of CO_2 to Methanol, *Curr. Opin. Green Sustain. Chem.* **2020**, *23*, 10–17.

(320) Zhang, G.; Wang, T.; Zhang, M.; Li, L.; Cheng, D.; Zhen, S.; Wang, Y.; Qin, J.; Zhao, Z.-J.; Gong, J. Selective CO_2 Electroreduction to Methanol via Enhanced Oxygen Bonding, *Nat. Commun.* **2022**, *13*, 7768–7778.

(321) Li, X.; Wang, S.; Li, L.; Zu, X.; Sun, Y.; Xie, Y. Opportunity of Atomically Thin Two-Dimensional Catalysts for Promoting CO_2 Electroreduction, *Acc. Chem. Res.* **2020**, *53*, 2964–2974.

(322) Khaidar, D. M.; Isahak, W. N. R. W.; Ramli, Z. A. C.; Ahmad, K. N. Transition Metal Dichalcogenides-Based Catalysts for CO_2 Conversion: An Updated Review, *Int. J. Hydrogen Energy* **2024**, *68*, 35–50.

(323) Back, S.; Jung, Y. TiC-and TiN-Supported Single-Atom Catalysts for Dramatic Improvements in CO_2 Electrochemical Reduction to CH_4, *ACS Energy Lett.* **2017**, *2*, 969–975.

(324) Yang, C.; Wang, J.; Chen, Y.; Liu, D.; Huang, S.; Lei, W. One-Step Template-Free Synthesis of 3D Functionalized Flower-Like Boron Nitride Nanosheets for NH_3 and CO_2 Adsorption, *Nanoscale* **2018**, *10*, 10979–10985.

(325) Liu, T.; Wang, Q.; Wang, G.; Bao, X. Electrochemical CO_2 Reduction on Graphdiyne: A DFT Study, *Green Chem.* **2021**, *23*, 1212–1219.

(326) Qin, G.; Cui, Q.; Du, A.; Sun, Q. Borophene: A Metal-Free and Metallic Electrocatalyst for Efficient Converting CO_2 into CH_4, ChemCatChem **2020**, *12*, 1483–1490.

(327) Ling, C.; Li, Q.; Du, A.; Wang, J. Computation-Aided Design of Single-Atom Catalysts for One-Pot CO_2 Capture, Activation, and Conversion, *ACS Appl. Mater. Interfaces* **2018**, *10*, 36866–36872.

(328) Liu, Z.; Xu, D.; Xia, M.; Lu, W.-D.; Lu, A.-H.; Wang, D. Understanding the Unique Antioxidation Property of Boron-Based Catalysts During Oxidative Dehydrogenation of Alkanes, *J. Phys. Chem. Lett.* **2021**, *12*, 8770–8776.

(329) Kim, D.; Shi, J.; Liu, Y. Substantial Impact of Charge on Electrochemical Reactions of Two-Dimensional Materials, *J. Am. Chem. Soc.* **2018**, *140*, 9127–9131.

(330) Kohn, W.; Becke, A. D.; Parr, R. G. Density Functional Theory of Electronic Structure, *J. Phys. Chem. C* **1996**, *100*, 12974–12980.

(331) Kresse, G.; Furthmüller, J. Efficiency of Ab-Initio Total Energy Calculations for Metals and Semiconductors using a Plane-Wave Basis Set, *Comput. Mater. Sci.* **1996**, *6*, 15–50.

(332) Nørskov, J. K.; Rossmeisl, J.; Logadottir, A.; Lindqvist, L.; Kitchin, J. R.; Bligaard, T.; Jonsson, H. Origin of the Overpotential for Oxygen Reduction at a Fuel-Cell Cathode, *J. Phys. Chem. B* **2004**, *108*, 17886–17892.

(333) Li, H.; Chen, G.; Zhang, K.; Wang, L.; Li, G. Dually Sulphophilic Chromium Boride Nanocatalyst Boosting Sulfur Conversion Kinetics Toward High-Performance Lithium–Sulfur Batteries, *Adv. Sci.* **2023**, *10*, 2303830 (1–10).

(334) Guo, Y.; Zhu, H.; Zhao, H.; Zhao, Q.; Zhou, C.; Suo, B.; Zou, W.; Jiang, Z.; Li, Y. A Theoretical Study of the Electrochemical Reduction of CO_2 on Cerium Dioxide Supported Palladium Single Atoms and Nanoparticles, *Phys. Chem. Chem. Phys.* **2021**, *23*, 26185–26194.

(335) Baskaran, S.; Jung, J. Mo_2CS_2-MXene Supported Single-Atom Catalysts for Efficient and Selective CO_2 Electrochemical Reduction, *Appl. Surf. Sci.* **2022**, *592*, 153339–153345.

(336) Zhao, X.; Levell, Z. H.; Yu, S.; Liu, Y. Atomistic Understanding of Two-Dimensional Electrocatalysts from First Principles, *Chem. Rev.* **2022**, *122*, 10675–10709.

(337) Choi, C.; Gu, G. H.; Noh, J.; Park, H. S.; Jung, Y. Understanding Potential-Dependent Competition Between Electrocatalytic Dinitrogen and Proton Reduction Reactions, *Nat. Commun.* **2021**, *12*, 4353.

(338) Su, Z.; Gao, G.; Kang, J. Potential Effects in Electrochemical Oxidation of Carbon Monoxide Catalyzed by Rh-N-Doped Graphene, *J. Phys. Chem. C* **2024**, *128*, 9940–9947.

(339) Kuhl, K. P.; Hatsukade, T.; Cave, E. R.; Abram, D. N.; Kibsgaard, J.; Jaramillo, T. F. Electrocatalytic Conversion of Carbon Dioxide to Methane and Methanol on Transition Metal Surfaces, *J. Am. Chem. Soc.* **2014**, *136*, 14107–14113.

(340) Ren, X.; Zhao, J.; Li, X.; Shao, J.; Pan, B.; Salamé, A.; Boutin, E.; Groizard, T.; Wang, S.; Ding, J., et al. In-Situ Spectroscopic Probe of the Intrinsic Structure Feature of Single-Atom Center in Electrochemical CO/CO_2 Reduction to Methanol, *Nat. Commun.* **2023**, *14*, 3401 (1–10).

(341) Zha, W.; Liu, D.; Ma, Z.; Wang, Y.; Wei, Y.; Ma, X.; Wang, L.; Zhang, Q.; Lou, B.; Yuan, R., et al. Efficient Electrochemical CO_2 Reduction on C_2N Monolayer Supported Transition Metals Trimer Catalysts: A DFT Study, *Appl. Surf. Sci.* **2021**, *564*, 150331–150337.

(342) Li, X.; Bi, W.; Chen, M.; Sun, Y.; Ju, H.; Yan, W.; Zhu, J.; Wu, X.; Chu, W.; Wu, C., et al. Exclusive Ni–N_4 Sites Realize Near-Unity CO Selectivity for Electrochemical CO_2 Reduction, *J. Am. Chem. Soc.* **2017**, *139*, 14889–14892.

(343) Peterson, A. A.; Abild-Pedersen, F.; Studt, F.; Rossmeisl, J.; Nørskov, J. K. How Copper Catalyzes the Electroreduction of Carbon Dioxide into Hydrocarbon Fuels, *Energy Environ. Sci.* **2010**, *3*, 1311–1315.

(344) Xiao, H.; Li, H.; Li, X.; Jiang, J. Effect of the Charge State on the Catalytic Activity of a Fullerene-Based Molecular Electrocatalyst: A Theoretical Study, *J. Phys. Chem. Lett.* **2022**, *13*, 7392–7397.

(345) Masood, Z.; Ge, Q. Comparative Study of Computational Hydrogen Electrodes and Constant Electrode Potential Models Applied to Electrochemical Reduction of CO_2 and Oxygen Evolution Reaction on Metal Oxides/Copper Catalysts, *J. Phys. Chem. C* **2023**, *127*, 23170–23179.

(346) Sun, Z.; Ma, T.; Tao, H.; Fan, Q.; Han, B. Fundamentals and Challenges of Electrochemical CO_2 Reduction using Two-Dimensional Materials, *Chem* **2017**, *3*, 560–587.

(347) Hicks, M. H.; Nie, W.; Boehme, A. E.; Atwater, H. A.; Agapie, T.; Peters, J. C. Electrochemical CO_2 Reduction in Acidic Electrolytes: Spectroscopic Evidence for Local pH Gradients, *J. Am. Chem. Soc.* **2024**, *146*, 25282–25289.

(348) Ewis, D.; Arsalan, M.; Khaled, M.; Pant, D.; Ba-Abbad, M. M.; Amhamed, A.; El-Naas, M. H. Electrochemical Reduction of CO_2 into Formate/Formic Acid: A Review of Cell Design and Operation, *Sep. Purif. Technol.* **2023**, *316*, 123811 (1–24).

(349) Cai, B.; Chen, X.; Wang, L.; Fu, H. Advanced Progress for Promoting Anodic Hydrogen Oxidation Activity and Anti-CO Poisoning in Fuel Cells, *ACS Catal.* **2024**, *14*, 13602–13629.

(350) Yang, Y.; Shi, Y.; Yu, H.; Zeng, J.; Li, K.; Li, F. Mitigating Carbonate Formation in CO_2 Electrolysis, *Next Energy* **2023**, *1*, 100030 (1–8).

(351) Shi, Z.; Zhang, Y.; Zeng, W.; Zhou, Q. A DFT Study on Adsorption of SF_6 Decomposition Gases (H_2S, SO_2, SO_2F_2 and SOF_2) on Sc-$MoTe_2$ Monolayer, *Sens. Actuators A. Phys.* **2023**, *360*, 114548–114560.

(352) Piosik, E.; Szary, M. J. Development of MoS_2 Doping Strategy for Enhanced SO_2 Detection at Room Temperature, *Appl. Surf. Sci.* **2023**, *638*, 158013–158023.

(353) Zaman, A.; Shahriar, R.; Hossain, S. T.; Akhond, M. R.; Mumu, H. T.; Sharif, A. A Graphene-Like BeS Monolayer as a Promising Gas Sensor Material with Strain and Electric Field Induced Tunable Response: A First-Principles Study, *RSC Adv.* **2023**, *13*, 23558–23569.

(354) Lu, Z.; Zhai, Y.; Liang, Q.; Wu, W. Promoting Sensitivity and Selectivity of NO_2 Gas Sensor Based on Metal (Pt, Re, Ta)-Doped Monolayer WSe_2: A DFT Study, *Chem. Phys. Lett.* **2020**, *755*, 137737–137742.

(355) Nath, U.; Sarma, M. Realization of Efficient and Selective NO and NO_2 Detection via Surface Functionalized h-B_2S_2 monolayer, *Phys. Chem. Chem. Phys.* **2024**, *26*, 12386–12396.

(356) Wang, T.; Zhao, R.; Zhao, X.; An, Y.; Dai, X.; Xia, C. Tunable Donor and Acceptor Impurity States in a WSe_2 Monolayer by Adsorption of Common Gas Molecules, *RSC Adv.* **2016**, *6*, 82793–82800.

(357) Nath, U.; Sarma, M. CO_2 Activation and Electrochemical Reduction to CH_3OH via Charge Modulation on Defect-Induced Free-Standing Bilayer Borophene, *J. Phys. Chem. C* **2025**, *129*, 13939–13953.

(358) Sathishkumar, N.; Wu, S.-Y.; Chen, H.-T. Charge-Modulated/Electric-Field Controlled Reversible CO_2/H_2 Capture and Storage on Metal-Free N-Doped Penta-Graphene, *J. Chem. Eng.* **2020**, *391*, 123577–123386.

(359) Tan, X.; Tahini, H. A.; Smith, S. C. Materials Design for Electrocatalytic Carbon Capture, *APL Mater.* **2016**, *4*, 053202(1–9).

(360) Lee, C.-M.; Senthamaraikannan, T. G.; Shin, D. Y.; Kwon, J. A.; Lim, D.-H. Graphite-Supported Single Copper Catalyst for Electrochemical CO_2 Reduction: A First-Principles Approach, *Comput. Theor. Chem.* **2021**, *1201*, 113277–113284.

(361) Hussain, J.; Jónsson, H.; Skúlason, E. Calculations of Product Selectivity in Electrochemical CO_2 Reduction, *ACS Catal.* **2018**, *8*, 5240–5249.

(362) Fujimoto, Y.; Saito, S. Formation, Stabilities, and Electronic Properties of Nitrogen Defects in Graphene, *Phys. Rev. B Condens. Matter* **2011**, *84*, 245446 (1–7).

(363) Phuc, H. V.; Hieu, N. N.; Hoi, B. D.; Hieu, N. V.; Thu, T. V.; Hung, N. M.; Ilyasov, V. V.; Poklonski, N. A.; Nguyen, C. V. Tuning the Electronic Properties, Effective Mass and Carrier Mobility of MoS_2 Monolayer by Strain Engineering: First-Principle Calculations, *J. Electron. Mater.* **2018**, *47*, 730–736.